DISS. ETH NO. 24690

Numerical Modeling of Morphological Response of Gravel-Bed Rivers to Sediment Supply

A thesis submitted to attain the degree of

DOCTOR OF SCIENCES of ETH ZURICH

(Dr. sc. ETH Zurich)

presented by

LUKAS VONWILLER

MSc ETH Env Eng, ETH Zurich

born on 29.09.1981

citizen of St. Gallen

accepted on the recommendation of

Prof. Dr. Robert M. Boes

Prof. Dr. Guido Zolezzi

Prof. Dr. Yasuyuki Shimizu

Dr. David F. Vetsch

2017

Acknowledgments

At first, I would like to express my gratitude to my doctoral supervisor, Prof. Dr. Robert M. Boes for the great opportunity and support to do this research study at VAW, and to my supervisor, Dr. David F. Vetsch for his support and vision during this time.

I am grateful to the Federal Office for the Environment (FOEN) for their financial support of this research project, which was part of the interdisciplinary research program *Sediment and Habitat Dynamics* from 2014 till 2017.

I would like to thank the members of the committee, Prof. Dr. Guido Zolezzi from the University of Trento in Italy and Prof. Dr. Yasuyuki Shimizu from the Hokkaido University in Japan, for taking their time to read my thesis and providing valuable feedback.

Furthermore, I thank all my colleagues at VAW, in particular the software team of BASEMENT, for having time to discuss and share their ideas, and my office colleagues for the warm atmosphere. A special thank goes to Dr. Annunziato Siviglia for his support, great interest, and valuable feedback for this thesis.

Finally, my most sincere gratitude goes to my parents Brigitte and Hans-Martin Vonwiller, my brothers Christoph and Matthias, and to my family Wararat and Emilia, you are my source of energy and love.

Abstract

Many Swiss gravel-bed rivers suffer from a distinct sediment deficit. In most cases, the sediment continuity is interrupted by dams, run-of-river hydropower plants, or sediment traps. River training measures over the last two centuries have widely led to straight river reaches bounded by non-erodible embankments. Consequently, degradation and armoring of the river bed has been observed in many cases. Sediment replenishment by artificial gravel deposits provides a possible measure to reestablish sediment continuity. This technique has increasingly gained in popularity over the last decade or so. It has been applied in a number of Swiss gravel-bed rivers, such as the Aare, Limmat, Reuss, and Rhine Rivers.

The first part of this thesis focused on numerical 2-D modeling of the erosion process of artificial gravel deposits, where lateral erosion is the relevant process for gravel entrainment. The numerical model was first validated for lateral erosion in a straight channel with uniform sediment based on the laboratory experiment of Ikeda (1981). The relevant model approaches to successfully reproduce lateral erosion were the gravitational bank collapse, lateral bed slope effect, and local bed slope effect on incipient motion. Based on these findings the numerical model was compared against data from laboratory experiments on gravel deposit erosion of Friedl (2017). The dynamics of the lateral erosion process as well as the observed erosion rates were well reproduced by the numerical model. Hence, the numerical model proved to be a suitable tool to assess the erosion process of artificial gravel deposits for river engineering applications.

The second part focused on the effect of sediment supply reduction on alternate free migrating bars, forced steady bars due to a local obstacle, and a forced point bar in a river bend. An important research question of this thesis was inspired by the laboratory experiments of Venditti *et al.* (2012) reporting that free non-migrating bars partly migrated out of the flume, while forced steady bars were eroded after sediment supply termination. Therefore, the present thesis

intends to shed light on the influence of sediment supply reduction on alternate free and forced bars. The focus was on the competition between the bed slope reduction (morphological 1-D effect) and the free bars response (morphological 2-D effects). Therefore, a hybrid approach was applied combining linear stability theory for free bars and numerical modeling. Linear stability theory for free bars with reduced bed slope suggests that free bars instability persists, but with increased bar height and wavelength. Similarly, the numerical results show that free bars persist over a wide range of sediment supply reduction. However, below a certain but small sediment supply rate, free migrating bars transformed to a non-migrating steady bar pattern. This transformation was influenced by the decrease of bar celerity and the increase of bar height and wavelength. Finally, bar migration stopped due to the emergence of bar tops from the water surface.

Numerical simulations with forced steady bars suggest increased bar height and wavelength for reduced sediment supply. Moreover, indications of upstream overdeepening were found in the case of a major morphological 1-D effect. In the case of a point bar in a river bend, an equilibrium approach to account for the effect of spiral flow motion on bed load transport direction was validated using a laboratory experiment of Yen & Lee (1995). Based on a similar setup with a 180° bended flume, numerical simulations were performed to study the effect of sediment supply reduction on the point bar morphology and grain sorting. The simulation results for decreasing sediment supply indicated a more pronounced point bar morphology and a shift of the point bar in downstream direction, while the upstream overdeepening increased. The grain sorting effects in the bend resulted in different areas with coarsening of the river bed depending on the sediment supply rate. However, in the case of complete sediment supply termination, the coarsening was most pronounced along the thalweg.

Sediment replenishment leads mainly to deposition along the thalweg and affects bed surface texture. However, sediment replenishment alone (i.e. without additionally widening a river section) is not sufficient to trigger significant morphological changes, such as turning a flat river bed into alternate free bars. Sediment replenishment remains an important measure to locally improve aquatic habitat, such as bed substrate suitable for spawning fish. In the context of river restoration, the reestablishment of the sediment continuum is an important objective along with, for instance, the increase of river width, habitat variability, flood protection, and energy production.

Zusammenfassung

Kiesführende Flüsse in der Schweiz leiden tendenziell unter Geschiebemangel. In den meisten Fällen ist die Geschiebekontinuität durch Staudämme, Flusskraftwerke oder Geschiebesammler unterbrochen. Zudem wurden viele Flussabschnitte im Zuge der flussbaulichen Masssnahmen in den letzten beiden Jahrhunderten korrigiert, begradigt und die Ufer gesichert. Über längere Zeit führt dies zu einer Eintiefung und Vergröberung der Flusssohle. Diesem Trend wird vermehrt mit künstlichen Geschiebezugaben entgegenzuwirken versucht, wie aktuelle Beispiele an der Aare, Limmat, Reuss und am Rhein zeigen.

Im ersten Teil der Arbeit wird auf die numerische 2-D Modellierung des Erosionsprozesses von künstlichen Geschiebeschüttungen eingegangen. Zuerst wird das numerische Model anhand der Laborexperimente von Ikeda (1981) validiert. Die massgebenden Modellansätze zur Abbildung der lateralen Erosionsprozesse in einem geraden Kanal sind der Böschungskollaps, der Effekt des lateralen Sohlengefälles auf die Geschiebetransportrichtung und der Effekt des lokalen Sohlengefälles auf den kritischen Shieldsparameter. Darauf basierend wird das numerische Modell mit Laborversuchen zum Erosionsverhalten von Geschiebeschüttungen von Friedl (2017) validiert. Sowohl der beobachtete Erosionsprozess als auch die Erosionsraten aus den Laborversuchen können mit dem numerischen Modell gut wiedergegeben werden. Das numerische Modell stellt ein geeignetes Werkzeug dar, um das Erosionsverhalten von Geschiebeschüttungen und den Geschiebeeintrag für verschiedene Abflüsse in der Praxis abzuschätzen.

Im zweiten Teil der Arbeit wird der Einfluss der Geschiebezugabe bzw. der Geschiebereduktion auf migrierende alternierende Bänke, auf stationäre alternierende Bänke und auf eine Kurvenbank untersucht. Die numerischen Untersuchungen sind unter anderem inspiriert von Venditti *et al.* (2012), die in ihren Laborexperimenten beobachteten, dass nicht-migrierende alternierende Bänke nach einer Geschiebereduktion teilweise aus dem Gerinne gewandert sind. Zudem

beobachteten sie, dass durch ein Hinderniss erzwungene stationäre alternierende Bänke nach einer Geschiebereduktion erodiert wurden. Das Ziel der numerischen Untersuchung ist somit die Verbesserung des Prozessverständnisses beim Verhalten von alternierenden Bänken auf eine Geschiebereduktion. Die Resultate deuten darauf hin, dass migrierende alternierende Bänke für einen Grossteil der reduzierten Sedimentzugaben nicht stark beeinflusst werden. Im Falle von sehr geringen Sedimentzugaben oder einer kompletten Zugabereduktion findet jedoch eine Transformation in stationäre alternierende Bänke statt. Dieser Prozess wird hervorgerufen durch eine Verlangsamung der Bankmigration und eine Erhöhung sowohl der Wellenlänge als auch der Bankhöhe. Dieses Verhalten stimmt grundsätzlich gut mit der linearen Theorie zu migrierenden alternierenden Bänken (Adami *et al.*, 2016b) überein, welche für ein reduziertes Sohlengefälle alternierende Bänke mit grösseren Bankhöhen und im super-resonanten Regime auch mit erhöhter Wellenlänge prognostiziert.

Die stationären alternierenden Bänke werden durch ein lokales Hindernis erzwungen. Die Resultate zeigen, dass die stationären alternierenden Bänke aufgrund einer Geschiebereduktion nicht erodiert werden. Es zeigt sich vielmehr, dass diese länger und höher werden. Im Falle von grösseren Sohlengefällsreduktionen sind Anzeichen von super-resonanten stationären Bänken oberstrom des Hindernisses zu erkennen. Schlussendlich wird das numerische Model mit einem Gleichgewichtsansatz zur Berücksichtigung des Einflusses der Kurvenströmung auf die Geschiebetransportrichtung anhand der Laborexperimente von Yen & Lee (1995) in einer 180° Kurve validiert. Die Untersuchung des Einflusses einer Geschiebereduktion auf die Morphologie einer vereinfachten 180° Kurve zeigt, dass die Kurvenbank durch Erosion an der Kurvenaussenseite stärker ausgeprägt ist im Falle von geringer Geschiebezugabe. Zudem resultiert eine starke Vergröberung der Flusssohle in der Kurve vor allem entlang dem Thalweg.

Geschiebezugaben als alleinige Massnahme werden nicht ausreichen, um morphologische Veränderungen in korrigierten kiesführenden Flüssen hervorzurufen. In den meisten Fällen ist eine Aufwertung der Flussmorphologie nur über eine zusätzliche Erhöhung der Flussbreite bzw. des Verhältnisses der Flussbreite zu Fliesstiefe zu erreichen. Es ist davon auszugehen, dass Geschiebezugaben vor allem lokale Effekte auf das Sohlensubstrat haben. Geschiebeschüttungen stellen somit eine sinnvolle Massnahme dar, aquatische Habitate lokal zu verbessern und geeignetes Sohlensubstrat für kieslaichende Fische zur Verfügung zu stellen.

Contents

1. Introduction

1.1. Background and Motivation

Many Swiss gravel-bed rivers suffer from a distinct sediment deficit. In most cases, sediment continuity is interrupted by dams, bed load traps, or run-of-river (ROR) hydropower plants (HPPs). Furthermore, river training measures in the last two centuries have widely led to straight river reaches bounded by non-erodible embankments. Consequently, river bed degradation has been observed in many cases (Schaelchli *et al.*, 2010). This typically results in armoring of the river bed, monotone river morphology, poor aquatic habitat, and destabilized foundations of infrastructure, such as bridges or dikes (Kondolf, 1997).

The revised Swiss water protection act (Gewässerschutzgesetz, GSchG) is in force since January 2011. This new legislative rule has given impetus to restore Swiss rivers to near-natural state as far as meaningfully possible. In particular, the impact of ROR-HPPs on sediment continuity needs to be addressed in the future. Consequently, bed load transport has to be restored by appropriate measures by the ROR-HPP operators.

Sediment replenishment by artificial gravel deposits (Fig. 1.1) is a possible measure to reestablish sediment continuity, e.g. below ROR-HPPs. Increased sediment supply is intended to stimulate morphological processes, and to improve aquatic habitat such as spawning ground for fishes (Zeug *et al.*, 2014). Meanwhile, this technique has been applied worldwide, for example, at the Reuss, Limmat, and Aare River in Switzerland (Schaelchli *et al.*, 2010), at the Moosach, Lech, and Isar River in Germany (Pulg, 2007), at the Trinity River, in the US State of California (Krause, 2012), at the Nunome River, and several other rivers in the Kizu River basin in Japan (Ock *et al.*, 2013). However, there are many open questions concerning the erosion process of artificial gravel deposits and the

Fig. 1.1.: Artificial gravel deposits at the Limmat River in Zurich, 2015 (left) and at the Aare River in Worblaufen, 2016 (right); Photos: L. Vonwiller

numerical modeling approaches needed to reproduce this dynamic process in detail. Furthermore, the effect of changes in sediment supply on river morphology, e.g. alternate bars, has not yet been fully understood.

The Federal Office for the Environment (FOEN) launched the interdisciplinary research program *Sediment and Habitat Dynamics* from 2014 till 2017. The main topics included sediment continuum, flood plains, and aquatic habitat for macro-invertebrates, fish and plants. Thereby, the focus was both on alpine streams and lowland gravel-bed rivers. The presented thesis was part of this research program and co-funded by FOEN.

1.2. Objectives

In a first phase of the thesis, the focus was put on numerical modeling of lateral erosion and in particular on the erosion process of artificial gravel deposits. As a first step, relevant numerical model approaches for lateral erosion should be identified and validated based on laboratory experiments of lateral erosion in straight channels (Ikeda, 1981). Based on this, the numerical model should be applied to reproduce the laboratory experiments of Friedl *et al.* (2018) on the erosion process of artificial gravel deposits (Fig. 1.2). With regard to the spatial scale, the erosion process takes place locally, while regarding the temporal scale, this process takes place mainly during flood events. The goal of this phase was to provide a validated tool supporting the planning of sediment replenishment by artificial gravel deposits.

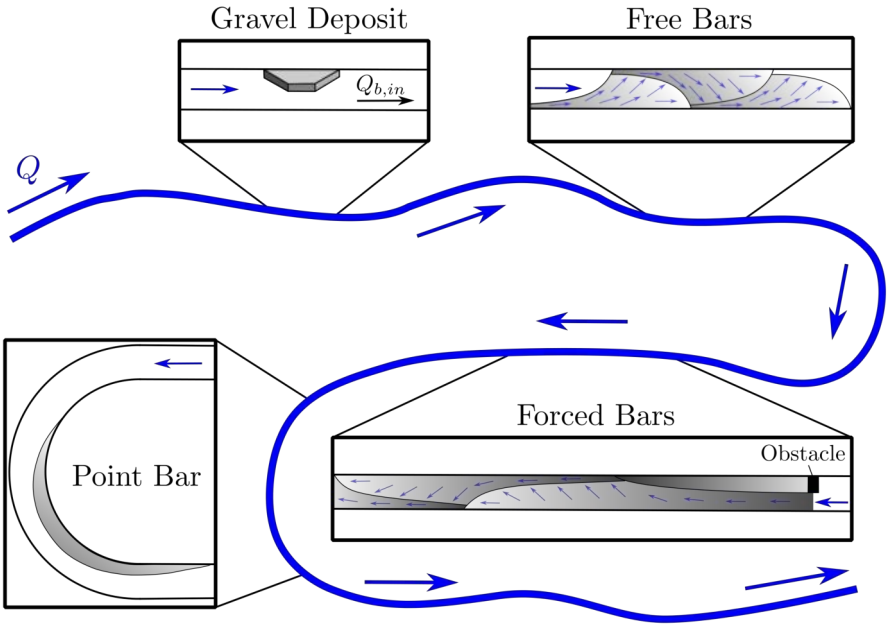

Fig. 1.2.: Conceptual sketch of the relevant processes, such as the erosion of artificial gravel deposits, the effect of sediment supply reduction on free bars and forced bars, and on a point bar in a river bend

In a second phase of the thesis, the goal was to investigate the effect of sediment supply on the morphology of gravel-bed rivers with non-erodible embankments. Generally, a sediment supply reduction (increase) leads to a bed slope decrease (increase). This morphological 1-D effect is studied in the present thesis by means of sediment supply reduction starting from equilibrium conditions. The focus was put on alternate bars morphology (free and forced bars) and a point bar in a river bend (see Fig. 1.2). The former puts the focus on reach scale effects with rather long morphological time scales, e.g. in the order of decades. For the latter, however, the grain sorting and erosion processes are rather local, while the temporal scale is on an intermediate level, with a shorter time scale for grain sorting effects and a medium time scale for the erosion process. For the simulation of river bends, an approach to account for the effect of spiral flow motion on the bed load transport direction has to be taken into account. The data from the laboratory experiment of Yen & Lee (1995) may be used for validation.

Another reason to study the effect of sediment supply reduction, in contrast to supply increase, was based on laboratory experiments from literature. For instance, Venditti *et al.* (2012) observed that free non-migrating bars started to migrate out of the flume after sediment supply termination, whereas forced bars

were eliminated by local erosion. On the other hand, Lisle *et al.* (1993) observed that free non-migrating bars started to emerge from the water surface after sediment supply decrease. These somewhat contradictory observations served as additional motivation for the present research project.

From that, the relevant research questions can be formulated as follows:

- What are the key model approaches and governing parameters required for numerical modeling of the erosion process of artificial gravel deposits?
- How do free migrating bars respond to sediment supply reduction? Do they migrate out of the channel after sediment supply termination?
- How do forced steady bars in a straight channel and a point bar in a river bend respond to sediment supply reduction?

The first research question is related to the first phase of the thesis and is relevant for the application of the numerical model for sediment replenishment by artificial gravel deposits. The second and third research questions are subject to the second phase of the thesis. This phase intends to shed light on the response of alternate bars and a point bar in a river bend to sediment supply reduction.

1.3. Methodology

This thesis is dedicated to the numerical modeling of the governing fluvial processes. This includes the erosion of artificial gravel deposits and the effect of sediment supply on river morphology, such as alternate bars and river bends with non-erodible embankments. Therefore, the numerical 2-D model of the software BASEMENT was used and further developed in the scope of the presented thesis. The software BASEMENT has been developed at the Laboratory of Hydraulics, Hydrology, and Glaciology (VAW) at ETH Zurich since 2002 (Vetsch *et al.*, 2017a) and can be downloaded for free.

In the first phase of this thesis, the numerical model was tested against laboratory data from gravel deposit erosion experiments at VAW. The latter were carried out in parallel to this work and in the scope of the PhD project of Friedl (2017). This composite modeling approach, combining laboratory and numerical models, helped to gain further insights on the erosion process of artificial gravel deposits.

In the second phase, linear stability theory for free bars was used to plan the setup of the numerical experiments and predict and verify the response of free bars to sediment supply reduction. Therefore, the TREMTO tool (Adami *et al.*, 2016b) was used, which includes the linear stability theory for free bars of Colombini *et al.* (1987).

1.4. Thesis Outline

The present thesis is divided into nine chapters. First, the literature review is given in Chap. 2 focusing on sediment replenishment, morphological response to sediment supply, alternate bars, river bend morphology and lateral erosion. Relevant fundamentals, such as bed load transport processes and linear stability theory for free bars, are presented in Chap. 3. The numerical 2-D model is presented in Chap. 4. The numerical model is validated in Chap. 5 based on laboratory experiments for lateral erosion in straight channels, morphology and grain sorting in a river bend, and free bars in straight channels. Subsequently, numerical simulations are performed on the local erosion process of artificial gravel and compared to laboratory experiments (Chap. 6). The morphological effects of sediment supply reduction focuses on free migrating bars (Chap. 7), forced bars due to a local obstacle on a reach scale, and a point bar in a river bend (Chap. 8). Finally, Chap. 9 summarizes and reaches conclusion on the presented findings along with some recommendations for practical application and an outlook on further research.

2. Literature Review

2.1. Sediment Replenishment by Artificial Gravel Deposits

Sediment replenishment by artificial gravel deposits is a possible measures to increase sediment supply in gravel-bed rivers. Therefore, sediment is obtained from sediment traps, stone quarries, and gravel pits or is excavated upstream of a run-of-river hydropower plant (ROR-HPP). Transport to the replenishment site is mostly done by heavy truck or conveyor belt. Finally, gravel is placed by front end loader or excavator. In some cases, gravel is directly entrained by the flow. In most cases however, artificial gravel deposits are placed in the form of gravel bars along the river embankment. Hence, the gravel will be eventually entrained during flood events.

The main objectives of artificial gravel deposits are (i) to reestablish bed load transport, (ii) to enhance aquatic habitat for macroinvertebrates, plants and fish, and (iii) to protect infrastructure by preventing further degradation (e.g. Bunte, 2004; Kondolf & Minear, 2004; Roni *et al.*, 2008). Artificial gravel deposits differ in the method of gravel addition (direct or indirect gravel addition, see Fig. 2.1), in the spatial scale of application (local, multi-reach and river-reach wide), and in the temporal scale of application (unique or reoccurring addition) (e.g. Bunte, 2004; Kondolf *et al.*, 2008).

With the method of indirect gravel addition, gravel deposits are created at logistically convenient places that are also hydraulically suitable for gravel entrainment (Bunte, 2004). In the case of lowland rivers, gravel deposits are placed into the low-flow zone, directly on the river bed (low-flow stockpile). Consequently, the gravel will be entrained during design flood, dispersed, and eventually deposited downstream. This is a natural distribution and restoration process. The indirect

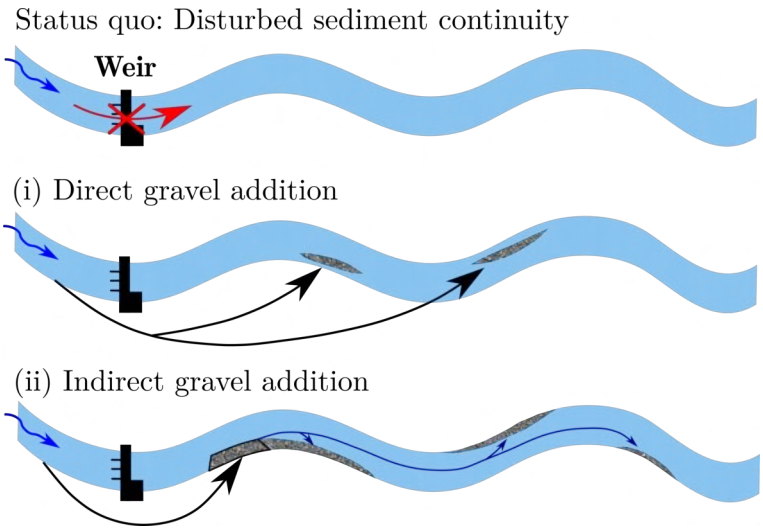

Fig. 2.1.: Direct vs. indirect gravel addition

gravel addition is the more popular method due to lower costs, practical feasibility and better site access (Bunte, 2004).

Using the method of direct gravel addition, morphological structures and aquatic habitats are directly created by appropriate gravel placement. For instance, gravel bars and riffles can be created in low velocity zones in order to re-establish spawning habitat for fish. This approach is limited, since access to the river site is often not straightforward. Furthermore, these artificial structures have to be placed carefully, otherwise they will be eroded completely during subsequent flood events (Pasternack *et al.*, 2004).

Schaelchli *et al.* (2010) report on sediment replenishment by artificial gravel deposits at two sites in the Aare River, in Switzerland. The plan form of the gravel deposit was similar to a long gravel bar and the height of the gravel deposit was designed such that small flood events can erode and disperse the gravel (indirect gravel addition). At the site in Aarwangen, downstream of the Bannwil ROR-HPP, volumes of 11.000 m^3 and 10.000 m^3 were added in 2005 and 2010, respectively (Fig. 2.2, left). At the site in Deitingen, downstream of the Flumenthal ROR-HPP, a volume of 12.000 m^3 was added in 2005 (Fig. 2.2, right). The gravel for the deposit at Deitingen was taken from a sediment retention basin of a tributary, the Emme River. The gravel for the deposit at Aarwangen was taken from a gravel pit, where the fine sediments were removed in order to reduce turbidity in the river. The maximum grain size diameter was around 50 mm and 60 mm for the sites in Aarwangen and Deitingen, respectively. The gravel deposit

Fig. 2.2.: Gravel deposit at the Aare River, at the sites Aarwangen (left) and Deitingen (right) in Switzerland, Photos: Flussbau AG

at Deitingen has been eroded more slowly than the one at Aarwangen, mainly due to the lower bed slope and the coarser grain size distribution. The main objective was to restore bed load transport and to enhance the aquatic habitat, e.g. for fish. Downstream of the gravel deposits a higher density of grayling larvae *Thymallus thymallus* was observed (Schaelchli *et al.*, 2010). Similar case studies can be found at the Moosach River, Lech River, and Isar River in Bavaria, Germany (Pulg, 2007).

At the Trinity River, in California (USA), gravel additions have been carried out since 1972 (Krause, 2012). The main objectives were to improve spawning habitat for salmon and to restore bed load transport. Gravel is added at several locations along a 20 km river reach downstream of the Lewiston Dam, where the average bed slope is approximately 0.25 %. During low-flow periods, gravel deposits were placed in the river (low-flow stockpiles), which were eventually eroded and dispersed by the flow. During high-flow releases, additional gravel was mechanically added and immediately entrained by the flow (Krause, 2012; Gaeuman, 2014). Both approaches represent methods of indirect gravel addition. The annually inserted gravel volume depends on the water availability in each year. On average, an annual volume of about 1.500 m^3 has been added, with up to 51.000 m^3 in particularly wet years. Gravel has been taken from on-site sources, e.g. old gravel pits, and was sorted out to have appropriate size for spawning salmon. The Trinity River Restoration Program has led to an improved aquatic habitat and restoration of spawning ground for salmon. Nevertheless, in an upcoming second phase of the project further improvements are planned (Buffington *et al.*, 2014). On the west coast of the USA several river rehabilitation projects can be found applying gravel additions for improving spawning habitat for salmon, such as in the Merced River (Stillwater Sciences, 2001, 2002; Albertson *et al.*, 2011; Downs *et al.*, 2011; Romanov *et al.*, 2012; Utz *et al.*, 2013), the

Lower Tuolumne River (McBain and Trush, 2004), Mokelumne River (Merz & Chan, 2005; Elkins *et al.*, 2007), and other coastal gravel-bed rivers in California, such as Jacoby, Prairie, and North Caspar Creeks (Lisle, 1989; Lisle & Lewis, 1992).

The Rhine River downstream of the ROR-HPP Iffezheim in Germany suffers from severe sediment deficit. To counteract this, gravel is brought into the river by large cargo ships. These measures have to be applied continuously in order prevent further erosion of the river bed and to protect infrastructure along the river in the long term. Annual replenishment volumes range between 100.000 m^3 and 215.000 m^3 (Kondolf, 1997; WSA, 2006). The gravel-sand mixture comes from local gravel pits. Since 1991, the mixture consists of 12 % sand and fines (< 2 mm), 12 % fine gravel (2-8 mm), 26 % medium gravel (8-16 mm), 25 % medium to coarse gravel (16-32 mm), and 25 % coarse gravel (> 32 mm) (WSA, 2006). Similar gravel additions are carried out at the Elbe River (Germany) between Mühlberg and the confluence with the Saale River (WSV, 2008). Since 1996, a gravel-sand mixture has been added to prevent further river bed erosion. Annual replenishment volumes range between 30.000 m^3 and 60.000 m^3. A similar case can be found at the Danube River in Austria, below the Freudenau ROR-HPP in Vienna. Interestingly, in this case, the river bed was further stabilized by adding only coarser fractions (40-70 mm) of naturally transported bed load material (Habersack & Doppler, 2011).

2.2. River Morphology Response to Sediment Supply

Venditti *et al.* (2012) performed experiments on the influence of sediment supply on alternate bars using both a laboratory flume and a field scale flume. In the former, alternate free non-migrating bars were formed, whereas in the latter alternate forced steady bars were formed due to an upstream channel constriction. Interestingly, in both cases alternate bars were observed to be eliminated after sediment supply termination. However, the mechanism for bar disappearance differed for the two experiments. The free non-migrating bars started to migrate downstream after sediment supply termination, while the forced bars were locally eroded (Venditti *et al.*, 2012). Lisle *et al.* (1993) performed laboratory experiments

to study the response of free non-migrating bars to sediment supply reduction. In contrast to the experiments of Venditti *et al.* (2012), they observed that higher areas of the bars emerged from the water surface due to incision along the thalweg.

Podolak & Wilcock (2013) performed laboratory experiments on the effect of sediment supply increase on a steady bar pattern. The steady bar morphology was forced by an obstacle occupying 25 % of flume width near the upstream boundary. Water and sediment were recirculated in the flume. However, sediment feed was increased twice during the experiment. As a consequence, the bed slope increased after each sediment feed. In this transition period towards a new equilibrium state, free bars with shorter wavelength formed and migrated over the steady bar pattern. The forced steady bars temporally disappeared during this period. In the end, however, the forced bar pattern prevailed again at the equilibrium state.

Nelson *et al.* (2015) performed laboratory experiments on the response of sediment supply to a straight channel with a sinusoidal varying width of non-erodible embankments. Starting from equilibrium conditions, sediment supply was terminated to create a sediment-starved river bed. Then sediment supply was increased either by using constant equilibrium sediment supply or by adding a sediment pulse of four times the equilibrium sediment supply. The main response to sediment supply was bed slope adjustment. However, the locations of pools and riffles persisted regardless of sediment supply (Nelson *et al.*, 2015).

Eaton & Church (2009) performed laboratory experiments on the effect of sediment supply using a sinusoidal channel with non-erodible embankments. The primary channel response to sediment supply was an adjustment of the bed state, such as change in grain size distribution (GSD) on the bed surface. However, the bed slope was affected only beyond a certain bed state adjustment. Based on Parker's bed load formula (Parker, 1990), they claimed that bed state adjustment would be able to absorb the fourfold of the sediment supply changes without significant effect on the bed slope (Eaton & Church, 2009).

Viparelli *et al.* (2011) analyzed the effect of gravel replenishment for the Trinity River using a numerical 1-D model. After removal of several dams, fine sediments filled up major parts of the pools along the river. Consequently, salmon population decreased dramatically due to the loss of spawning grounds. They concluded that

a combination of artificial floods and gravel replenishment is expected to recover and coarsen the river bed surface texture. Hence, spawning habitat quality for salmon could be potentially increased by gravel replenishment (Viparelli *et al.*, 2011).

Various laboratory experiments on the propagation of sediment deposits and sediment waves, sometimes also referred to as sediment pulses, and the effect on river morphology can be found in literature. Lisle *et al.* (1997, 2001) found sediment wave propagation to be predominantly dispersive with only little evidence of translation. The dispersive propagation of the wave showed no significant effect on a free migrating alternate bar morphology (Lisle *et al.*, 1997). Cui *et al.* (2003a) performed laboratory experiments on sediment deposit propagation focusing on the influence of grain size. The initial topography consisted of an armored river bed with three wavelengths of alternate bars in the lower half of the flume. Sediment deposits were observed to propagate along the flume by translation, dispersion, or a combination of both. However, dispersion was found to be dominant in most experiments. When the grain size of the deposit was the same as the sediment feed, dispersion of the deposit was the dominant process. Furthermore, the alternate bar pattern in the lower half of the flume was suppressed and the coarser surface layer showed increased mobility compared to the reference state. When the grain size of the deposit was coarser than the sediment feed, the erosion of the deposit was much slower and strongly dispersive. In this case, only a weak tendency to flatten out the alternate bars was observed. When the grain size of the deposit was finer than the sediment feed, the erosion process was the fastest and showed significant translation in addition to dispersion. Alternate bars were washed out completely. Furthermore, the armor layer disappeared due to an increased mobility of the coarser fractions (Cui *et al.*, 2003a). Cui *et al.* (2003b) compared their experimental findings described above with numerical 1-D simulations. The model successfully reproduced the predominantly dispersive deformation of sediment deposits. However, the model had some difficulties to reproduce translation in the case of the fine gravel deposit. Venditti *et al.* (2010) performed laboratory experiments on the effect of the grain size of the replenishment on the river bed mobility. They observed decreasing flow roughness and increasing flow velocity in the case of finer sediments added to a coarser bed. Eventually, this mobilized coarser grain fractions, broke up the armor layer and hence, led to finer river bed composition. Sklar *et al.* (2009)

observed deposit movement to experience increased translation for smaller deposit volume and finer deposit material. Furthermore, larger deposit volumes were found to create longer-lasting improvements in bed texture compared to smaller deposit volumes (Sklar *et al.*, 2009). Humphries *et al.* (2012) found significant influence of the discharge hydrograph on the deposit movement type (translation or dispersion). Hydrographs with larger peaks and steeper rising and falling limbs increased translation of gravel deposit propagation. However, smaller, more flat hydrographs caused predominantly dispersive behavior (Humphries *et al.*, 2012).

Elgueta-Astaburuaga & Hassan (2017) investigated the effect of different sediment feed scenarios. The sediment feed scenario affected mainly bed slope (sediment storage), bed load transport, and bed surface texture. The relaxation time was defined as the time required for the bed load transport rate to readjust to nearly no feed conditions. Multiple small sediment pulses were found to have a similar effect on bed load transport and sediment storage as a constant feed rate, especially if the relaxation time was larger than the time between two pulses (Elgueta-Astaburuaga & Hassan, 2017).

Several field studies, partly combined with laboratory experiments, were reported to examine phases of river bed degradation (e.g. after dam construction) and river bed aggradation (e.g. after dam removal). Madej *et al.* (2009) performed laboratory experiments based on the Redwood Creek (California, USA) by applying two consecutive cycles of sediment feeding and sediment termination. Beforehand, an initial steady alternate bar morphology was established without sediment feed. The main response to sediment feed was increased bed slope due to sediment storage, and finer bed surface texture. For moderate sediment feed river morphology was not significantly affected compared to pre-feed condition. However, for larger sediment feed, bed surface texture became even finer, and the main channel filled up completely. Hence, the cross-channel bed relief decreased during this phase. The main channel shifted to the other side of the flume at certain locations. Pryor *et al.* (2011) reported laboratory experiments based on the Cuneo Creek (California, USA) using even more cycles of aggradation and degradation. They observed a hysteresis effect between the bed load transport rate and the storage volume (bed slope) in the flume. Bed load transport rates (for a given storage volume) were smaller during aggradation compared to phases during degradation. Furthermore, sediment input increase resulted in an increase

of the wetted width, a more shallow channel, and a braided pattern. However, as sediment input was decreased again, bed slope decreased, bed texture became coarser, and a single-thread channel was observed again (Pryor *et al.*, 2011). Similar observations were reported by Marti (2006) in laboratory experiments on braided rivers. Marti (2006) performed laboratory experiments on braided river morphology and reduced sediment supply to 20 % of the initial bed load transport capacity. As a result, the most dominant river branch started to degrade vertically. Consequently, water flow increasingly concentrated in a single river branch, which finally resulted in a single-thread channel (Marti, 2006). In addition, some field surveys focused on river morphology response to sediment supply after dam removal (e.g. Major *et al.*, 2012; East *et al.*, 2015). East *et al.* (2015) observed over all aggradation of about one meter and locally even more where pools were filled up with sediment. River morphology changed from a pool-riffle pattern to a braided pattern. However, increased fine sediment input had significant negative ecological effects, e.g. clogging of river bed (East *et al.*, 2015).

2.3. Morphology of Alternate Bars

Alternate bars can be subdivided into free migrating bars and forced steady bars (Colombini *et al.*, 1987; Zolezzi *et al.*, 2005). The former, also referred to as free bars, can be attributed to an intrinsic instability mechanism of water flow and non-cohesive sediment transport in nearly straight channel (Colombini *et al.*, 1987). The latter, herein referred to as steady bars, are forced due to a local planform discontinuity, such as a river curvature or a local flow contraction (Zolezzi & Seminara, 2001). An interesting example for free bars and steady bars can be found at the Alpine Rhine River. Adami *et al.* (2016a) analyzed Landsat images of alternate bars at the Alpine Rhine River covering a period of 30 years. The evaluated river reach was 41.7 km long from the confluence of the Landquart River to the confluence of the Ill River. As a result of their analysis, longer non-migrating bars were detected in the upper subreach, whereas shorter free migrating bars were found in the lower subreach. Bar wavelength of free migrating bars and steady bars compared well to the prediction from linear stability theory for free and forced bars, respectively (Adami *et al.*, 2016a).

Laboratory experiments on alternate bars were reported in literature by various

researchers (e.g. Ikeda, 1982c; Jäggi, 1983; Lanzoni, 2000a,b; Crosato *et al.*, 2011). For instance, Ikeda (1982c) performed laboratory experiments on free bars using uniform sediment ($d_m = 1.3\,\text{mm}$, $\sigma = 0.3\,\text{mm}$). The straight flume was 15 m long and 0.32 m wide and was able to cover a wide range of bed slopes ($0.0496 \leq S \leq 0.0186$). Different empirical relations were proposed for wavelength and bar height (see Ikeda, 1982c). Jäggi (1983, 1984) performed laboratory experiments on the formation of free bars using different but fairly uniform sediment mixtures (sand and PVC granulate, $0.52 \leq d_m \leq 4.0\,\text{mm}$). The flume was 15 m long and 0.3 m wide and allowed for bed slope adjustment ($0.012 \leq S \leq 0.02$). An empirical criteria for free bar formation was proposed as a function of the bed slope S and the ratio of river width to mean grain size W/d_m (see Jäggi, 1984).

Lanzoni (2000a,b) performed laboratory experiments on free bars using uniform sediment (Lanzoni, 2000a) and non-uniform, bi-modal sediment (Lanzoni, 2000b). The geometric mean grain size was $d_g = 0.48\,\text{mm}$ and $d_g = 0.49\,\text{mm}$ and the geometric standard deviation was $\sigma_g = 1.3$ and $\sigma_g = 3.3$ for uniform and non-uniform sediment, respectively ($d_g = \sqrt{d_{84}d_{16}}$ and $\sigma_g = \sqrt{d_{84}/d_{16}}$ for log-normal GSD). The flume was 55 m long and 1.5 m wide, and allowed for bed slope adjustment between 0.16 % and 0.52 %. The free bar height was found to be smaller for non-uniform sediment compared to uniform sediment. However, the bar wavelength was comparable in both cases.

Crosato *et al.* (2011) performed laboratory experiments on free bars and steady bars using uniform sediment ($d_{50} = 0.238\,\text{mm}$). The flume was 26 m long, 0.6 m wide, and had a bed slope of 0.374 %. The aspect ratio β indicated super-resonant conditions ($\beta > \beta_R$, see Chap. 3.4.1). Initially, free bars were continuously formed in the lower half of the flume and migrated downstream. After three weeks, they observed a first stabilizing non-migrating bar, which consequently grew in amplitude. Then, after six weeks, two more non-migrating bars were observed. This observation was supported by reproducing non-migrating bar pattern using a numerical 2-D model. They assumed that the free bar morphology could represent only a transient stage and therefore, would not be representative for the final morphological pattern. Accordingly, the non-migrating bars could be an intrinsic response of alluvial river bed and might play an important role for incipient meandering (Crosato *et al.*, 2011).

Eekhout *et al.* (2013) performed a long-term field-scale experiment on the free bar development in a straight sand-bed channel and the influence of an unsteady discharge. Theoretical approaches from Tubino (1991) and Crosato & Mosselman (2009) confirmed the presence of free bars observed in the field-scale experiment.

Various authors proposed a linear stability theory for small amplitude free bars in straight channels with non-erodible embankments (e.g. Callander, 1969; Parker, 1976; Blondeaux & Seminara, 1985; Colombini *et al.*, 1987; Tubino, 1991; Schielen *et al.*, 1993; Tubino *et al.*, 1999; Lanzoni & Tubino, 1999; Lanzoni, 2000a). As a result, the critical aspect-ratio (half width-to-depth ratio) can be determined, above which free bar instability theoretically occurs, for a given discharge, bed slope, and grain size. The dominant wavelength can be attributed to the fastest, exponentially growing, small amplitude perturbation (Colombini *et al.*, 1987). Furthermore, Colombini *et al.* (1987) proposed a weakly non-linear analytical predictor of equilibrium bar height by introducing a dampening term for exponential bar growth. Blondeaux & Seminara (1985) found the resonant threshold value for the governing parameters, where non-migrating and non-amplifying free bars theoretically occur. They found that this resonance controls river meander growth and hence they found a link between the free bar theory and the bend theory of river meanders. Schielen *et al.* (1993) showed that fluctuations of the bar amplitude occur due to a dispersive behavior of wave groups. The minimum length scale to observe this phenomena is 65 times the flume width (Schielen *et al.*, 1993). Weakly non-linear theories were proposed to study the influence of an unsteady discharge on free bar instability (Tubino, 1991), or the effect of meander curvature on free bar instability (Tubino & Seminara, 1990). Lanzoni (2000a) developed a linear stability theory taking into account the curvature effect, dispersive effects due to depth-averaging, and the influence of local bed slope on the bed load transport rate. The linear stability model agreed fairly well with observations from experiments using uniform sediments, especially in terms of bar wavelength and bar celerity (Lanzoni, 2000a). Lanzoni & Tubino (1999) prosed a linear stability theory for non-uniform sediment using two grain classes. They found that for large Shields stress free bar instability is decreased, while for Shields stress near the threshold value of incipient motion, free bar instability is increased compared to uniform sediment.

Various numerical 2-D studies on alternate bar development have been reported

in literature (e.g. Takebayashi *et al.*, 1999; Defina, 2003; Jang & Shimizu, 2005; Crosato *et al.*, 2011; Siviglia *et al.*, 2013; Iwasaki *et al.*, 2016; Qian *et al.*, 2017). For instance, Takebayashi *et al.* (1999) performed numerical 2-D simulations using a finite difference method. Free bars were triggered by placing an obstacle near the inflow boundary on the right side of the channel. They focused on the effect of uniform and non-uniform sediments. In the case of uniform sediment, free bar wavelength and bar height were larger and hence, bar celerity was smaller, compared to non-uniform sediment. This behavior was attributed to a smaller lateral variation of bed shear stress in the case of non-uniform sediment (Takebayashi *et al.*, 1999).

Defina (2003) simulated free bars using a numerical 2-D finite element model with uniform sediment. The main focus was to study different approaches to trigger free migrating bars. This was mainly investigated by using initial topographies containing different wavelength. Bar development as well as equilibrium characteristics (wavelength, bar height, bar celerity) was strongly affected by the selected wavelength of the initial topography. Alternatively, free bars were triggered using an initial topography containing multiple erodible bumbs on the left side of the channel, and a periodic single erodible bumb perturbation near the upstream boundary. For the former, free bars were triggered at different locations and hence, interaction was observed between two consecutive trains of free bars. For the latter, free bar amplification did strongly depend on the frequency at which the bumb was added to the channel.

Bernini *et al.* (2009) performed numerical 2-D simulations using a finite difference method with uniform sediment. Free bars were triggered by an erodible bump near the inlet. Hence, a train of free bars formed, migrated downstream, and eventually moved out of the domain. Free migrating bar development and bar properties were found to depend strongly on the lateral bed slope effect. Bar height, bar wavelength, and bar celerity compared reasonably well with experimental data, empirical approaches, and numerical results from literature.

Siviglia *et al.* (2013) performed numerical 2-D simulations using a finite volume method with uniform sediment. Steady bars in a straight flume were forced by an obstacle occupying 50 % of the flume width. The numerical model fairly well reproduced the sub-resonant and the super-resonant steady bar formation showing the characteristic downstream and upstream overdeepening (non-migrating

spatially decaying bars), respectively.

Qian *et al.* (2017) performed numerical 2-D simulations of free bars with uniform and non-uniform sediments. The model was validated using laboratory experiments from Lanzoni (2000a,b). However, free bars were not triggered by random initial bed perturbation (Lanzoni, 2000a), but rather by introducing a small bump occupying half the channel width. The model successfully reproduced coarser bar heads and finer pools for full transport (transport of all grain classes). Furthermore, finer bar heads and coarser pools were obtained for partial bed load transport (with some immobile grain classes), as this would explain some ambiguities from previous studies on grain sorting over alternate bars (Qian *et al.*, 2017).

2.4. River Bend Morphology with Non-erodible Embankments

Experiments on 180° river bends in laboratory flumes have been performed by various researchers (see e.g. Rozovskii, 1961; Struiksma *et al.*, 1985; Odgaard & Bergs, 1988; Yen & Lee, 1995; Zolezzi *et al.*, 2005; Blanckaert, 2011). Struiksma *et al.* (1985) performed laboratory experiments with four different bend planforms including a mild bend ($B/R = 0.13$), a moderate bend ($B/R = 0.4$), and a sharp bend ($B/R = 0.68$). They presented six runs using steady inflow and equilibrium sediment transport rates at the upstream boundary. The medium grain size was between 0.3 and 0.8 mm with a geometric standard deviation in the range of $0.19 < \sigma_g < 2.3$. The morphological changes were analyzed for equilibrium conditions. Additionally, Struiksma *et al.* (1985) performed numerical 2-D simulations using the uniform bed load formula of Engelund & Hansen (1972). The bed load transport direction was corrected for the effect of lateral bed slope and for the effect of spiral flow motion according to Rozovskii (1961). For certain runs, they considered the inertia of the spiral flow motion to account for the development and decay of the spiral flow intensity (Struiksma *et al.*, 1985).

Odgaard & Bergs (1988) performed flume experiments in a 180° bend with a curvature ratio of $B/R = 0.19$. The bed material consisted of sand with a median grain size of $d_{50} = 0.3$ mm and a geometric standard deviation of $\sigma_g = 1.45$. The

experiment was performed with a constant discharge of $0.153\,\mathrm{m}^3/\mathrm{s}$ and a bed slope of $0.116\,\%$. Both water and sediment were recirculated with a pump. The maximum scour depth was observed in the first half of the bend at 60°. The final topography was measured at equilibrium condition.

Yen & Lee (1995) performed flume experiments in a 180° bend with curvature ratio $B/R = 0.25$. They performed five runs using different hydrographs. The bed material consisted of non-uniform sediment with a mean grain size $d_m = 1\,\mathrm{mm}$ and a geometric standard deviation of the grain size distribution $\sigma_g = 2.5$. However, no sediment was added at the upstream boundary. The focus was on the topographical changes as well as grain sorting effects in the bend. At the outer side of the bend, the mean diameter was around three times higher at the end of the experiments compared to the initial mean diameter $d_{m,0}$ (coarsening). On the other hand, at the inner side of the bend the mean diameter was 0.6 to 0.7 times smaller compared to $d_{m,0}$ (fining). The most distinct transverse sorting was observed at the cross section at 90° of the bend (Yen & Lee, 1995). The area of maximum deposition at the inner side of the bend was located between section 75° and 90°. The maximum scour depth was observed between section 165° and 180°.

Zolezzi *et al.* (2005) performed flume experiments in flumes with 180° and 270° bend with a curvature ratio of $B/R = 0.24$. The river bed consisted of uniform material with a mean grain size of 1 mm, and had a slope of $1.1\,\%$. Steady inflow and equilibrium bed load transport rates were applied at the upstream boundary. The topographical changes were analyzed in time, until equilibrium was reached. The focus was on the formation of forced steady bars in the upstream and downstream reach of the bend depending on the aspect ratio $\beta = B/(2h_0))$, the ratio of half-channel width $B/2$ to the reference uniform approach flow depth h_0. The resonant threshold value β_R defines whether steady bars can be expected to form in the downstream reach (sub-resonant, $\beta < \beta_R$) or in the upstream reach (super-resonant, $\beta > \beta_R$) (Blondeaux & Seminara, 1985; Zolezzi & Seminara, 2001). For the first time, they found experimental evidence of upstream overdeepening under super-resonant conditions, which is in good agreement with the linear stability theory for two-dimensional steady perturbations of bottom topography proposed by Zolezzi & Seminara (2001).

Blanckaert (2011) investigated sharp meander bends with curvature ratio $B/R = 0.79$, where B denotes the channel width and R the radius of the bend. Sharp meander bends are defined to have curvature ratios of $B/R > 0.5$ (Blanckaert, 2011). The hydraulics in sharp bends considerably differs from bends with more moderate or mild curvature. The differences in sharp bends are mainly related to a distinct flow separation and recirculation zone at the inner bank, an additional secondary flow cell at the outer bank, and a different secondary flow saturation (Blanckaert, 2011).

Parker & Andrews (1985) developed an analytical model for the topography and grain sorting effects in meander bends. They focused on the equilibrium state of two main effects: the bed load transport direction due to gravitational effect on lateral bed slope (pointing outwards) and the bed load transport direction due to spiral flow motion in the bend (pointing inwards). The former effect increases with grain size. Therefore, coarser grains increasingly move towards the outer side over the course of the bend. The latter effect results in a net flux of finer material towards the inner side of the bend. Therefore, the location of the coarser bed usually changes from the inner side of the meander bend to the outer side typically at or near the bend apex (Parker & Andrews, 1985).

Hafner (2008) performed laboratory experiments and extended the numerical morphodynamic 2-D model of Schmautz (2003) to include the effects of spiral flow motion on bed load transport in river curvature. Two large scale laboratory experiments were performed based on the morphology of the Isar River. The meandering channel consisted of one meander wavelength with two consecutive river bends with opposite curvatures. The first run was without sediment input, whereas the second run was limited to half of the transport capacity. The numerical model was able to reproduce the bank erosion for the given situation. The correction of the bed load transport direction due to the spiral flow motion provided the biggest improvements. Furthermore, minor improvements were obtained by taking dispersion terms in the momentum equations and non-equilibrium spiral flow intensity into account. The radius was estimated based on the water surface inclination and the change in direction of the depth-averaged flow velocity.

Begnudelli *et al.* (2010) presented a state-of-the-art numerical morphodynamic 2-D model using unstructured grids. They included dispersion terms in the momentum equation and added a correction of bed load direction due to spiral flow motion

in the river bend. The radius of the river bend was estimated using a sub-grid approach. Therefore, for each computational cell the mean velocity vector was determined including neighbouring velocities within a predefined radius. Then, the curve radius was determined based on the change in direction of three successive mean velocity vectors in streamwise direction. The model was successfully tested against experimental data of Odgaard & Bergs (1988) for bed deformation in a 180° bend. Furthermore, various other numerical morphodynamic 2-D models were reported in literature, which included advanced model approaches, such as dispersion terms in the momentum equation, correction of sediment transport direction due to lateral bed slope and spiral motion in river curvatures, and bank collapse (e.g. Nagata *et al.*, 2000; Darby *et al.*, 2002; Rinaldi *et al.*, 2008; Duan & Julien, 2010; Asahi *et al.*, 2013; Nicholas *et al.*, 2013).

2.5. Lateral Erosion Processes

2.5.1. Lateral Erosion in Straight Channel

Laboratory experiments on lateral erosion in straight channels with non-cohesive, erodible embankments were performed by various researchers (e.g. Ikeda, 1981; Ikeda *et al.*, 1988; Diplas, 1990; Izumi *et al.*, 1991; Schmautz, 2003). They mainly studied the temporal development of lateral erosion and the final equilibrium state (Ikeda, 1981; Izumi *et al.*, 1991; Schmautz, 2003). Mostly, predictors for the channel width, depth, and cross-sectional shape of the stable straight channel were proposed depending on discharge, bed load, bed slope, and bed material (see e.g. Parker, 1978; Ikeda, 1981; Diplas, 1990). In contrast to threshold channels, where bed shear stress falls below the threshold value in the whole cross section, equilibrium channels are characterized by vanishing lateral but non-vanishing streamwise bed load transport, e.g. in the middle of the channel (Kovacs & Parker, 1994).

Kovacs & Parker (1994) proposed a mathematical and numerical model to describe the temporal evolution of the lateral erosion based on a cross-sectional approach. The dynamic equilibrium channel shape and width were characterized by vanishing lateral but non-vanishing streamwise bed load transport. The formulation in vector form included the bed load transport formula of Ashida & Michiue (1972),

a force balance analysis to account for a reduced incipient motion criterion on arbitrary bed slope, and the assumption of infinite bed load transport rates on slopes with vanishing critical Shields stress. The model agreed fairly well with the laboratory experiments of Ikeda (1981).

Vigilar & Diplas (1997) proposed a mathematical and numerical model based on a momentum-diffusion equation. The cross-sectional approach consisted of a channel with a flat bed region and curved banks. The cross-sectional geometry was iteratively adapted, for given discharge and bed slope or given bed load transport, until equilibrium state had been reached. The equilibrium was reached for stable banks (no further widening) with continuous bed load transport (stable channel with mobile bed). The model was successfully tested against experimental data (Ikeda, 1981; Diplas, 1990). A similar model was developed by Pizzuto (1990).

Ikeda (1981) investigated lateral erosion in a straight channel using non-cohesive sandy material. He performed 14 experiments in a small flume, 2.0 m long, 0.3 m wide and 20 experiments in a large flume, 15.0 m long, 0.5 m wide. The left side of the flume was limited by a vertical glass wall representing the symmetry axis. The mobile bed and mobile bank was formed in a half-trapezoidal shape. By considering only half of the cross section and the fixed glass wall, the tendency towards meandering was minimized. For experimental run No 17, for example, detailed data on the temporal development of two cross sections were presented. For this particular run, constant discharge of 4.13 l/s was used with a bed slope of 0.215 %. Bed and bank material consisted of sand with a mean diameter of $d_m = 1.3$ mm and standard deviation of $\sigma_g = 1.3$. Total run time of the experiment was twelve hours. During the experiment, longitudinal sand ridges were formed, which were related to secondary flow cells (Ikeda, 1981).

Schmautz (2003) studied lateral erosion in straight channels by means of laboratory experiments and numerical simulations. Small scale laboratory experiments were performed similar to Ikeda's experiments (Ikeda, 1981) to study stable channel width, depth, and cross-sectional shape. Large scale laboratory experiments were performed using an outdoor flume, 100 m long and 8 m wide. Eight large scale tests were performed based on hydraulic and morphological conditions of the Isar River and the Iller River. The bed slope of the Isar River and the Iller River was 0.085 % and 0.155 %, respectively. In the large scale tests, scour was observed

in the upper reach over the first few meters from the inflow boundary. However, deposition occurred in the downstream reach due to lateral erosion along the channel. Therefore, the channel width increased over the length of the flume and eventually an equilibrium width was reached in the lower part. The numerical 2-D model was based on a finite element method using a structured grid. The bed load transport formula for uniform sediment of Meyer-Peter & Müller (1948) was extended to non-equilibrium sediment transport using a loading law. The criteria for incipient motion was defined based on the critical Shields stress considering the force-balance of a single grain on arbitrary bed slope. The transport direction on side slope was defined based on two different types of grain movement, such as (i) rolling and sliding and (ii) saltation. Furthermore, bank collapse was considered based on a geometrical approach. The numerical model was able to reproduce the lateral erosion of three large scale laboratory experiments fairly well. Based on the numerical simulations, a simplified approach was proposed to estimate the equilibrium channel width based on discharge, bed slope, mean grain size, sediment input, and length of the considered river reach.

Requena (2008) performed laboratory experiments on lateral erosion in gravel-bed rivers. Seven experimental runs were performed for bed slopes between 1.1 and 1.25 % using a coarse sediment mixture ($d_{50} = 3.17\,\text{mm}$, $\sigma_g = 3.28$). Furthermore, four experiments were performed for bed slopes of 0.4 % using a fine sediment mixture ($d_{50} = 0.7\,\text{mm}$, $\sigma_g = 2.73$). Bank erosion and equilibrium channel width were described as function of discharge, critical discharge to break up armor, sediment input, bed slope, and grain size. Bank erosion was observed to be reduced in some cases due to grain sorting and armoring effects of the river bed near the bank toe.

2.5.2. Bank Failure Process

Nardi *et al.* (2012) performed laboratory experiments on lateral erosion and bank failure using a non-cohesive gravel-sand mixture. The experiments were conducted in a basin with still water, varying only the water level as main parameter. Bank failure was observed to occur during the rising phase of the water level. This was due to reduced apparent cohesion as the water level increased. Furthermore, bank erosion would potentially increase in the case of fluvial entrainment at the bank toe (Nardi *et al.*, 2012).

Numerical morphodynamic 2-D models often take the gravitational bank collapse of non-cohesive material into account using a geometrical approach. Thereby, bank material is transported in the direction of the steepest slope to the neighboring computational cells, until the angle of repose is reached again (see e.g. Wu, 2008). Furthermore, the angle of repose can be distinguished for submerged and dry cells. Hence, a larger angle of repose (steeper slope) can be assigned to dry cells to mimic apparent cohesion effect (see e.g. Volz *et al.*, 2012).

Model approaches for cohesive soils are generally based on the stability analysis (factor of safety) with regard to a particular failure mechanism (e.g. Thorne & Tovey, 1981; Osman & Thorne, 1988; Thorne & Osman, 1988; Thorne & Abt, 1993; Darby & Thorne, 1996; Thorne *et al.*, 1998; Mosselman, 1998; Darby *et al.*, 2000; Simon *et al.*, 2000; Nagata *et al.*, 2000; Cancienne *et al.*, 2008; Langendoen & Alonso, 2008; Midgley *et al.*, 2012; Sutarto *et al.*, 2014). Darby *et al.* (2002) coupled a bank stability model with a numerical hydraulic 2-D model using a curvilinear computational grid. The focus was on meandering rivers with planar slip failures as main failure mechanism. The presented model was tested against field data and experimental data. Overall, the model was able to capture the macro-scale features fairly well, but underestimated the scour depth at the outer bank of river bends and, consequently, underestimated lateral erosion rates (Darby *et al.*, 2002).

Samadi *et al.* (2009) analyzed uncertainty of the input parameters of a stability model for planar slip failure by local sensitivity and Monte-Carlo analysis. They found a very high likelihood of generating unreliable predictions due to the uncertainty of input parameters. In numbers, more than 80 % of the predictions do not fulfill the requirements of a precision of $< \pm 15\,\%$. Therefore, they suggest to improve sampling strategies of relevant morphological and sedimentological bank parameters including statistical variation and uncertainty quantification (Samadi *et al.*, 2009).

3. Fundamentals

3.1. Incipient Motion of Sediment

3.1.1. Forces on Single Sediment Particle

Let us consider a single submerged sediment particle lying on an inclined bed with a slope equal to the angle of repose γ and without dynamic flow forces as depicted in Fig. 3.1. For this simple case the absolute value of the resisting static friction force $\vec{F}_R$ is given by

$$|\vec{F}_R| = \mu_s F_{G\hat{z}}, \tag{3.1}$$

where μ_s = coefficient of static Coulomb friction, and $F_{G\hat{z}}$ = component of the submerged weight force $\vec{F}_G = \alpha_1(\rho_s - \rho)\vec{g}d^3$ perpendicular to the bed, with α_1 = shape factor, ρ_s = sediment density, ρ = fluid density, $\vec{g}$ = gravitational acceleration vector, and d = grain size diameter of particle. In this situation the sediment particle is at rest but also at the critical point just before motion (incipient motion), where $\vec{F}_R$ corresponds to the submerged weight force component in the direction of the inclined bed surface $\vec{F}_{G\hat{x}}$. Introducing $\vec{F}_{G\hat{x}} = \vec{F}_{G\hat{z}} \tan\gamma$, we find that $\tan\gamma \approx \mu_s$ at incipient motion. This simplification neglects the interaction with other sediment particles.

Additional forces occur in the case of hydrodynamic flow over particles. The drag force F_D results from the flow acting on a sediment particle and can be defined as

$$F_D = C_D \alpha_2 d^2 \frac{\rho u_0^2}{2}, \tag{3.2}$$

where C_D = drag coefficient, α_2 = particle shape factor related to drag force, and u_0 = average approach flow velocity.

The lift force F_L results from flow-induced pressure differences above and below

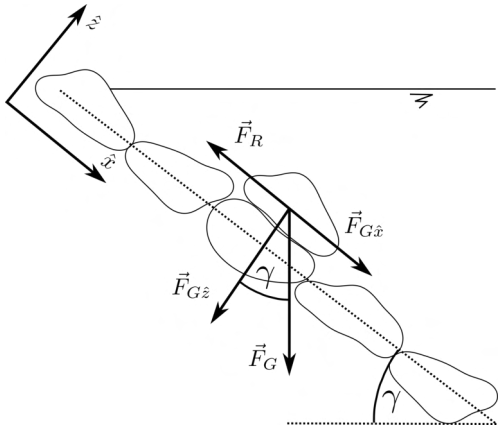

Fig. 3.1.: Static forces acting on a single submerged sediment particle on inclined bed with slope equal to the friction angle γ

submerged particles and is given as

$$F_L = C_L \alpha_3 d^2 \frac{\rho u_0^2}{2}, \tag{3.3}$$

where C_L = lift coefficient, and α_3 = particle shape factor related to lift force. The lift force acts normal to the flow direction, against the submerged weight force and thus reduces resisting friction (Eq. 3.1).

At incipient motion all forces acting on a single sediment particle (Fig. 3.2) are balanced:

$$\vec{F}_{res} = \vec{F}_R + \vec{F}_D + \vec{F}_G + \vec{F}_L + \vec{F}_i = 0, \tag{3.4}$$

where $\vec{F}_i$ denotes forces related to dynamic friction, hydrodynamic turbulence, particle interaction, and particle exposure effect (see e.g. Vollmer & Kleinhans, 2007). Depending on the degree of simplification, different approaches for incipient motion have been proposed by various authors (e.g. van Rijn, 1989; Vollmer & Kleinhans, 2007). Further details on incipient motion on arbitrary bed slope are provided in section 3.1.3.

The direction of the resulting force $\vec{F}_{Res}$ acting on a single sediment particle on an arbitrary bed slope deviates from the drag force $\vec{F}_D$ by an angle φ_b (Fig. 3.2). Thereby, the submerged weight force perpendicular to the bed $\vec{F}_G'$ plays a major role. This effect of lateral bed slope on the bed load transport direction is further described in section 3.2.3.

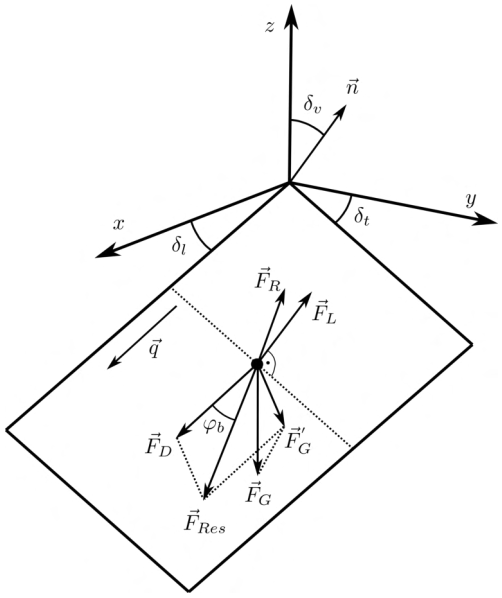

Fig. 3.2.: Forces acting on single sediment particle on arbitrary bed slope, where δ_l = longitudinal bed slope in flow direction and δ_t = transversal bed slope, adapted from Chen *et al.* (2010)

3.1.2. Incipient Motion on Planar Bed

Water flow in a river exerts hydrodynamic forces on sediment particles on the bed. Eventually, particles will start to move when driving forces are larger than resisting forces (incipient motion). Due to the stochastic nature of turbulence and sediment movement in alluvial rivers, incipient motion as well is a stochastic process. However, for river engineering applications a threshold concept is widely used, below which sediment transport is of no practical importance (Paintal, 1971). The point of incipient motion based on a threshold is loosely defined and is subjective to the investigator. It can be best described with terms like "several grains moving" or "weak movement" (Yang, 2006). Another widely used approach is to extrapolate the bed shear stress to zero transport rate. This can be done based on experimental data of sediment transport rates for a number of flow states above threshold condition (e.g. Meyer-Peter & Müller, 1948).

The most widely used approach in river engineering for the estimation of incipient motion of uniform granular material is based on the work of Shields (1936). He performed laboratory experiments on incipient motion using different granular materials with focus on the influence of particle shape and specific weight. A similarity approach for the condition of incipient motion was derived using a

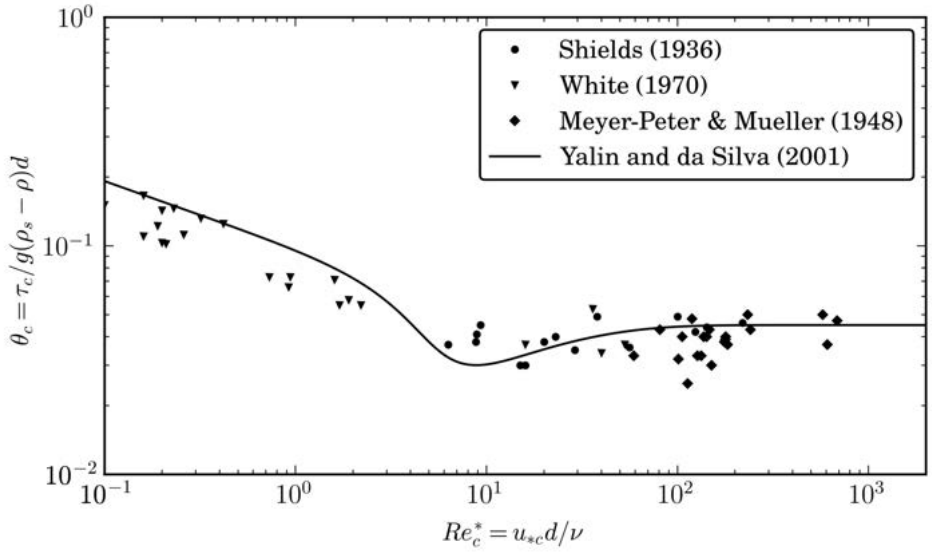

Fig. 3.3.: Shields diagram with selected data on incipient motion studies (Buffington & Montgomery, 1997) and transport inception function according to Yalin & da Silva (2001)

simplified force balance analysis acting on a single sediment particle. However, the weight force due to the bed slope was neglected arguing that for gentle bed slopes the gravity component is negligible (error within one percent). Finally, he derived the following functional relationship at threshold condition ($\tau_b = \tau_c$):

$$\theta_c = \frac{\tau_c}{g\rho(s-1)d} = f\left(Re_c^*\right), \qquad \text{with} \quad Re_c^* = \frac{u_{*c}d}{\nu} = \frac{\tau_c^{1/2}d}{\rho^{1/2}\nu}, \tag{3.5}$$

where θ_c = critical Shields stress for incipient motion, also referred to as critical dimensionless bed shear stress, τ_c = critical bed shear stress, τ_b = bed shear stress ($\tau_b = u_0^2\rho/c_f^2$ with u_0 = average approach flow velocity, c_f = dimensionless Chézy friction coefficient), g = gravitational acceleration, $s = \rho_s/\rho$ = specific density (ρ_s = sediment density and ρ = water density), d = grain size diameter of particle, Re_c^* = critical particle Reynolds number, $u_{*c} = (\tau_c/\rho)^{1/2}$ = critical shear velocity, and ν = kinematic viscosity.

Based on the derived relationship (Eq. 3.5), Shields (1936) plotted the experimental data at threshold condition on a diagram (Fig. 3.3). The original Shields diagram was limited to the range of $2 < Re_c^* < 600$ for the critical particle Reynolds number. However, the validity range was significantly increased by var-

ious authors adding experimental data to the Shields diagram. A comprehensive overview and collection of data on incipient motion is provided by Buffington & Montgomery (1997). Based on their findings the critical Shields stress is usually found in the range of $0.03 \leq \theta c \leq 0.09$ for movable bed. The critical Shields stress of 0.047 reported by Meyer-Peter & Müller (1948) can be considered as an average value over the entire Shields curve (Buffington & Montgomery, 1998). The scope of the Shields diagram is limited to relative submergence $R_h/d > 25 - 40$ and to gentle bed slopes $S < 0.005$ (Shields, 1936). Therefore, the original Shields diagram is often considered to be valid for planar bed or gentle bed slopes only (e.g. van Rijn, 1989; Chiew & Parker, 1994; Dey, 2003).

Transformed Shields Diagram

The drawback of the Shields diagram is that τ_c (Eq. 3.5) appears on both the x- and the y-axis. Therefore, an iterative approach is required to determine the critical Shields stress. However, this is often not suitable for practical applications, such as numerical modeling. Therefore, a transformed Shields diagram can be obtained by introducing the dimensionless grain diameter D^* as a combination of the particle Reynolds number Re^* and the critical Shields stress θ_c according to Eq. 3.6 (Yalin & da Silva, 2001).

$$D^* = \frac{(Re^*)^2}{\theta_c} = d \left(\frac{(s-1)\, g}{\nu^2} \right)^{1/3} . \tag{3.6}$$

Fig. 3.4 shows the transformed Shields diagram allowing to directly read θ_c for a given grain size with diameter d. Based on experimental data, Yalin & da Silva (2001) approximated the transformed Shields diagram by the transport inception function as follows

$$\theta_c = 0.13 D^{*-0.392} \exp(-0.015 D^{*2}) + 0.045 \left(1 - \exp(-0.068 D^*)\right) . \tag{3.7}$$

An alternative approximation of the transformed Shields diagram is proposed by van Rijn (1984) according to Eq. (3.8). Furthermore, this approach can be adapted to set the critical Shields stress to $\theta_c = 0.047$ (instead of 0.055) for larger dimensionless grain diameters ($D^* > 80$). A comparison of the presented

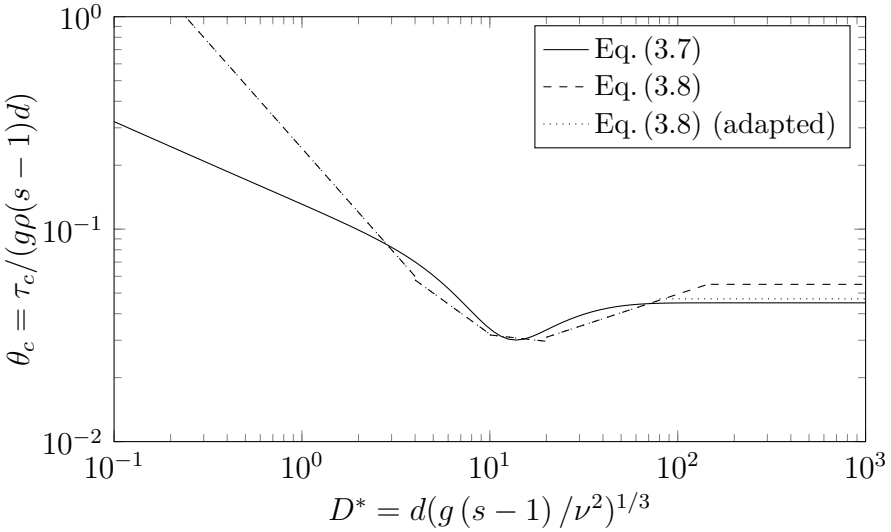

Fig. 3.4.: Transformed Shields diagram with transport inception function according to Yalin & da Silva (2001) (Eq. 3.7) and van Rijn (1989) (Eq. 3.8)

transport inception functions is shown in Fig. 3.4.

$$\begin{aligned}
\theta_c &= 0.24\left(D^*\right)^{-1}, && \text{for } 1 \leq D^* \leq 4 \\
\theta_c &= 0.14\left(D^*\right)^{-0.64}, && \text{for } 4 < D^* \leq 10 \\
\theta_c &= 0.04\left(D^*\right)^{-0.1}, && \text{for } 10 < D^* \leq 20 \\
\theta_c &= 0.013\left(D^*\right)^{0.29}, && \text{for } 20 < D^* \leq 150 \\
\theta_c &= 0.055, && \text{for } D^* > 150
\end{aligned} \tag{3.8}$$

3.1.3. Incipient Motion on Arbitrary Bed Slope

As already mentioned in section 3.1.2, the Shields diagram is only valid for planar bed or gentle bed slopes. On inclined bed slope, the submerged weight force $\vec{F}_G$ cannot be neglected anymore (see e.g. Fig. 3.2). Thus the force balance on a single grain depends strongly on the bed slope. Different approaches are reported in literature to correct the critical Shields stress θ_c to account for the bed slope effect. In the following, the critical Shields stress corrected for arbitrary bed slope δ is referred to as $\theta_{c,\delta}$.

The corrected critical Shields stress θ_{c,δ_l} for longitudinal bed slope δ_l is proposed

according to Eq. (3.9) by several authors (e.g. Luque & Van Beek, 1976; van Rijn, 1989; Chiew & Parker, 1994; Dey, 2003).

$$\frac{\theta_{c,\delta_l}}{\theta_c} = k_l = \cos\delta_l \left(1 - \frac{\tan\delta_l}{\tan\gamma}\right) = \frac{\sin\left(\gamma + \delta_l\right)}{\sin\gamma} \tag{3.9}$$

Thereby, γ denotes the angle of repose of bed material, δ_l the bed slope angle in longitudinal direction of the flow (see e.g. Fig. 3.2). Note that bed slope δ_l is defined negative in downhill direction and positive in uphill direction.

For the effect of the transversal slope δ_t on the critical Shields stress a correction according to Eq. (3.10) is proposed by several authors (e.g. Ikeda, 1982a; Kovacs & Parker, 1994; Chiew & Parker, 1994). Note that the orientation of lateral slope does not matter (see Fig. 3.2). Hence, the sign of δ_t in Eq. (3.10) does not affect the correction.

$$\frac{\theta_{c,\delta_t}}{\theta_c} = k_t = \cos\delta_t \sqrt{1 - \frac{\tan^2\delta_t}{\tan^2\gamma}} \tag{3.10}$$

In order to account for arbitrary bed slope δ, van Rijn (1989) proposed to combine the correction factors k_l and k_t for bed slope in longitudinal flow direction and for bed slope transversal to flow direction, respectively (Eq. 3.11).

$$\frac{\theta_{c,\delta}}{\theta_c} = k_l k_t = k \tag{3.11}$$

According to Chen *et al.* (2010), the product of the factors in Eq. (3.11) does not properly reproduce the balance of forces on a combined longitudinal and transverse bed slope. Dey (2001) proposed an empirical approach as

$$k = 0.954 \left(1 + \frac{\delta_l}{\gamma}\right)^{0.745} \left(1 - \frac{|\delta_t|}{\gamma}\right)^{0.372}. \tag{3.12}$$

Furthermore, the analytical approach of Dey (2003) reads

$$k = \frac{1}{(1-\eta\tan\gamma)\tan\gamma}\left(-\left(\sin\delta_l + \eta\tan^2\gamma\sqrt{\cos^2\delta_l - \sin^2\delta t}\right)\right.$$
$$+\left[\left(\sin\delta_l + \eta\tan^2\gamma\sqrt{\cos^2\delta_l - \sin^2\delta t}\right)^2 + \left(1-\eta^2\tan^2\gamma\right)\right. \tag{3.13}$$
$$\left.\left.\left(\cos^2\delta_l\tan^2\gamma - \sin^2\delta_t\tan^2\gamma - \sin^2\delta_l - \sin^2\delta_t\right)\right]^{0.5}\right),$$

where η = ratio of lift force to drag force. Chen *et al.* (2010) proposed another analytical approach, which reads

$$k = \frac{1}{\tan\gamma}\left(\cos^2\left(\frac{\pi}{2}-\delta_l\right) - 1 + \frac{1+\tan^2\gamma}{(1+\tan^2\delta_l+\tan^2\delta_t)}\right)^{0.5} + \cos\left(\frac{\pi}{2}-\delta_l\right). \tag{3.14}$$

The different approaches are compared in Fig. 3.5, with $\gamma = 34°$, and $\eta = 0.5$ for the approach of Dey (2003). There are differences, especially for high arbitrary bed slope (combined longitudinal and transversal bed slope). The approaches of van Rijn (1989) and Dey (2001) predict $\theta_{c,\delta}/\theta_c$ to become zero for transversal bed slope equal to the angle of repose ($\delta_t = \gamma$), while the approaches of Dey (2003) and Chen *et al.* (2010) predict $\theta_{c,\delta}/\theta_c = 0$ already for smaller transversal bed slope due to the combination with the longitudinal bed slope.

Kovacs & Parker (1994) derived a general vector formulation for the force balance taking into account submerged weight force, drag force, and resisting friction force. In addition, the vector formulation of Schmautz (2003) included the lift force. The friction force is approximated in both cases as static friction ($\tan\gamma = \mu_s$). Vollmer & Kleinhans (2007) developed a force balance model that further included the effect of pressure fluctuation in the bed, macroscale flow structures, and shallow flow.

In contradiction to the force balance model described above, in literature the argument can be found that laboratory experiments, natural rivers, and mountain torrents indicate that the critical Shields stress increases with increasing streamwise bed slope (e.g. Shvidchenko *et al.*, 2001; Lamb *et al.*, 2008). This can be

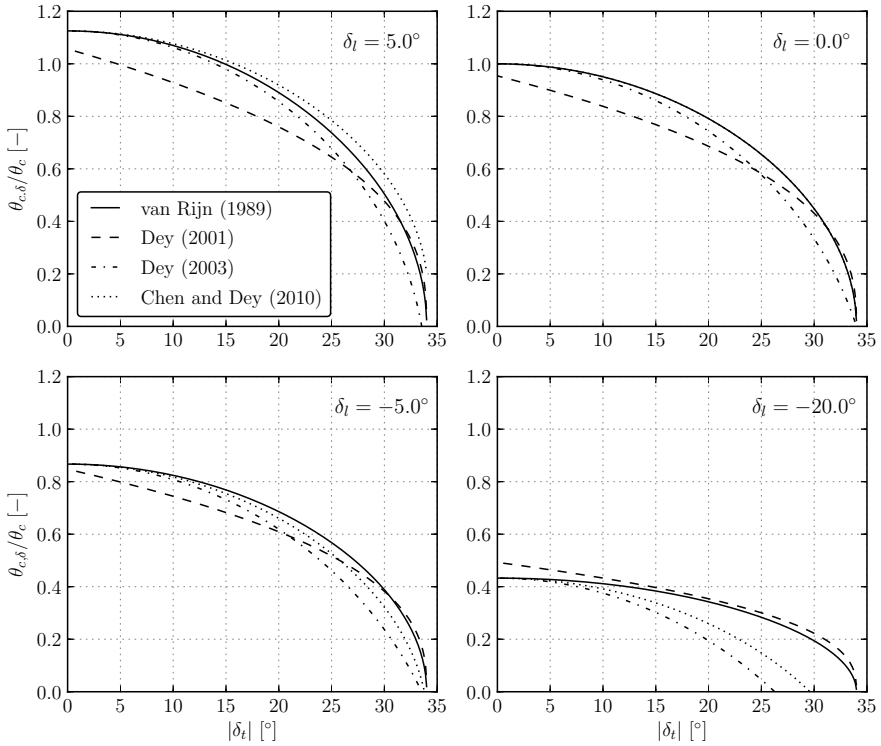

Fig. 3.5.: Approaches of critical Shields stress correction for combined longitudinal and transveral bed slope δ_l, and δ_t, respectively, using an angle of repose $\gamma = 34°$, and $\eta = 0.5$ for Dey (2003)

explained by taking other factors into account such as particle emergence, relative roughness, turbulent fluctuations, and changes in local flow velocity (Lamb *et al.*, 2008). In particular for mountain torrents, these effects outweigh the effect of the submerged weight force component, which would usually decrease the critical Shields stress.

3.2. Bed Load Transport

3.2.1. Empirical Bed Load Transport Formulas

Sediment transport in rivers occurs due to the flow of water exerting shear stress on sediment particles on the river bed. Bed load is defined as sediment (e.g. gravel) transported close to the river bed. The motion of sediment particles can be described as rolling, sliding or saltating (jumping) (Graf, 1971). Attempts

to describe bed load transport rates on the basis of hydraulic parameters by a mathematical relation are hereinafter referred to as bed load formulas.

DuBoys (1879) proposed one of the first bed load formula, which reads in its basic form as

$$q_b = \chi \tau_b \left(\tau_b - \tau_c\right), \tag{3.15}$$

where $q_b = |\vec{\mathbf{q}}_\mathbf{b}|$= absolute value of the specific compact volumetric bed load transport rate (volume without porosity, per unit time and unit width [m^2/s]), τ_b = bed shear stress, τ_c = critical bed shear stress, and χ = factor depending on sediment characteristics [$m^6/(N^2 s)$] (Shen, 1971). Bed load formulas using a shear stress relationship as in Eq. (3.15) are classified as *duBoys-type* formulas (Graf, 1971).

Schoklitsch (1930) formulated the following discharge relationship

$$q_b = \chi^* S_h^k \left(q - q_c\right), \tag{3.16}$$

where χ^* = dimensionless factor depending on specific weight, mixture and form of the particles, q = specific discharge of water, q_c = critical specific discharge of water at which particles start to move, S_h = slope of water surface, and k = empirical parameter ($k \approx 2$). Bed load formulas using a discharge relationship are classified as *Schoklitsch-type* formulas (Graf, 1971). The third type of bed load formulas are based on statistical considerations and are classified as *Einstein-type* formulas (Einstein, 1936; Graf, 1971).

Various other bed load formulas have been reported in literature (e.g. Engelund & Hansen, 1972; Ackers & White, 1973). A popular bed load formula was developed by Meyer-Peter & Müller (1948) at VAW, ETH Zurich, which reads in its original form as

$$\gamma_w \frac{Q'}{Q} \left(\frac{k_{st,b}}{k_{st,r}}\right)^{3/2} hS = A(\gamma_s - \gamma_w) d_m + B \left(\frac{\gamma_w}{g}\right)^{1/3} g_{s,sub}^{2/3}, \tag{3.17}$$

where $g_{s,sub}$ = specific bed load rate of the submerged weight ($g_{s,sub} = g_s(\gamma_s - \gamma_w)/\gamma_s$, with g_s = specific weight transport rate), γ_w = specific weight of water, γ_s = specific weight of sediments, Q' = reduced discharge due to sidewall

roughness, Q = total discharge, $k_{st,b}$ = Strickler coefficient of total bed roughness (including bed forms), $k_{st,r}$ = Strickler coefficient for grain roughness, h = water depth, S = bed slope, d_m = mean grain size diameter of the sediments, and g = gravitational acceleration, A and B were parameters fitted to the experimentally measured bed load transport rates. They obtained values of 0.047 and 0.25 for A and B, respectively. Note that $A \approx 0.047$ was obtained by extrapolation of g_s to a zero bed load transport rate. For the onset of bed load transport they subjectively found $A \approx 0.03$.

The original Eq. (3.17) can be transformed into a duBoys-type formula expressing the dimensionless bed load transport rate as

$$\Phi = \frac{q_b}{\sqrt{(s-1)g d_m^3}} = \alpha \left(\mu_r \theta - \theta_c\right)^{3/2}, \tag{3.18}$$

where q_b = specific bed load, α = bed load pre-factor ($\alpha = 8$), θ = Shields stress, also denoted as dimensionless bed shear stress ($\theta = |\vec{\mathbf{u}}|^2/(c_f^2 g(s-1)d_m)$, with $\vec{\mathbf{u}} = (u, v)^T$ = depth-averaged flow velocity vector and c_f = dimensionless Chézy friction coefficient), $\mu_r = (k_{st,b}/k_{st,r})^{3/2}$ = bed forms factor, and θ_c = critical Shields stress. Note that Eq. (3.18) applies for wide channels ($Q'/Q \approx 1$). The flume experiments were performed with bed slopes between 0.04 % and 2.3 % using uniform and non-uniform bed material with mean grain size between 0.4 and 28.65 mm (Meyer-Peter & Müller, 1948).

Bed load formulas, such as Eq. (3.18), can be used to determine the bed load of sediment mixtures. Thereby, the sediment mixture is approximated by a characteristic grain size diameter, such as the mean grain size diameter d_m (e.g. Meyer-Peter & Müller, 1948; Bagnold, 1966), the median grain size diameter d_{50} (e.g. van Rijn, 1984; Parker, 2008), the geometric grain size diameter d_g (Parker, 2008), or the mean fall diameter d_{mf} (Engelund & Hansen, 1972).

3.2.2. Hiding Function for Non-Uniform Bed Load

Approaches for non-uniform bed load transport will be applied if grain sorting effects are of interest. Sediment mixtures are transported in a different manner than uniform bed material. Smaller grains are sheltered behind larger grains and hence, they are hiding from the water flow (hiding effect). On the other hand,

exposure of larger grains is more pronounced (exposure effect). Consequently, the mobility of single fractions within the sediment mixture tends towards equal mobility (Parker, 2008). This hiding and exposure effect is taken into account by using hiding functions. A comprehensive overview is given by Sutherland (1992), who mainly distinguished between *threshold derived* hiding functions F_{hc} applied on the critical Shields stress θ_c and *transport derived* hiding functions F_{ht} applied directly on the driving part of bed load formula, e.g. on the Shields stress θ.

Various non-uniform bed load transport formulas have been proposed in literature (e.g. Einstein, 1950; Egiazaroff, 1965; Ashida & Michiue, 1972; Ribberink, 1987; Sutherland, 1992; Parker, 1990; Hunziker, 1995; Wu *et al.*, 2000; Wilcock & Crowe, 2003). Depending on the formula, the hiding function is applied on (i) the critical Shields stress θ_c (see e.g. Egiazaroff, 1965; Ashida & Michiue, 1972; Ribberink, 1987; Wu *et al.*, 2000), (ii) the Shields stress θ (see e.g. Ribberink, 1987; Hunziker, 1995), (iii) the excess of the Shields stress $(\theta - \theta_c)$ (see e.g. Hunziker, 1995), and (iv) the reference Shields stress θ_r, which is related to the reference transport rate above which bed load transport is considered to be significant (see e.g. Parker, 1990; Wilcock & Crowe, 2003). Therefore, hiding functions are hardly comparable to each other and only apply to a specific bed load formula.

Threshold derived hiding functions F_{hc} determine the critical Shields stress θ_{ci} for each grain size i based on the critical Shields stress θ_{cm} of the characteristic grain size diameter (e.g. the mean grain size d_m) according to Eq. (3.19). However, Parker (2008) claims that the geometric mean grain size d_g is more suitable to characterize sediment mixtures.

$$\theta_{ci} = F_{hc}\theta_{cm} \tag{3.19}$$

Thus the specific bed load rate is a function of the Shields stress θ_i of grain size i and the hiding function F_{hc} applied to the critical Shields stress $(F_{hc}\theta_{cm})$, which can be written as

$$q_{bi} = f\left(\theta_i, F_{hc}\theta_{cm}\right). \tag{3.20}$$

Ashida & Michiue (1972) extended the hiding function of Egiazaroff (1965) according to Eq. (3.21) for smaller grain sizes $(d_i/d_m \leq 0.4)$.

$$F_{hc} = \begin{cases} \left(\dfrac{\log(19)}{\log\left(19\dfrac{d_i}{d_m}\right)} \right)^2, & \text{for } \dfrac{d_i}{d_m} > 0.4, \\ 0.85 \left(\dfrac{d_i}{d_m} \right)^{-1}, & \text{for } \dfrac{d_i}{d_m} \leq 0.4, \end{cases} \tag{3.21}$$

Furthermore, hiding functions in terms of a power law relation can be found in literature (e.g. Andrews, 1983; Sutherland, 1992; Parker, 2008) reading

$$F_{hc} = \frac{\theta_{ci}}{\theta_{cm}} = \left(\frac{d_i}{d_m} \right)^{-b}, \tag{3.22}$$

where the exponent b typically ranges between 0.6 and 1.0 (Sutherland, 1992; Parker, 2008). A value of $b = 0$ corresponds to no effect from hiding and exposure, whereas $b = 1$ corresponds to equal mobility for all grain sizes characterized by the critical Shields stress θ_{cm} of the mean grain size d_m of the mixture. The combination of Eq. (3.19) with Eq. (3.21) or Eq. (3.22) leads to an increased threshold θ_{ci} for smaller grains, whereas θ_{ci} tends to decrease for larger grains, compared to θ_{cm} of the mixture. Alternatively, θ_{ci} can be determined as follows

$$\theta_{ci} = F_{hcs}\theta_i, \tag{3.23}$$

where $F_{hcs} = F_{hc}\theta_{cm}/\theta_i$ (see Sutherland, 1992).

Transport derived hiding functions F_{ht} are applied directly to the driving part of the bed load formula, such as the Shields stress θ_i for each grain size i, which can be expressed as (see e.g. Sutherland, 1992)

$$q_{bi} = f\left(F_{ht}\theta_i\right), \tag{3.24}$$

where q_{bi} is the bed load transport rate of grain size i.

Parker *et al.* (1982) defined a reference shear stress θ_r above which significant bed load transport is observed. Therefore, a critical Shields stress is omitted and

the hiding function F_{htr} is applied to the reference shear stress θ_{r50} of the median grain size d_{50} of the mixture as

$$F_{htr} = \frac{\theta_{ri}}{\theta_{r50}} = \left(\frac{d_i}{d_{50}} \right)^{-b}, \tag{3.25}$$

where θ_{ri} denotes the reference Shields stress of grain size i. Note that the exponent b is in the same range as in Eq. (3.22).

3.2.3. Lateral Bed Slope Effect

Generally, bed load is considered to be transported in the same direction as the main flow direction. However, bed load transport on a lateral bed slope has an additional lateral, downhill component due to the gravitational force acting on the bed material (e.g. Kikkawa *et al.*, 1976; Ikeda, 1982b). Consequently, the bed load transport direction on lateral bed slope differs from the main flow direction. In this context, the lateral bed slope is defined as the part of the bed slope that is laterally, or transversally, inclined with respect to the main flow direction (e.g. river embankment).

The deviation of the bed load transport direction due to the lateral bed slope effect is depicted in Fig. 3.6 within the two-dimensional Cartesian coordinate system. Note that direction is defined in mathematical sense, i.e. counterclockwise for positive angles. In this regard, the bed load transport direction is written as

$$\frac{q_{b,y}}{q_{b,x}} = \tan\left(\varphi_q + \varphi_b \right), \tag{3.26}$$

where $q_{b,x}$ and $q_{b,y}$, denotes the x- and y-component of bed load transport $\vec{q}_b$, respectively, φ_q = main flow direction, and φ_b = bed load transport direction with respect to main flow direction. The general formulation for the lateral bed slope effect on bed load transport direction reads (see e.g. Parker *et al.*, 1982; Sekine & Kikkawa, 1992)

$$\tan \varphi_b = -\,\mathrm{f}\left(\theta\right) \vec{s} \cdot \vec{n}_q, \quad \text{where } \vec{s} \cdot \vec{n}_q < 0, \tag{3.27}$$

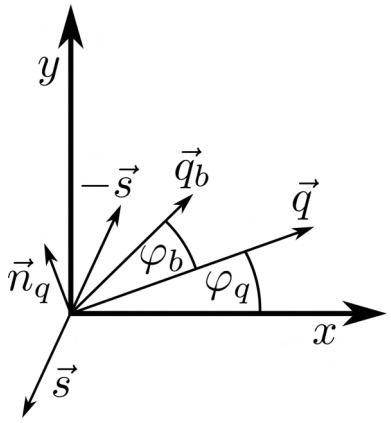

Fig. 3.6.: Deviation φ_b of bed load transport $\vec{q}_b$ regarding main flow direction due to bed slope $\vec{s}$ (positive uphill, negative downhill)

where $\vec{n}_q$ denotes the normal vector of $\vec{q}$, where $\vec{n}_q$ points in downhill direction ($\vec{s} \cdot \vec{n}_q < 0$), $\vec{s} = (\frac{\partial z_b}{\partial x}, \frac{\partial z_b}{\partial y})$ denotes the bed slope (positive uphill, negative downhill), with z_b = bed elevation. Furthermore, f $\left(\theta\right)$ is a function of the Shields stress defined as

$$\mathrm{f}\left(\theta\right) = N_l \left(\frac{\theta_c}{\theta}\right)^{M_l}, \tag{3.28}$$

where N_l = coefficient of the lateral bed slope approach, also referred to as Ikeda parameter, and M_l = exponent of the lateral bed slope approach. This approach is comparable to the approach proposed by Talmon *et al.* (1995), where the Ikeda parameter is defined as $r = \sqrt{\theta_c} N_l = \sqrt{0.05} N_l \approx 0.224 N_l$ ($M_l = 0.5$). Note that the critical Shields stress is not corrected for local bed slope effect and usually has a constant value (e.g. $\theta_c = 0.05$). In the following, approaches for the lateral bed slope effect from the literature are described in more detail, while an overview is shown in Table 3.1.

Besides Ikeda's experiments on lateral erosion in straight channels (Ikeda, 1981, see also section 2.5.1), Ikeda (1982a) performed laboratory experiments using a wind tunnel 4 m long with a cross section of 0.1 times 0.3 m, which could be tilted up to 40 ř. The bed material consisted of two different well-graded non-cohesive sands with median grain size of $d_{50} = 0.42$ and 1.3 mm (Ikeda, 1982a). Ikeda (1982b) combined the data of the water flume and wind tunnel experiments for a comprehensive analysis of the lateral bed slope effect on bed load transport.

Finally, in a discussion with Parker (Parker, 1984; Ikeda, 1984), they defined N_l as

$$N_l = \frac{1 + c_L \mu_d}{\mu_d}, \tag{3.29}$$

where c_L = ratio of lift coefficient to drag coefficient, and μ_d = coefficient of dynamic Coulomb friction. Assuming $c_L = 0$ and $\mu_d = 0.7$ they came up with a value for $N_l = 1.43$, and $M_l = 0.5$ (see Table 3.1; Parker, 1984; Ikeda, 1984). Johannesson & Parker (1989) extended this analysis by introducing a correction factor λ_l in the denominator of Eq. (3.29) and different values for c_L and μ_d (see Table 3.1).

Hasegawa (1981) proposed the following expression

$$N_l = \frac{1}{\sqrt{\mu_s \mu_d}}, \tag{3.30}$$

where μ_s, and μ_d denote the coefficient of static and dynamic Coulomb friction, respectively. Finally, choosing $\mu_s = 1.0$, and $\mu_d = 0.7$ resulted in $N_l = 1.20$ (Hasegawa, 1981).

Sekine & Kikkawa (1992) developed a numerical model for saltating grains. Their model included a deterministic approach for particle trajectories and a probabilistic approach for collision of particles with the bed surface. Sekine & Parker (1992) extended the model for the case of lateral bed slope. For saltating grains, they proposed $N_l = 0.75$ and $M_l = 0.25$.

Schmautz (2003) performed similar experiments as Ikeda (1982b) using a flume 6.0 m long and 0.525 m wide. The experiments were used for numerical 2-D model calibration. Thereby, the approach from Sekine & Parker (1992) was used for saltating grains and Eq. (3.31) was proposed to account for sliding and rolling grains. The two approaches were combined by weighting depending on the Shields parameter (Schmautz, 2003).

$$N_l = \frac{\sqrt{1 + c_L \tan\gamma}}{\tan\gamma} \tag{3.31}$$

Thereby, γ denotes the internal friction angle of the bank material.

Talmon *et al.* (1995) conducted laboratory experiments using a straight flume,

60 m long, 1 m wide, and with constant bed slope. The initial topography consisted of a sinuous bed profile in transverse direction. Lateral bed load transport was observed by a flattening of the bed profile during experiments. However, dunes formed during the experiment having similar time scales as the lateral transport process. The bed material consisted of well graded sand with $d_{50} = 0.8$ mm. The value that best fitted their data was $N_l = 2.63$, what is in accordance with the value found by Johannesson & Parker (1989). Zanke *et al.* (2008) performed similar experiments using fine sand ($d_m = 0.25$ mm), coarse sand ($d_m = 0.96$ mm), and fine gravel ($d_m = 3.0$ mm). In this case, bed forms were also observed during the experiments. Ripples formed in the case of fine sand, whereas dunes appeared in the case of coarse sand. They proposed different values for N_l and M_l depending on the bed material (see Table 3.1).

Table 3.1.: Approaches for lateral bed slope effect and corresponding parameters N_l and M_l (see Eq. 3.28) from different authors; in some cases $\theta_c = 0.05$ was used to determine values of N_l; Acronyms used in the comments column: Analytical Analysis (AA), Laboratory Experiments (LE), Numerical Simulations (NS)

References	**Formula for N_l**	**Value of N_l**	**Value of M_l**	**Comments**
Ikeda (1988, 1982b), Parker (1984)	$\frac{1+c_L\mu_d}{\mu_d}$	1.43	0.5	AA, LE, $\mu_d = 0.7$, $c_L = 0$
Johannesson & Parker (1989), Sekine & Parker (1992)	$\frac{1+c_L\mu_d}{\lambda\mu_d}$	2.67	0.5	AA, LE, $\mu_d = 0.43$, $c_L = 0.85$, $\lambda_l = 1.19$
Talmon *et al.* (1995)	$\frac{1}{1.7\sqrt{\theta_c}}$	2.63	0.5	LE, NS
Zanke *et al.* (2008)	$\frac{P}{\sqrt{\theta_c}}$	3.57 1.10 0.84	0.5 0.0 0.0	LE, P = parameter fine sand (ripples) coarse sand (dunes) fine gravel
Hasegawa (1981)	$\frac{1}{\sqrt{\mu_s\mu_d}}$	1.20	0.5	AA, $\mu_s = 1.0$ $\mu_d = 0.7$
Struiksma *et al.* (1985)	$\frac{1}{f_s\theta_c}$	10-20	1.0	AA, NS f_s: grain shape factor $(1 \leq f_s \leq 2)$
Sekine & Parker (1992)		0.75	0.25	Model for saltating grains
Schmautz (2003)	$\frac{\sqrt{1+c_L\tan\gamma}}{\tan\gamma}$	1.45	0.5	Rolling and sliding grains, $c_L = 0.3$, $\gamma = 37.5°$
Schmautz (2003)		0.83 0.75	0.5 0.25	Saltating grains for $\theta \leq 1.5\theta_c$ for $\theta > 1.5\theta_c$

3.2.4. Curvature Effect

Flow motion in river bends is three-dimensional and shows a spiral flow structure. Thereby, velocity vectors at the water surface point towards the outer side of the bend, whereas near-bed velocity vectors point towards the inner side of the bend (e.g. Thorne *et al.*, 1985, Fig. 3.7). In the case of steep outer embankments, small reverse (counter-rotating) cells occur with a lateral scale of approximately the water depth (Bathurst *et al.*, 1977). In this section the focus is on two phenomena arising in river bends. The first phenomenon is related to the transverse inclination of the water surface observed in river bends (Fig. 3.8). Thereby, a simple relationship is presented between the lateral inclination of the water surface and the radius of the river bend. The second phenomenon is related to the deviation of the bed shear stress from the depth-averaged flow direction due to the spiral flow in river bends. The purpose is to correct the bed load transport direction in depth-averaged numerical models.

Rozovskii (1961) proposed an estimation for the water surface inclination (angle ε between inclined water surface and horizontal plane, Fig. 3.8) as

$$\tan\varepsilon = \frac{\Delta h}{W} = \alpha \frac{u^2}{g R_c}, \tag{3.32}$$

where Δh = water surface difference between left and right embankment, W = channel width, u = mean flow velocity, g = acceleration of gravity, R_c = radius to center line of river bend, and α = parameter to account for the influence of friction; $\alpha = \alpha_s$ for smooth bottom (Eq. 3.33) and $\alpha = \alpha_r$ for rough bottom (Eq. 3.34) (Rozovskii, 1961).

$$\alpha_s = 1 + \frac{g}{\kappa^2 C^2} \tag{3.33}$$

$$\alpha_r = \alpha_s + 0.8 \left(\frac{\sqrt{g}}{\kappa C} \right)^2 \tag{3.34}$$

Herein κ denotes the von Kármán constant and C the Chézy friction coefficient. Transversal friction stresses tend to dampen the spiral flow motion. However, this effect can be neglected ($\alpha \approx 1$) in most cases (Rozovskii, 1961).

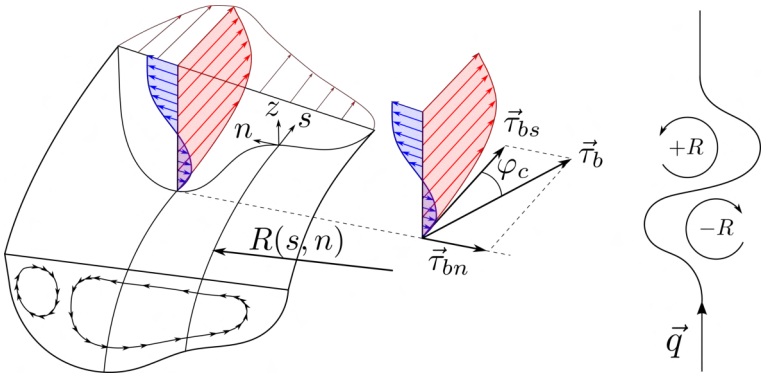

Fig. 3.7.: Effect of spiral flow in river bend on bed shear stress $\vec{\tau}_b$ with deviation angle from main flow direction φ_c and sign of radius R (positive counterclockwise, negative clockwise), Figure adapted from Blanckaert (2011)

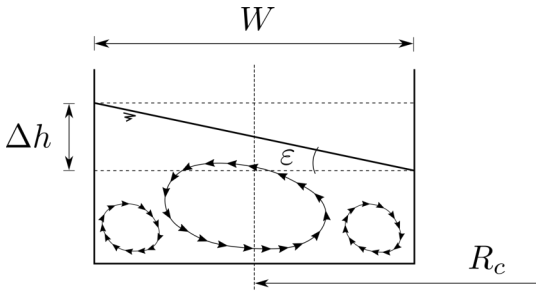

Fig. 3.8.: Definition sketch of the lateral water surface inclination in a river bend with rectangular cross section

Spiral flow motion of the water in river bends affects bed load transport direction (Fig. 3.7). The general formulation for the deviation angle φ_c of the bottom shear stress $\vec{\tau}_b$ from the main flow direction due to the curvature effect is given as

$$\tan\varphi_c = \frac{|\vec{\tau}_{bn}|}{|\vec{\tau}_{bs}|} = -N_* \frac{h}{R}, \tag{3.35}$$

where $\vec{\tau}_{bs}$ and $\vec{\tau}_{bn}$ denote bed shear stress in the flow direction and normal to the flow direction, respectively, h = water depth, N_* = curvature factor depending on bed roughness ($N_* = f(C)$, where C = Chézy friction coefficient), and $R = R(s,n)$ = local radius of the river bend (Fig. 3.7). Note that the radius R and hence, the deviation angle φ_c are defined mathematically positive and

negative in counterclockwise and clockwise direction, respectively (Fig. 3.7).

Rozovskii (1961) performed laboratory experiments on flow of water in bends of open channels. The experimental data was used to validate analytical models, e.g. for the lateral distribution of depth-averaged velocity in river bends. For smooth bottom, frictional bed shear stress can be neglected and N_* can bed estimated based on Eq. (3.36) and Eq. (3.37):

$$N_* = \frac{2}{\kappa^2}\left(1 - a\frac{\sqrt{g}}{\kappa C}\right), \tag{3.36}$$

where κ = von Kármán constant ($\kappa \approx 0.40$), C = Chézy friction coefficient $[m^{1/2}/s]$, and a = factor between 0.5 (Schuurman *et al.*, 2016) and 1.0 (Rozovskii, 1961);

$$N_* = \frac{8}{45}\frac{m_g^2}{g}\left(1 - 0.067\frac{m_g}{C}\right), \tag{3.37}$$

where $m_g \approx g/\kappa$ denotes a constant with values between 22 and 24 (Rozovskii, 1961).

For a rough bottom, the frictional bed shear stress should be considered (Rozovskii, 1961). In this case, N_* can be estimated by Eq. (3.38) or Eq. (3.39), for example.

$$N_* = \frac{8}{45}\frac{m_g^2}{g}\left(1 - \frac{11}{15}\frac{m_g}{C}\right) \tag{3.38}$$

$$N_* = \frac{1}{\kappa^2}\left(2 + \frac{\sqrt{g}}{\kappa C}\left(0.8(1 + \ln(k_s/h)) - 2\right)\right) \tag{3.39}$$

Herein k_s denotes the equivalent sand roughness.

The presented approaches to estimate the curvature factor are compared in Fig. 3.9. The curvature factor N_* decreases for increasing friction (decreasing C). Note that the laboratory experiments of Rozovskii (1961) focused on flumes with $C = 30\,\mathrm{m}^{1/2}/\mathrm{s}$ and $C = 60\,\mathrm{m}^{1/2}/\mathrm{s}$.

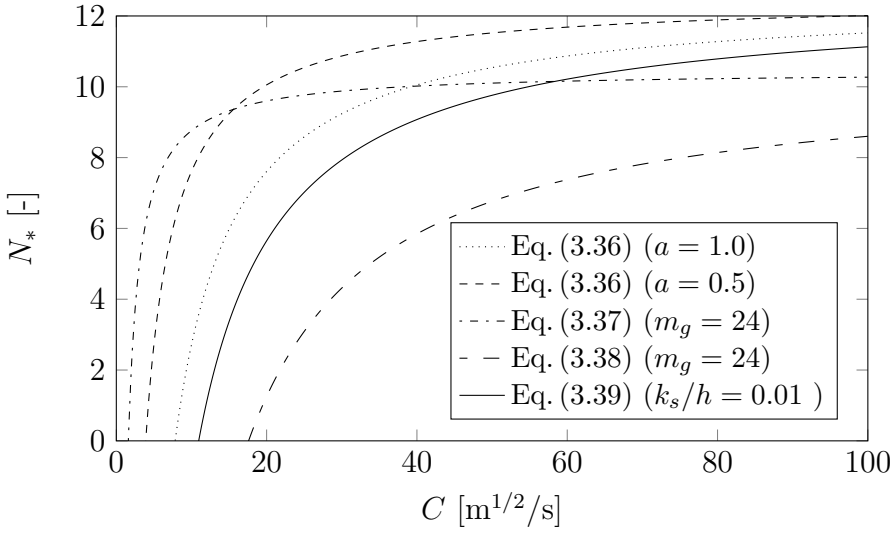

Fig. 3.9.: Comparison of different approaches to estimate the curvature factor $N_* = f(C)$ used in Eq. (3.35)

Engelund (1974) proposed a curvature factor of $N_* = 7.0$ for natural rivers (error smaller than 3 %). In the laboratory experiments of Rozovskii (1961), the curvature factor was in the range of $10 \leq N_* \leq 12$. Rozovskii's values of the curvature factor, compared to Engelund's value, were greater due to the rather smooth experimental flume (higher C).

3.3. Bank Failure Mechanism

Bank erosion depends on fluvial sediment entrainment and destabilization processes (Thorne, 1982). In the former process, sediment is entrained (i) directly at the embankment and (ii) due to erosion at the basal area of the embankment and subsequent gravitational bank failure. The basal area can be defined as the lower bank and bed area near the bank toe reaching into the bed area up to one or two times the bank height (Thorne, 1982). The main sediment transport processes are bed load in stream-wise direction and lateral bed load due to lateral bed slope effect and curvature effect in river bends. The river bank is destabilized by weakening and weathering processes due to climatic effects. Thereby, precipitation, solar radiation, cycles of wetting and drying, frost, and internal erosion play the major role. Furthermore, river banks are destabilized by water intrusion, piping and additional water weight. The groundwater table plays an important role for the pore water pressure in the banks.

The following is an overview of the basic mechanisms of river bank failure (see Fig. 3.10). More details can be found in the literature (see e.g. Thorne, 1982; Pizzuto, 2008; Rinaldi & Darby, 2008; Rinaldi & Nardi, 2013). For composite river banks, consisting of non-cohesive and cohesive materials and layers, different combinations of bank failure mechanisms occur in nature (Thorne & Tovey, 1981). For instance, Springer *et al.* (1985) identified tension cracks and the filling of these cracks with water as the key process for the destabilization of composite river banks at the alluvial Ohio River.

Bank stability can be investigated by comparing stabilizing forces F_R to driving forces F_D on a failure plane (see e.g. Thorne, 1982; Darby & Thorne, 1996). Thereby, the factor of safety is defined as

$$F_s = \frac{\sum F_R}{\sum F_D}, \tag{3.40}$$

where $F_s < 1$ expresses unstable banks, $F_s > 1$ stable banks, and $F_s = 1$ critical stability with the bank at the point of failure.

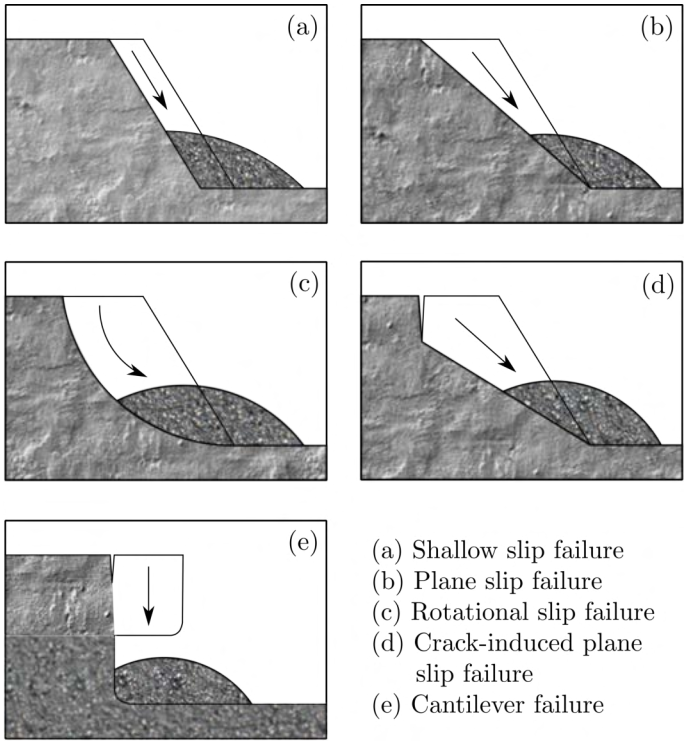

Fig. 3.10.: Basic mechanisms of river bank failure (see e.g. Thorne, 1982; Rinaldi & Darby, 2008; Pizzuto, 2008; Rinaldi & Nardi, 2013)

3.3.1. Non-cohesive Banks

Bank erosion by fluvial sediment entrainment takes place grain by grain. Furthermore, fluvial erosion at the basal area of the embankment leads to an increased bank slope, which eventually exceeds the angle of repose. Consequently, gravitationally induced bank collapse will transport the sediment down to the bank toe and will deposit with a slope corresponding to the angle of repose (Wu, 2008). The shallow slip failure and the plane slip failure describe relevant failure mechanisms of non-cohesive banks (see Fig. 3.10).

For non-cohesive bank material, the factor of safety can be expressed as

$$F_s = \frac{(\sigma_n - p_w)\tan\gamma}{F_{Gp}} = \frac{(F_G\cos\delta - p_w)\tan\gamma}{F_G\sin\delta}, \tag{3.41}$$

where F_G = weight force, σ_n = normal shear stress on the plane, p_w = pore water pressure, F_{Gp} = weight force parallel to the plane, γ = friction angle, and δ = bank angle.

In the case of completely dry or completely submerged bank material, the pore water pressure is zero. This results in $\gamma = \delta$ for limiting bank stability ($F_s = 1$). Hence, bank collapse occurs if the bank slope is equal to or greater than the angle of repose ($\delta \geq \gamma$).

If the bank is only partially submerged, the pore water pressure can significantly impact bank stability. For instance, a rapid drawdown of the groundwater table can cause positive pore water pressure. This leads to a smaller limiting slope for bank collapse than the friction angle ($\delta < \gamma$). However, if the bank material is only partially saturated, negative pore water pressure can cause apparent cohesion. In such cases, the limiting bank slope exceeds the friction angle ($\delta > \gamma$). In particular the combination of these effects causes river bank failure. In the falling limb of a flood, for instance, the upper part of the soil is stabilized by apparent cohesion, whereas the underlying soil is destabilized by the additional weight and positive pore water pressure from the higher groundwater table.

3.3.2. Cohesive and Composite Banks

The analysis of cohesive and composite banks is generally based on the stability analysis (factor of safety) with regard to a particular failure mechanism, e.g. shallow slip failure, plane slip failure, rotational slip failure, crack-induced plane slip failure, and cantilever failure (Thorne & Tovey, 1981; Osman & Thorne, 1988; Thorne & Osman, 1988; Thorne & Abt, 1993; Darby & Thorne, 1996; Thorne *et al.*, 1998; Mosselman, 1998; Darby *et al.*, 2000; Simon *et al.*, 2000; Nagata *et al.*, 2000; Cancienne *et al.*, 2008; Langendoen & Alonso, 2008; Midgley *et al.*, 2012; Sutarto *et al.*, 2014). The most important aspects are the assumption of the relevant failure mechanism, fluvial entrainment, geotechnical characteristics of the bank material, shape of the bank profile, surface water level, and ground water table to estimate pore water pressures.

For instance, the factor of safety for a shallow slip failure of a cohesive bank can be expressed as

$$F_s = \frac{c' + (\sigma_n - p_w)\tan\gamma}{F_{Gp}} = \frac{c' + (F_G \cos\delta - p_w)\tan\gamma}{F_G \sin\delta}, \tag{3.42}$$

where c' denotes soil cohesion as a force per unit area (e.g. [kPa]). Therefore, the

limiting bank slope of cohesive banks is generally larger than in the case of non-cohesive banks (Eq. 3.41). However, the stability of cohesive banks additionally depends on the bank height, e.g. in the case of a plane slip failure, rotational slip failure, and crack-induced plane slip failure (Thorne, 1982).

3.4. Linear Stability Theory for Free Bars

Alternate free migrating bars are formed due to an intrinsic instability mechanism of water flow and non-cohesive bed load transport in approximately straight river reaches (Colombini *et al.*, 1987). Therefore, they are often referred to as free bars (Zolezzi & Seminara, 2001). The objective here is to give a brief overview on the linear stability theory of free bars. For this purpose the TREMTO tool (Adami *et al.*, 2016b) was used, which is based on the linear stability theory of Colombini *et al.* (1987). More details can be found in the literature (e.g. Zolezzi & Seminara, 2001; Adami, 2016) The linear stability theory was used to plan the setup for numerical 2-D simulations (non-linear), as well as to predict free bar stability for reduced equilibrium bed slope.

The underlying mathematical model consists of the non-linear 2-D shallow-water equations for water flow and the 2-D Exner-equation for sediment continuity. The governing equations are simplified to such an extent to allow for an analytical solution while maintaining the main physical properties of the equations. Typically, the assumptions include constant values of discharge, channel width, bed slope, equilibrium bed load transport, uniform sediment grain size, and constant Shields parameter over the whole channel. Furthermore, it is generally assumed that the river consists of a rectangular straight infinitely long channel. Finally, this leads to the steady 2-D shallow-water equations, the unsteady Exner-equation, and closures for hydraulic friction and uniform bed load transport (Tubino *et al.*, 1999).

Within the framework of linear stability theory, small (strictly infinitesimal) perturbations ε are added to the water depth, flow velocity, and bed topography (usually applied to their dimensionless variables). For instance, bed topography

z_b is perturbed as

$$z_b(x, y, t) = z_{b,0}(x) + \varepsilon e^{\Omega t} \sin\left(\frac{2\pi y}{W}\right) \cos(\lambda x - \omega t) + c.c., \tag{3.43}$$

$$\text{with} \quad \lambda = \frac{\pi W}{L}, \tag{3.44}$$

where $z_{b,0}(x)$ = initial flat bed topography, W = river width, L = bar wavelength, Ω = growth rate, ω = angular frequency of temporal perturbation, λ = dimensionless wavenumber, and $c.c.$ = complex conjugate.

The three governing non-dimensional parameters (i-iii) determine the state of the system. The (i) half-width to depth ratio β, referred to as aspect ratio in the following, is defined as

$$\beta = \frac{W}{2h_0}, \tag{3.45}$$

where h_0 = reference uniform flow depth (subscript 0 denotes reference uniform flow on undisturbed bed). The (ii) relative roughness is defined as

$$d_s = \frac{d_{50}}{h_0}, \tag{3.46}$$

where d_{50} denotes the median grain size diameter where fifty percent is finer. Finally, the (iii) Shields stress is defined as

$$\theta = \frac{S}{(s-1)d_s}, \tag{3.47}$$

where S denotes the bed slope and s the ratio between the density of the solid and water phase ($s = \rho_s/\rho \approx 2.65$). Finally, the analytical solution for Ω and ω is calculated for given λ, β, d_s, and θ. Hence, linear stability theory for free bars allows to estimate conditions of free bar instability (Ω) and migration properties (ω), such as downstream or upstream propagation of information related to the development of small amplitude two-dimensional bed perturbations (see e.g. Zolezzi & Seminara, 2001; Adami, 2016).

3.4.1. Marginal Curves for Free Bars Instability and Migration

For given hydraulic and bed load conditions (θ, β, d_s) the growth rate Ω and the angular frequency ω can be determined as a function of the wavenumber λ. Finally, β can be plotted against λ for vanishing growth rate ($\Omega = 0$) and vanishing angular frequency ($\omega = 0$). This marginal curves divide the (β, λ)-plane into different areas to identify free bar instability and free bar migration properties (Fig. 3.11). Free bars are marginally stable for vanishing growth rate ($\Omega = 0$, no amplification and no suppression). Free bars instability occurs in the regions I and II with positive growth rate ($\Omega > 0$, gray scale in Fig. 3.11), while free bars instability is suppressed in the region III with negative growth rate ($\Omega < 0$, white area in Fig. 3.11). Hence, free bar instability can be expected for an aspect ratio larger than the critical aspect ratio ($\beta > \beta_C$, super-critical conditions). The dominant bar wavenumber of the free bar instability λ is related to the maximum growth rate (typically $0.35 \leq \lambda \leq 0.5$). Note that the range of the dominant wavenumber is rather broad due to the flat marginal curve for free bar instability ($\Omega = 0$) near the minimum.

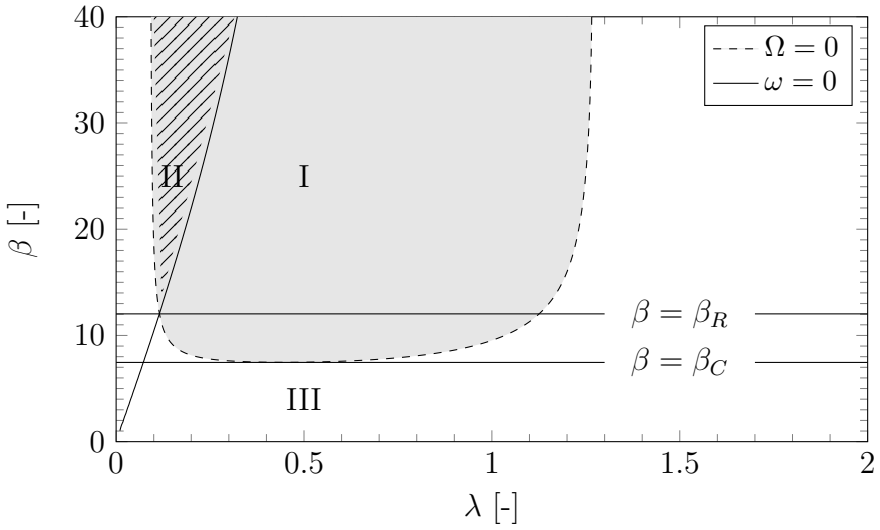

Fig. 3.11.: Marginal curves for free bar instability ($\Omega = 0$) and free bar migration ($\omega = 0$) using $\theta = 0.1$, $d_s = 0.03$, Chézy's friction law, Wong & Parker (2006) bed load formula, and $N_l = 1.38$ ($r = N_l\sqrt{\theta_c} = 0.3$) (Adami *et al.*, 2016b)

Furthermore, non-migrating free bars are defined by vanishing angular frequency ($\omega = 0$). Downstream migration takes place in region I ($\omega < 0$), while upstream migration can be expected in region II ($\omega > 0$, hatched area in Fig. 3.11). This

limit is defined by the resonant aspect ratio β_R for vanishing growth rate and angular frequency ($\Omega = \omega = 0$). Hence, for super-resonant conditions ($\beta > \beta_R$) information related to the development of small-amplitude 2-D bed perturbation may propagate upstream (Zolezzi & Seminara, 2001).

3.4.2. Comparison of Free Migrating and Forced Steady Bars

Alternate free bars have a characteristic wavelength L to river with W ratio of $L/W \sim 6 - 10$ (Adami *et al.*, 2016a) (see Fig. 3.12 (i)). This corresponds to a dimensionless wavenumber of $\lambda \sim 0.35 - 0.50$. On the other hand, alternate bars can be forced due to a local persistent planform discontinuity (e.g. obstacle, narrowing, river bend). The forced bars show only spatial variability and are non-migrating, hence steady. Steady bar wavelength is about twice the wavelength of free bars ($L/W \sim 15 - 20$) (Adami *et al.*, 2016a). Hence, typical dimensionless wavenumbers are found around $\lambda \sim 0.15 - 0.2$ (see Fig. 3.12 (ii)). Usually, forced bars under submerged conditions decay in space over approximately 2 - 3 wavelengths. Under sub-resonant conditions ($\beta < \beta_R$), forced steady bars are only triggered downstream of the local planform discontinuity (hence downstream overdeepening), while under super-resonant conditions ($\beta > \beta_R$), forced bars are expected to appear predominantly upstream of the obstacle (hence upstream overdeepening) (Zolezzi & Seminara, 2001). The damping rate of the forced bar amplitude is higher far from the resonant condition, while it is smaller when approaching resonant condition (Adami, 2016).

The linear theory for forced bars generally refers to a finite straight channel reach, as compared to the linear stability theory for free bars assuming an indefinitely long straight channel reach. The linear theory for forced bars additionally assumes a steady Exner-equation and imposes non-periodic boundary conditions to represent the effect of the local persistent perturbation (Adami, 2016).

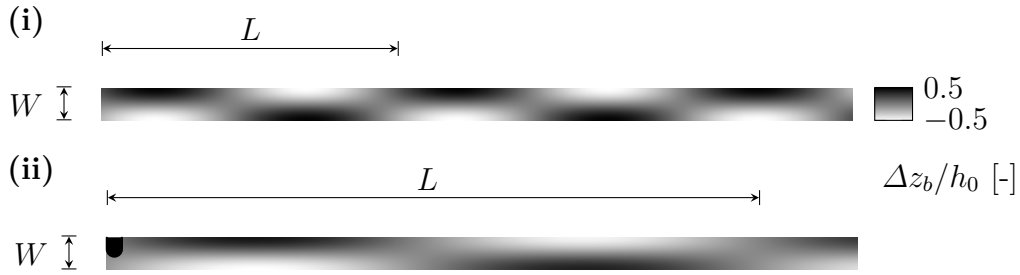

Fig. 3.12.: Sketch of alternate bar topography for (i) free bars ($L/W = 9$) and (ii) forced steady bars due to an obstacle at the left boundary ($L/W = 19$); Δz_b = bed elevation change, H_{BM} = bar height

3.4.3. Predictor for Bar Mode and Bar Height

Parker (1976) defined alternate bars as morphological pattern of first lateral mode ($m = 1$), and hence delimited them from higher lateral modes, such as central bars ($m = 2$) or braided pattern ($m \geq 3$) according to Fig. 3.13. Crosato & Mosselman (2009) proposed a predictor for the lateral bar mode m based on linear stability analysis as

$$m^2 = 0.17g\frac{(b-3)W^3S}{\sqrt{(s-1)d_{50}}CQ}, \tag{3.48}$$

where C = Chézy friction coefficient, Q = discharge, and b = degree of non-linearity of sediment transport with respect to depth-averaged flow velocity, with a usual value of $b = 10$ for gravel bed rivers, and $b = 4$ for sand rivers (Crosato & Mosselman, 2009).

Colombini *et al.* (1987) proposed a predictor for bar height at equilibrium condition

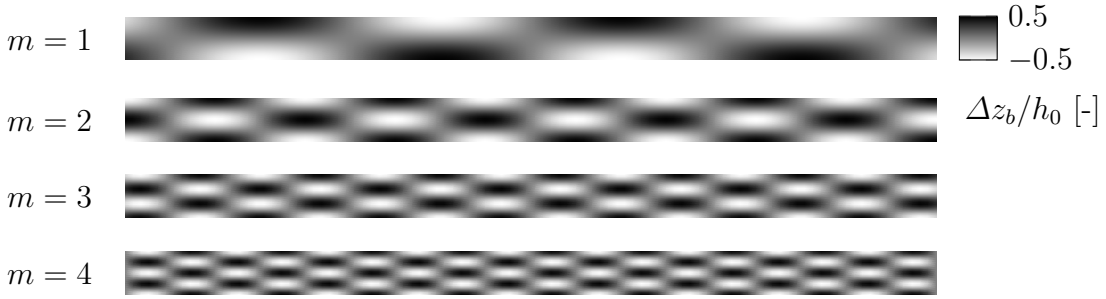

Fig. 3.13.: Sketch of free bar topography for different lateral modes m

H_{BM} for free alternate bars ($m = 1$) based on a weakly non-linear approach as

$$H_{BM} = h_0 \left[b_1 \left(\frac{(\beta - \beta_C)}{\beta_C} \right)^{1/2} + b_2 \left(\frac{(\beta - \beta_C)}{\beta_C} \right) \right] \quad \text{for} \quad \beta < 2\beta_C, \tag{3.49}$$

where b_1 and b_2 are functions of θ and d_s. Details on $b_1(\theta, d_s)$ and $b_2(\theta, d_s)$ are provided in Colombini *et al.* (1987) or Adami (2016). Typically the factors b_1 and b_2 are in the range $[0.8, 1.1]$ and $[0.5, 0.8]$, respectively. The bar height was defined as the difference between maximum and minimum bed elevations. However, the pool depth appeared to be slightly larger than the bar head height with respect to mean bed elevation. Hence, the maximum relative scour was expressed as $\eta_M/H_{BM} = 0.57$ (Colombini *et al.*, 1987).

In contrast to the approaches described above, the empirical approaches from Ikeda (1982c) and Jäggi (1983) neglect the influence of the dimensionless bed shear stress θ. The approach of Ikeda (1982c), for instance, agrees fairly well with Eq. (3.49), where most of the differences were found to be within a margin of $\pm 40\%$ (see Colombini *et al.*, 1987).

3.5. Goodness of Fit Measures

In the following goodness of fit measures are presented, which will subsequently be used to evaluate morphological numerical simulations. For further details the reader is referred to Sutherland *et al.* (2004). The mean absolute error (MAE) is determined as

$$\text{MAE} = \frac{1}{N} \sum_{j=1}^{N} |y_j - x_j| = \langle |Y - X| \rangle, \tag{3.50}$$

where Y denotes a set of N predictions (model) $y_1, y_2, .., y_N$, X a set of N observations $x_1, x_2, .., x_N$, where each element of Y can be compared to X at the same place in space and time. Note that linear interpolation between observations might be necessary for evaluation. Furthermore, the $\langle\rangle$-brackets denote a mean value.

The mean square error (MSE) and the root mean square error (RMSE) are determined according to Eq. (3.51) and Eq. (3.52), respectively.

$$\mathrm{MSE} = \frac{1}{N}\sum_{j=1}^{N}\Big(y_j - x_j\Big)^2 = \langle\big(Y - X\big)^2\rangle \tag{3.51}$$

$$\mathrm{RMSE} = \sqrt{\frac{1}{N}\sum_{j=1}^{N}\Big(y_j - x_j\Big)^2} = \sqrt{\langle\big(Y - X\big)^2\rangle} \tag{3.52}$$

The Brier Skill Score (BSS) is defined as

$$\mathrm{BSS} = 1 - \frac{\mathrm{MSE}(Y,X)}{\mathrm{MSE}(B,X)}, \tag{3.53}$$

where B denotes a set of N observations of the initial topography $b_1, b_2, .., b_N$. The classification of Sutherland *et al.* (2004) to evaluate morphological model results is shown in Table 3.2. Note that $\mathrm{RMSE} = \sqrt{\mathrm{MSE}}$ has the same dimension as the observations, e.g. [m], while BSS is dimensionless.

Table 3.2.: Classification of Brier Skill Score (BSS) for model evaluation, adapted from Sutherland *et al.* (2004)

Evaluation	**BSS**
Excellent	$0.8 - 1.0$
Good	$0.6 - 0.8$
Reasonable	$0.4 - 0.6$
Poor	$0.0 - 0.4$
Bad	< 0.0

3.6. Morphological 1-D Effect

The morphological 1-D Effect is referred to as the response of the equilibrium bed slope S_0 to a change in bed load supply $q_{b,in}$. For instance, starting from an equilibrium bed load supply $q_{b,1}$ and corresponding bed slope $S_{0,1}$, a reduced bed load supply $q_{b,2}$ would lead to a smaller equilibrium bed slope $S_{0,2}$ (Fig. 3.14).

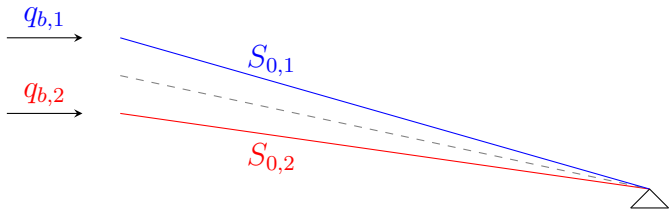

Fig. 3.14.: Sketch of the morphological 1-D effect ($S_0 = f(q_{b,in})$) for bed load supply $q_{b,1} > q_{b,2}$

The equilibrium bed slope for the steady solution of the Saint-Venant-Exner model using the bed load formula of Meyer-Peter & Müller (1948) reads

$$S_0 = \frac{C_S}{q^{6/7}} \left[\left(\frac{\phi}{\alpha} \right)^{1/e} + \theta_c \right]^{10/7}, \qquad \text{where} \quad C_S = k_{st}^{6/7} \left[(s-1)\, d_{50} \right]^{10/7}, \quad (3.54)$$

q = specific discharge, $\phi = q_b / \sqrt{g(s-1)d_{50}^3}$ = dimensionless specific bed load transport rate, d_{50} = median grain size diameter, k_{st} = Strickler coefficient, α = bed load pre-factor, e = bed load exponent, and θ_c = critical Shields stress (Vetsch *et al.*, 2017b).

Eq. (3.54) can be used to estimate the morphological 1-D effect as a function of bed load transport ϕ and specific discharge q (see Fig. 3.15). As marked in Fig. 3.15, for instance, the equilibrium bed slope of $S_0 = 0.005$ is obtained for $\phi = 0.045$ and $q = 13.3\,\mathrm{m}^2/\mathrm{s}$. For decreasing (increasing) bed load transport, the equilibrium bed slope would decrease (increase) accordingly.

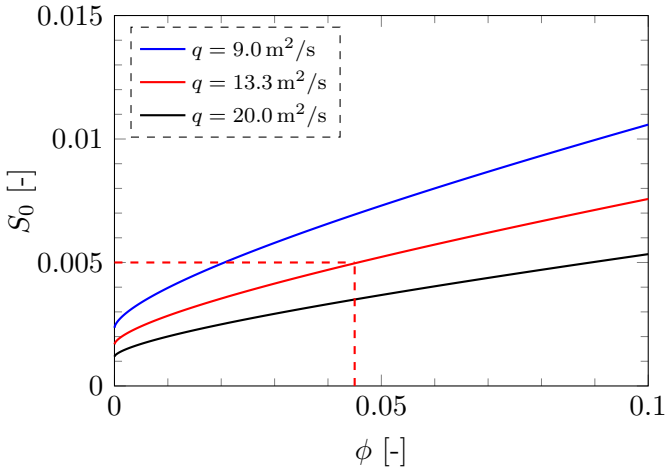

$\alpha = 4.93$

$e = 1.6$

$\theta_c = 0.047$

$d_{50} = 87.7\,\mathrm{mm}$

$k_{st} = 31.7\,\mathrm{m}^{1/3}/\mathrm{s}$

Fig. 3.15.: Steady solution of the Saint-Venant-Exner model using the MPM bed load formula for varying specific discharge q

4. Numerical Model

4.1. Overview

In the scope of the present thesis, the numerical 2-D model of the software BASEMENT (Vetsch *et al.*, 2017a) was used and further developed, particularly with regard to bed load transport. Fig. 4.1 provides an overview of the numerical model and the relevant submodules. In the following, the numerical model is described in more detail.

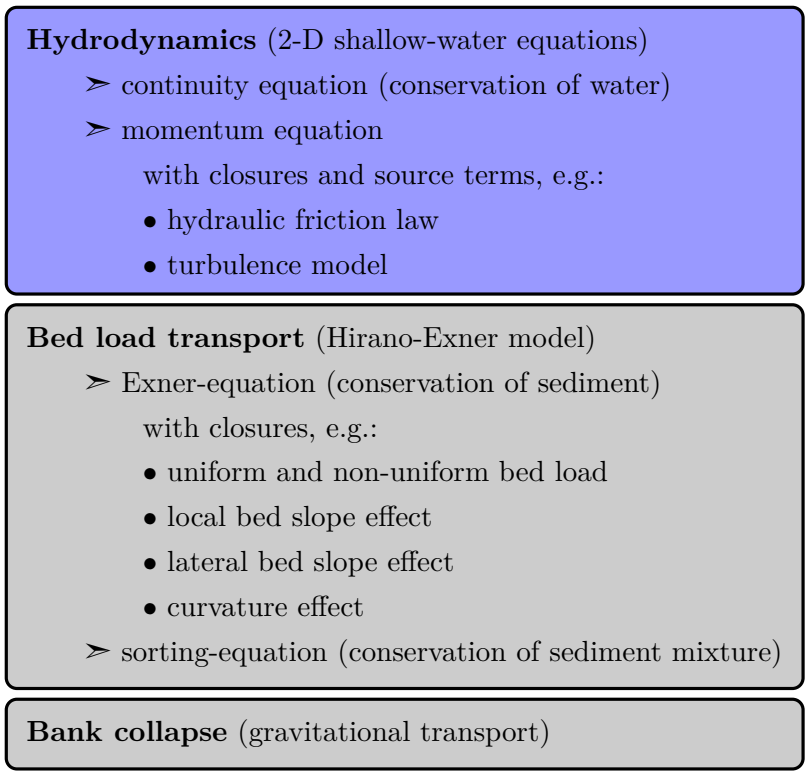

Fig. 4.1.: Overview of the numerical 2-D model and submodules

4.2. Hydrodynamics

The shallow-water equations (SWE) describe the two dimensional horizontal flow of water over arbitrary topography. They consist of the continuity-equation and the momentum-equations in x- and y-direction. The SWE is written in conserved vector form as

$$\frac{\partial \mathbf{U}}{\partial t} + \frac{\partial \mathbf{F}}{\partial x} + \frac{\partial \mathbf{G}}{\partial y} + \mathbf{S} = 0, \tag{4.1}$$

where $\mathbf{U} = (h, q, r)^T$ denotes the vector of the conserved variables, with $h =$ water depth, and $q = uh$ and $r = vh$ are the specific water discharge in x- and y-direction, respectively. Thereby, u and v denote the depth-averaged flow velocity in x- and y-direction, respectively. $\mathbf{F}$ and $\mathbf{G}$ are the flux vectors (Eq. 4.2), whereas $\mathbf{S}$ denotes the source term vector (Eq. 4.3).

$$\mathbf{F} = \begin{pmatrix} q \\ \frac{q^2}{h} + \frac{gh^2}{2} - \frac{h}{\rho}\tau_{xx} \\ \frac{qr}{h} - \frac{h}{\rho}\tau_{yx} \end{pmatrix}; \qquad \mathbf{G} = \begin{pmatrix} r \\ \frac{qr}{h} - \frac{h}{\rho}\tau_{xy} \\ \frac{r^2}{h} + \frac{gh^2}{2} - \frac{h}{\rho}\tau_{yy} \end{pmatrix} \tag{4.2}$$

$$\mathbf{S} = \begin{pmatrix} 0 \\ gh\frac{\partial z_b}{\partial x} + \frac{\tau_{bx}}{\rho} \\ gh\frac{\partial z_b}{\partial y} + \frac{\tau_{by}}{\rho} \end{pmatrix} \tag{4.3}$$

Turbulent shear-stresses τ_{xx}, $\tau_{xy} = \tau_{yx}$, and τ_{yy} can be considered with an algebraic turbulence model using a dynamic eddy viscosity approach according to Eq. (4.4-4.6).

$$\frac{\tau_{xx}}{\rho} = 2\nu_t \frac{\partial u}{\partial x} \tag{4.4}$$

$$\frac{\tau_{xy}}{\rho} = \frac{\tau_{yx}}{\rho} = \nu_t \left(\frac{\partial u}{\partial x} + \frac{\partial v}{\partial y} \right) \tag{4.5}$$

$$\frac{\tau_{yy}}{\rho} = 2\nu_t \frac{\partial v}{\partial y} \tag{4.6}$$

Thereby, ρ denotes the water density and the turbulent viscosity ν_t is determined as

$$\nu_t = \frac{\kappa}{6} u_* h, \tag{4.7}$$

where κ = von Kármán constant ($\kappa \approx 0.40$), and $u_* = \sqrt{\tau_b/\rho}$ = shear velocity. The bed shear stresses in x- and y-direction, τ_{bx} and τ_{by}, respectively, are determined as

$$\frac{\tau_{bx}}{\rho} = \frac{u|u|}{c_f^2} \quad \text{and} \quad \frac{\tau_{by}}{\rho} = \frac{v|v|}{c_f^2}, \tag{4.8}$$

where c_f denotes the dimensionless Chézy friction coefficient. The latter can be determined, for instance, using the logarithmic friction law according to Yalin & da Silva (2001) as

$$c_f = \frac{|\vec{\mathbf{u}}|}{u_*} = \frac{1}{\kappa} \ln\left(11 \frac{h}{k_s}\right), \tag{4.9}$$

or the logarithmic friction law according to Einstein (1950) as

$$c_f = \frac{|\vec{\mathbf{u}}|}{u_*} = 5.75 \log_{10}\left(12 \frac{h}{k_s}\right), \tag{4.10}$$

where $\vec{\mathbf{u}} = (u, v)^T$ = depth-averaged flow velocity vector, and k_s = equivalent sand roughness. Note that Eq. 4.10 is often referred to as Chézy's friction law (e.g. Faeh, 1997; Vetsch *et al.*, 2017a).

4.2.1. Initial and Boundary Conditions

The initial conditions define the hydraulic variables for all cells at the beginning of the simulation. Depending on the problem at hand, the initial conditions

correspond to a dry bed ($h = q = r = 0$) or to a certain flow state with defined values for h, q, and r. However, a steady hydraulic state obtained by an initial simulation, where inflow equals outflow, is generally preferred as initial condition.

The boundary conditions define the hydraulic state at the boundary of the computational domain. The wall boundary condition is an impermeable vertical wall, such as the side-walls of a rectangular lab channel. Usually, the inflow and outflow boundaries are based on the assumption that uniform flow occurs at the boundary. Hence, the hydraulic boundary variables are determined by a uniform flow law with given specific discharge and bed slope.

Optionally, the bed slope at the boundary can be dynamically adjusted due bed elevation change at the inflow boundary, e.g. in the case of reduced or increased sediment supply. Therefore, the mean value of the bed elevation change at the inflow boundary $\Delta z_{b,ib}$ is related to a reference length L_{ref}. For instance, L_{ref} can be approximated by the flow length in the computational domain, e.g. the channel length. Hence, the bed slope for uniform flow at time t is calculated as

$$S_0^t = S_0^{t=0} + \Delta z_{b,ib}/L_{ref}, \tag{4.11}$$

where $S_0^{t=0}$ is the initial bed slope at the boundary. Note that $\Delta z_{b,ib}$ is negative in the case of erosion and positive in the case of deposition.

4.2.2. Numerical Approach

The numerical model approach is briefly described below with reference to (Vetsch *et al.*, 2017a) for further details. The SWE (Eq. 4.1) are solved with a finite volume method using an explicit Godunov-type upwind scheme on an unstructured triangular mesh (Volz *et al.*, 2012). The Riemann problem at the cell interfaces can be solved with the exact Riemann solver (Toro, 2009) or the approximate HLLC Riemann solver (Toro *et al.*, 1994). A special treatment is performed at edges with transition from wet to dry (wetting and drying algorithm). This includes the state of involved cells (partially or fully wet), the minimum water depth to define wet cells, and an estimation of the wave speed to solve the Riemann problem at wet-dry interfaces (Vetsch *et al.*, 2017a).

4.3. Bed Load Transport

4.3.1. Hirano-Exner Model

The Exner-equation (Eq. 4.12) describes the temporal evolution of the bed elevation z_b and is the mass balance for sediment.

$$(1-p)\frac{\partial z_b}{\partial t} + \sum_{i=1}^{n}\left(\frac{\partial q_{bx,i}}{\partial x} + \frac{\partial q_{by,i}}{\partial y}\right) = 0 \tag{4.12}$$

Thereby, $q_{bx,i}$ and $q_{by,i}$ denote the bed load fluxes in x- and y-direction, respectively. The control volume for Eq. (4.12) is the active stratum (active layer plus active sublayer) with thickness $L_a + L_{sub}$.

Hirano (1971) introduced an active layer as a control volume for non-uniform bed load transport to account for sorting effects at the river bed surface. The concept is sketched in Fig. 4.2 and described in the following. The active layer with thickness L_a is the control volume for all grain fractions f_i of the corresponding grain size diameters d_i ($i = 1...n$, where n is the total number of grain fractions). Only sediment within the active layer is available for bed load transport during one numerical time step. In the present thesis, a constant L_a was assumed during simulation. The "active" sublayer with a thickness of L_{sub} is located just below the active layer. Here, the lower limit of the sublayer z_{sub} was assumed to reach down to a defined fixed bed level z_{fix} ($z_{sub} = z_{fix}$). The source term $S_{f,i}$ represents an imaginary flux due to the movement of the active layer and is used to balance the grain fractions of the active layer and the sublayer, f_i and f_i^{sub}, respectively. In the case of erosion (active layer moves downwards), there is a flux of grain fractions from the sublayer to the active layer ($S_{f,i} > 0$, Eq. (4.14) for $\partial z_b/\partial t < 0$). Hence, the sublayer acts as a feed of grain fractions to the active layer. In the case of deposition (active layer moves upwards), there is a flux of grain fractions from the active layer to the sublayer ($S_{f,i} < 0$, Eq. (4.14) for $\partial z_b/\partial t > 0$). Thus, the sublayer acts as a sink of grain fractions.

The continuity equation of each grain class i in the active layer is given by the

sorting equations as

$$(1-p)\frac{\partial\left(f_i L_a\right)}{\partial t}+\frac{\partial q_{bx,i}}{\partial x}+\frac{\partial q_{by,i}}{\partial y}-S_{f,i}=0, \quad \text{where } i=1...n, \tag{4.13}$$

where the source term of the grain fractions reads

$$S_{f,i}=\begin{cases}-\dfrac{\partial z_b}{\partial t}f_i^{sub}, & \text{for } \dfrac{\partial z_b}{\partial t}<0\\ -\dfrac{\partial z_b}{\partial t}f_i, & \text{for } \dfrac{\partial z_b}{\partial t}>0\end{cases} \tag{4.14}$$

Finally, the sublayer is updated as

$$(1-p)\frac{\partial\left(z_b-L_a-z_{sub}\right)}{\partial t}+\sum_{i=1}^{n}S_{f,i}=0. \tag{4.15}$$

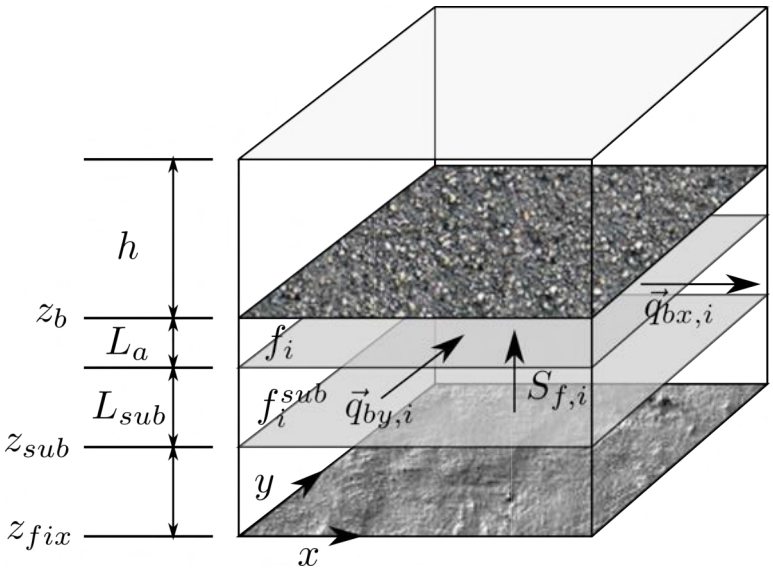

Fig. 4.2.: Sketch of Hirano model for non-uniform bed load transport

The Exner-equation (Eq. 4.12) and the sorting equations (Eq. 4.13) are integrated over the sediment cells and solved with an explicit Euler method (Volz *et al.*, 2012). These equations, together with an empirical closure for the bed load transport fluxes (see Chap. 4.3.3), are solved after the computation of the hydraulic variables for the actual time step (uncoupled solution of hydro- and morphodynamic equations).

4.3.2. Incipient Motion

The critical Shields stress can be defined as a constant value (e.g. $\theta_c = 0.047$) or may be obtained by the transformed Shields diagram according to

- Yalin & da Silva (2001) (Eq. 3.7)
- van Rijn (1984) (Eq. 3.8)

The effect of local bed slope on θ_c can be determined according to

- van Rijn (1989) (Eq. 3.11)
- Chen *et al.* (2010) (Eq. 3.14)

Further details on the incipient motion on planar or arbitrary sloped bed are given in Chap. 3.1.

4.3.3. Empirical Closures for Bed Load Transport

Bed load transport rates can be estimated based on empirical formulas. For instance, the original bed load formula of Meyer-Peter & Müller (1948) was developed for uniform sediment (Eq. 3.18). This bed load formula can be extended to non-uniform sediments (see e.g. Ribberink, 1987). The total bed load transport $q_b = |\vec{q}_b|$ is determined as the sum of the transport rates of each grain class. For n grain classes, each represented by fraction f_i in the active layer, q_b reads

$$q_b = \sum_{i=1}^{n} f_i \alpha \sqrt{g(s-1)d_i^3}(\theta_i - F_{hc}\theta_c)^e, \tag{4.16}$$

where α = bed load pre-factor, e = bed load exponent, g = gravitational acceleration, $s = \rho_s/\rho$ = specific density (ρ_s = sediment density and ρ = water density), d_i = grain size diameter for grain class i, θ_i = Shields stress of grain class i ($\theta_i = |\vec{\mathbf{u}}|^2/(c_f^2 g(s-1)d_i)$, with $\vec{\mathbf{u}} = (u, v)^T$ = depth-averaged flow velocity vector and c_f = dimensionless Chézy friction coefficient), F_{hc} = hiding function according to Ashida & Michiue (1972) (Eq. 3.21), and θ_c = critical Shields stress ($\theta_{c,\delta}$ in case the local bed slope effect is taken into account). The original bed load pre-factor and exponent have values of $\alpha = 8$ and $e = 1.5$, respectively

(Meyer-Peter & Müller, 1948), but have been readjusted to $\alpha = 4.93$ and $e = 1.6$, respectively (Wong & Parker, 2006).

The bed load transport direction deviates from the depth-averaged flow direction due to (i) lateral bed slope with respect to flow direction and (ii) spiral flow motion in river bends. These two effects are detailed in the following.

4.3.4. Lateral Bed Slope Effect

On a plane inclined laterally to the flow direction, the gravitational force acting on non-cohesive bed material leads to a downhill component of the bed load transport, which deviates from the main flow direction (e.g. Kikkawa *et al.*, 1976; Ikeda, 1982b). In the following, this is referred to as lateral bed slope effect. The deviation of the bed load transport direction of grain class i with respect to the main flow direction ($\varphi_{b,i}$) is determined as

$$\tan \varphi_{b,i} = -N_l \left(\frac{\theta_c}{\theta_i} \right)^{M_l} \vec{s} \cdot \vec{n}_q, \qquad \text{where } \vec{s} \cdot \vec{n}_q < 0, \tag{4.17}$$

where $\vec{n}_q$ = unit vector pointing in downhill direction perpendicular to $\vec{q}$, $\vec{s} = (\frac{\partial z_b}{\partial x}, \frac{\partial z_b}{\partial y})^T$ = bed slope (positive uphill, negative downhill), N_l = factor for lateral bed slope approach, also referred to as Ikeda parameter, and M_l = exponent of lateral bed slope approach (see Fig. 3.6).

For more details on the lateral bed slope effect along with a detailed overview on different approaches from literature for N_l and M_l it is referred to Table 3.1 (Chap. 3.2.3).

4.3.5. Curvature Effect

Spiral flow motion in a river bend exerts a bed shear stress pointing towards the inner side of the river bend. For further details on the curvature effect it is referred to Chap. 3.2.4.

The deviation of the bed load transport direction with respect to the main flow direction due to the curvature effect in equilibrium condition can be written

as

$$\tan \varphi_* = -N_* \frac{h}{R}, \tag{4.18}$$

where N_* = coefficient of the curvature effect, h = water depth, and R = radius of river bend. The coefficient of the curvature effect typically takes a value of $N_* = 7.0$ for natural rivers (Engelund, 1974). Furthermore, $N_* = f(C)$ can be determined depending on the Chézy friction coefficient according to Eq. (3.36).

Local estimates of the radius R on an unstructured triangular grid can be obtained based on local information of the lateral water surface inclination or based on the velocity vectors. These two approaches are described in the following.

Radius Estimation Based on Water Surface Inclination

The centrifugal force of the water flow in a river bend leads to a transversal inclination of the water surface with a higher water level on the outer side of the bend (Fig. 3.8, Chap. 3.2.4). The hydrostatic pressure difference, which builds up between the two embankments, forces the water to flow back at the bottom. Consequently, a spiral flow motion develops in river bends. The local estimation of the river bend radius R for a triangular element e based on the local water surface inclination is sketched in Fig. 4.3.

The plane that describes the water surface in element e can be approximated by a plane with the normal vector $\vec{n}_{ws}$ using the information of the water surface elevation of the neighbor elements ζ_i $(i = 1, 2, 3)$ as

$$\overrightarrow{n}_{ws} = \overrightarrow{\zeta_i \zeta_{i+1}} \times \overrightarrow{\zeta_i \zeta_{i+2}}. \tag{4.19}$$

The projection of the specific discharge $\vec{q}$ onto the water surface plane is given as

$$\vec{q}_p = \vec{n}_{ws} \times \left(\vec{q} \times \vec{n}_{ws} \right). \tag{4.20}$$

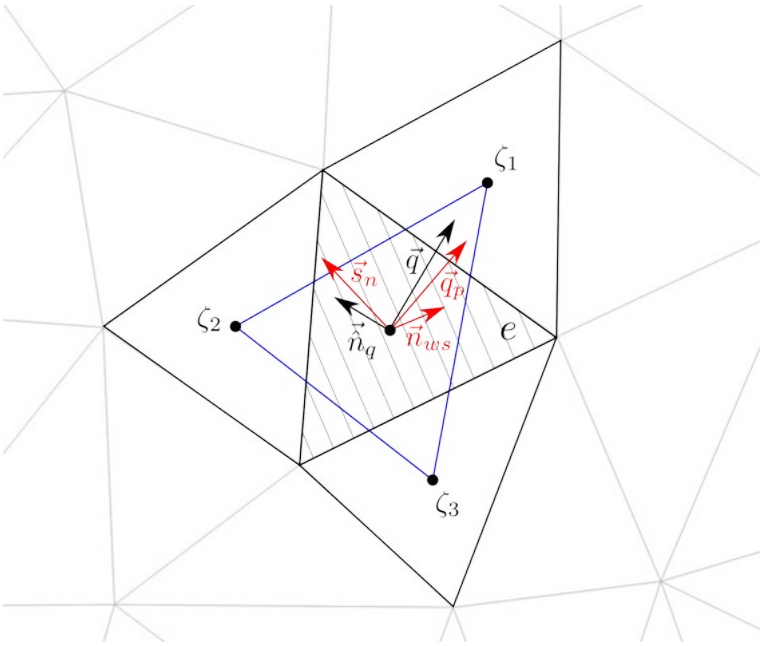

Fig. 4.3.: Definition sketch and stencil for the estimation of the local river bend radius for a triangular element e based on lateral water surface slope, note: 2-D vectors (black) are orthogonal, and 3-D vectors (red) are orthogonal

Therefore, the plane defining the water surface normal to the flow direction is determined as

$$\vec{s}_n = \vec{q}_p \times \vec{n}_{ws}. \tag{4.21}$$

Finally, the radius R can be determined using Eq. (3.32) as

$$R = \frac{\alpha u^2}{g\left(\nabla \vec{s}_n \cdot \vec{\hat{n}}_q\right)}, \tag{4.22}$$

where $\vec{\hat{n}}_q$ = unit normal vector of $\vec{q}$ pointing in uphill direction of the water surface plane ($\vec{s}_n \cdot \vec{\hat{n}}_q > 0$). Therefore, $\nabla \vec{s}_n \cdot \vec{\hat{n}}_q$ denotes the water surface slope normal to the flow direction.

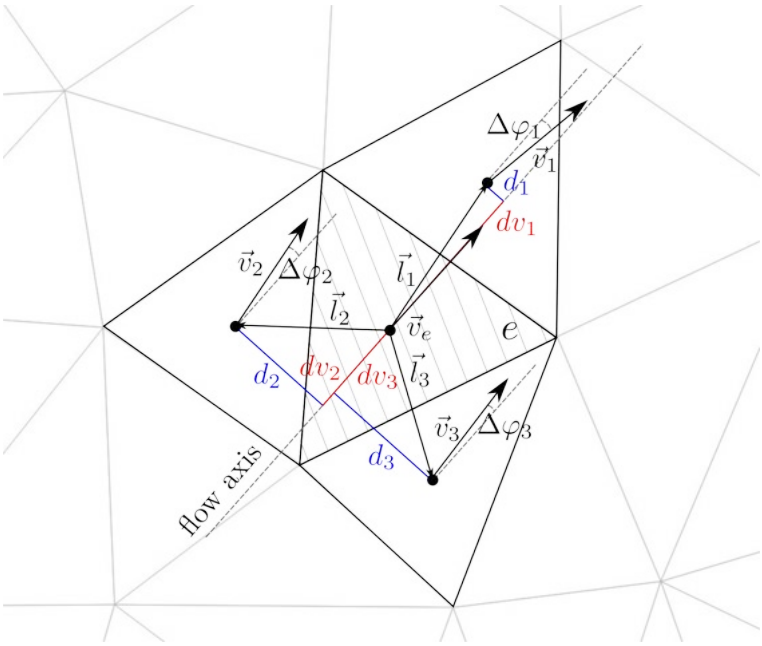

Fig. 4.4.: Definition sketch for radius estimation based on velocity vectors

Radius Estimation Based on Velocity Vectors

The curve radius R of the river bend can be determined based on the direction of the depth-averaged flow velocity vectors as

$$R = \frac{\Delta s}{\Delta \varphi}, \tag{4.23}$$

where Δs = distance over which the flow direction changes and $\Delta\varphi$ = rate of change. For a local estimate of R, the velocity vector $\vec{v}_e$ of the triangular element e and the velocity vectors of the neighbor cells $\vec{v}_i$ $(i = 1, 2, 3)$ are used (see Fig. 4.4). The contributions of the velocity vectors of the neighboring elements are weighted by the distance dv_i between the element center point and the projection of the neighbor center point on the flow axis given by $\vec{v}_e$ (Eq. 4.24) and inversely weighted by the distance d_i between the element center point and the flow axis (Eq. 4.25).

$$dv_i = \sqrt{|\vec{l}_i|^2 - d_i^2} \tag{4.24}$$

Thereby, $|\vec{l_i}|$ denotes the distance between the center point of element e and its neighboring elements i ($i = 1, 2, 3$) and d_i is defined as

$$d_i = \frac{|\vec{l_i} \times \vec{v_e}|}{|\vec{v_e}|} \tag{4.25}$$

Finally, the radius R is determined as a weighted mean according to

$$R = \frac{\sum_{i=1}^{3} \frac{dv_i^2}{d_i^2} \frac{\Delta s_i}{\Delta \varphi_i}}{\sum_{i=1}^{3} \frac{dv_i^2}{d_i^2}}. \tag{4.26}$$

4.3.6. Bank Failure

Gravitational bank failure is based on a geometrical approach, where bank collapse occurs if the local bed slope will exceed a predefined critical angle for dry and wet elements, γ_{dry} and γ_{wet}, respectively. The effect of apparent cohesion can be reproduced to some degree by considering a larger angle for the material than its angle of repose.

In the case of bank failure, the sediment volume that has to be transported to restore the angle of repose can be determined in each element. This volume is added to the bed load flux over the edges to the surrounding, lower elements. The geometrical bank failure approach can be computationally expensive. Local bank collapse might lead to an increased bed slope downhill. Hence, this may trigger a cascade of bank collapse downhill. Therefore, an abort criterion during one numerical time step can significantly reduce computation time, such as a necessary minimal volume change and a maximal number of iterations to check for morphological changes in the computational mesh. The bank failure approach implemented in BASEMENT was tested for simplified geometry and was successfully validated for modeling of embankment breaching (see Volz, 2013).

4.3.7. Numerical Time Step and Morphological Factor

For explicit time integration, the numerical time step Δt is constrained by the Courant-Friedrichs-Levy (CFL) criterion as

$$CFL = \frac{|\vec{\mathbf{u}}|+c}{\Delta x/\Delta t} \leq 1.0, \tag{4.27}$$

where $|\vec{\mathbf{u}}|$= absolute value of the depth-averaged flow velocity vector, $c = \sqrt{gh}$ = characteristic wave speed, Δt = numerical time step, $\Delta x = \Omega/l_e$ = grid spacing, with Ω = triangular cell area and l_e = cell edge length. The actual numerical time step is the minimal value over all edges of the computational grid.

In order to reduce computational costs, simulations can be accelerated using a morphological factor as described in the following. Assuming (i) only minor changes in bed elevation during a numerical time step Δt determined by the CFL condition (Eq. 4.27) and (ii) approximately steady flow condition during several subsequent Δt, sediment transport can be calculated based on the same hydraulic variables during $m_f \Delta t$, where m_f is the morphological factor. For instance, with a morphological factor of ten, the hydraulic variables are updated every tenth numerical time step ($10\Delta t$). Note that this only affects hydraulics, as morphology is still updated every numerical time step (Δt).

4.3.8. Bed Perturbation

Bed perturbation can be applied to introduce a disturbance to trigger free bars. Therefore, the bed elevation of the node i at time t is perturbed as

$$z_{b,i}(t, \varepsilon) = z_{b,i}(t) + \varepsilon_i(t), \tag{4.28}$$

where $z_{b,i}(t)$ = bed elevation of node i at time t and $\varepsilon_i(t)$ = perturbation offset of node i in the numerical grid for this time step. Bed perturbation is applied randomly in space on all nodes using a random number generator for each node that returns: $-\varepsilon$, $+\varepsilon$, or zero. The bed perturbation approach is only applied to cells, where the local water depth h is significantly larger than the bed perturbation, e.g. $h > 10\varepsilon$. Boundary cells are excluded from this approach. This

bed perturbation approach can be applied at defined time intervals, e.g. daily. Generally, $|\varepsilon|$ is in the order of one percent of the uniform approach flow depth h_0. Note that the global mass conservation (over the whole grid) is ensured by the randomness of the bed perturbation approach.

4.3.9. Initial and Boundary Conditions

The initial conditions define the bed elevation and the grain size distribution for all cells at the beginning of the simulation. The bed elevation is defined in the computational mesh. However, the bed elevation can also be used from an old simulation (restart).

The boundary conditions define the bed load transport at the boundaries of the computational domain. The wall boundary condition is an impermeable vertical wall, same as in the case of hydraulics. Usually, the bed load transport rate is defined at the inflow boundary and is distributed over the boundary cells. However, a transparent bed load boundary is defined downstream. Thereby, the bed load transport over the boundary corresponds to the bed load that is transported to the boundary cell. This guarantees a fixed downstream boundary (no erosion/deposition).

5. Model Validation

5.1. Lateral Erosion in Straight River Reach

5.1.1. Introduction

The aim of this chapter is to validate the numerical model and to assess the influence of the main approaches used for modeling lateral erosion processes. These are in particular the (i) correction of the critical Shields stress due to local bed slope, (ii) correction of the bed load transport direction due to gravitational influence of lateral bed slope, and (iii) bank collapse. Therefore, the laboratory experiment of Ikeda (1981) on fluvial lateral erosion in a straight channel was used as reference data for the validation. The simulation of this experiment significantly helped to validate and improve the numerical model. Sensitivity analysis was performed to evaluate the governing model parameters. These findings were essential for further modeling of the erosion process of artificial gravel deposits (see Chap. 6).

5.1.2. Reference Laboratory Experiment

Ikeda (1981) investigated lateral erosion in a straight channel using non-cohesive sandy material. The laboratory flume was 15 m long, 0.5 m wide, and had a bed slope of 0.215 %. A constant discharge of 4.13 l/s was applied at the upstream boundary (run No 17). Data of the exact sediment feed are not available, but sediment was fed in the laboratory experiment at the upstream boundary in order to minimize erosion at the inlet. However, erosion at the inlet was not completely avoided due to limited sediment supply from the embankment. The initial mobile bed corresponds to a half symmetrical model of a trapezoidal channel, where the

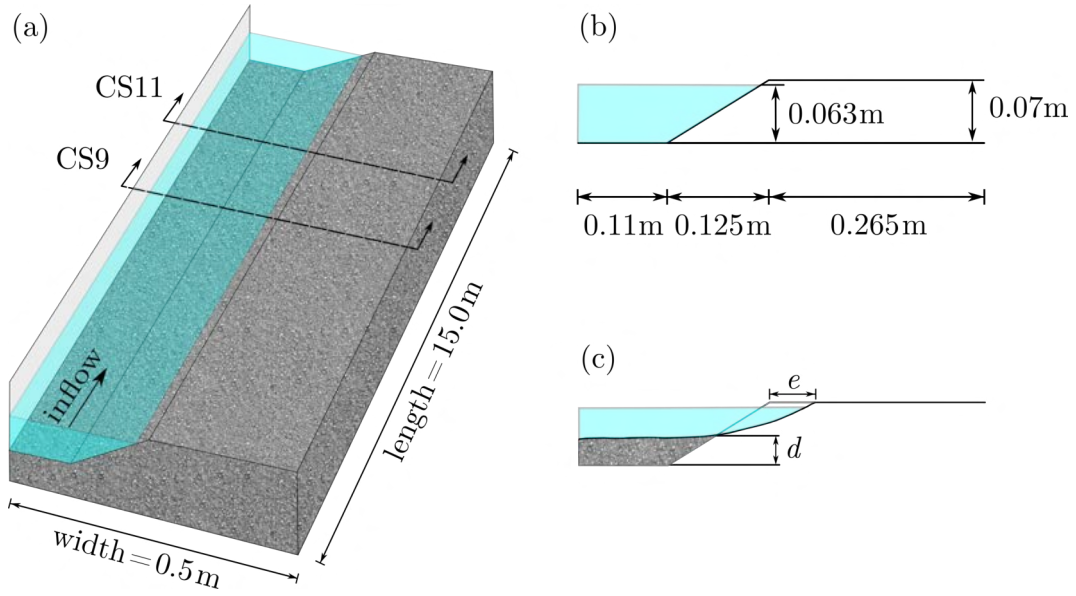

Fig. 5.1.: (a) Ikeda's laboratory setup with reference cross sections CS9 and CS11, (b) geometry of CS9 and CS11, and (c) definition sketch of lateral erosion of width e and deposition at bank toe of depth d

left side was limited by a vertical glass wall (see Fig. 5.1). The duration of the laboratory experiment was twelve hours. The topography was measured in the two cross sections CS9 and CS11, 9 m and 11 m from the inlet, respectively. The bed and the bank material consisted of a well-graded sand with median diameter of $d_{50} = 1.3$ mm and a geometric standard deviation of $\sigma_g = 1.3$. The tendency towards meandering was prevented by the fixed glass wall (Ikeda, 1981).

5.1.3. Numerical Model Setup

The topography was parametrized based on the laboratory experiments (Fig. 5.1). The computational grid was discretized using approx. 35,000 elements. In addition to this medium discretized grid, a finer and coarser grid were evaluated in the scope of a sensitivity analysis (Table 5.1).

At the upstream hydraulic boundary a constant discharge of 4.13 l/s was defined assuming uniform flow with the same bed slope as in the channel. Similarly, uniform flow was defined for the downstream hydraulic boundary condition. The initial hydraulic conditions consisted of a steady flow field. The roughness of the channel bed and the embankments were defined with an equivalent sand roughness of $k_s = 3$ mm using Einstein's logarithmic friction law according to Eq. (4.10)

Table 5.1.: Overview of the computational grids

Grid	Mean element size [cm^2]	Number of elements
fine	1.4	55,000
medium	2.2	35,000
coarse	3.4	22,000

valid for hydraulic rough boundaries. The initial water depth of h_0 =60.2 mm matched fairly well with the measured water depth of $h_{0,ref}$ =61.0 mm. Note that during the simulation the water table slightly increased by 2.4 mm, which was found to be in good agreement with the increase of 2.5 mm in Ikeda's experiment Ikeda (1981).

Sediment was added at the upstream boundary according to the local transport capacity, whereas a transparent boundary condition was applied downstream. The uniform bed load transport was modeled according to Eq. (3.18) using a mean grain size of $d_m = 1.3$ mm. The latter corresponds to the median grain size according to Ikeda's laboratory experiment Ikeda (1981) ($d_m = d_{50}$). The bed load pre-factor α was used as calibration parameter. The critical Shields stress was determined based on the approach of van Rijn (1984) given by Eq. (3.8). The lateral bed slope effect on the bed load transport direction was determined by Eq. (4.17) using the lateral transport factor N_l as calibration parameter. Bank collapse was taken into account by the geometrical approach (Chap. 4.3.6) using different angles of repose for dry and wet material, γ_{dry} and γ_{wet}, respectively.

5.1.4. Results

The numerical model was calibrated using the medium size computational grid (Table 5.1). The following parameters were found for the calibrated model: Bed load pre-factor $\alpha = 1.6$, lateral transport factor $N_l = 1.4$, and angle of repose for dry and wet material $\gamma_{dry} = 34°$ and $\gamma_{wet} = 30°$, respectively. The calibrated numerical model agreed fairly well with Ikeda's reference data over the entire time span of twelve hours for cross section CS9 (Fig. 5.2) and cross section CS11 (Fig. 5.3). This was further quantified by means of goodness-of-fit measures, such as the Brier Skill Score (BSS) and the root mean square error (RMSE) (see

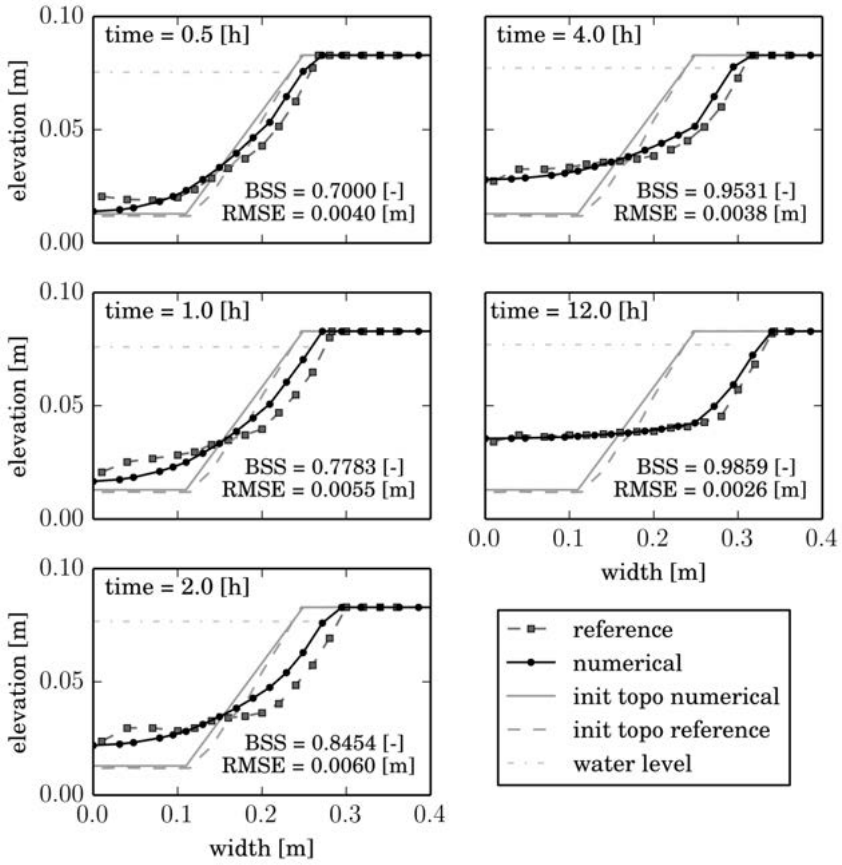

Fig. 5.2.: Validation of numerical model at cross section CS9 9 m from the inlet using Ikeda's reference data

Chap. 3.5). The BSS continuously improved over time for both cross sections. For cross section CS9, the BSS improved from *good* agreement for the first two time steps to *excellent* agreement for the last three time steps. The RMSE increased during the first three time steps and decreased during the last two time steps. However, the evaluation for cross section CS11 was even slightly better. In this case, the BSS indicated a *good* agreement for the first time step and an *excellent* agreement for the last four time steps. Furthermore, the continuous decrease of the RMSE indicates an increasing agreement over the course of the simulation. Note that the initial topography of the numerical model was created based on the given geometry (see Fig. 5.1 b) and only marginally deviates from the initial topography of the laboratory experiments (see Fig. 5.2).

A sensitivity analysis was performed for the governing model parameters. Thereby, the focus was put on the deposition height exactly at the bank toe (d) and the

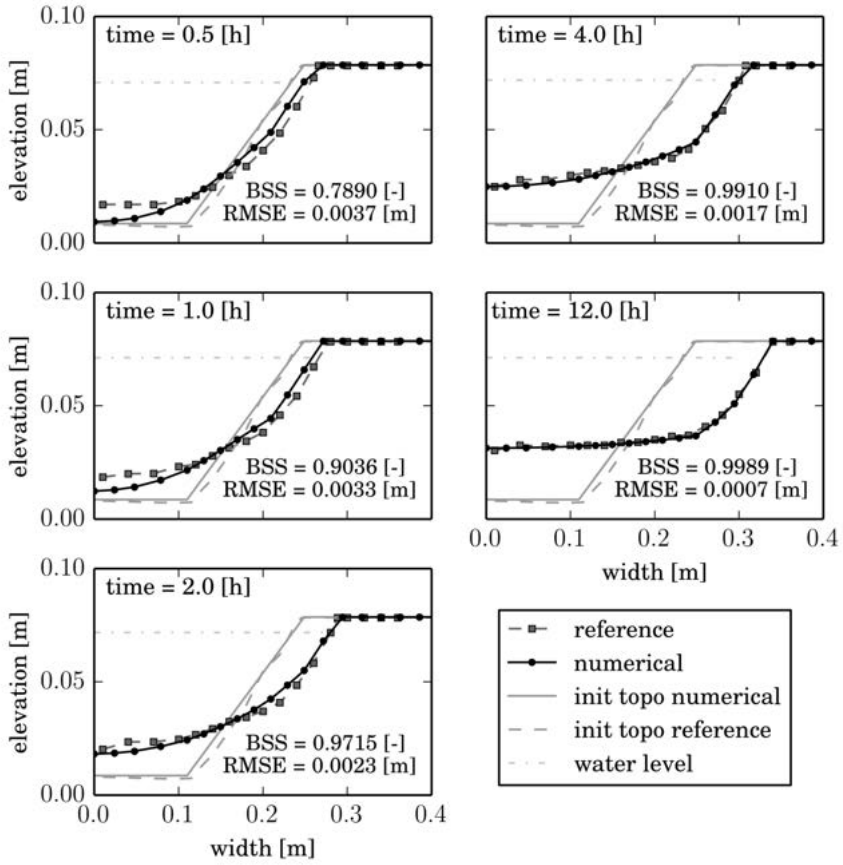

Fig. 5.3.: Validation of numerical model at cross section CS11 11 m from the inlet using Ikeda's reference data

amount, or width, of the lateral erosion (e) of the first node above the water surface including a margin of ten percent of the freeboard (Fig. 5.1, c). In order to refer to Ikeda's experimental data, deposition d and lateral erosion e were compared to the reference data d_{ref} and e_{ref}, respectively. Thus, perfect model fit would result in values of $d/d_{ref} = e/e_{ref} = 1.0$ (e.g. straight black line in Fig. 5.4). Note that the presented sensitivity analysis focused on cross section CS11, whereas corresponding results of cross section CS9 can be found in Appendix A.1.

Firstly, the three main model approaches were evaluated: the (i) correction of the critical Shields stress due to the local bed slope, (ii) lateral transport approach, and (iii) bank collapse. Based on the calibrated model, these approaches were deactivated separately to get an idea of their influence (Fig. 5.4). Without correction of the critical Shields stress, the lateral erosion process was too slow. Furthermore, without adjustment of the bed load direction due to lateral bed

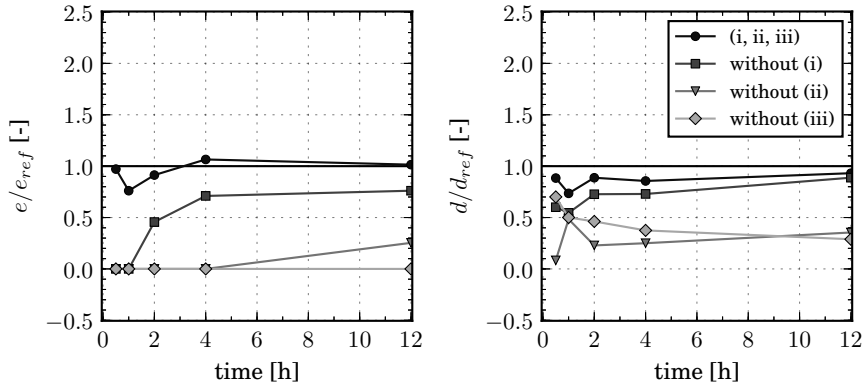

Fig. 5.4.: Sensitivity of (i) local bed slope effect, (ii) lateral bed slope effect, and (iii) bank collapse with regard to lateral erosion e (left) and deposition d (right) at CS11

slope, lateral transport from the bank towards the middle of the channel was insufficient. Besides the dislocation of material due to slope collapse, the bank collapse was essential for lowering the dry nodes at the top of the bank. Based on these findings it can be concluded that all three model approaches (i-iii) are necessary to properly capture lateral erosion dynamics of Ikeda's laboratory experiment.

Secondly, sensitivity was evaluated for the (i) bed load pre-factor α, (ii) lateral bed slope factor N_l (Ikeda parameter), (iii) angle of repose γ for bank collapse, and (iv) grid resolution. The bed load pre-factor α turned out to be a sensitive parameter with regard to lateral erosion e and deposition in the channel d (Fig. 5.5). Compared to the calibrated model, larger values of α increased the amount of lateral erosion e and vice versa (Fig. 5.5, left). Furthermore, larger α increased deposition d during the first two hours due to increased lateral sediment entrainment. After twelve hours, however, the deposition d was smaller due to generally increased transport capacity (Fig. 5.5, right).

The lateral bed slope factor N_l was a sensitive parameter as well. This refers in particular to the amount of lateral erosion and to a lower degree to the deposition (Fig. 5.6). Compared to the calibrated model, larger values of N_l increased the amount of lateral erosion e and vice versa (Fig. 5.6, left). Hence, the deposition d increased as well due to increased lateral sediment entrainment (Fig. 5.6, right).

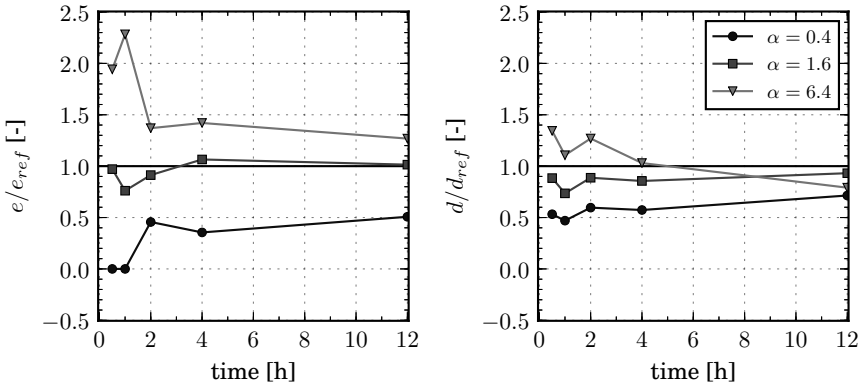

Fig. 5.5.: Sensitivity of bed load pre-factor α with regard to lateral erosion e (left) and deposition d (right) at CS11

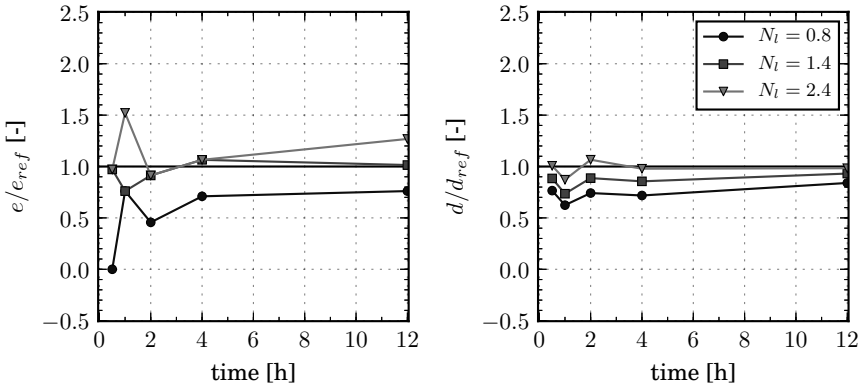

Fig. 5.6.: Sensitivity of lateral bed slope factor N_l with regard to lateral erosion e (left) and deposition d (right) at CS11

The angle of repose for dry and wet material (γ_{dry} and γ_{wet}), which are relevant to trigger bank collapse, were also sensitive parameters concerning lateral erosion e and deposition d (Fig. 5.7). In order to simplify the sensitivity analysis, identical values for critical angles were chosen for dry and wet material. Compared to the reference run ($\gamma_{dry} = \gamma_{wet} = 34°$), larger critical angles led to a decreased amount of lateral erosion e and vice versa (Fig. 5.7, left). A similar, but less pronounced trend was observed for the deposition d (Fig. 5.7, right).

Finally, the grid resolution affected the lateral erosion process in particular during the initial phase of the experiment (Fig. 5.8). Compared to the medium and fine grid, the lateral erosion was apparently underestimated when using the coarse grid, e.g. for time $t = 0.5\,\text{h}$, $t = 2.0\,\text{h}$, and $t = 4.0\,\text{h}$ (Fig. 5.8, left). Furthermore,

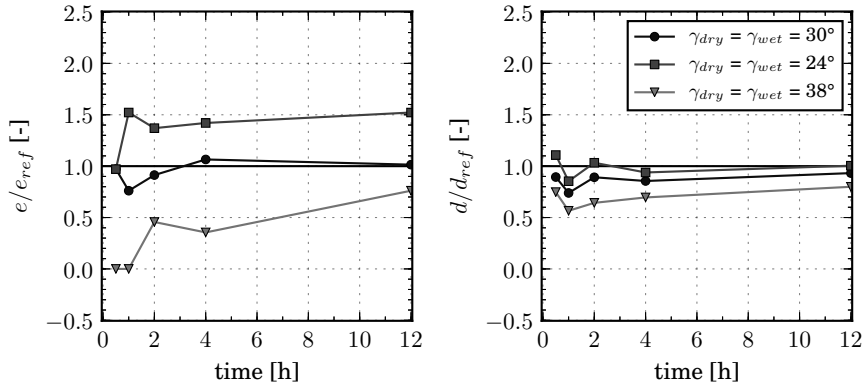

Fig. 5.7.: Sensitivity of angle of repose for dry and wet material (γ_{dry} and γ_{wet}) with regard to lateral erosion e (left) and deposition d (right) at CS11

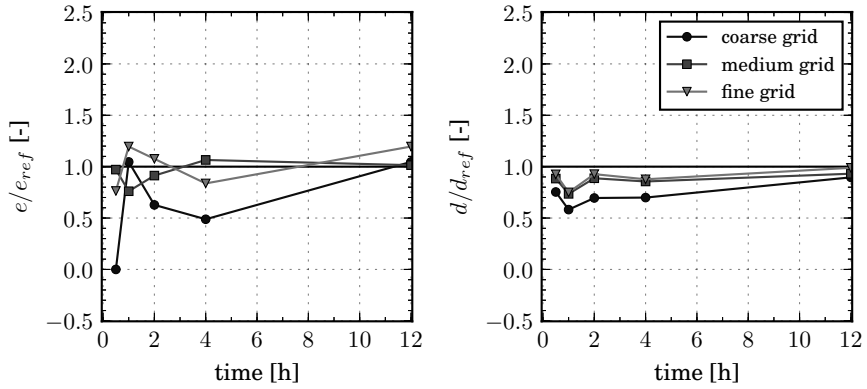

Fig. 5.8.: Sensitivity of grid resolution with regard to lateral erosion e (left) and deposition d (right) at CS11

the simulation with the coarse grid tended to underestimate the deposition in the channel, in particular during the first four hours. However, discrepancies almost vanished at $t = 12.0\,\text{h}$ (Fig. 5.8, right). The simulation with the fine mesh did not significantly improve the results compared to the simulation with the medium grid (Figure 5.8, left).

Anyhow, with the present approach the local bed slope is controlled by local grid resolution, i.e. morphological changes on different grid size Δy result in different bed slope angles γ (Fig. 5.9). Obviously, all relevant model approaches, such as the (i) local bed slope effect, (ii) lateral bed slope effect, and (iii) bank collapse, finally depend on the local bed slope. Consequently, the calibration of

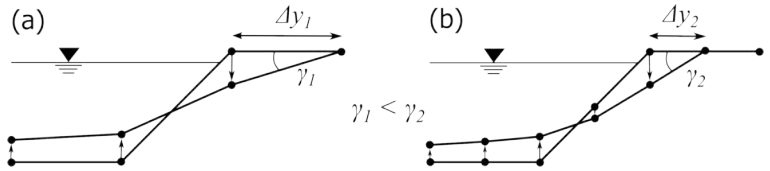

Fig. 5.9.: Sketch of the grid dependency with local bed slope angle γ for a (a) coarse grid ($\Delta\gamma_1 > \Delta\gamma_2$) and (b) fine grid

the governing parameters corresponds to a certain grid resolution.

5.1.5. Discussion

Ikeda's experiment was used by various authors to validate mathematical and numerical models on equilibrium channels based on a cross-sectional approach (Pizzuto, 1990; Kovacs & Parker, 1994; Vigilar & Diplas, 1997, 1998; Choi & Joung, 2012). Furthermore, Abderrezzak *et al.* (2016) used Ikeda's experiments to validate a numerical 2-D model. Their simulation results were evaluated with a Brier Skill Score (BSS) ranging between 0.78 and 0.94 over the whole simulation, with BSS = 0.91 after twelve hours. However, the results presented here show a slightly better agreement with the laboratory experiments. For instance, the evaluation after twelve hours shows an excellent agreement with BSS = 0.99 and 1.0 for CS9 (Figure 5.2) and CS11 (Figure 5.3), respectively. Furthermore, the numerical results of Abderrezzak *et al.* (2016) overestimated the lateral erosion (e according to Fig. 5.1c) in the beginning, while e was underestimated at the end of the experiment. Thus, the numerical model presented here also better reflects the temporal dynamics. The main differences between the two numerical models are based on the approaches to account for bed slope effects. Abderrezzak *et al.* (2016) corrected both the magnitude of the bed load transport due to bed slope in flow direction and the bed load transport direction due to lateral bed slope effect, both approaches proposed by Koch and Flokstra (Koch & Flokstra, 1981; Abderrezzak *et al.*, 2016). Because the bed slope of the channel in the laboratory experiments is rather small (0.215 %), Abderrezzak *et al.* (2016) found no significant influence when increasing the effect of bed slope in flow direction on the magnitude of the bed load transport. Although Abderrezzak *et al.* (2016) used a different bed load formula (van Rijn) and another approach to account for local bed slope effect, they mentioned that this did not significantly improve the results. In contrast, the local bed slope effect on the critical Shields stress significantly improved the

temporal dynamics of the presented lateral erosion process. Finally, Abderrezzak *et al.* (2016) used different parameter values for the lateral bed slope effect in their model ($M_l = 1.0$, $N_l = 3.14$; with $\theta_c = 0.045$ in Eq. 3.27)), leading to a stronger lateral bed slope effect compared to the simulations presented herein. However, it is difficult to compare lateral bed slope effects for different numerical models because this approach adds diffusion to the numerical model. The sensitivity analysis presented above indicates that an increased Ikeda parameter N_l generally increases lateral erosion and consequently also increases deposition in the middle of the channel. A general approach for the lateral bed slope effect was proposed by Schmautz (2003) distinguishing different types of grain movement, such as rolling and sliding ($N_l = 1.45$, $M_l = 0.5$) and saltation ($N_l = 0.75$, $M_l = 0.25$). Recent laboratory experiments from Baar *et al.* (2018) suggest that the lateral bed slope effect depends on grain size, sediment mobility (θ/θ_c), and secondary flow intensity in the case of river bends.

5.1.6. Summary

The influence of three main model concepts was analyzed, in particular the (i) local bed slope effect, (ii) lateral bed slope effect, and (iii) bank collapse. Therefore, the laboratory experiment of Ikeda (1981) on lateral erosion in a straight, trapezoidal channel was used as reference data. In summary, each of the presented model concepts was necessary to capture the dynamics of the lateral erosion process. For instance, without the bank collapse approach, it was not possible to lower the non-submerged nodes of the embankment. Furthermore, the correction of the critical Shields stress due to local bed slope was necessary to correctly capture erosion dynamics. This approach mainly changed the timing for incipient motion and to a minor extent the absolute value of bed load transport on the embankment. Finally, the correction of bed load transport direction due to lateral bed slope improved the lateral erosion dynamics. The most sensitive model parameters were found to be the bed load transport factor, the lateral transport factor, and the angle of repose triggering gravitational transport (in decreasing order of sensitivity). After sound calibration of these parameters, the numerical model was able to capture the lateral erosion process of Ikeda's laboratory experiment.

5.2. Morphology and Grain Sorting in River Bend

5.2.1. Introduction

Morphology in a river bend is formed by spiral flow motion due to centrifugal force (see section 3.2.4). In the following, the numerical model is validated against data from the laboratory experiment of Yen & Lee (1995). They performed experiments on morphology and grain sorting effects in a 180° flume bend using different hydrographs. These experiments have been used by various researchers for numerical model validation (e.g. Fischer-Antze *et al.*, 2009; Bui & Rutschmann, 2010).

5.2.2. Reference Laboratory Experiment

Yen & Lee (1995) performed laboratory experiments using a flume with a 180° bend. The channel had a slope of $S = 0.2\,\%$, a radius of the bend along the center line of $R_c = 4\,\mathrm{m}$, a width of $W = 1\,\mathrm{m}$, and a straight reach of 11.5 m before and after the bend. According to the ratio $R_c/W = 4$, the curvature of this river bend can be characterized as moderate (see Blanckaert, 2011). Different triangular-shaped hydrographs with varying peak flow and duration were applied in the experiments. All runs started from a base flow of $Q_0 = 0.02\,\mathrm{m}^3/\mathrm{s}$, which corresponds to a base flow depth of $h_0 = 0.0544\,\mathrm{m}$ and a shear velocity of $u_{*0} = 0.031$ m/s. Subsequently, Run No 4 was used for validation of the numerical model. There, the hydrograph had a duration of 300 min with a peak discharge of $Q_P = 0.053\,\mathrm{m}^3/\mathrm{s}$ at $t_P = 100\,\mathrm{min}$. The bed material consisted of sand with a median diameter of $d_{50} = 1.0\,\mathrm{mm}$ and a geometric standard deviation of $\sigma_g = 2.5$.

The focus of the laboratory experiment was on bed morphology and grain sorting in the channel bend. Topography was measured across various cross sections at the peak and at the end of the hydrograph. Dimensionless morphological change $\Delta z_b/h_0$ was reported in the form of contour plots and selected cross section data. The bed surface grain size distribution was sampled by pouring wax on predefined areas on the bed surface. Then, grain sorting was evaluated by comparing the median grain size diameter at the end of the experiment (d_{50}) to the initial median grain size diameter of the mixture ($d_{50,0}$).

5.2.3. Numerical Model Setup

The numerical model was built as explained in the previous section based on Yen & Lee (1995). The triangular and unstructured computational mesh consisted of approximately 8,000 cells resulting in 12-14 cells across the channel width.

At the upstream hydraulic boundary the discharge was defined assuming uniform flow condition with the same slope as the flume. Furthermore, uniform flow condition was defined as well for the downstream hydraulic boundary. The hydraulic initial condition was defined with a steady flow field. Hydraulic friction was modeled with the logarithmic friction law according to Eq. (4.9). Equivalent sand roughness was determined based on local grain size composition as $k_s = 3d_{90}$, where d_{90} denotes the local characteristic grain size diameter where 90 percent is finer. An algebraic turbulence model was applied using the dynamic eddy viscosity approach (Eq. 4.7).

The bed load formula of Meyer-Peter & Müller (1948) extended for non-uniform bed load transport was applied according to Eq. (4.16). Bed load pre-factor and exponent were set to $\alpha = 4.93$ and $e = 1.6$, respectively (Wong & Parker, 2006). The active layer thickness was set to a constant value of $L_a = 9.7\,\text{mm}$, which is approximately three times d_{90}. The direction of bed load transport was corrected for lateral bed slope effect and curvature effect. For the former, the Ikeda parameter was set to $N_l = 1.4$, whereas for the latter curvature factor N_* was determined dynamically according to Eq. (3.36) using $a = 1$. The grain size distribution from reference laboratory experiment was determined using a log-normal distribution with median grain size of $d_{50} = 1.0\,\text{mm}$, and geometric standard deviation of $\sigma_g = 2.5$ (Fig. 5.10). This grain size distribution was discretized using nine grain classes.

5.2.4. Results

The curve radius R is required for the correction of the bed load transport direction due to spiral flow motion in the river bend (see section 4.3.5). The estimation of R was tested with both approaches based on the lateral water surface inclination (Eq. 4.22) and based on the velocity vectors (Eq. 4.26). Both approaches produced reasonable estimates of R (Fig. 5.11). Therefore, both approaches resulted in

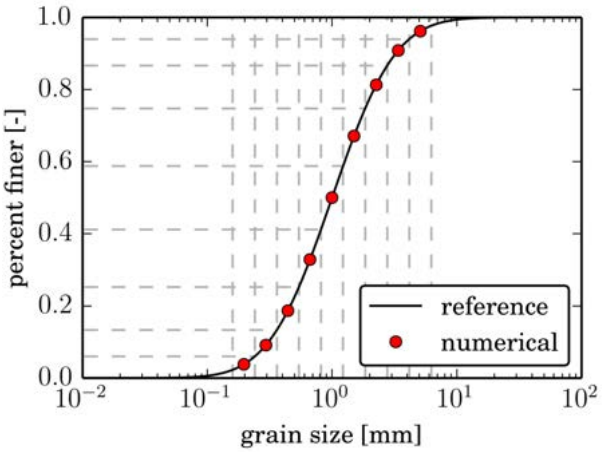

Fig. 5.10.: Reference grain size distribution ($d_{50} = 1.0\,\text{mm}$, $\sigma_g = 2.5$ and discretization with nine grain classes for numerical modeling

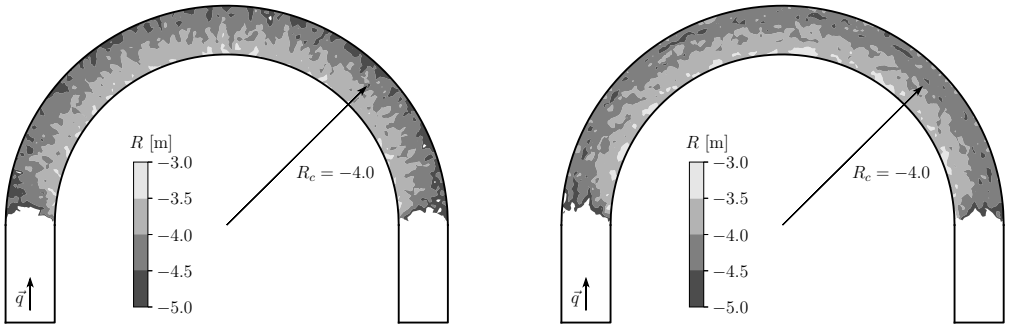

Fig. 5.11.: Estimation of the radius R based on velocity vectors (left) and water surface elevation (right) for laboratory experiment of Yen & Lee (1995) with radius of center line R_c

a similar point bar morphology and grain sorting. Subsequently, the approach based on the velocity vectors was used, unless indicated otherwise.

The point bar topography forced by the river bend is reproduced fairly well by the numerical simulation compared to the laboratory data of Yen & Lee (1995) (Fig. 5.12). Furthermore, the grain sorting effect was captured qualitatively well (Fig. 5.13). However, the abrupt lateral change from coarser ($d_{50}/d_{50,0} = 3$) to finer bed ($d_{50}/d_{50,0} < 1$) between 90 and 120 degrees was not reproduced by the numerical model.

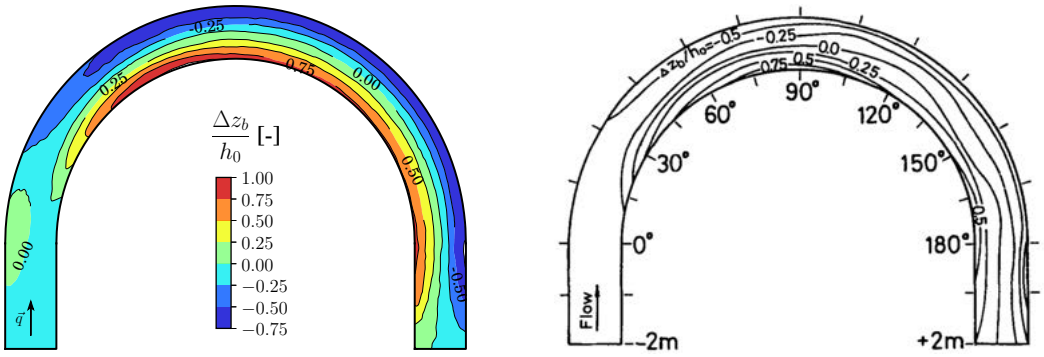

Fig. 5.12.: Morphological change $\Delta z_b/h_0$ (normalized with approach flow depth h_0) in numerical model (left) and laboratory experiment of Yen & Lee (1995) (right)

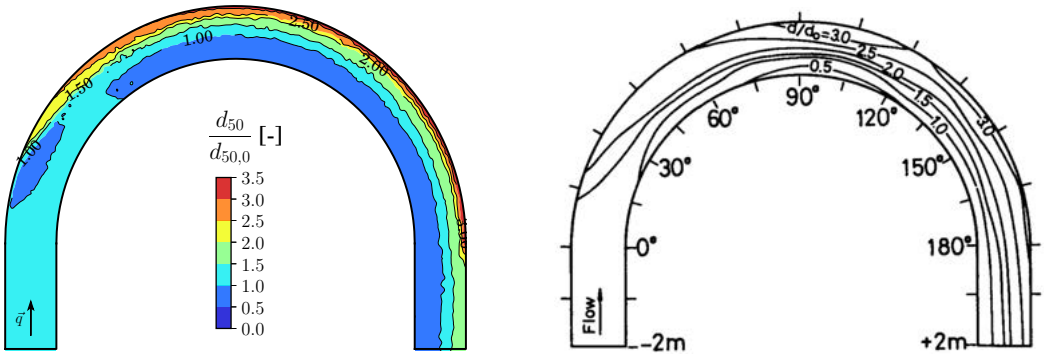

Fig. 5.13.: Grain sorting effects indicated by the relative median grain size diameter $d_{50}/d_{50,0}$ ($d_{50,0}$ = initial median grain size diameter of the mixture) in numerical model (left) and laboratory experiment of Yen & Lee (1995) (right)

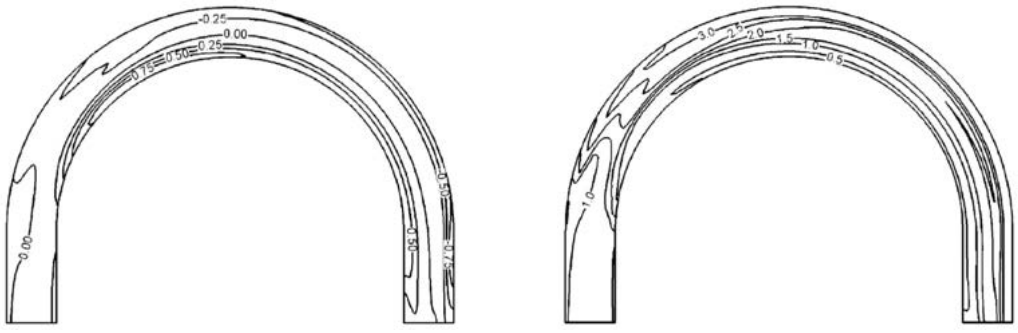

Fig. 5.14.: Morphological change $\Delta z_b/h_0$ (left) and grain sorting effects $d_{50}/d_{50,0}$ (right) of numerical 3-D simulation from Fischer-Antze *et al.* (2009)

5.2.5. Discussion

The following discussion focuses on a comparison with other numerical models and experimental studies, and limitations and possible improvements of the presented numerical model. The presented simulation results seem to have no significant drawback compared to numerical 3-D simulations from literature for the same laboratory experiment (Yen & Lee, 1995). For instance, Fischer-Antze *et al.* (2009) validated their 3-D model for topography and grain sorting (Fig. 5.14). The point bar topography was well reproduced, similar to the results presented herein (see Fig. 5.12). The location of the erosion at the outer side of the bend was slightly better reproduced by the presented numerical 2-D model. However, the numerical 3-D simulation slightly better reproduced grain sorting effects, especially the fining of the bed composition at the inner side of the bend.

Generally, at the entrance of a bend with flat bed, the absolute depth-averaged flow velocity $|\vec{\mathbf{u}}|$ is larger near the inner side compared to the outer side of the bend (see e.g. Rozovskii, 1961; De Vriend, 1977; Ghobadian & Mohammadi, 2011). Therefore, in this place, the bed shear stress and the bed load transport capacity are slightly higher. This effect at the beginning of the bend was reproduced qualitatively correctly by the numerical model. This is shown in Fig. 5.15 (a) for a mild to moderate curved 180° bend ($R_c/W = 6.7$) as an example. Over the course of the bend, however, usually a transition of the maximum flow velocity takes place towards the outer side of the bend. This cannot be correctly reproduced by the numerical model for the initial state with flat bed. However, in the course of the simulation, the correction of the bed load transport direction due to spiral flow forms a point bar at the inner side of the bend. Hence, the flow velocities adapt accordingly, which finally results in a flow velocity distribution with higher absolute values at the outer side of the bend in the second half of the flume (Fig. 5.15, (b)).

Blanckaert (2005) commented on the limitations of numerical 2-D models to correctly reproduce the depth-averaged flow velocity field in a river bend. He argued that dispersion terms would improve the lateral distribution of the depth-averaged flow velocity, especially in the case of a flat bed. However, for a typical situation of a distinct point bar topography in a river bend, the influence of the topography on the lateral velocity distribution dominates over the correction using dispersion term to account for secondary flow effect (Blanckaert, 2005).

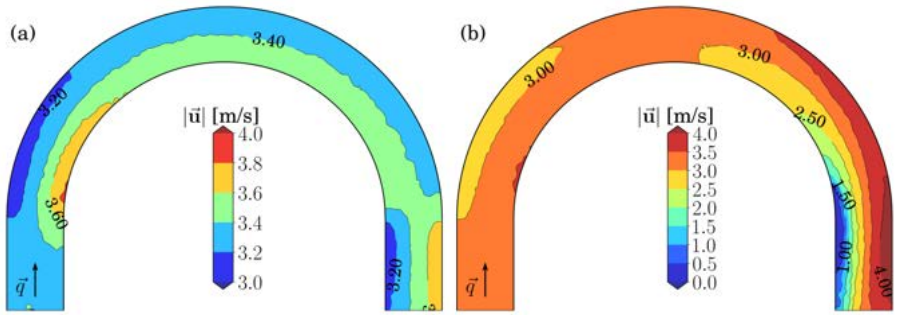

Fig. 5.15.: Absolute depth-averaged flow velocity for (a) flat non-mobile bed and (b) mobile-bed point bar morphology for $q_{b,in}/q_{b,0} = 1.0$ of setup 5

Hence, for fully developed topography in river bends, the inclusion of dispersion terms would not necessarily improve the model results. On the contrary, the correction of the depth-averaged flow velocity can be overestimated, especially when neglecting the feedback from downstream velocity and secondary circulation in the case of sharp bends (Blanckaert, 2005).

Ghobadian & Mohammadi (2011) performed hydraulic 3-D simulations using a 180° bend with rectangular cross section. They compared depth-averaged flow velocities with experimental data from literature. Clearly, the maximum velocity path started near the inner side of the bend, similar to the laboratory experiments of Rozovskii (1961). Then, the maximum velocity path changed towards the outer side of the bend along the first half of the bend. In the case of mobile bed, Fischer-Antze *et al.* (2009) compared numerical 3-D simulations with the laboratory experiment of Yen & Lee (1995). They obtained a similar morphology at the beginning of the 180° bend as presented here showing slightly higher bed elevation on the left side in flow direction (see Fig. 5.14, left).

Guan *et al.* (2016) proposed a numerical model adding only dispersion terms to correct the depth-averaged flow velocity for the curvature effect without correcting the bed load transport direction. They concluded that the most significant model improvements, besides the dispersion terms, were obtained by taking into account non-uniform sediments. Struiksma *et al.* (1985), however, only included an non-equilibrium approach to correct the bed load transport direction due to curvature effect without including dispersion terms. Their model agreed fairly well with the bed deformation in river bends obtained from laboratory experiments. Hafner (2008) proposed a morpho-dynamic 2-D model using uniform

sediment and compared simulations with laboratory experiments on self-dynamic development of two consecutive river bends with erodible embankments. The geometry was based on the Isar River in Germany with two consecutive bends of curve angles of 60° and 75°. The most significant improvements were obtained using an equilibrium approach to account for spiral flow motion effect on bed load direction, similar to the one presented here. Only minor improvements were obtained by further taking into account the development length of the curvature effect on bed load transport direction (non-equilibrium approach) and the dispersion terms to correct the depth-averaged flow velocities due to spiral flow motion (Hafner, 2008).

5.2.6. Summary

In order to account for the effect of spiral flow motion in river bends on bed load transport direction, an equilibrium approach from Engelund (1974) was validated based on the laboratory data from Yen & Lee (1995). Therefore, the curve radius R was estimated based on velocity vectors and lateral water surface inclination. Both approaches resulted in a reasonable estimate of R, and hence similar topography and grain sorting were obtained. The point bar topography of the laboratory experiments of Yen & Lee (1995) was reproduced fairly well by the presented numerical 2-D model. Grain sorting effects were reproduced qualitatively reasonably well. For mobile bed and developed point bar topography, the presented model is an appropriate tool to investigate the effect of sediment supply.

5.3. Alternate Free Migrating Bars

5.3.1. Introduction

This section is dedicated to the introduction of free bar properties and the validation of the numerical model for the simulation of free migrating bars. The latter includes the model approach to trigger free bars, the influence of lateral bed slope effect and morphological factor, and the comparison of free bar properties with information from linear and weakly non-linear theory, such as wavenumber, bar height, and bar celerity. The goals are to validate the numerical model at equilibrium conditions (equilibrium bed load supply and bed slope) and to get a dynamic equilibrium of free bars. The latter is used to define the initial conditions for further simulations, such as for the investigation of the effect of sediment supply reduction on free bars (Chap. 7).

5.3.2. Representation of Free Bars Properties

Free migrating bars cause the bed elevation on the orographic left and right side of the channel ($z_{b,left}$ and $z_{b,right}$, respectively) to deviate from the initial flat bed $z_{b,0}$ (see Fig. 5.16 a). Thereby the bar wavelength L is defined as the length of one bar unit, such as for instance the distance between to consecutive bar heads. Note that the depicted bar wavelength $L \approx 9W$ (W = channel width) is typical for free bars ($\lambda \approx 0.35$, see section 3.4.2).

Fast Fourier Transform (FFT) can be used to detect the frequency components within a periodic signal, such as the amplitude of a free bar pattern. Therefore, the spatial signal of the bar amplitude was transformed to the spatial frequency domain using FFT. Thereby, the bar amplitude signal was limited upstream to values larger than ten percent of the uniform approach flow depth. Finally, the frequency with the maximum amplitude f_{AP} in the spatial frequency domain was attributed to the signal (sine wave) with the dominant wavenumber λ of the free bar pattern (see e.g. Crosato *et al.*, 2011). Additionally, the bar wavenumber can also be determined locally by automatic detection of the bar heads. Hence, the local bar wavenumber λ_{local} can be estimated based on the local wavelength L_{local}, which is the distance between two consecutive bar heads on the same side of the

flume ($\lambda_{local} = \pi W/L_{local}$). However, in the presence of both free and steady bar signals, neither method can provide a complete picture of the situation. Note that in such cases, FFT detects different peaks in the spatial frequency domain. However, in the following the dominant frequency is attributed to the dominant bar wavenumber λ.

The bar amplitude is defined as the difference between the orographic left and right bed elevation $z_{b,left}$ and $z_{b,right}$ respectively ($A = z_{b,left} - z_{b,right}$, see Fig. 5.16 b). The absolute value of the bar amplitude $|A|$ was found to be an important quantity of the free bar pattern, especially in relation with the uniform approach flow depth h_0. The bar height is defined as the maximum difference between the deposition and scour within one bar unit, e.g. $H_{BM} = max(\Delta z_{b,left}) - min(\Delta z_{b,left})$ (see Fig. 5.16 b). This figure shows that the bar height of $H_{BM} = 2.55\,\mathrm{m}$ ($|A| = 2.2\,\mathrm{m}$) is in good agreement with the weakly non-linear theory on free bars of Colombini *et al.* (1987) with $H_{BM} = 2.57\,\mathrm{m}$ (Eq. 3.49 with $b_1 = 0.96$ and $b_2 = 0.81$). Note that the maximum relative scour $\eta_M/H_{BM} = 0.57$ is exactly the same as the maximum relative scour according the weakly non-linear theory for free bars of Colombini *et al.* (1987).

The bar celerity of single bar heads $c_{b,i}$ was determined by tracking bar head position $x_{b,i}$ over time (Fig. 5.17). The temporal resolution for this analysis was $\Delta t = 7200\,\mathrm{s}$. In this case, the bar head detection was limited to $|A|/h_0 \geq 0.1$. The spatial averaging over all bar head positions n during one time step Δt is determined as

$$c_{b,n} = 1/n \sum_{i=1}^{n} (\Delta x_{b,i}/\Delta t). \tag{5.1}$$

Finally, the mean bar celerity is obtained by temporal averaging of $c_{b,n}$ over time intervals T as

$$c_b = 1/T \sum_{t=1}^{T} c_{b,n}, \tag{5.2}$$

where t denotes the time. For this case, this resulted in a mean bar celerity of $c_b = 20.8\,\mathrm{m/h}$. This agreed fairly well with $c_b = 24.3\,\mathrm{m/h}$ obtained from the linear stability theory (Adami *et al.*, 2016b) using the approach of Nino & Garcia (1992). Note that Fig. 5.17 reveals also the pulsing phenomena of bar groups. Certain bar wave groups move with different celerity than single bars over certain periods. Hence, the bar wave group celerity varies roughly between 16 m/h and 26 m/h. In literature this phenomena was also referred to as anomalous dispersion

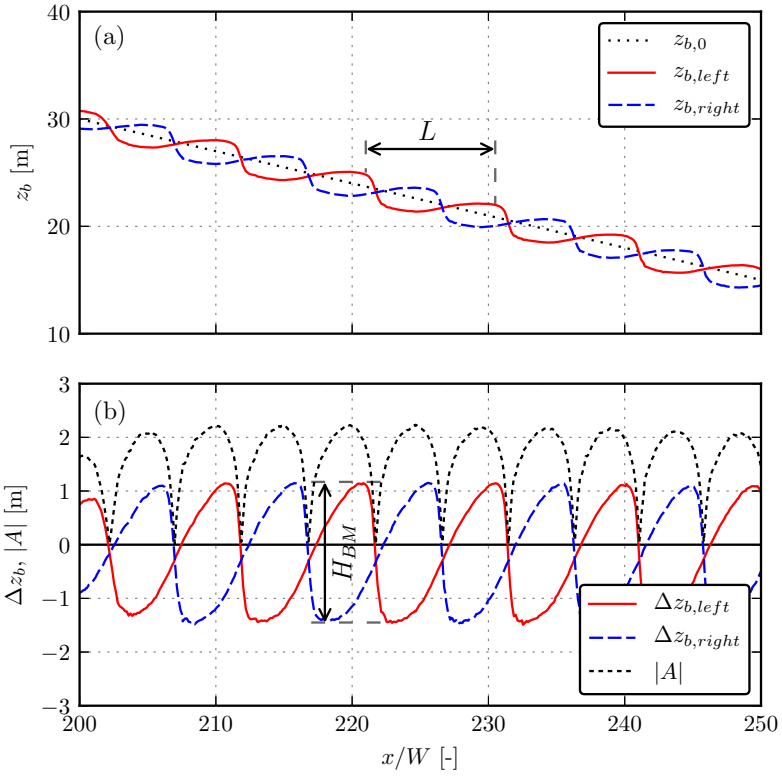

Fig. 5.16.: Free bars (a) bed elevation on the orographic left and right side of the channel $z_{b,left}$ and $z_{b,right}$, respectively, and (b) bed elevation changes on the orographic left and right side of the channel $\Delta z_{b,left}$ and $\Delta z_{b,right}$, respectively, absolute bar amplitude $|A|$, and bar height H_{BM}

(e.g. Schielen *et al.*, 1993; Seminara, 1998).

5.3.3. Influence of Lateral Bed Slope Effect

The lateral bed slope effect accounts for the effect of gravitation on bed load transport direction (see section 3.2.3). This approach introduces additional diffusion to the numerical model. The total numerical diffusion in a model is composed of both the numerical diffusion due to the discretization scheme and the diffusion induced by the lateral bed slope effect (Adami, 2016; Mosselman & Le, 2016; D. *et al.*, 2017). On the one hand, free bar amplification would build up too strong without additional lateral diffusion. On the other hand, bar amplification can be suppressed completely if lateral diffusion becomes too strong.

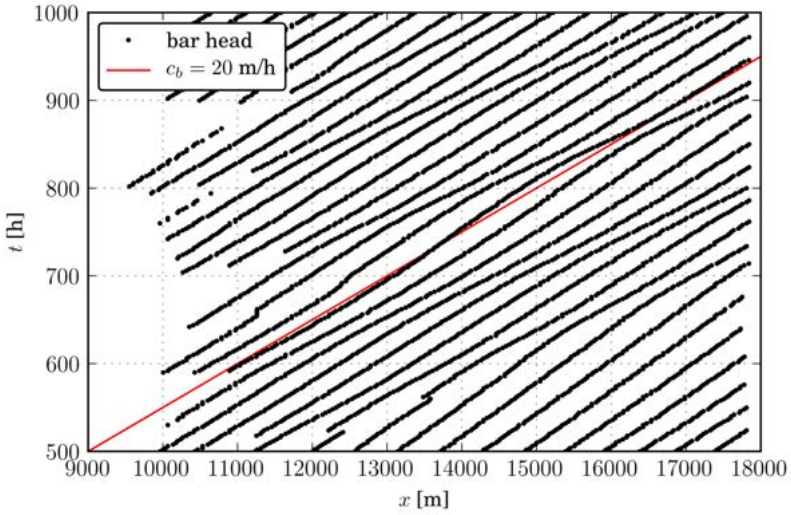

Fig. 5.17.: Bar head positions for estimation of bar celerity for equilibrium bed load transport

This additional lateral diffusion must be balanced with the numerical diffusion. Hence, the Ikeda parameter N_l is the key parameter to model free bars (Fig. 5.18). The unstructured and triangular computational mesh consisted of approximately 52,000 cells.

The absolute free bar amplitude $|A|$ is growing in time and space depending on N_l during simulation starting from flat bed. The results for varying N_l for uniform and non-uniform sediment are depicted in Fig. 5.18, and Fig. 5.19, respectively. In the case of too little lateral diffusion ($N_l = 0.90$), bar heads eventually emerged from the water surface ($|A|/h_0 > 1$, where $h_0 =$ uniform approach flow depth). The amplitude of free bars decreased gradually for increasing lateral diffusion. At the other extreme, free bar growth was suppressed completely ($N_l = 2.03$). For $N_l = 1.35$, the relative bar height ($H_{BM}/h_0 = 0.87$) corresponded quite well to the relative bar height of $H_{BM}/h_0 = 0.88$ according to Eq. (3.49) ($b_1 = 0.96$, $b_1 = 0.81$). Dynamic equilibrium established approximately after $t = 15 - 20$ d, where free bars continuously grew and migrated in cyclical repetition. The spatial and temporal development of free bars depends on the relative distance to the critical aspect ratio $(\beta - \beta_C)/\beta_C$, the numerical diffusion, and the lateral diffusion. The dimensionless bar wavenumber λ showed typical values of free bars ($0.35 \leq \lambda \leq 0.4$). This is within the lower half of the range suggested by linear stability theory for free bars ($0.35 \leq \lambda \leq 0.45$).

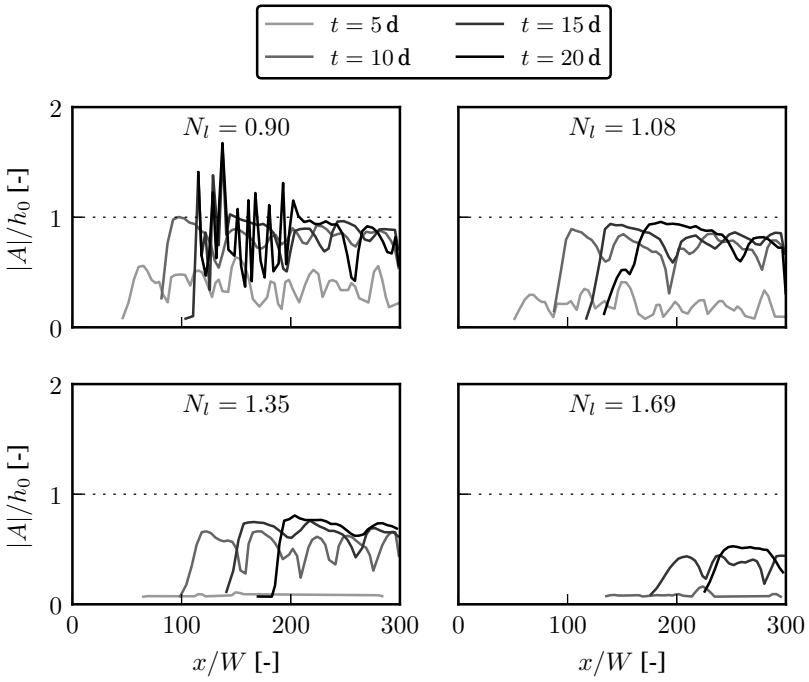

Fig. 5.18.: Influence of Ikeda parameter N_l on temporal and spatial bar amplification using uniform sediment with bed perturbation

5.3.4. Triggering of Free Bars

For numerical simulations free bars have to be triggered, especially in the case of uniform sediment (Bernini *et al.*, 2009). In the present work, free bars were triggered by perturbing the river bed at predefined time intervals and randomly in space (see section 4.3.8 for details). Time intervals between 1 and 24 hours have shown no significant influence on free bar amplification. In the following, two-hourly intervals were applied unless indicated otherwise. For non-uniform sediment, free bars can be triggered due to grain sorting effects. Thereby, changes of grain size composition in the active layer migrate downstream. This effect is often referred to as sorting waves (see e.g. Stecca *et al.*, 2014). Sorting waves were most dominant in the beginning of simulation starting from flat bed using the same grain size distribution in active layer and sublayer. The influence of sorting waves decays over time due to reaching equilibrium grain size composition of the active layer in the case of equilibrium bed load supply. It is important to note that sorting waves depend also on the number of grain classes, bed load formula, and numerical approach. Furthermore, in the case of sediment supply reduction, sorting waves were continuously triggered due to erosion at the channel

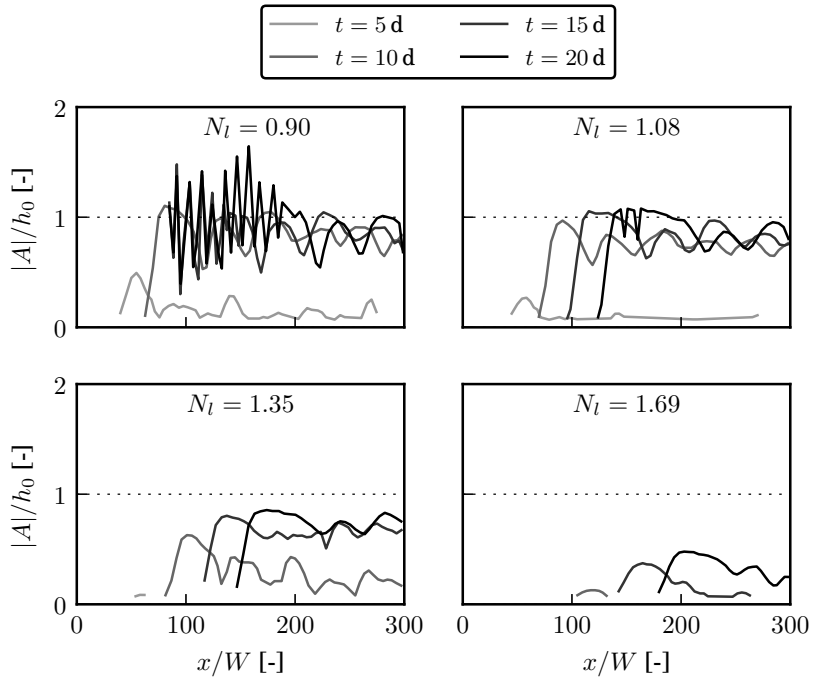

Fig. 5.19.: Influence of Ikeda parameter N_l on temporal and spatial bar amplification using non-uniform sediment without bed perturbation

inlet. However, bar amplification for non-uniform sediment was sightly different compared to uniform sediment. Hence, a little higher Ikeda parameter N_l (more lateral diffusion) was needed for non-uniform sediment to get the comparable free bar amplification. Interestingly, free bar amplification for non-uniform sediment was somewhat more damped at the beginning of the simulation compared to uniform sediment. This is consistent with linear stability theory for free bars suggesting smaller bar growth rates for non-uniform sediment valid for strictly infinitesimal disturbances (Lanzoni & Tubino, 1999; Tubino *et al.*, 1999).

Finally, the bed perturbation approach was also applied for simulations with non-uniform sediments (see Fig. 5.20). This might be useful for equilibrium sediment supply conditions in order to consistently perturb the system. However, this results in slightly higher bar amplitudes. This can be attributed to the combination of perturbation originating from sorting waves and bed perturbation. Therefore, bar amplification depends on the perturbation approach (see e.g. also Bernini *et al.*, 2009).

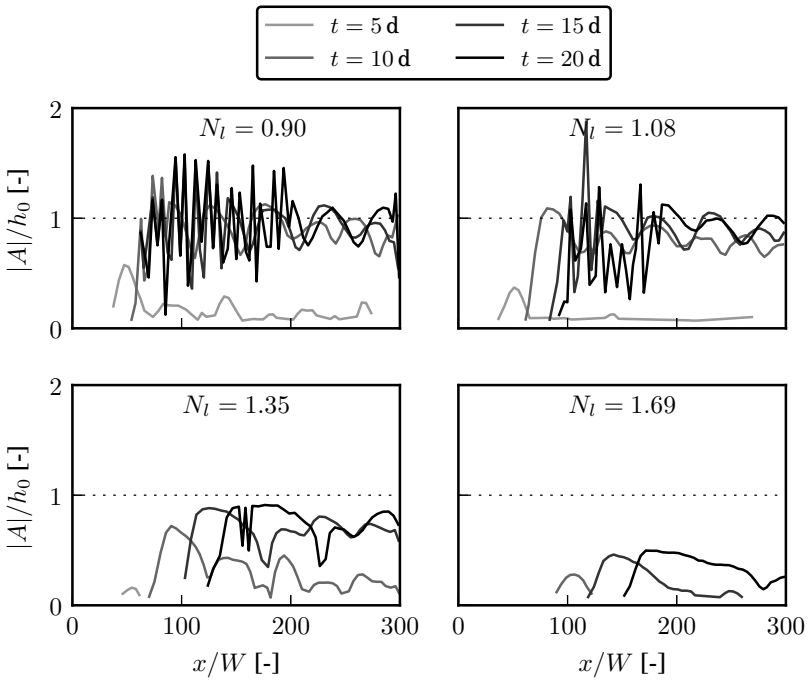

Fig. 5.20.: Influence of Ikeda parameter N_l on temporal and spatial bar amplification using non-uniform sediment with bed perturbation

5.3.5. Influence of Morphological Factor

The morphological factor m_f is used to speed up numerical simulations (see section. 4.3.7). The influence of m_f on free bar properties is shown in Fig. 5.21. For increasing m_f, the relative bar amplitude $|A|/h_0$ increases, while the bar wavenumber λ first decreases slightly and then increases slightly to a constant value. Overall, the influence on $|A|/h_0$ and λ is rather small for $m_f < 40$.

5.3.6. Discussion

Generally, for numerical simulations of free bars an approach is required to trigger free bars. Various approaches were reported in literature, such as the placement of an erodible obstacle near the inflow boundary (Takebayashi *et al.*, 1999; Defina, 2003; Jang & Shimizu, 2005; Bernini *et al.*, 2009; Qian *et al.*, 2017), initial periodic topography in space with a defined bar wavelength (Defina, 2003), and random perturbation of the discharge at the upstream boundary in transverse direction of 0.1 % (Iwasaki *et al.*, 2016) and 1 % and 5 % (Crosato *et al.*, 2011). Defina

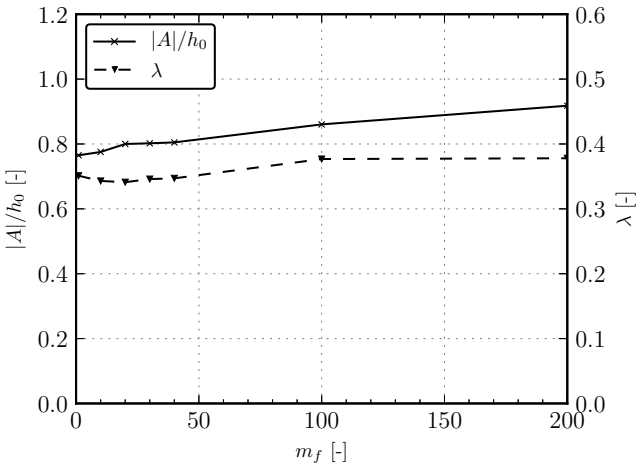

Fig. 5.21.: Influence of morphological factor m_f on free bar amplitude $|A|/h_0$ and wavenumber λ

(2003) noticed that the initial free bar formation and equilibrium bar properties were significantly affected by the choice of the perturbation approach, such as the wavelength of the initial topography and the placement of multiple obstacles. The bed perturbation approach used here, on the other hand, is randomly applied in space at a predefined time interval starting from flat bed (section 4.3.8). This allows to reach a dynamic equilibrium, where free bars are continuously formed and migrate downstream.

As shown in section 5.3.3, the Ikeda parameter N_l affects the bar formation and the equilibrium bar height. The lateral bed slope effect introduces (lateral) diffusion to the numerical simulation. Therefore, the Ikeda parameter N_l (the intensity of the lateral bed slope effect) depends on the numerical diffusion (Total diffusion = lateral diffusion + numerical diffusion). The value of N_l can be determined, for instance based on a comparison of the bank height with the weakly non-linear theory of Colombini *et al.* (1987) (Eq. 3.49). In this way an Ikeda prameter of $N_l = 1.35$ was found to be a reasonable value for uniform sediments, as shown in Fig. 5.18. N_l typically ranges between 1.2 and 3.57 (assuming $M_l = 0.5$ in Eq. 3.28) according to laboratory experiments and analytical analysis (see Table 3.1) and seems to depend also on the bed material (Zanke *et al.*, 2008).

Defina (2003) performed numerical simulations based on setup of the laboratory experimental run P1505 of Lanzoni (2000a) and successfully reproduced the main free bar properties, such as height, wavelength, and celerity. The present

numerical model was tested for the same setup using Einstein's logarithmic friction law (Eq. 4.10 with $k_s = 0.0072$), MPM bed load formula (Eq. 3.18 with $\mu_r = 0.74$ as in Defina (2003)), Ikeda parameter of $N_l = 1.9$, and a flume length of 120 m as compared to 55 m of the flume used by Lanzoni, while all other settings were adopted from Lanzoni (2000a). The free bar properties were reproduced fairly well (observation in parenthesis), such as the bar height $H_{BM} = 0.06\,\mathrm{m}$ (0.07 m), the bar wavelength $L = 11.0\,\mathrm{m}$ (10.0 m), and the bar celerity $c_b = 3.0\,\mathrm{m/h}$ (2.8 m/h).

5.3.7. Summary

In this section, the most important model approaches were validated for the simulation of free bars. This includes the lateral bed slope effect, the bed perturbation approach, and the influence of the morphological factor. The lateral bed slope effect introduces additional diffusion to the numerical simulation. Hence, the Ikeda parameter N_l is crucial for the formation of free bars. Indeed, free bars will be suppressed completely if N_l is too high, while free bar instability grow too strongly in case of too small values of N_l. In the latter case, this can lead to an emergence of the bar heads from the water surface. For the model setup, which will be used later to study the effect of sediment supply reduction, free bar properties were plausibly reproduced, such as the wavenumber ($\lambda = 0.35$) and the bar celerity ($c_b = 20.8\,\mathrm{m/h}$) according to the linear stability theory for free bars (Adami *et al.*, 2016b), and the relative bar height ($H_{BM}/h_0 = 2.87$) according to the weakly non-linear stability theory for free bars (Colombini *et al.*, 1987). Finally, the numerical simulation of the laboratory experiment of Lanzoni (2000a) (run P1505) was in good agreement with the observed free bar properties. Numerical simulations generally require an approach to trigger free bars. The approach presented here is based on small random bed perturbations in space at defined time intervals. This approach turned out to be robust and time intervals between 1 and 24 hours had no significant influence on free bar properties. Finally, the effect of the morphological factor m_f was found to have only minor effect on the free bar amplitude and wavelength for $m_f < 40$. Overall, the presented numerical model is suitable to investigate the response of free bars to sediment supply reduction in a next step (see Chap. 7).

6. Erosion Process of Artificial Gravel Deposits

6.1. Introduction

Sediment replenishment in gravel-bed rivers can be carried out by means of artificial gravel deposits (see section. 2.1). In this section the validated numerical model (see section. 5.1) is applied to study the erosion process of artificial gravel deposits. Thereby, the numerical simulations are compared with the laboratory experiments from Friedl (Friedl *et al.*, 2016; Friedl, 2017; Friedl *et al.*, 2018). After describing the experimental and numerical setup, the results focus on the erosion process and the downstream sediment supply.

6.2. Reference Laboratory Experiment

The laboratory experiments on erosion of artificial gravel deposits were performed in a trapezoidal flume with fixed bed and fixed embankments (Friedl, 2017). The geometry of the gravel deposit and the cross section of the flume are depicted in Fig. 6.1. The experimental setup was inspired by the Reuss River below the ROR-HPP Bremgarten-Zufikon in Switzerland. The flume had a length of 35 m, a channel width of $W = 2\,\mathrm{m}$, and a bed slope of $S = 0.172\,\%$. The laboratory experiments were based on Froude similarity scaled by 1:25. The examined parameters were: water discharge Q, deposit width to channel width ratio W_d/W, deposit height H_d, and mean grain size diameter d_m of the sediment mixture (Table 6.1). The approach flow depth h_0 corresponds to the uniform approach flow depth without gravel deposit in the flume (Friedl, 2017).

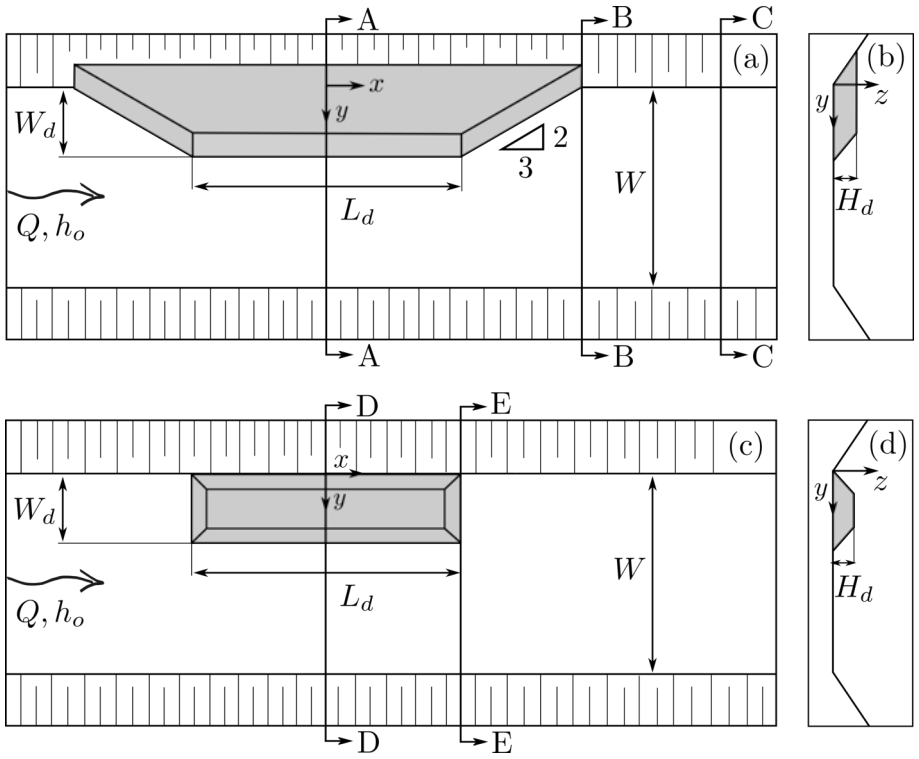

Fig. 6.1.: Geometry of trapezoidal gravel deposit (connected to shore) with plan view (a), cross section A-A (b) and rectangular gravel deposit (off shore) with plan view (c), cross section D-D (d)

Soil settling of the gravel deposit was observed at the beginning of most of the laboratory experiments. Hence, the porosity of the gravel deposit in the laboratory experiments was higher than that of the transported and downstream deposited sediment. The topography was measured in cross sections at a distance of half a meter at irregular time intervals with a Laser Distance Measurement Sensor with an accuracy of < 1 mm (Friedl *et al.*, 2018). Based on this, the downstream sediment supply $Q_{b,sup}$ was evaluated for 4-5 time steps depending on the experimental run. Thereby $Q_{b,sup}$ was defined as the sediment supply to the downstream river reach just below the gravel deposit (e.g. cross section B-B in Figure 6.1). However, the experimental values of $Q_{b,sup}$ contain a certain degree of uncertainty, because the bulk density from the initial gravel deposit $\rho_b = 1370\,\mathrm{kg/m^3}$ (porosity $p = 0.48$) differed from the bulk density of the material deposited in the near-bank zone with $\rho_b = 1800\,\mathrm{kg/m^3}$ ($p = 0.32$) (Friedl, 2017). However, Friedl (2017) corrected the values of $Q_{b,sup}$ for the effect of soil settling during the first time step. Nevertheless, the experimental data of $Q_{b,sup}$ provide reasonable information regarding the overall erosion process and are used to

compare the numerical model with the laboratory experiments for the influence of geometrical parameters, discharge, and grain size distribution. The experiments lasted between 1,800 and 10,800 seconds depending on the hydraulic load and the erosion rate. This corresponds to a duration between 9,000 and 54,000 seconds in prototype scale.

6.3. Numerical Model Setup

The numerical simulations were performed in prototype scale (1:1) using different setups according to Table 6.1. The unstructured and triangular computational mesh consisted of approximately 30,000 cells. In order to capture the lateral erosion dynamics, the spatial resolution of the gravel deposit was rather high using 15 - 20 cells in lateral direction. This resulted in computational times of approximately real-time speed.

Table 6.1.: Overview of the experimental setup and numbering (Exp. No.) according to Friedl (2017) using prototype values (^{a} only numerical simulation)

Exp. No.	Geometry	W_d [m]	H_d [m]	L_d [m]	d_m [mm]	σ_g [-]	Q [m^3/s]	h_0 [m]
2	trapezoidal	10.0	3.75	50.0	37.5	2.38	356	2.5
5	trapezoidal	12.5	3.75	50.0	37.5	2.38	356	2.5
7	trapezoidal	15.0	3.75	50.0	37.5	2.38	228	1.9
8	trapezoidal	15.0	3.75	50.0	37.5	2.38	356	2.5
9	trapezoidal	15.0	3.75	50.0	37.5	2.38	703	3.75
11	trapezoidal	15.0	2.50	50.0	37.5	2.38	356	2.5
14	trapezoidal	15.0	1.25	50.0	37.5	2.38	356	2.5
17	trapezoidal	12.5	3.75	200.0	37.5	2.38	356	2.5
25	trapezoidal	15.0	3.75	50.0	50.0	2.25	356	2.5
28	trapezoidal	15.0	3.75	50.0	25.0	2.03	356	2.5
37	rectangular	15.0	3.75	50.0	37.5	2.38	228	1.9
38	rectangular	15.0	3.75	50.0	37.5	2.38	356	2.5
39^a	rectangular	15.0	3.75	50.0	37.5	2.38	703	3.75
47^a	trapezoidal	12.5	3.75	100.0	37.5	2.38	356	2.5

At the upstream hydraulic boundary, constant discharge was defined assuming uniform flow with the same slope as in the flume. Similarly, uniform flow was defined

at the downstream hydraulic boundary. The hydraulic initial condition was defined using a steady flow field. First, the hydraulic calibration aimed to reproduce the approach flow depth h_0 in the channel without a gravel deposit in the flume based on the laboratory experiments (Table 6.1). Hydraulic friction was accounted for using Yalin's logarithmic friction law according to Eq. (4.9). The equivalent sand roughness of the channel bed and the embankments of $k_s = 125\,\text{mm}$ resulted in a good agreement (laboratory experiment in brackets): h_0 =1.95 m (1.9 m), 2.54 m (2.5 m), and 3.74 m (3.75 m) for a discharge of Q =228 m^3/s, 356 m^3/s, and 703 m^3/s, respectively. Furthermore, Friedl performed Acoustic Doppler Velocimetry (ADV) measurements fixing the topography after 1 h (prototype scale) of erosion for experimental setup No. 8 (Friedl, 2017), which are used for validation of the numerical model (Figure 6.2). The depth-averaged flow velocities are compared to the flow velocities from the ADV measurements at a relative height of 0.368 of the local water depth. At this height, the flow velocity corresponds to the depth-averaged flow velocity (Yalin & da Silva, 2001). The lateral distribution of the depth-averaged flow velocities was reproduced fairly well at all cross sections. The ADV measurements indicate that the flow is attached to the embankment apart from the lower end of the deposit, where recirculation occurs and 3-D effects influence the flow separation zone.

No sediment was added at the upstream boundary, while a transparent sediment boundary condition was applied at the downstream boundary. The initial topography corresponded to the inital geometry of the laboratory experiment. The gravel deposits were erodible, whereas the bed and the embankments were non-erodible. The bed load formula according to Meyer-Peter & Müller (1948) extended for non-uniform sediments was used according to Eq. (4.16). Thereby, a similar level of bed load transport as in the laboratory experiments was found with a bed load pre-factor of $\alpha = 6.0$ and a bed load exponent of $e = 1.5$. Furthermore, for the gravel deposit and the area with deposited material, the effect of local grain-size friction was applied using $k_s = 2.5 d_{90}$, where d_{90} denotes the local grain size diameter in the active layer where 90 percent is finer. Note that this is in good agreement with the findings of Cheng (2016) suggesting $k_s = \sigma_g^{1.05} d_{90} = 2.22 d_{90}$ (with $\sigma_g = 2.14$ according to Fig. 6.3). The active layer thickness was set to a constant value of $L_a = 2 d_{90,0}$, where $d_{90,0}$ denotes the initial characteristic grain size diameter of the general grain size distribution where 90 percent is finer ($d_{90,0} = 68\,\text{mm}$, Fig. 6.3). The critical Shields stress was determined according to

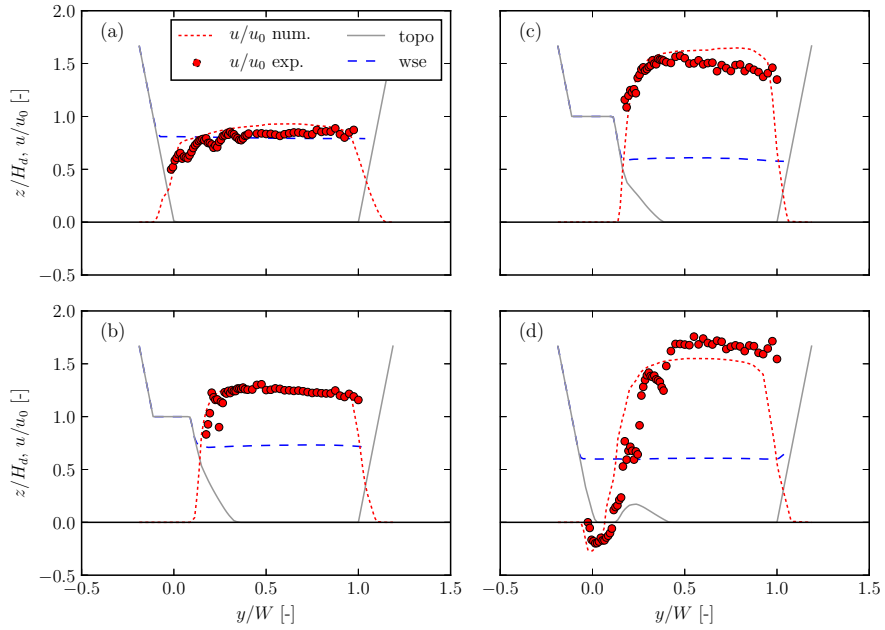

Fig. 6.2.: Normalized depth-averaged flow velocity u/u_0 of numerical simulation (red dashed line) and experimental data (red circles) after 1 h of erosion of exp. No. 8 at cross sections at $x = -67$ m (a), $x = -20$ m (b), $x = 22.5$ m (c), and $x = 51.25$ m (d); topography (topo): gray solid line, water surface elevation (wse): blue dashed line. For positioning of cross sections (x-coordinate) see Figure 6.1; approach flow velocity $u_0 = 2.65$ m/s (prototype scale) according to Friedl (2017)

Yalin & da Silva (2001) (Eq. 3.7) and the local bed slope effect was taken into account according to van Rijn (1989) (Eq. 3.11). The lateral bed slope effect was determined according to Eq. (4.17) using an Ikeda parameter of $N_l = 2$. The bank collapse approach was applied using an angle of repose for dry and wet material of $\gamma_{dry} = 40°$ and $\gamma_{wet} = 30°$, respectively.

The grain size distribution of the gravel deposit from the laboratory experiment was discretized for the numerical simulations using seven grain classes (Fig. 6.3). Similarly, the grain size distributions of the fine and coarse sediments are depicted in Fig. 6.4. The porosity of the sediment was defined with $p = 0.4$, which is the mean value between the porosity of the gravel deposit ($p = 0.48$) and the porosity of the deposited material in the near-bank zone ($p = 0.32$) observed in the laboratory experiments.

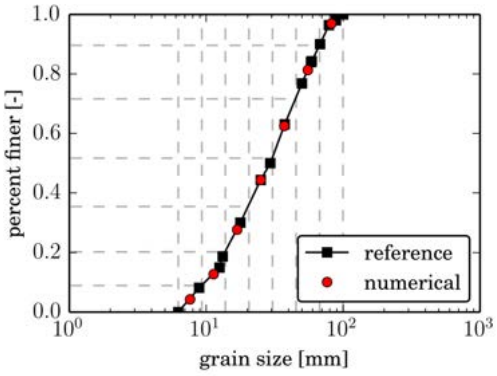

Fig. 6.3.: Grain size distribution of the laboratory experiment (reference) of the medium coarse mixture with $d_m = 37.5$ mm, $\sigma_g = 2.14$ and grain sizes for the numerical simulation (red circles) using seven grain classes (dashed gray lines)

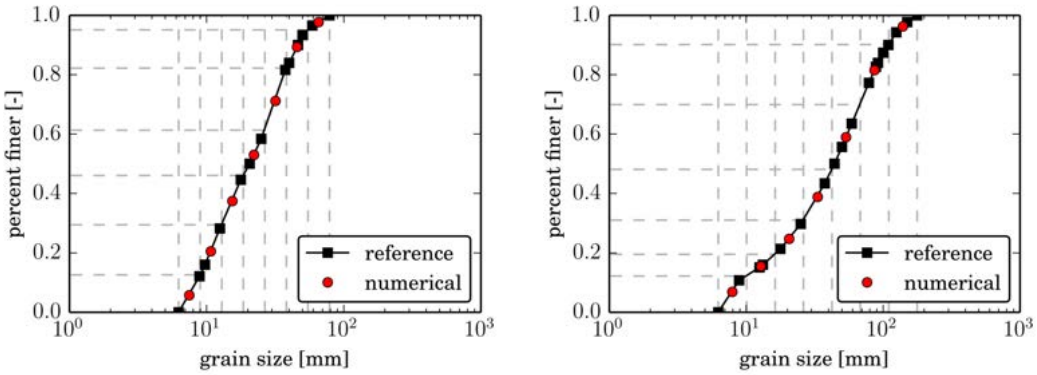

Fig. 6.4.: Grain size distribution of the laboratory experiments (reference) of the fine mixture (left, $d_m = 25.0$ mm, $\sigma_g = 2.0$) and the coarse mixture (right, $d_m = 50.0$ mm, $\sigma_g = 2.2$) and grain sizes for numerical simulation (red circles) using seven grain classes (dashed gray lines)

6.4. Results

6.4.1. Erosion Process

The process of the gravel deposit erosion and the successive deposition downstream is analyzed based on the experimental setup No. 8 (Table 6.1) at the cross section in the middle of the gravel deposit and at the cross section 75 m downstream of the gravel deposit, respectively. The erosion process of the gravel deposit is shown in Fig. 6.5 for the cross section in the middle of the gravel deposit. Compared with the laboratory experiment, the erosion process was captured very well by the numerical model over the whole time span of ten hours ($0.85 \leq \text{BSS} \leq 0.996$ (excellent according to Table 3.2), $0.028 \leq \text{RMSE} \leq 0.065$). The eroded sediment eventually deposited downstream (Fig. 6.6). A flow separation and recirculation zone was observed at the end of the gravel deposit (Friedl *et al.*, 2016), which was also reproduced by the numerical model (Fig. 6.2). Despite some limitations in reproducing 3D flow structures, the depth-averaged numerical model was able to well reproduce the process of downstream sediment deposition ($0.716 \leq \text{BSS} \leq 0.971$ (good - excellent), $0.030 \leq \text{RMSE} \leq 0.060$).

6.4.2. Sediment Supply to Downstream Reach

The downstream supply rate $Q_{b,sup}$ was defined as the bed load transport to the downstream river reach just below the gravel deposit (cross section B-B and E-E in Fig. 6.1 for trapezoidal and rectangular gravel deposits, respectively). For the analysis of the numerical results, $Q_{b,sup}$ was determined based on the change in sediment volume in the flume upstream from cross section B-B averaging over time intervals of 1,500 or 3,000 seconds. In contrast, the evaluation of $Q_{b,sup}$ in the laboratory experiments was based on interpolation of cross-sectional data at four to five irregular time intervals (Friedl, 2017). Before discussing the results, the effects of geometrical parameters, discharge, and grain size distribution on the supply rate are investigated according to the sensitivity analysis of the laboratory experiments of Friedl (2017).

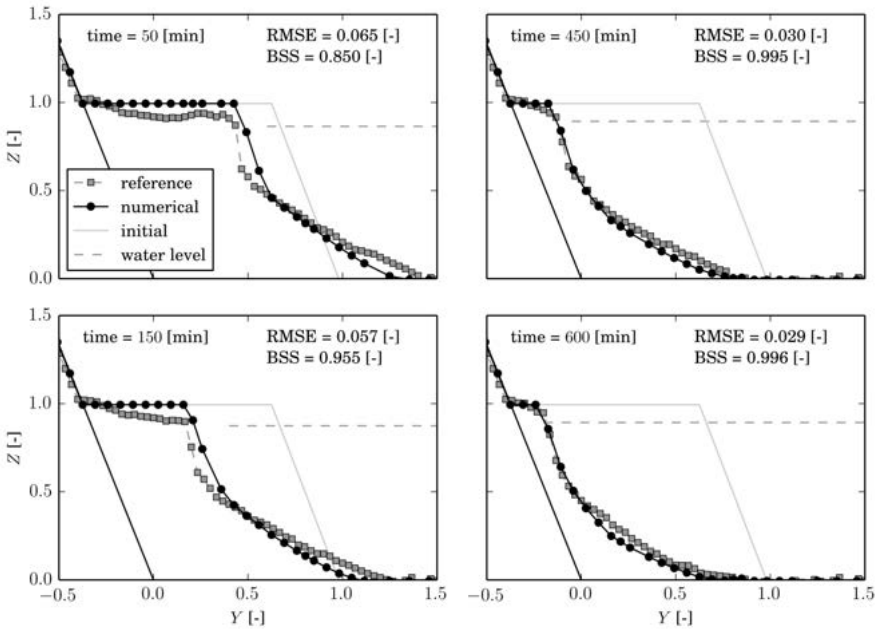

Fig. 6.5.: Erosion process of gravel deposit (Exp. No. 8) for cross section A-A (see Fig. 6.1) in the middle of the gravel deposit (axes normalized, $Y = y/W_d$, $Z = z/H_d$)

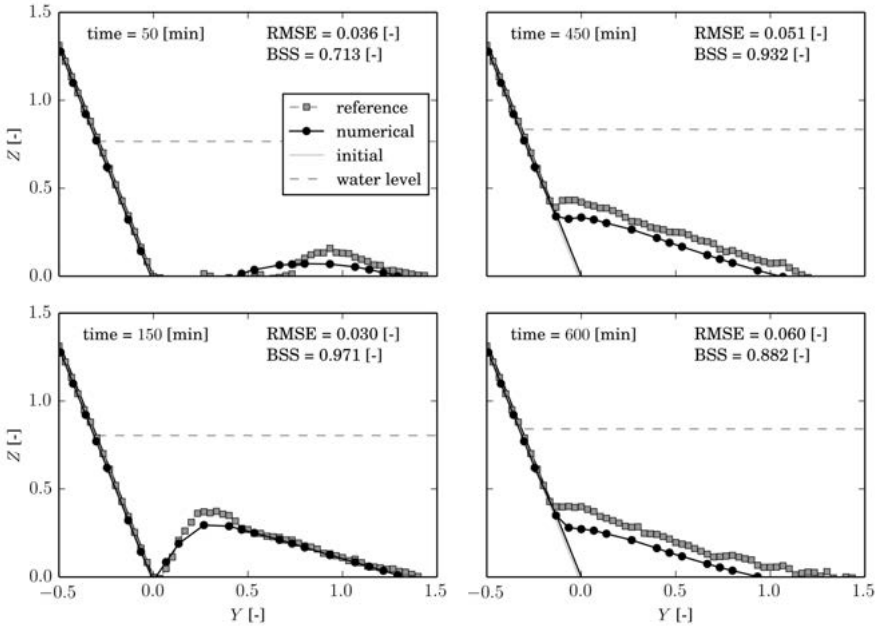

Fig. 6.6.: Deposition process (Exp. No. 8) for cross section C-C, 75 m downstream of the gravel deposit (axes normalized, $Y = y/W_d$, $Z = z/H_d$)

Influence of Geometrical Parameters

The influence of the deposit width W_d was studied in terms of a variation of $W_d/W = 0.2$, 0.25, and 0.3 (Table 6.1). The supply rates obtained from the numerical model corresponded fairly well to those found in the laboratory experiments (Fig. 6.7). However, differences were observed for the initial phase of the experiments.

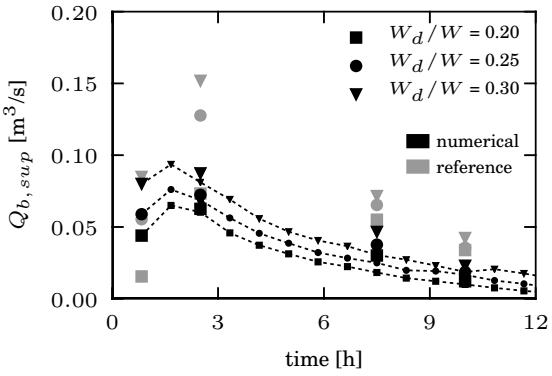

Fig. 6.7.: Influence of deposit width W_d (normalized by the channel width W) on $Q_{b,sup}$ in the laboratory experiment and numerical model

The influence of the deposit height H_d was analyzed in terms of a variation of $H_d/h_0 = 0.5$, 1.0, and 1.5 (see Table 6.1). The gravel deposit was submerged during the laboratory experiment of run No. 11 and 14 with $H_d/h_0 = 0.5$ and $H_d/h_0 = 1.0$, respectively. The erosion process of the submerged gravel deposit and the dry gravel deposit observed in the laboratory experiment were slightly different. The non-submerged gravel deposits were eroded predominantly by lateral erosion, while the submerged gravel deposits experienced additional erosion on top of the gravel deposit. The erosion rates from the numerical simulations are in good agreement with the laboratory experiments (Fig. 6.8).

The influence of the deposit length L_d was analyzed in terms of a variation of $L_d/W = 1.0, 2.0, 4.0$ (Table 6.1). The erosion rates obtained from the numerical simulations agree well with the erosion rates from the laboratory experiments (Fig. 6.9).

The laboratory experiments of Friedl (2017) on gravel deposit erosion were implemented using trapezoidal (on shore) and rectangular (off shore) geometry

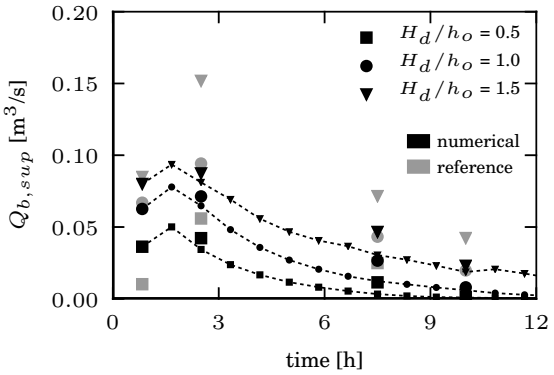

Fig. 6.8.: Influence of deposit height H_d (normalized by approach flow depth h_0) on $Q_{b,sup}$ in the laboratory experiment and numerical model

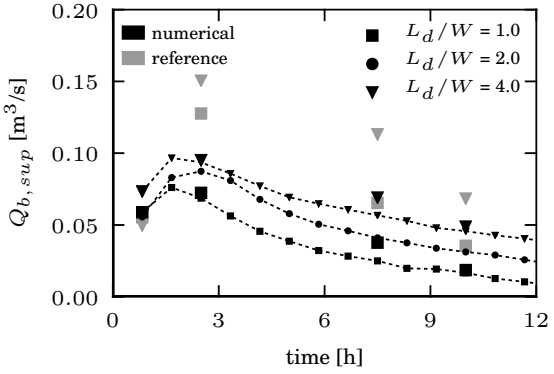

Fig. 6.9.: Influence of deposit length L_d (normalized by channel width W) on $Q_{b,sup}$ in the laboratory experiment and numerical model

(see Fig. 6.1). Most of the laboratory runs used trapezoidal gravel deposits. However, two laboratory runs were performed using the rectangular geometry (Table 6.1). The erosion rates from numerical simulations are compared to the laboratory experiments in Fig. 6.10. The rectangular deposits eroded much faster compared to the trapezoidally shaped gravel deposits (Fig. 6.11). This was mainly due to the fact that the erosion has been taking place on both sides of the rectangular deposit. Hence, the erosion rate was found to amount to around twice the erosion rate of trapezoidal gravel deposit.

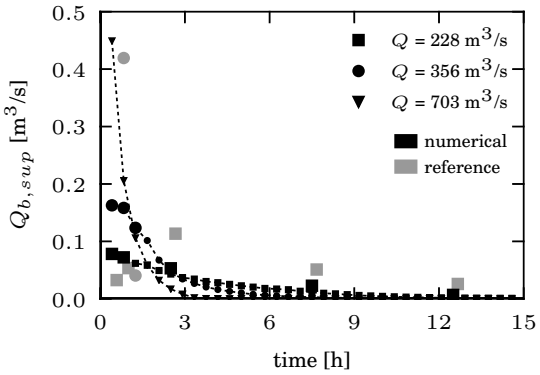

Fig. 6.10.: Influence of discharge Q on $Q_{b,sup}$ for rectangular (off shore) gravel deposit in the laboratory experiment and numerical model

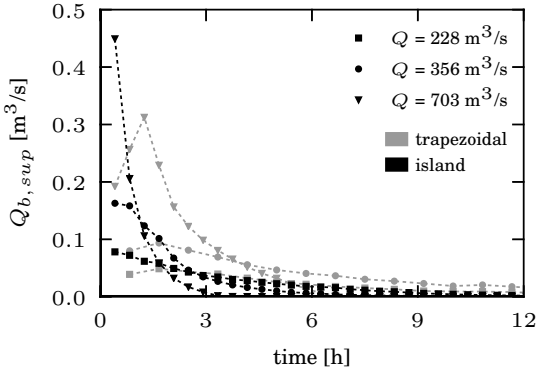

Fig. 6.11.: Influence of discharge Q on $Q_{b,sup}$ for trapezoidal (on shore) and rectangular (off shore) gravel deposit in the numerical model

Influence of Discharge

The influence of discharge Q was investigated with experimental run No. 7, 8, and 9 (Table 6.1). The gravel deposit was submerged in the laboratory experiment No. 9 ($Q = 703\,\mathrm{m}^3/\mathrm{s}$). During the first hour, the supply rate obtained from the laboratory experiment and the numerical model differ quite significantly (Fig. 6.12). However, for the rest of the experiment the numerical model is generally in good agreement with the laboratory experiment and tends to follow the trend towards smaller erosion rates for smaller discharges.

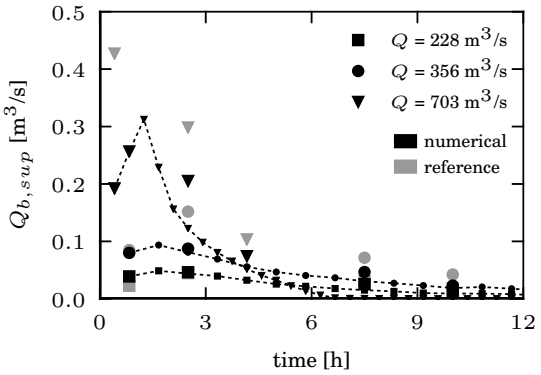

Fig. 6.12.: Influence of discharge Q on $Q_{b,sup}$ in the laboratory experiment and numerical model

Influence of Grain Size Distribution

The influence of the grain size distribution of the sediment mixture was investigated using a (i) fine mixture with mean grain size $d_m = 25.0\,\text{mm}$, (ii) medium mixture with $d_m = 37.5\,\text{mm}$, and (iii) coarse mixture with $d_m = 50.0\,\text{mm}$ (Table 6.1). The general trend towards smaller erosion rates for coarser mixtures was reproduced fairly well by the numerical model after 30 minutes (Fig. 6.13). The slower erosion and the smaller downstream sediment supply of the coarser sediment mixture can be explained by the larger d_m and grain sorting processes. Smaller downstream deposition were observed for the coarser mixture compared to the finer mixture in the laboratory experiments and as well in the numerical model.

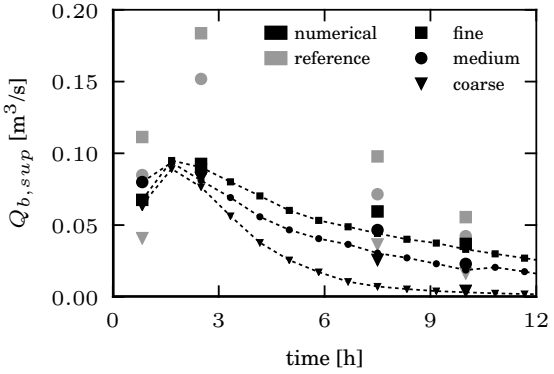

Fig. 6.13.: Influence of grain size distribution on $Q_{b,sup}$ in the laboratory experiment and numerical model

6.4.3. Sediment Balance

A sediment balance was performed at the end of the numerical simulation ($t = 54000\,\mathrm{s}$) to get an idea about the downstream sediment supply out of the flume (V_{out}). The sediment volume that stays in the flume is divided into the part that locally remains near the gravel deposit (V_1) and the volume that is deposited in the flume (V_2). The latter two were distinguished by the cross section B and E in the case of trapezoidal deposits and rectangular deposits, respectively (see Fig. 6.1 for location).

Table 6.2 shows an overview of the sediment balance, while Fig. 6.14 displays the percentage of the sediment that is transported out of the flume compared to the initially added sediment (V_{out}/V_{init}) depending on the Shields stress of the uniform approach flow without gravel deposit in the flume ($\theta_0 = Sh_0/((s-1)d_m)$). As expected, the downstream sediment supply strongly depends on the Shields stress. Therefore, the hydrology of a river is a key factor for the assessment of sediment replenishment by artificial gravel deposits.

Table 6.2.: Volume analysis of the initially added sediment volume V_{init} and the sediment volume that remains near the deposit V_1, stays in the flume downstream of the deposit V_2, and the downstream sediment supply out of the flume V_{out}

Exp. No.	θ_0 [-]	Q [$\mathrm{m^3/s}$]	V_{init} [$\mathrm{m^3}$]	V_1/V_{init} [%]	V_2/V_{init} [%]	V_{out}/V_{init} [%]
2	0.069	365	2487	17.3	16.4	66.3
5	0.069	365	3319	19.8	23.4	56.8
7	0.053	228	4231	58.4	24.9	16.7
8	0.069	365	4231	19.4	25.3	55.3
9	0.104	703	4231	0.1	0.0	99.9
11	0.069	365	2219	9.5	11.0	79.5
14	0.069	365	1111	11.9	8.0	80.1
17	0.069	365	10267	49.0	15.4	35.6
25	0.052	365	4231	55.4	23.0	21.6
28	0.104	365	4231	3.5	19.6	76.9
37	0.053	228	2207	20.8	44.7	34.5
38	0.069	365	2207	6.3	11.5	82.2
39[a]	0.104	703	2207	0.0	0.1	99.9
47[a]	0.069	365	5634	30.4	23.4	46.2

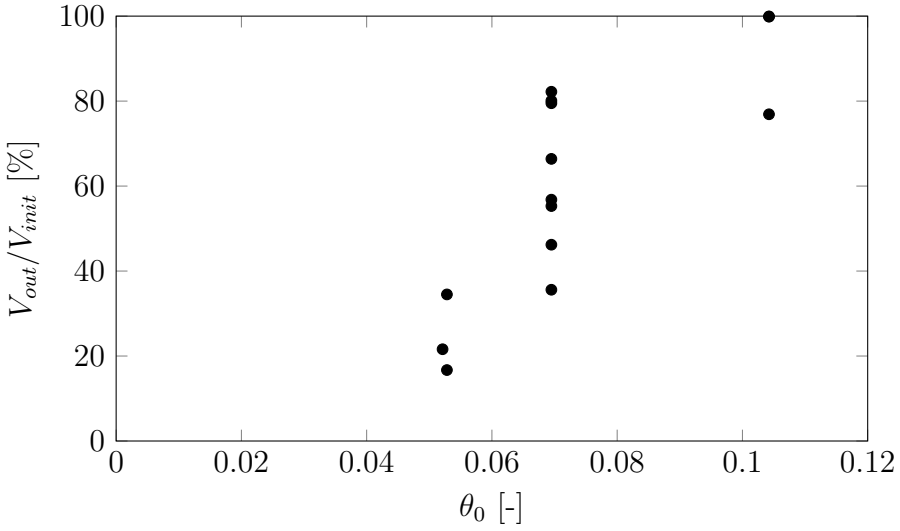

Fig. 6.14.: Bed load volume transported out of the flume V_{out} compared to the initial deposited volume V_{init} (see Table 6.2) for the relevant Shields stress $\theta_0 = Sh_0/((s-1)d_m)$

6.5. Summary

Sediment replenishment by artificial gravel deposits is a measure to address sediment deficit in rivers. A composite modeling approach was used to investigate the erosion process of gravel deposits. Laboratory experiments carried out by Friedl *et al.* (2016) were used for a comparison with the presented numerical 2-D model including the Hirano model for non-uniform bed load transport. The main model approaches were adopted from the evaluation of the numerical model for lateral erosion in straight river reaches (see section 5.1). This mainly includes the correction of the critical Shields stress due to local bed slope, the lateral bed slope effect, and the gravitationally induced bank collapse (e.g. see Vonwiller *et al.*, 2015). The erosion dynamics observed in the laboratory experiments were excellently reproduced by numerical model ($0.85 \leq \text{BSS} \leq 0.996$). Moreover, the numerical model well reproduced the deposition downstream of the gravel deposit ($0.716 \leq \text{BSS} \leq 0.971$). Furthermore, downstream sediment supply rates were in good agreement with the laboratory experiment, except for the initial phase (approx. first hour). On the one hand, the settling of gravel deposits observed in the beginning of the laboratory experiments cannot be taken into account by the numerical model. On the other hand, the numerical model was not able to fully

capture the rapid erosion process at the beginning of the experiments. However, the successive erosion process can be reproduced fairly well for all investigated configurations. The analysis of the sediment volumes at the end of the simulation ($t = 54000\,\mathrm{s}$) suggests that the discharge and hence the hydrology of a river is a key factor for the assessment of sediment replenishment by artificial gravel deposits.

The numerical 2-D model proved to be a suitable tool to predict erosion rates for sediment replenishment by artificial gravel deposits. However, for using the model as a design and planning tool for practical applications the following points should be considered:

- Bank collapse considered reasonable values for the critical angles of dry and wet material γ_{dry} and γ_{wet}, respectively;
- Lateral bed slope effect used reasonable value for the Ikeda parameter in the range of $1.4 \leq N_l \leq 2.0$;
- Local bed slope effect on the critical Shields stress were taken into account, e.g. using Van Rijn's approach (van Rijn, 1989, Eq. 3.11);
- The effect of grid resolution should be investigated in a sensitivity analysis;
- A high resolution of the computational grid for the gravel deposit is required, e.g. 15 - 20 cells over the width of the gravel deposit;
- Consider grain sorting effects on hydraulic friction in case of non-uniform sediment: Dynamically determine the equivalent sand roughness based on actual local grain size composition, e.g. $k_s \approx 2.5 d_{90}$;
- Use of non-uniform bed load formula to account for sorting effects, e.g. Eq. (4.16) with bed load pre-factor and bed load exponent within reasonable range ($4.93 \leq \alpha \leq 8.0$, $1.5 \leq \epsilon \leq 1.6$);
- Over all, the erosion of the gravel deposit is sensitive to the water discharge and hence to the flood hydrograph used for modeling.

Taking into account these points, the erosion process for arbitrary gravel deposit geometry and hydraulic conditions can be estimated fairly well for practical applications. In a first step the erosion rates and the bed load supply to the downstream river reach can be determined using a local model, with a length

of approximately ten times the river width. The output of the local model can then be used as an input for reach scale modeling of the downstream effect of sediment replenishment, e.g. at the upstream boundary or by means of an external source.

7. Free Bars Response to Sediment Supply Reduction

7.1. Introduction

Alternate free migrating bars develop as an intrinsic instability mechanism of non-cohesive bed load transport and water flow interaction in approximately straight channels with non-erodible banks (Blondeaux & Seminara, 1985; Colombini *et al.*, 1987; Schielen *et al.*, 1993). Therefore, they are referred to as free bars in the following (Zolezzi *et al.*, 2005). Free bars can be described as a large-scale morphological pattern of the order of several channel widths (Colombini *et al.*, 1987; Lanzoni & Tubino, 1999). Parker (1976) characterized alternate free bars as morphological pattern of first lateral mode ($m = 1$), and hence delimited them from higher mode bars, such as central bars ($m = 2$) or braided pattern ($m \geq 3$) (see Fig. 3.13). A good example for alternate free bars is the reach of the Alpine Rhine River between the Landquart River tributary upstream and the Ill River tributary downstream (Jäggi, 1983; Adami *et al.*, 2016a).

In the literature, the response of free bars to sediment supply reduction and complete sediment supply termination was investigated in laboratory experiments by Lisle *et al.* (1993) and Venditti *et al.* (2012), respectively. In the former, the top of the free non-migrating bars started to emerge from the water surface shortly after sediment supply reduction. In the latter, free non-migrating bars started to migrate downstream after sediment supply termination. Non-migrating bars persisted in the lower part, whereas bars were eliminated in the upper part. These two experiments with partially contradictory observations served as motivation to make the following numerical investigation.

The effect of changing sediment supply on river morphology can be studied by

either decreasing or increasing sediment supply. The change of sediment supply will cause the bed slope of the channel to adopt to a new equilibrium state. In the case of sediment supply increase, more sediment is added than can be transported. This creates a sediment wedge with a locally increased bed slope. This front migrates downstream until the bed slope in the flume has adapted to the increased sediment supply. In contrast, a sediment supply decrease leads to an erosion wedge that extends in downstream direction starting from the upstream boundary. The formation of the erosion wedge usually has a smoother transition and is not exactly the reverse process of the deposition process. Therefore, the case of sediment supply decrease is generally more straightforward to implement for both numerical and laboratory experiments. Nevertheless, the governing processes are not completely disconnected between these two approaches, e.g. the effect of sediment supply on the equilibrium bed slope. On this basis, the approach of sediment supply reduction was adopted in the following. A dynamic equilibrium state with free bars was (see Chap. 5.3) served as initial condition to investigate free bars response to sediment supply reduction.

Sediment supply affects bed slope and bed load transport within the flume. The change in bed slope due to the change in sediment supply is hereinafter referred to as morphological 1-D effect (see section 3.6). The morphological 1-D effect eventually affects free bar properties, such as bar wavelength, bar amplitude, and bar celerity. The response of free bars properties is referred to as morphological 2-D effect. The present study focuses on the competition between the morphological 1-D and 2-D effects. The numerical simulations were performed using uniform sediments. This allows to study the basic morphological processes unaffected by grain sorting effects. As an integral part of this study, linear stability theory for free bars is used for the planning of the numerical model setup, prediction of the morphological 1-D effect (reducing equilibrium bed slope), and the interpretation of the numerical results. This should contribute to a further understanding the mechanism of free bars response to sediment supply reduction.

This chapter is structured as follows: After describing the setup of the numerical experiment, the linear stability theory for free bars is presented for both the initial equilibrium state and for decreasing bed slope (morphological 1-D effect). The numerical results are then presented for decreased sediment supply using fractions of the initial equilibrium bed-load transport capacity. Thereby, the focus was on the competition between the morphological 1-D and 2-D effects. Finally,

the results are compared to laboratory experiments from literature along with some discussion on the limits of the presented approach.

7.2. Numerical Model Setup

The geometry of the numerical experiment consisted of a straight rectangular channel (Fig. 7.1). The channel had an initial equilibrium bed slope of $S_0 = 0.005$, a width of $W = 60\,\mathrm{m}$, and a length L of 300 times the width ($L/W = 300$). Free bars were triggered by random disturbances of the river bed of size ε at two-hourly intervals, where ε was one percent of the uniform approach flow depth h_0 (see section 4.3.8). The unstructured and triangular computational mesh consisted of approximately 52,000 cells with ten to twelve cells over the river width.

The bed load transport formula of Wong & Parker (2006) was used for uniform grain size d_{50}. The critical Shields stress was constant ($\theta_C = 0.047$) throughout the whole simulation without correction due to local bed slope. The factor for the lateral bed slope effect was set to $N_l = 1.35$ for the numerical simulations. The effect of N_l on free bar formation was investigated in more detail in section 5.3.3. Constant specific sediment supply $q_{b,in}$ (m^2/s) was added at the upstream sediment boundary. A transparent sediment boundary condition was applied at the downstream boundary. Therefore, a fixed control section (non-erodible) was imposed at the downstream boundary. Constant water discharge Q was applied at the upstream boundary assuming uniform flow conditions for a constant initial bed slope in the case of equilibrium sediment supply, while an adapting bed slope was applied in the case of sediment supply reduction. Similarly, uniform flow was applied at the downstream boundary. The bed slope was dynamically adjusted in case of morphological change at the upstream boundary. Chézy's logarithmic friction law was applied using equivalent sand roughness $k_s = 2.5d_{50}$. The Froude number was 0.85 for the initial bed slope of $S_0 = 0.005$, and decreased to 0.63 for bed slope of $S = 0.0025$ in case of complete sediment supply termination. The minimum water depth to define wet cells was set to 0.01 m.

The numerical model setup was determined based on information derived from the linear stability theory for free bars (see Chap. 3.4). Three different setups are considered: (1) sub-critical condition ($\beta < \beta_C$), (2) super-critical condition ($\beta_C < \beta$), and (3) super-resonant condition ($\beta_R < \beta$) (Table 7.1). Each setup had

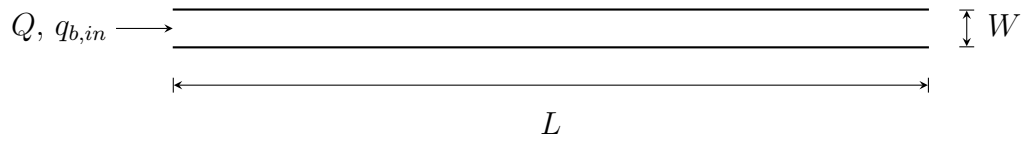

Fig. 7.1.: Definition sketch (top view) of straight river channel for free bars simulation

the same initial bed slope S_0, Shields stress θ, relative roughness $d_s = d_{50}/h_0$, and constant river width W. This results in the same neutral curve for bar instability ($\Omega = 0$) and neutral curve for bar migration ($\omega = 0$). Hence, free bar conditions can be described with the same critical aspect ratio for free bar amplification (β_C) and resonant aspect ratio (β_R). Finally, only the dimensional parameters water discharge Q (450, 800, and 1500 m^3/s) and median grain size d_{50} (64.6, 87.7, and 133.5 mm) were varied to obtain three setups (Table 7.1).

Table 7.1.: Setup of numerical experiments: (1) sub-critical, (2) super-critical, and (3) super-resonant conditions, with dimensional parameters, non-dimensional parameters, and threshold values from linear stability theory

	setup 1 $\beta < \beta_C$	setup 2 $\beta_C < \beta < \beta_R$	setup 3 $\beta_R < \beta$
W [m]	60	60	60
S_0 [-]	0.005	0.005	0.005
Q [m^3/s]	1500	800	450
h_0 [m]	4.45	2.92	2.15
d_{50} [mm]	133.5	87.7	64.6
θ [-]	0.1	0.1	0.1
d_s [-]	0.03	0.03	0.03
β [-]	6.7	10.3	13.9
β_C [-]	7.5	7.5	7.5
β_R [-]	12.0	12.0	12.0

First, the dynamic equilibrium of free bar morphology was established using equilibrium bed-load transport capacity at the upper boundary ($q_{b,0}$). Then, the effect of reduced specific sediment supply $q_{b,in}$ was investigated by applying

different fractions of the equilibrium bed load transport capacity ($q_{b,in}/q_{b,0} = 0.75, 0.5, 0.25, 0.125, 0.0625, 0.0$). For instance, $q_{b,in}/q_{b,0} = 0.0$ corresponds to the condition of complete sediment supply termination.

In order to reduce computational costs, simulations were accelerated using a morphological factor of $m_f = 20$ (see section 4.3.7). This value was found to be a good compromise between keeping the simulations realistic (section 5.3.5) and handling the computational time at an acceptable level. The simulation time of $t_s = 1200$ days resulted in a computation time (cost) of $t_c = 14$ days using 10 cores of a standard 3.0 GHz Intel Xeon processor (corresponding to a real time speed of $RTS = t_s/t_c = 86$).

7.3. Linear Stability Analysis for Reduced Bed Slope

The three presented setups (Table 7.1) are characterized by the same marginal stability curve (θ, d_s) and different aspect ratio β_i ($i = 1, 2, 3$, Fig. 7.2). Thereby, the same hydraulic friction law and the same bed load formula were used as for the numerical simulations (see section 7.2). The linear stability analysis was performed with a factor for the lateral bed slope effect of $N_l = 1.4$. However, this holds only for the initial bed slope with equilibrium sediment supply. A reduction of the sediment supply $q_{b,in}$ results in a reduction of the equilibrium bed slope S (morphological 1-D effect). Assuming that the flow conditions adapt instantaneously to a reduction of the equilibrium bed slope S and keeping the dimensional parameters constant (W, Q, and d_{50}) the marginal curves can be calculated for reduced bed slope. Accordingly, Fig. 7.3 shows the relative difference to the critical aspect ratio $(\beta - \beta_C)/\beta_C$ and the relative difference to the resonant aspect ratio $(\beta - \beta_R)/\beta_R$ for varying bed slope. Thereby, $(\beta - \beta_C)/\beta_C > 0$ ($(\beta - \beta_R)/\beta_R > 0$) denotes super-critical (super-resonant) conditions, while $(\beta - \beta_C)/\beta_C < 0$ ($(\beta - \beta_R)/\beta_R < 0$) denotes sub-critical (sub-resonant) conditions. This provides an analytical prediction of the marginal curves for free bar instability and free bar migration for varying equilibrium bed slope. Hence, for the sub-critical conditions (setup 1), free bar instability was predicted to remain sub-critical ($(\beta - \beta_C)/\beta_C < 0$) for almost all bed slopes (Fig. 7.3 a). According to linear stability theory it would be theoretically possible to find a configuration

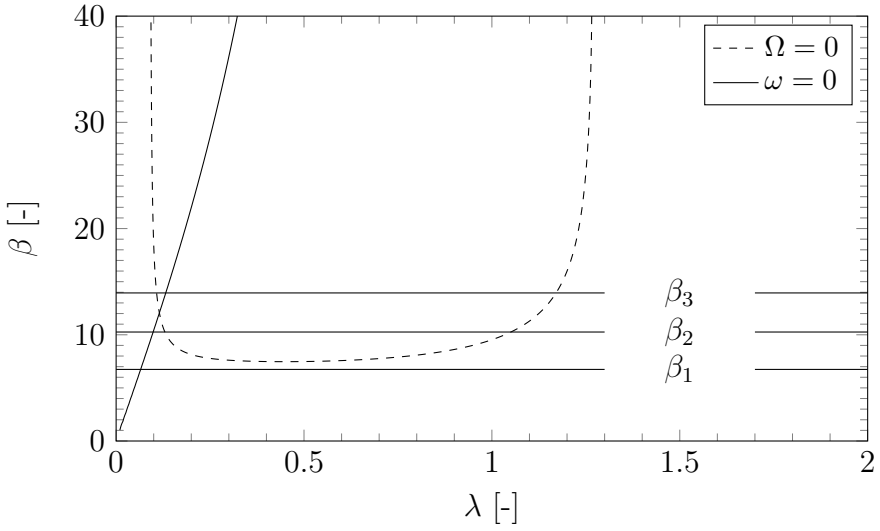

Fig. 7.2.: Marginal curves of free bar instability ($\Omega = 0$) and free bar migration ($\omega = 0$) for $\theta = 0.1$ and $d_s = 0.03$ using Chézy's friction law, Wong & Parker (2006) bed load formula, and Ikeda parameter $N_l = 1.38$

with fixed dimensional parameters, where the conditions would change from sub-critical to super-critical for decreasing and increasing bed slope. However, a major bed slope change would be required for this rather theoretical case. In the case of the super-critical condition (setup 2) free bar instability was expected to remain always super-critical ($(\beta - \beta_C)/\beta_C > 0$) (Fig. 7.3b). In other words, free bars instability is predicted for reduced bed slope. Fig. 7.3 b also shows that for decreasing bed slope, conditions for bar migration change from sub-resonant ($(\beta - \beta_R)/\beta_R < 0$) to super-resonant conditions ($(\beta - \beta_R)/\beta_R > 0$) for $S < 0.003$. Therefore, longer bars (smaller λ) and non-migrating bars (decreasing bar celerity) can be expected when approaching the resonant value β_R. The bar height can be expected to increase due to the increase of the relative difference to the critical aspect ratio for free bar instability ($(\beta - \beta_C)/\beta_C$), especially for major bed slope decrease. Finally, for the super-resonant condition (setup 3), the free bar instability would remain super-critical ($(\beta - \beta_C)/\beta_C > 0$) and bar migration super-resonant ($(\beta - \beta_R)/\beta_R > 0$) independent from bed slope (Fig. 7.3c). In this case, even larger bar height can be expected, again due to an increasing value of $(\beta - \beta_C)/\beta_C$.

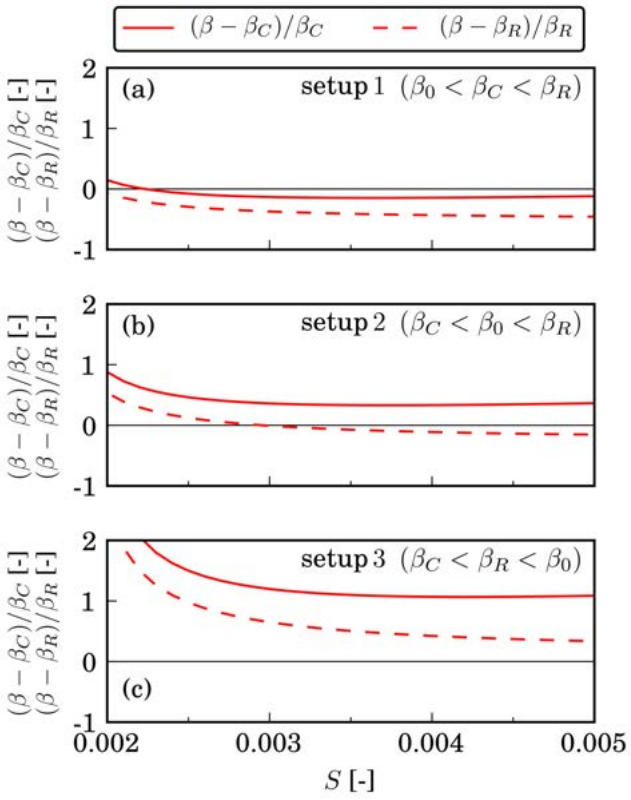

Fig. 7.3.: Linear stability theory for reduced bed slope S (starting from $S = 0.005$) with initial aspect ratio β_0 for (a) setup 1: sub-critical, (b) setup 2: super-critical, and (c) setup 3: super-resonant conditions

7.4. Non-linear Numerical Analysis for Reduced Sediment Supply

7.4.1. Relevant Setup and Initial Equilibrium Condition

The free bars response to sediment supply reduction was studied by means of numerical 2-D simulations. Three different initial setups were defined for equilibrium conditions (bed slope and bed load transport) according to Table 7.1. The purpose of setup 1 (sub-critical) was to validate the numerical model for the ability to suppress free bar instability according to linear stability theory. In this case, the numerical simulation correctly predicted the suppression of free bar instability. During the numerical simulation of setup 3 (super-resonant), however, free bars formed and eventually the top of the bars emerged from the water surface. Finally, this resulted in a non-migrating steady bar pattern in the whole

channel. In this case, sediment supply reduction would not cause any significant effects other than erosion along the thalweg. Hence, numerical 2-D simulations with reduced sediment supply focused on setup 2 starting with super-critical, but sub-resonant conditions (Table 7.1, Fig. 7.3 b).

The morphological time scale t_m was used to scale the temporal evolution. Here, t_m was defined as the time which would be required to erode the entire sediment volume given by channel length L and initial bed slope ($S_0 = 0.005$) assuming constant equilibrium bed load transport ($q_{b,0} = 4.69 \times 10^{-3}\, m^2/s$). Hence, t_m is defined as

$$t_m = \frac{S_0 L^2}{2 q_{b,0}}. \tag{7.1}$$

This corresponds to roughly 2000 days, and is half of the characteristic morphodynamic response time scale of rivers proposed by Wong & Parker (2006).

Initially, a free bar pattern was generated for equilibrium conditions (S_0, $q_{b,0}$). The obtained free bars pattern can be characterized by a wavenumber of $\lambda = 0.35$, a relative bar amplitude of $|A|/h_0 = 0.75$, and a mean bar celerity of $c_b = 20.8\,\mathrm{m/h}$ (see also Chap. 5.3). Thereby, the bar amplitude is defined as $A = z_{b,left} - z_{b,right}$, where $z_{b,left}$ and $z_{b,right}$ denote the bed elevation on the orographic left and right side of the channel, respectively (see Fig. 5.16). This dynamic equilibrium of migrating free bars served as initial condition to further investigate the effect of sediment supply reduction.

7.4.2. Sediment Supply Termination

First of all, the focus is on the case of complete sediment supply termination ($q_{b,in}/q_{b,0} = 0.0$). After sediment supply was suddenly terminated, a train of free bars formed near the upper boundary and eventually migrated downstream. A similar model behavior was observed by Bernini *et al.* (2009) after placing an erodible bump near the upstream boundary. Hence, the sudden sediment supply reduction acts like a temporary additional disturbance triggering free bars. However, after this train of free bars merged with the free bars in the lower part of the channel, free bars were again continuously formed in the middle region of the channel.

The temporal change of bed load transport q_b and bed slope S (morphological 1-D effect) together with the free bars response (2-D effects) are shown in Fig. 7.4 for four different time steps ($t/t_m = 0.0, 0.15, 0.3, 0.45$). Thereby, the 2-D effects are expressed by the relative absolute value of the bar amplitude $|A|/h_0$, the local bar wavenumber λ_{local}, and the dominant wavenumber λ of the spatial bar amplitude signal using Fast Fourier Transform (see section 5.3 for more details). The bed load transport was averaged over single bar units (bar wavelength), while the bed slope was the spatial derivative of the average bed elevation of single bar units. This analysis showed that the morphological 1-D effect played a major role and significantly influenced the 2-D effects. As a result, wavenumbers $(\lambda, \lambda_{local})$ decreased and relative bar amplitude $|A|/h_0$ increased accordingly. Eventually, the top of free bars started to emerge from the water surface. This abrupt change significantly influenced the further morphological development. The bars with emerging bar tops stopped to migrate and subsequently acted as local obstacles. This further triggered the development of steady bars downstream decaying over two to three wavelengths (see $t/t_m = 0.45$ in Fig. 7.4). In the case of reaching super-resonant conditions, there is also the possibility of an upstream influence of the steady bars. At the end of the simulation ($t/t_m = 0.6$), non-migrating steady bar pattern was found in the whole channel with zero bed load transport in the upper half of the channel and slowly trending towards negligible bed load transport in the lower half of the channel.

The increase of the bar amplitude and the following bar elongation are analyzed in more detail for the case of complete sediment supply reduction ($q_{b,in}/q_{b,0} = 0.0$). Therefore, the dominant wavenumber λ and the maximum absolute amplitude in the channel ($\max(|A|)/h_0$) were tracked over time (Fig. 7.5). On the one hand, λ continuously decreased until the steady bar signal became dominant at around $t/t_m = 0.43$ ($\lambda = 0.15$). On the other hand, $\max(|A|)/h_0$ increased until $t/t_m = 0.3$, followed by sudden increase due to emerging bars. In the subsequent transition period ($0.3 \leq t/t_m \leq 0.45$), the free bar pattern transformed to a steady bar pattern. In the end of this transition period, the dominant λ dropped from 0.25 to 0.15, indicating the dominance of the steady bar pattern. Finally, the steady bar pattern remained and the bar amplitude further increased due to further vertical erosion along the thalweg. However, the most essential results appear in the first half of the simulation ($t/t_m \leq 0.3$) revealing a clear trend of decreasing λ and increasing $\max(|A|)/h_0$ due to the morphological 1-D effect.

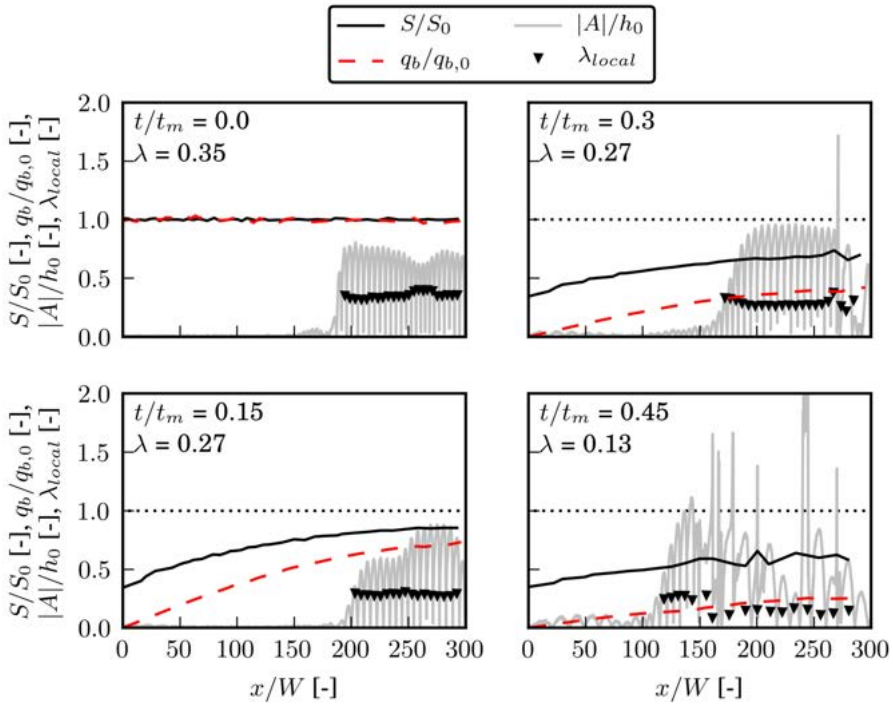

Fig. 7.4.: Morphological 1-D and 2-D effects due to sediment supply termination ($q_{b,in}/q_{b,0} = 0.0$)

On the other hand, the non-linear transition from free migrating bars to free non-migrating bars in the second half of the simulation ($t/t_m > 0.3$) can rather be seen as general trend towards a steady bar pattern.

To better understand the emergence of the top of the free bars from the water surface during the simulation of sediment supply termination, the Shields stress θ and the bed elevation change z_b were analyzed at the orographic right side of the channel. Generally, the smallest values of θ/θ_C were observed in the pools just downstream of the bar heads (see e.g. $t/t_m = 0$, Fig. 7.6). This was found to be in good agreement with numerical simulations presented by Qian *et al.* (2017). As described above, the bars elongated (longer bars and pools) and increased in height due to the morphological 1-D effect. Fig. 7.6 shows that bed shear stress falls below critical shear stress in certain pools ($\theta/\theta_C < 1$), well before bars emerged from the water surface. Nevertheless, free bars were still able to migrate downstream. However, more and more pools became apparent for which the Shields stress fell below the critical threshold ($\theta/\theta_C < 1$). The bar amplitude and bar wavelength increased accordingly. From a certain point in time, the Shields stress fell below the critical threshold also near single bar heads. It has to be

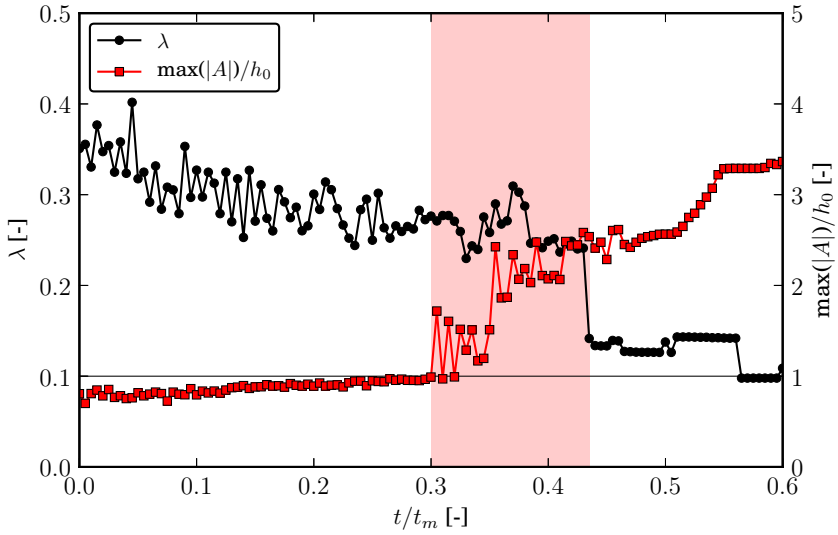

Fig. 7.5.: Temporal and spatial development of free bar properties (λ, $max(|A|)/h_0$) due to sediment supply termination ($q_{b,in}/q_{b,0} = 0.0$)

mentioned that this has happened well before the top of the bar heads fell dry. What makes a detailed analysis more difficult is the fact that free bars continued to migrate and merged with the areas of vanishing bed load transport (pools). However, it can be concluded that the emergence of the bars from the water surface was effectively triggered by locally vanishing bed load transport, first in the pools and finally near the bar heads. Finally, the actual emergence of the bar top from the water surface and the further increase of the bar amplitude was due to continuous erosion along the thalweg.

The mean bar celerity c_b was determined by spatial and temporal averaging of the local bar celerities (see section 5.3) using time intervals T of ten days ($T = t/t_m = 0.005$). Fig. 7.7 shows that c_b continuously decreases due to the morphological 1-D effect. Finally, c_b abruptly decreases from 8.5 m/h to nearly zero at $t/t_m = 0.45$. This was found to be in good agreement with the point in time where a dominant steady bar wavelength was detected using FFT (Fig. 7.5).

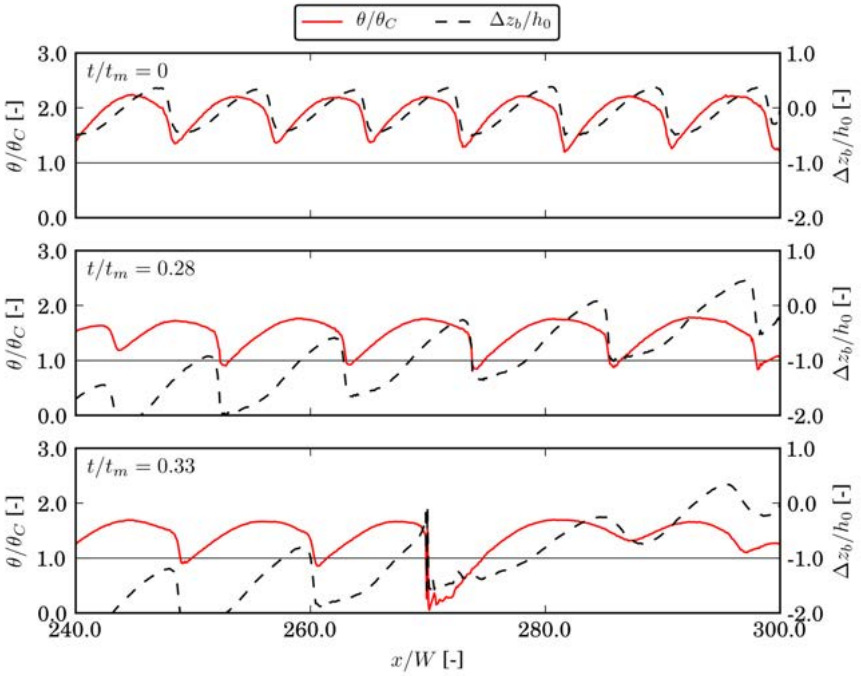

Fig. 7.6.: Temporal development of Shields stress θ and bed elevation change Δz_b on the right side of the channel

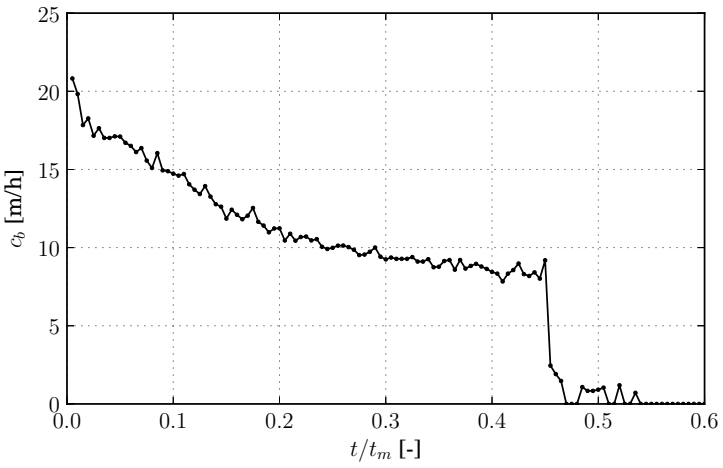

Fig. 7.7.: Response of the mean bar celerity c_b due to sediment supply termination ($q_{b,in}/q_{b,0} = 0.0$)

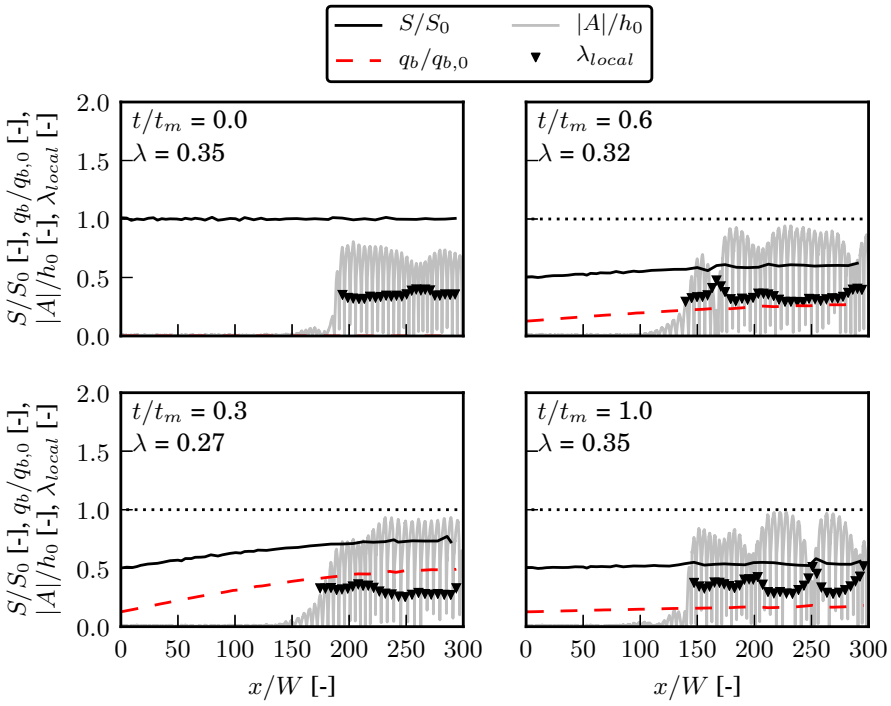

Fig. 7.8.: Morphological 1-D and 2-D effect due to sediment supply reduction to $q_{b,in}/q_{b,0} = 0.125$ over the entire morphological time scale ($0.0 \leq t/t_m \leq 1.0$)

7.4.3. Varying Sediment Supply Reduction

The free bars response was further evaluated for varying sediment supply rates, such as $q_{b,in}/q_{b,0} = 0.0625$, 0.125, 0.25, 0.5, and 0.75. Similar to the case of sediment supply termination, the free bar pattern responded to a small sediment feed of $q_{b,in}/q_{b,0} = 0.0625$ by transforming into a non-migrating steady bar pattern. However, this transformation process was slightly delayed compared to complete sediment supply termination due to the small sediment feed and hence slower morphological 1-D effect. On the other hand, the free bar pattern persisted for sediment supply rates $q_{b,in}/q_{b,0} \geq 0.125$, e.g. see Fig. 7.8. The figures of all runs ($q_{b,in}/q_{b,0} = 0.0, 0.0625, 0.125, 0.25, 0.5, 0.75$) are shown in Appendix A.2.

An overall picture of the free bars response to different sediment supply rates is shown in Fig. 7.9a using the same simulation time as in the case of sediment supply termination ($t/t_m = 0.6$, nearly equilibrium). Note that at this point in time the equilibrium bed slope and bed load transport was not yet fully reached in the whole channel. However, for the largest sediment supply reduction for which no transformation takes place ($q_{b,in}/q_{b,0} = 0.125$), the simulation was performed over

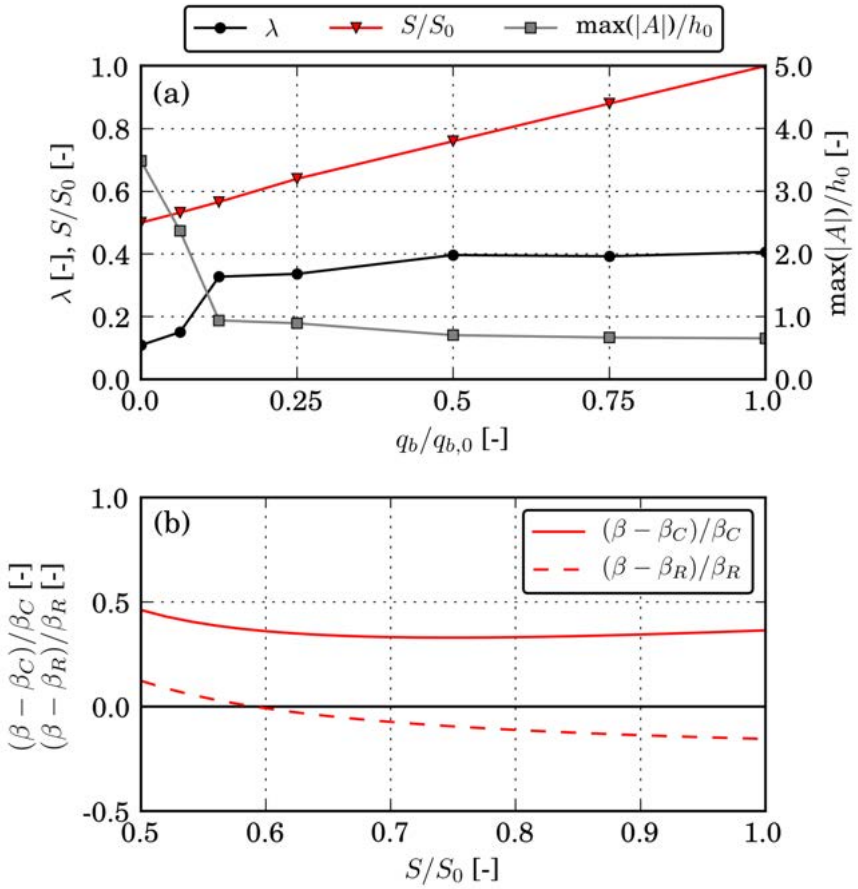

Fig. 7.9.: Free bars properties for (a) different sediment supply rates at quasi equilibrium ($t/t_m = 0.6$) and (b) linear stability theory for reduced bed slope

the entire morphological time scale t_m (see Fig. 7.8). However, this did not lead to any significant change in the free bar pattern. The bed load transport reduction averaged over the last bar unit before the outflow boundary ($q_b/q_{b,0} = 0.139$) deviated only slightly from the sediment supply reduction ($q_{b,in}/q_{b,0} = 0.125$). Note that the sediment flux at the outflow boundary includes fluctuations due to the migration of free bars. The relative change of the bed slope S/S_0 was estimated by the vertical erosion at the upper boundary in relation to the flume length. However, the change in bed slope was not uniform over the entire channel. Bed slope reduction was more pronounced in the upper part of the channel (see Fig. 7.4).

Linear stability theory predicted super-critical condition ($(\beta - \beta_C)/\beta_C > 0$) for varying bed slope (Fig. 7.9 b). Hence, linear free bar instability corresponds well

with the findings from numerical (non-linear) simulations showing a free bar pattern. However, for a bed slope change of $S/S_0 < 0.6$, linear stability theory suggested bar migration condition to become super-resonant ($(\beta - \beta_R)/\beta_R > 0$). This means that information related to two dimensional bed perturbations might propagate upstream and free bars are expected to have longer wavelength, hence smaller λ. This provides a possible explanation of the numerical simulations with decrease of λ for decreasing sediment supply and bed slope. The increase of A/h_0 can be explained by the increase of the relative difference to the critical aspect ratio for free bars ($(\beta - \beta_C)/\beta_C$, see Eq. 3.49).

7.5. Discussion

Different responses of free bar morphology to sediment supply reduction were reported in literature based on laboratory experiments. For instance, Lisle *et al.* (1993) observed the emergence of the top of bars from the water surface and vertical incision already for sediment supply reduction of $q_{b,in}/q_{b,0} = 0.32$. Further sediment supply reduction ($q_{b,in}/q_{b,0} = 0.10$) resulted in further incision and only in minor morphological changes. Lisle *et al.* (1993) observed emerging bars immediately after reducing sediment supply, whereas in the present study bar emergence occurred after major bed slope adjustment. However, the general trend towards a steady bar pattern due to emergence of the top of bars from the water surface is in good agreement with the presented numerical results. In contrast, Venditti *et al.* (2012) observed in the Berkley laboratory experiment that initially free non-migrating bars started to migrate out of the flume after sediment supply termination. Finally, bars disappeared in the upstream part of the flume, but persisted in the downstream part. The final bar pattern seemed to contain an alternate bar signal with increased wavelength (see Fig. 2q in Venditti *et al.*, 2012). The surface grain-size heterogeneity and bed slope were reduced after sediment supply termination. However, the bed slope reduced to a greater extend in the lower part of the flume compared to the upper part. This was exactly opposite to what was obtained with the numerical simulations presented herein, where bed slope reduction was more pronounced in the upper part. Linear stability theory was applied for the initial and final experimental conditions as reported in Venditti *et al.* (2012) using Chézy's friction law, Wong & Parker (2006) bed load formula, and $N_l = 1.38$. This indicates that free bar instability had been super-critical

and free bar migration had been super-resonant for both initial conditions with bars ($\beta > \beta_R > \beta_C$, 11.0 > 4.5 > 3.5, respectively) and final conditions with bars eliminated ($\beta > \beta_R > \beta_C$, 10.3 > 3.0 > 2.4, respectively). However, this provides only a rough indication on the reported conditions and should be further investigated, e.g. using numerical simulations. However, it is still unclear how an initial non-migrating bar pattern started to migrate downstream after sediment supply termination. As a working hypothesis, a possible explanation could be that the bars near the upstream boundary experienced an elongation and thereby pushed the downstream bars further downstream. Hence, the bars started to migrate and stopped as soon as they reached typical wavelength for steady bars. Interestingly, Podolak & Wilcock (2013) observed in laboratory experiments that rather short free bars migrated over a forced steady bar pattern during the transition period after increased sediment feed. However, at equilibrium state with steeper bed slope the steady bar pattern was dominant again (longer bar wavelength). Unfortunately, a comparison is rather difficult due to the influence of the forced bars.

Generally, experimental flumes were limited in their length allowing only for a limited number of free bar wavelengths, e.g. three wavelengths (Venditti *et al.*, 2012) or four to five wavelengths (Lanzoni, 2000a). The field scale experiment of Eekhout *et al.* (2013) on free non-migrating bars, albeit without sediment supply variation, turned out to be influenced by both hydrology and vegetation. Hence, laboratory experiments on alternate bars are still a challenge and are associated with considerable cost and effort.

Even tough numerical model experiments are generally not limited in space, there are other things that should be considered. Generally, the formation of free bars and the emergence of the bars from the water surface can be influenced by different reasons in a numerical simulation, such as the lateral bed slope effect (Ikeda parameter), computational grid resolution, critical Shields stress, wetting and drying algorithm, and simulation speed up using morphological factor. Indeed, the lateral bed slope effect plays a significant role for free bar formation and the equilibrium bar height (Bernini *et al.*, 2009). However, it is only necessary to ensure that the additional lateral diffusion (and hence the Ikeda parameter N_l) fit with the numerical diffusion due to the discretization scheme (see section 5.3.3). The influence of the wetting and drying algorithm using a minimum water depth to define dry cells can be assumed to be negligibly small, since the bar tops

emerged from the water surface due to continuous erosion along the thalweg. The influence of the morphological factor m_f on the free bar formation was found to be rather small for $m_f < 40$ (see section 5.3.5).

The presented numerical simulations were based on uniform bed load transport. However, additional numerical simulations were performed with non-uniform sediment to ensure that the behavior does not change completely. The grain size distribution had a geometric standard deviation of $\sigma_g = 2$ with the same median grain size d_{50} as in the case of uniform sediment and was discretized with five grain classes. It was found that the general trend towards a non-migrating steady bar pattern remains the same as in the case of uniform sediment. However, the difference was that this behavior occurred for a less pronounced sediment supply reduction (higher sediment supply rates, $q_{b,in}/q_{b,0} \leq 0.25$) compared to the case of uniform sediment. Note that the morphological 1-D effect (decreasing bed slope) was less pronounced due to grain sorting effects. Lanzoni & Tubino (1999) proposed a linear stability theory for free bars with non-uniform sediment using two grain classes. Interestingly, they found that grain sorting effects may disadvantage free bar instability (increasing β_C, stabilizing effect) for high Shields stress compared to uniform sediment, while grain sorting effects may favor free bar instability (decreasing β_C, destabilizing effect) in the case of low Shields stress, especially when approaching the threshold value (θ_C). Furthermore, grain sorting effect was found to increasingly favor free bar instability (decreasing β_C) in the case of increasing relative grain roughness $d_s = d_{50}/h_0$. This is qualitatively in good agreement with the numerical simulations for reduced sediment supply using non-uniform sediment. For the same bed slope, the relative grain roughness d_s is likely to be larger due to grain sorting effects compared to the case of uniform sediment. Furthermore, for decreasing bed slope (morphological 1-D effect) and Shields stress approaching the threshold value, free bar instability tends to be increasingly favored compared to uniform sediment.

7.6. Summary

The response of free bars to sediment supply reduction was first investigated using linear stability theory for reduced equilibrium bed slope. Thereby, three different initial conditions were defined, resulting in the following three setups: (1)

sub-critical, (2) super-critical and sub-resonant, and (3) super-resonant conditions. In summary, conditions for setup 1 and setup 3 were predicted to remain sub-critical and super-resonant, respectively, independent from bed slope. For setup 2, however, super-critical and sub-resonant conditions were predicted to change to super-resonant conditions. The relative difference to the critical aspect ratio $((\beta - \beta_C)/\beta_C)$ increased, especially for major bed slope reduction. Therefore, it can be assumed that the bar height will increase for reduced sediment supply. At resonant conditions, free bar instability is non-amplifying and non-migrating per definition. However, for super-resonant conditions, information related to two-dimensional bed perturbations may also propagate upstream (Zolezzi & Seminara, 2001). The wavelength of such an instability is generally larger than that of downstream migrating free bars. It can therefore be assumed that the bar wavelength will increase and bar celerity will decrease for reduced sediment supply, especially when approaching resonant conditions.

Numerical simulations with reduced sediment supply were then performed to support the findings from linear stability theory. The goal of this study was to shed light on the non-linear response of free bars to sediment supply reduction focusing on the competition between the morphological 1-D effect (bed slope) and the morphological 2-D effects (bar properties). The numerical simulation of setup 1 (sub-critical) successfully suppressed free bar formation. Therefore, no simulations with reduced sediment supply were carried out for this setup. In the case of super-resonant conditions (setup 3), free bars formed and eventually the top of the bars emerged from the water surface resulting in a non-migrating steady bar pattern. Sediment supply reduction would not further alter this bar pattern, except for erosion along the thalweg. Hence, the numerical simulations to investigate the free bars response to sediment supply reduction was based on setup 2 (super-critical and sub-resonant conditions). In this case, it was found that only major morphological 1-D effect significantly influenced morphological 2-D effects. Indeed, sediment supply reduction of $q_{b,in}/q_{b,0} \geq 0.5$ had almost no 2-D effects, while $0.125 \leq q_{b,in}/q_{b,0} \leq 0.25$ only slightly increased the bar amplitude and wavelength. However, free migrating bars transformed to a non-migrating bar pattern below a certain, but small, sediment feed rate ($q_{b,in}/q_{b,0} \leq 0.0625$) due to the emergence of the bar tops from the water surface. This process was initiated by decreasing bar celerity and increasing bar amplitude. The bed shear stress locally decreased and eventually fell below the critical bed shear stress, first

in the pools and eventually on the top of the bars. The top of the bars started to emerge from the water surface due to continuous erosion along the thalweg, well before the minimum water depth was reached on the bars. Additional numerical simulations with non-uniform sediment suggested that this transition to a steady bar pattern will be shifted towards larger sediment supply rates (less pronounced sediment supply reduction) compared to uniform sediment.

The presented findings combining linear stability theory and numerical simulations suggest that free bars response to sediment supply reduction depends on the initial condition for free bar instability. Sediment supply reduction will unlikely alter free bar patterns to flat river bed morphology, e.g. by erosion or migration out of the channel. However, the morphological 1-D effect will affect free bar properties, such as bar amplitude, bar wavelength, and bar celerity. Reversely, the linear theory suggests that increased bed slope, and hence increased sediment supply, will unlikely alter flat river bed ($\beta < \beta_C$) to free bar morphology ($\beta > \beta_C$). Hence, for most rivers, morphology would rather improve by increasing the aspect ratio β, i.e. the river width, for which significant bed load transport can be expected over a wide range of discharge ($\beta > \beta_C$ for $\theta >> \theta_C$).

The presented free bars response to sediment supply reduction are qualitatively in accordance with the experimental observations of Lisle *et al.* (1993) and may give further insight and additional explanations for observations from other studies in literature. However, further experimental and numerical investigations are necessary to verify these findings. On the one hand, linear stability theory and numerical simulations using non-uniform sediment would allow to investigate the effect of grain sorting on free bar formation for different conditions (θ, d_s, β). On the other hand, laboratory experiments on free bars response starting from super-critical but sub-resonant conditions ($\beta_R > \beta > \beta_C$) would help to better understand the emergence of the bar tops from the water surface when approaching resonant conditions. The optimal flume length should contain several free bar wavelengths and interaction with forced steady bars should be avoided to limit the focus on free bars.

8. Forced Steady Bars Response to Sediment Supply Reduction

The focus in the present chapter is on the response of forced steady bars to sediment supply reduction. Firstly, the reach scale is examined in a straight channel, where steady alternate bars are forced due to a local obstacle (section 8.1). Thereby, a relevant task was to study the effect of sediment supply reduction on the forced steady bar pattern, such as bar wavelength and amplitude. Secondly, the effect of sediment supply reduction on a point bar in a 180° river bend is investigated in section 8.2. Thereby, the focus is more locally on the point bar morphology and grain sorting effects in the river bend.

8.1. Forced Bars Due to Local Obstacle

Forced steady bars in a river are forced due to local planform discontinuities, such as a local channel narrowing due to a persistent obstacle or a river bend. Usually, steady bars are about twice as long as free bars and gradually decay over two or three wavelengths under submerged conditions (Chap. 3.4). The aim of this chapter is to investigate the response of forced steady bars to sediment supply reduction. Therefore, an obstacle was placed into a straight channel acting as a channel narrowing to force steady bars. Starting from the equilibrium bed slope and corresponding bed load transport capacity, the sediment supply was reduced using different fractions of the initial bed load transport capacity. This chapter is structured as follows: After the description of the numerical model setup, the results are presented, discussed and compared to observations of laboratory experiments from literature.

8.1.1. Numerical Model Setup

The topography consisted of a straight rectangular channel with an initial bed slope of $S_0 = 0.005$, a channel width of $W = 60\,\mathrm{m}$, and a channel length of $L_c = 300W$ (Fig. 8.1), similar to the topography used for the case of free bars (Chap. 7). From the latter, the model setup and model parameters were adopted, unless indicated otherwise. In the present case, the main difference was the placement of an obstacle in the channel at $x/W = 150$ on the orographic left side. The obstacle had a trapezoidal-shaped form, a width of half the channel width ($W_g = W/2$), a length of $L_g = W/6$, and an inclination angle with respect to the channel wall of $\alpha_g = 30°$ (Fig. 8.1).

First, an initial dynamic equilibrium state with alternate bar morphology was established using equilibrium bed load transport capacity at the upper boundary ($q_{b,0}$). The effect of specific sediment supply rates $q_{b,in}$ was investigated by feeding fractions of the equilibrium bed load transport capacity ($q_{b,in}/q_{b,0} = 0.75$, 0.5, 0.25, 0.125, 0.0625, 0.0).

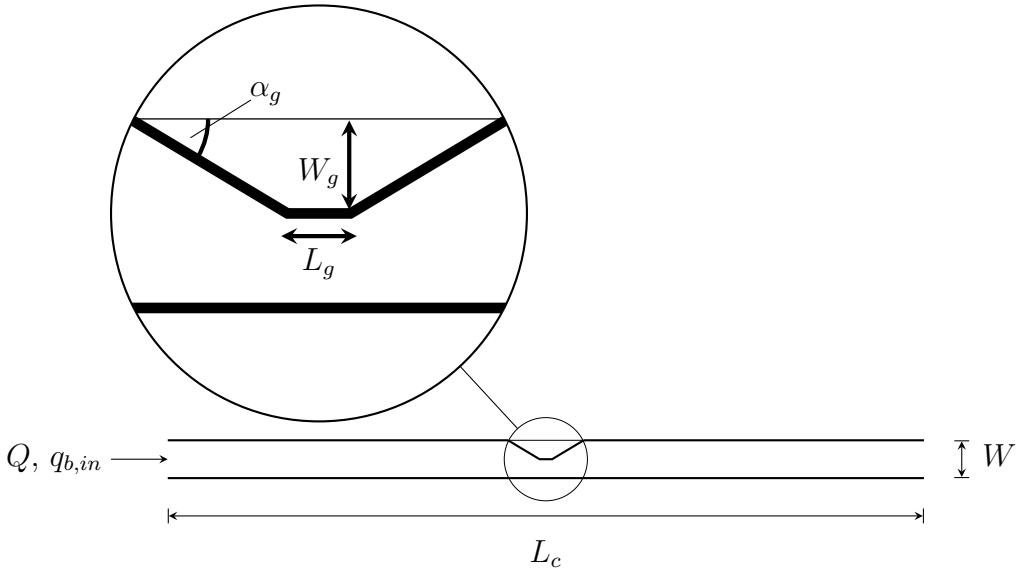

Fig. 8.1.: Sketch of the straight channel with the obstacle, where the subscript g denotes the obstacle

8.1.2. Results

Relevant Setup and Initial Equilibrium Condition

The same three setups as in the case of free bars were tested for equilibrium bed load transport capacity (Table 7.1). In the case of setup 1 (sub-critical), steady bars formed downstream of the obstacle consisting of roughly one bar wavelength. The model correctly predicted the suppression of free bar instability even with the additional flow perturbation introduced by the obstacle. For setup 3 (super-resonant), first several steady bars (2-3 wavelengths) formed downstream of the obstacle. Furthermore, shorter free bars also formed in the whole channel. Hence, both free bars and steady bars signals were present in the channel. Eventually, the top of the bars started to emerge from the water surface one after the other. Finally, this resulted in a non-migrating steady bar pattern in the whole channel. In this case, a sediment supply reduction would not further affect the steady bar pattern, except for erosion along the thalweg.

The present numerical study on the forced bars response to sediment supply reduction is based on setup 2 (super-critical, sub-resonant), similar to the case of free bars (Table 7.1, Fig. 7.3). First, initial conditions were created using equilibrium sediment supply ($q_{b,in}/q_{b,0} = 1.0$, $S/S_0 = 1.0$). Steady bars formed downstream of the obstacle decaying over roughly two to three wavelengths, while free migrating bars formed further downstream (see Fig. 8.2, $t/t_m = 0.0$). Based on this, the effect of sediment supply reduction was investigated. Similar to the case of free bars, the morphological time scale t_m was used to scale the temporal evolution (Eq. 7.1).

Sediment Supply Termination

First, the focus is on the case of complete sediment supply termination ($q_{b,in}/q_{b,0} = 0.0$). Over the course of the simulation, the bed slope continuously decreased over the whole channel (morphological 1-D effect, Fig. 8.2). As a result, the steady bars became longer (decreasing bar wavenumber λ) and the bar amplitude A increased over time (morphological 2-D effect). However, free bars eventually formed not only downstream of the steady bars but also upstream of the obstacle. Hence, free bars eventually interacted with the forced steady bars. The free bar

amplification was favored by the increase of the relative difference to the critical aspect ratio ($(\beta - \beta_C)/\beta_C$) (see Chap. 7). Interestingly, the first bar top which emerged from the water surface, was just upstream of the obstacle shortly before $t/t_m = 0.37$ with a free bar wavelength of $\lambda \approx 0.4$ (Fig. 8.2). Furthermore, long steady bars with rather small amplitude were likely to influence free bar formation in the first third of the flume (see Fig. 8.2 at $t/t_m = 0.37$). This process was most likely influenced by the obstacle and super-resonant conditions.

At the end of the simulation ($t/t_m = 0.55$), a non-migrating steady bar pattern was found in the whole channel ($\lambda \approx 0.15$). Clearly, there are indications of super-resonant steady bars upstream of the obstacle (upstream overdeepening), which were more pronounced than the forced bars downstream of the obstacle (see Fig. 8.2 for $t/t_m = 0.55$). Under super-resonant conditions, linear theory for forced bars suggests that the 2-D morphodynamic influence is predominantly felt upstream (Zolezzi & Seminara, 2001). Note that the marginal curves for bar migration and hence also the effect of bed slope on the relative difference to the resonant aspect ratio ($(\beta - \beta_R)/\beta_R$) are the same as in the case of free bars (Fig. 7.3).

Finally, the bed slope reduced to roughly $S/S_0 = 0.4$ in the upper part and to $S/S_0 = 0.5$ over the whole remaining channel except for the vicinity of the obstacle. Note that at the end of the simulation ($t/t_m = 0.55$) the equilibrium bed slope and bed load transport was not yet fully reached in the whole channel. The bed load transport is quasi zero in the upper half of the channel and slowly tends to zero in the lower half of the channel (Fig. 8.2).

The final non-migrating steady bar pattern had similarities to the free bar pattern with complete sediment supply termination (Fig. 7.4). However, the transition process to the final steady bar pattern was different. The main difference was the place of the first emerging bar from the water. In this case, the top of the steady bars started to emerge from the water surface near the obstacle. In the case of free bars, however, the location of the first emerging bar was in the lower half of the channel.

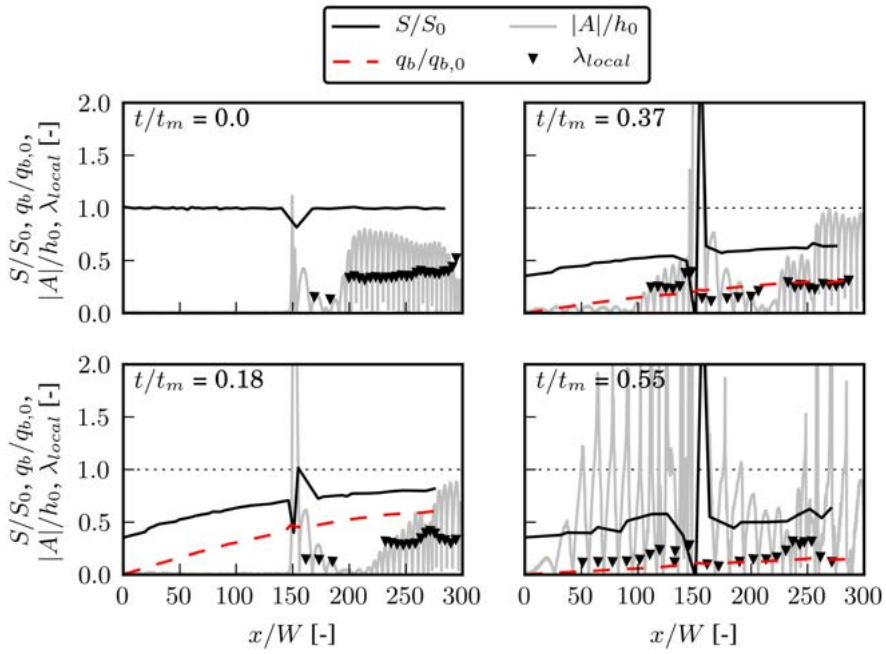

Fig. 8.2.: Morphological 1-D and 2-D effect due to complete sediment supply termination ($q_{b,in}/q_{b,0} = 0.0$)

Varying Sediment Supply Reduction

The forced bars response to varying sediment supply ($q_{b,in}/q_{b,0} = 0.0625$, 0.125, 0.25, 0.5, and 0.75) is evaluated in the following. Fig. 8.3 shows the maximum absolute bar amplitude max($|A|$) and the bar wavenumber λ of the first bar wavelength L downstream of the obstacle for different sediment supply rates. This shows that the bar amplitude and wavelength increase (λ decreases) for decreasing sediment supply. Hence, the forced bars were not eroded as observed in the experiments by Venditti *et al.* (2012). The present results suggest an increased dominance of forced bars for decreasing sediment supply.

Sediment supply reduction and the resulting morphological 1-D effect did not significantly alter the steady bar pattern in cases where $q_{b,in}/q_{b,0} \geq 0.5$. For instance, in the case of $q_{b,in}/q_{b,0} = 0.5$, Fig. 8.4 shows a steady bar pattern with characteristic local bar wavenumber λ_{local} around 0.15 and a typical free bar pattern downstream ($\lambda_{local} \approx 0.4$). Further sediment supply reduction ($q_{b,in}/q_{b,0} = 0.25$) increased the dominance of the steady bar signal in downstream direction (Fig. 8.3). Finally, for sediment supply rates of $q_{b,in}/q_{b,0} \leq 0.125$, upstream effects

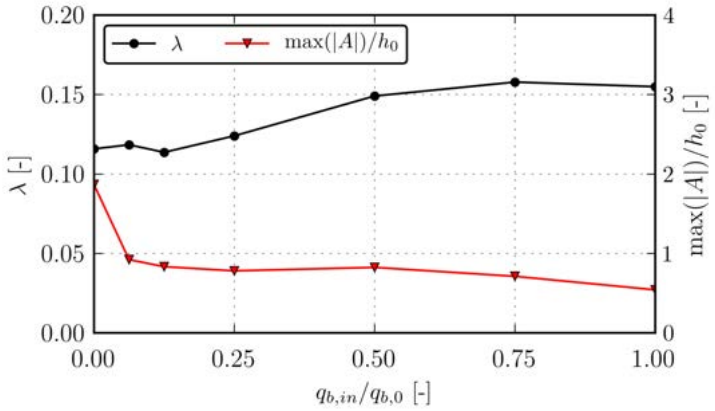

Fig. 8.3.: Response of the first steady bar amplitude downstream of the obstacle due to sediment supply reduction

of the obstacle became eventually possible due to super-resonant conditions (Fig. 8.5). The figures of all runs with varying sediment supply are shown in Appendix A.3.

8.1.3. Discussion

Venditti *et al.* (2012) performed a laboratory experiment at field scale forcing steady bars due to a local obstacle (sandbag) at the inflow boundary. The experiment was conducted at the Saint Anthony Falls Laboratory (SAFL) and was therefore referred to as the SAFL experiment. The flume length was roughly twenty times the width ($L_c/W = 20$), and hence contained roughly one steady bar wavelength. The flume was equipped with a full recirculation of water and sediment. First, an initial steady bar pattern was developed in the flume. After complete sediment supply termination, the top of the first bar downstream of the obstacle emerged from the water surface and became longer. However, bar pattern further downstream was reported to be eliminated. The authors observed a correlation between the reduction of surface sediment heterogeneity and the elimination of the steady bar pattern. The observation of the emerging bar top downstream of the obstacle is in good agreement with the presented numerical findings. In contradiction, however, the numerical results suggest that the steady bar pattern further downstream does not erode due to sediment supply termination. On the contrary, the steady bar wavelength increased and hence the area of the steady bar influence increased in downstream direction.

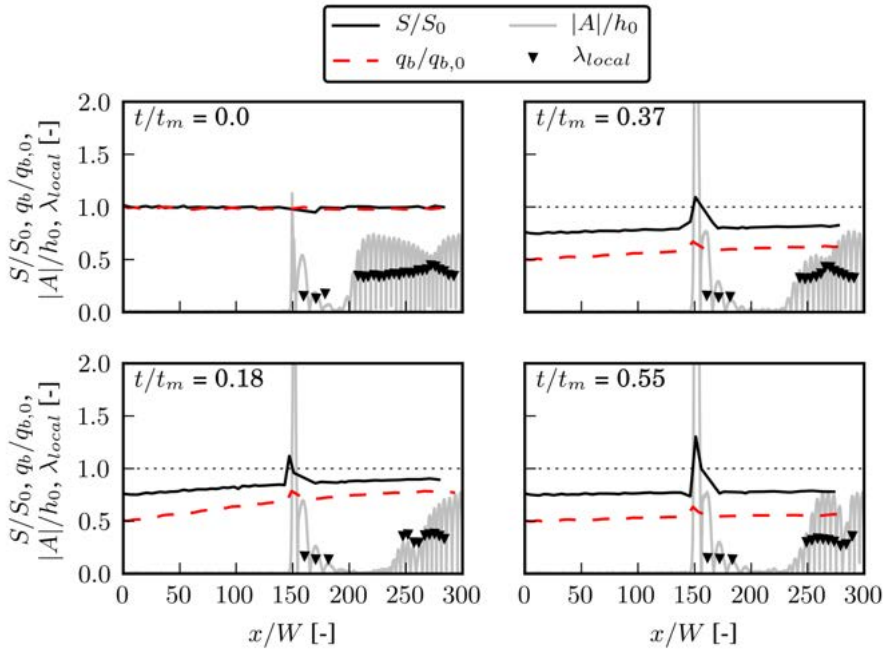

Fig. 8.4.: Morphological 1-D and 2-D effect due to sediment supply reduction to $q_{b,in}/q_{b,0} = 0.5$

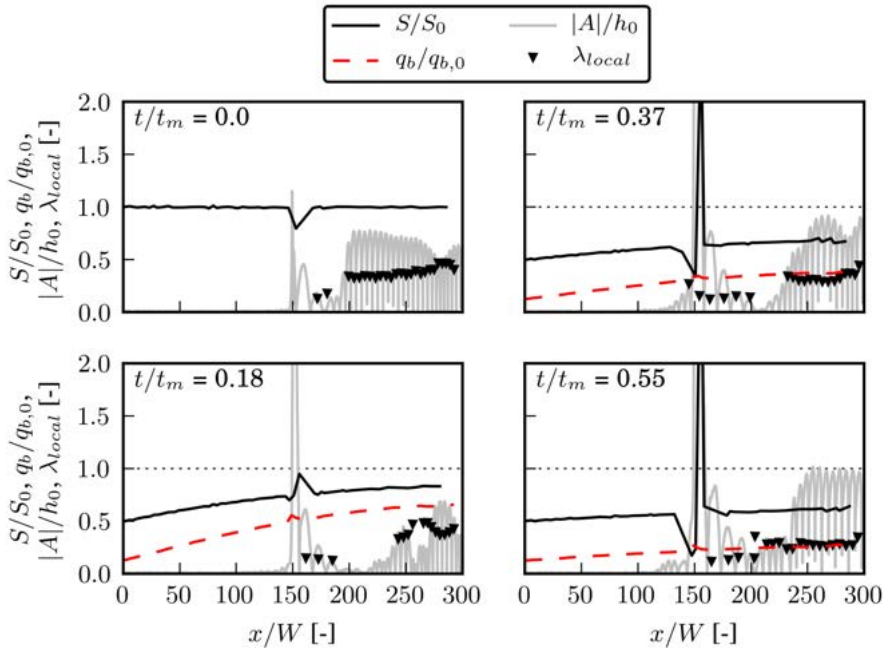

Fig. 8.5.: Morphological 1-D and 2-D effect due to sediment supply reduction to $q_{b,in}/q_{b,0} = 0.125$

The ratio of the steady bar wavelength L to channel width W is likely to be around $L/W \sim 15 - 20$. However, in the case of reproducing the whole history from full bed load transport capacity towards vanishing bed load transport, the steady bar wavelength likely corresponds to the upper limit. These findings might provide new insights with regard to the response of steady bars to sediment supply reduction reported in the laboratory experiment of Venditti *et al.* (2012). Indeed, the topography further downstream after sediment supply termination seems to still contain a steady bar signal, with an increased bar wavelength (see Fig. 8c in Venditti *et al.*, 2012). In this way, their experimental findings are consistent with the presented numerical findings. However, it should be pointed out that their experimental settings (discharge, grain size, bed slope, and flume width), and spatial and temporal scales are different to the numerical experiments, and therefore no complete comparison can be made.

Podolak & Wilcock (2013) performed laboratory experiments to study the effect of sediment supply increase on forced steady bar pattern. The steady bars were forced due to an obstacle placed at the inlet of the flume. The flume recirculated water and sediment over the whole duration of the experiment. The sediment supply was increased in two augmentation steps, each followed by a recovery period. The first augmentation step approximately doubled the bed load transport ($q_b/q_{b,0} = 2.2$), whereas the second augmentation step nearly tripled the bed load transport ($q_b/q_{b,0} = 3.1$) at the new equilibrium state. During the transition period to the new equilibrium state with increased bed slope, free bars with shorter wavelength migrated over the steady bar pattern, whereas the latter was suppressed during this period. However, finally the steady bar pattern reemerged and ultimately prevailed over the free bar signal in equilibrium conditions. The final steady bar pattern with increased sediment supply, but steeper bed slope, was similar to the initial steady bar pattern.

The interaction between free bars and steady bars was investigated by Vanzo *et al.* (2001) combining information from linear theory for free bars and (non-linear) numerical simulations. They found that for increasing aspect ratio β, free bars would increasingly dominate the steady bars, mainly due to an increase of free bar amplitude ($A = f(\beta - \beta_C)$). Furthermore, another governing parameter was the relative distance between the critical and resonant aspect ratio $(\beta_C - \beta_R)/\beta_R$. For decreasing values of $(|\beta_C - \beta_R|)/\beta_R$, Vanzo *et al.* (2001) found bar wavelengths closer to the size of steady bars. Indeed, this might be another possible reason

for the observed dominance of the steady bar pattern after sediment supply termination.

8.1.4. Summary

The present numerical study focused on the response of forced steady bars to sediment supply reduction in a straight channel. Therefore, steady bars were forced by a local obstacle placed longitudinally in the middle of the channel on the orographic left side. Initially, a dynamic equilibrium was established with steady bars just downstream of the obstacle and free bars further downstream. This initial condition was used to study the effect of sediment supply reduction using various fractions of the initial equilibrium bed load transport capacity.

The present findings suggest that for decreasing sediment supply the area of influence of the steady forced bars increases in downstream and as well in upstream direction in the case of super-resonant conditions. The downstream influence, indicated by longer steady bars, was evident for $q_{b,in}/q_{b,0} \leq 0.25$ compared to the initial steady bar pattern. Finally, a non-migrating steady bar pattern in the whole channel resulted in the case of complete sediment supply termination ($q_{b,in}/q_{b,0} = 0$). Hence, the present results suggest that steady bars are not eroded due to sediment supply termination, in contrast to the observations in the laboratory experiment of Venditti *et al.* (2012).

The morphological 1-D effect changed conditions for free bar migration and for the direction of the influence of forced steady bars (downstream or upstream overdeepening) from sub-resonant to super-resonant conditions. Upstream influence of the obstacle was observed, especially in the case of complete sediment supply termination towards the end of the simulation. This is in good agreement with the linear theory of steady bars suggesting that two dimensional bed perturbations can propagate upstream in the case of super-resonant conditions (Zolezzi & Seminara, 2001).

A composite modeling approach combining linear stability theory, numerical simulations, and laboratory experiments would allow to gain further insights in river morphology response to changes in sediment supply.

8.2. Point Bar in 180° River Bend

A point bar is formed at the inner side of a river bend due to the spiral flow motion (Chap. 3.2.4). The numerical model was previously validated based on the laboratory experiments of Yen & Lee (1995) in a flume with a 180° bend. The morphology and grain sorting effects observed in the laboratory experiment were well reproduced by the numerical model (Chap. 5.2).

The aim of the present numerical study is to investigate the effect of sediment supply reduction on point bar topography and on grain sorting effects in a river bend. The topography was simplified using a 180° river bend, similar to the laboratory experiment used for validation of the numerical model. The river width, the bed slope, the bend radius, and the grain size distribution were inspired by the Reuss River below the ROR-HPP Bremgarten-Zufikon in Switzerland. Similar to the numerical studies on free and forced bars, the sediment supply was reduced starting from the equilibrium bed load transport capacity.

After the description of the numerical model setup, results are presented for uniform and non-uniform sediment. Finally, the results are compared to laboratory experiments and numerical studies from literature along with some discussion on the limits of the numerical model.

8.2.1. Numerical Model Setup

The numerical experiment was based on the situation of the Reuss River below the ROR-HPP Bremgarten-Zufikon in Switzerland. The complexity of the topography was reduced by using a 180° river bend with rectangular cross section. The main characteristics included the bend radius to the center line $R_c = 200\,\mathrm{m}$, the channel length before and after the river bend $L_c = 400\,\mathrm{m}$, the river width $W = 60\,\mathrm{m}$, and the equilibrium bed slope $S_0 = 0.002$ (Fig. 8.6). According to the ratio $R_c/W = 6.7$, the curvature of this river bend can be classified as mild to moderate (see Blanckaert, 2011).

The numerical study includes different model setups (Table 8.1). Thereby, mainly the representation of the sediment (uniform, non-uniform), the approach to determine the curvature factor (constant, dynamic), and the water discharge were investigated as described in the following.

Table 8.1.: Model setups with different sediment (U: uniform, N-U: non-uniform), curvature factor ($N_* = 7$, $N_* = f(C)$), and water discharge Q

setup	sediment		N_* [-]		Q [m^3/s]	
	U	N-U	7	$f(C)$	500	800
1	x		x		x	
2	x			x	x	
3	x		x			x
4	x			x		x
5		x	x		x	
6		x		x	x	
7		x	x			x
8		x		x		x

The model parameters were adopted from the validated model described in Chap. 5.2, unless specified differently. Bed load transport was modeled using both uniform and non-uniform sediment. In both cases, the median grain size was $d_{50} = 20.0\,\text{mm}$. However, for non-uniform sediment, the grain size distribution was idealized by a log-normal distribution with a geometric standard deviation of $\sigma_g = 2.0$ (Fig. 8.7). This results in a characteristic grain size diameter of $d_{90} = 48.6\,\text{mm}$, where 90 percent of the grain size distribution is finer. For the numerical simulations, the non-uniform sediment was represented with seven grain classes using the approach of Parker (2004). Initially, the same grain size distribution was defined for both the active layer and the sublayer. However, over the course of the simulation the active layer coarsened depending on water discharge and sediment supply. The active layer had a thickness of $L_a = 0.6\,\text{m}$ and was constant during the simulations. This is rather high with respect to the characteristic grain size d_{90} ($L_a \approx 12 d_{90}$). However, this was found to be a reasonable value, especially considering the point bar morphology and the erosion along the thalweg in the case of to sediment supply reduction. The curvature factor N_* was determined with two different approaches. The first approach considered a constant curvature factor of $N_* = 7.0$, which corresponds to a typical value for natural rivers (Engelund, 1974). The second approach, however, determined the curvature factor as a function of local bed friction ($N_* = f(C)$) according to Eq. (3.36) with $a = 1.0$.

Yalin's logarithmic friction law (Eq. 4.10) was applied using an equivalent sand

roughness $k_s = 50\,\text{mm}$ and $k_s = 2.5d_{90}$ for uniform and non-uniform sediment, respectively. For the latter, the equivalent sand roughness was locally, dynamically determined based on the actual characteristic grain size diameter d_{90} in the active layer. A constant water discharge Q was applied at upstream hydraulic boundary with $Q = 500\,\text{m}^3/\text{s}$ and $Q = 800\,\text{m}^3/\text{s}$ corresponding to flood return periods of the Reuss River at Mellingen of roughly two years and hundred years, respectively. Uniform flow was assumed at the upstream and downstream boundary starting with an initial bed slope of $S_0 = 0.002$. However, the bed slope was dynamically adjusted due to erosion at the upstream boundary. The morphological factor was set to five to accelerate the numerical simulations. The numerical time step was roughly 0.09 s based on the CFL condition. Hence, the hydraulics were computed roughly every 0.45 s, while morphology was still updated every 0.09 s. This can be justified by the steady water inflow at the upper boundary.

According to the linear stability theory, free bars instability was sub-critical ($\beta < \beta_C$) for the water discharge of Q =800 m^3/s. For the smaller discharge of Q =500 m^3/s, however, the conditions were super-critical and sub-resonant ($\beta_C < \beta < \beta_R$). For the latter, this suggests that steady bar influence is to be expected in downstream direction. It should be noted that the channel length L_c was too short to study alternate steady bars and free bars in the straight parts of the channel. However, the focus was on the point bar morphology and grain sorting effects in the river bend.

First, the initial morphology was created starting from flat bed. Thereby, specific sediment supply $q_{b,in}$ corresponded to equilibrium bed load transport capacity $q_{b,0}$ ($q_{b,in}/q_{b,0} = 1.0$). In the case of non-uniform sediment, grain sorting has already taken place in the river bend. This configuration was further used as an initial condition for simulations with reduced sediment supply. Therefore, different fractions of initial, equilibrium bed load transport capacity were used, such as $q_{b,in}/q_{b,0} = 0.75$, 0.5, 0.25, and 0.0.

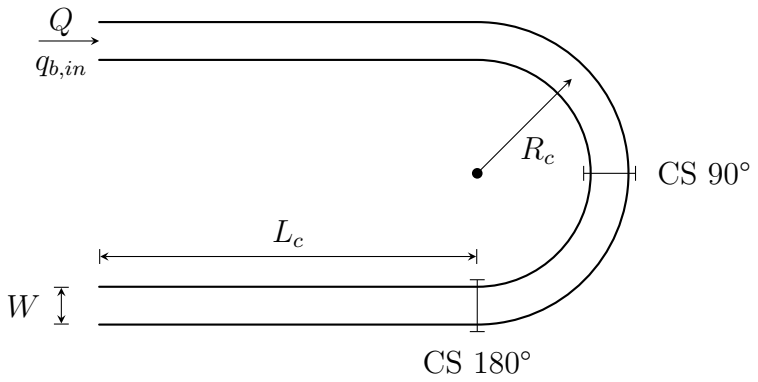

Fig. 8.6.: Definition sketch of the topography with straight section and 180° river bend

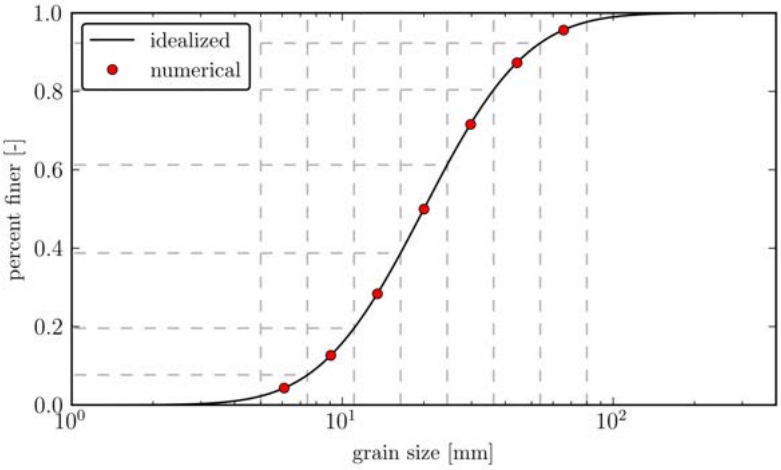

Fig. 8.7.: Idealized grain size distribution ($d_{50} = 20.0\,\text{mm}$, $\sigma_g = 2.0$) represented by seven grain size fractions for numerical simulations

8.2.2. Results

First, the simulation results using uniform sediment (setup 1-4) are reported, followed by the results using non-uniform sediment (setup 5-8). Contour plots of the bed level change for varying bed load supply are based on setup 1 and setup 5 for uniform sediment and non-uniform sediment, respectively. For the sake of completeness, however, the figures of all results are shown in the Appendix A.4. The presented results correspond to quasi equilibrium conditions, where the

relative sediment supply reduction at the outflow deviated from the relative inflow reduction by a maximum of 0.8 %.

The numerical model includes two approaches affecting the bed load transport direction. Namely, the lateral bed slope effect and the curvature effect due to the spiral flow motion in the river bend. These two processes act in opposite direction and compete against each other, until they eventually establish an equilibrium forming a point bar in the river bend. Further details on the lateral bed slope effect and curvature effect can be found in section 3.2.3 and section 3.2.4, respectively.

Uniform Sediment

Sediment supply reduction primarily leads to river bed degradation. Fig. 8.8 shows the bed elevation change Δz_b for different sediment supply rates at cross sections CS 90° and CS 180° (see Fig. 8.6 for location). The corresponding contour plots of Δz_b are depicted in Fig. 8.9. Thereby, Δz_b is normalized by the uniform approach flow depth h_0.

As sediment supply rate decreases, it seems that the river bed relief ($z_{b,max} - z_{b,min}$) almost remains the same at CS 90°, while it increases at CS 180° (Fig. 8.8). This indicates a certain shift of the point bar in downstream direction. However, the initial small over-deepening at the beginning of the bend becomes more pronounced for decreasing sediment supply. Finally, in the case of complete sediment supply termination ($q_{b,in}/q_{b,0} = 0$, Fig. 8.9), a transition of the thalweg from the inner side at the beginning of the bend towards the outer side can be observed, typically along the first half or around the apex of the bend (CS 90°).

The over-deepening at the beginning of the bend is more pronounced for the simulations with the lower discharge of $Q = 500\,\mathrm{m}^3/\mathrm{s}$ (setup 1 and 2) compared to those with the higher discharge of $Q = 800\,\mathrm{m}^3/\mathrm{s}$ (setup 3 and 4). The curvature effect on the point bar topography is stronger in the case where the curvature factor is dynamically computed based on the local Chézy friction coefficient ($N_* = f(C)$), as opposed to a constant value of $N_* = 7$. In the former case, the top of the point bar eventually slightly emerged from the water surface at CS 180° (Fig. 8.10).

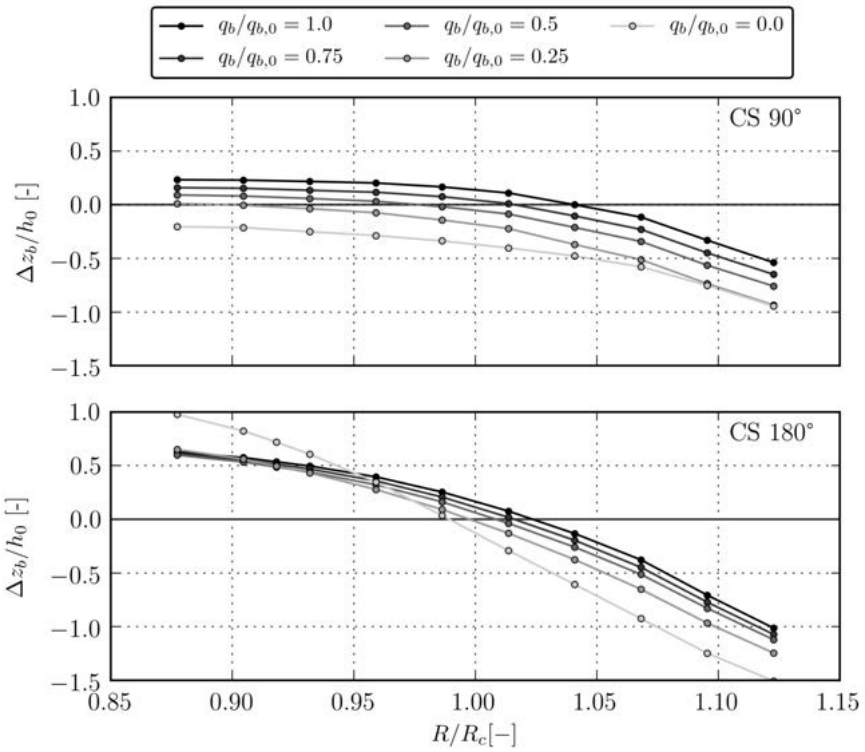

Fig. 8.8.: Bed elevation change Δz_b due to sediment supply reduction at CS 90° and CS 180°: uniform sediment, $Q = 500\,\mathrm{m}^3/\mathrm{s}$, $N_* = 7$ (setup 1)

Non-Uniform Sediment

The general model behavior using non-uniform sediment is similiar to the one with uniform sediment. The morphological changes are shown for CS 90° in Fig. 8.11a and as contour plot in Fig. 8.12. The same influence of the curvature factor and the discharge can be observed as in the case of uniform sediment. However, as expected, erosion is slightly damped in the case of non-uniform sediment. This is mainly attributed to the development of a coarser bed composition in the active layer, especially at the outer side of the bend. This effect becomes even more pronounced for lower sediment supply rates. The point bar with non-uniform sediment was formed slightly more upstream compared to the simulation using uniform sediment (e.g. compare Fig. 8.9 and Fig. 8.12). These differences can be mainly attributed to the grain sorting effects and the determination of bed shear stress based on local grain size distribution.

Fig. 8.11 shows the bed elevation change and the grain sorting effects at CS 90° for varying sediment supply. Grain sorting effects, and hence the fining and the

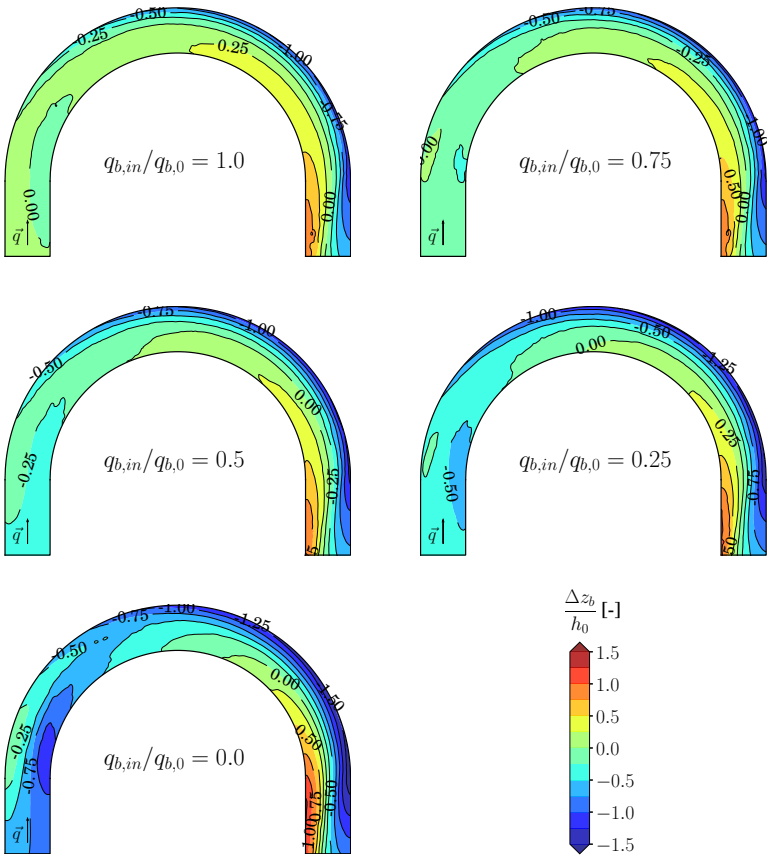

Fig. 8.9.: Bed elevation change Δz_b due to sediment supply reduction: uniform sediment, $Q = 500\,\mathrm{m}^3/\mathrm{s}$, $N_* = 7$ (setup 1)

coarsening in the active layer, are indicated by the local median grain size d_{50} normalized by the initial median grain size $d_{50,0} = 20\,\mathrm{mm}$ and are depicted as contour plot in Fig. 8.13. This shows that the bed starts to erode and coarsen from the upstream boundary due to sediment supply reduction. First, the erosion and coarsening of the river bed is more pronounced at the outer side of the bend. Obviously, bed degradation and bed coarsening are most severe in the case of complete sediment supply termination ($q_{b,in}/q_{b,0} = 0$). In this case, the coarsening of the river bed is most pronounced along the thalweg. The coarsening at the upper part of the point bar seems to start already at $q_{b,in}/q_{b,0} = 0.75$, although on a small area. More significant coarsening becomes evident for $q_{b,in}/q_{b,0} \leq 0.25$

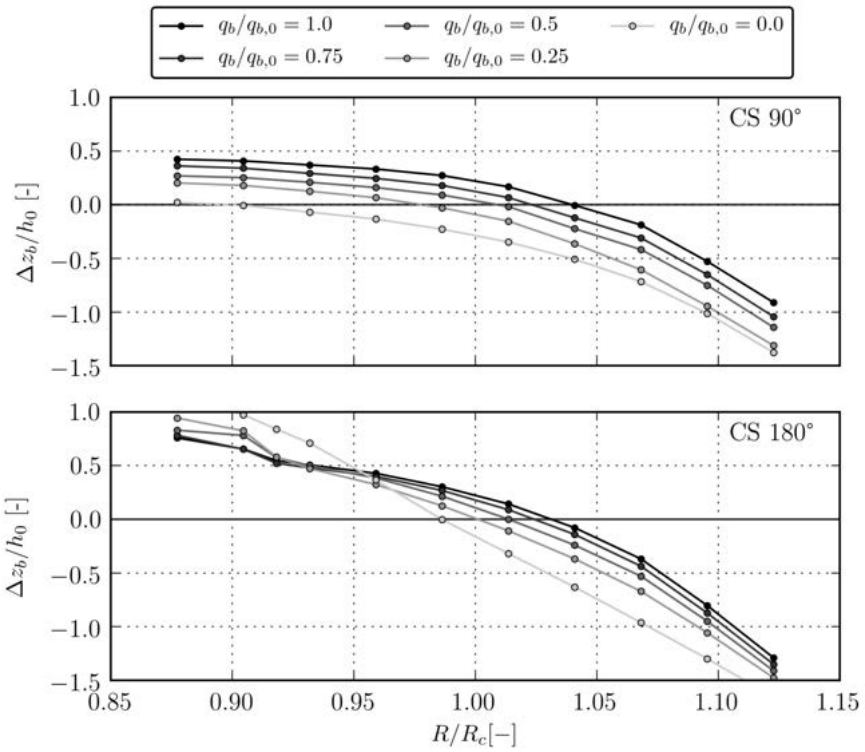

Fig. 8.10.: Bed elevation change Δz_b due to sediment supply reduction at CS 90° and CS 180°: uniform sediment, $Q = 500\,\mathrm{m}^3/\mathrm{s}$, $N_* = f(C)$ (setup 2)

also in the lower part of the point bar.

8.2.3. Discussion

The resulting topography from the numerical simulations contained some characteristic pattern of a bend in a meandering river. This pattern was getting even more pronounced for decreasing sediment supply. For instance, a typical feature of a bend in a meandering river is the course of the thalweg. The thalweg along consecutive bends usually starts at the inner side of a bend and changes over the course of the bend towards the outer side of the bend, typically around the apex (e.g. Dietrich & Smith, 1983; Eaton & Church, 2009). This pattern was particularly pronounced in the case of complete sediment supply termination (see Fig. 8.12, $q_{b,in}/q_{b,0} = 0.0$). Such a pattern, although much less pronounced, is also visible for equilibrium bed load transport ($q_{b,in}/q_{b,0} = 1.0$). At the beginning of the simulation with flat bed, this is influenced by the slightly higher flow velocities

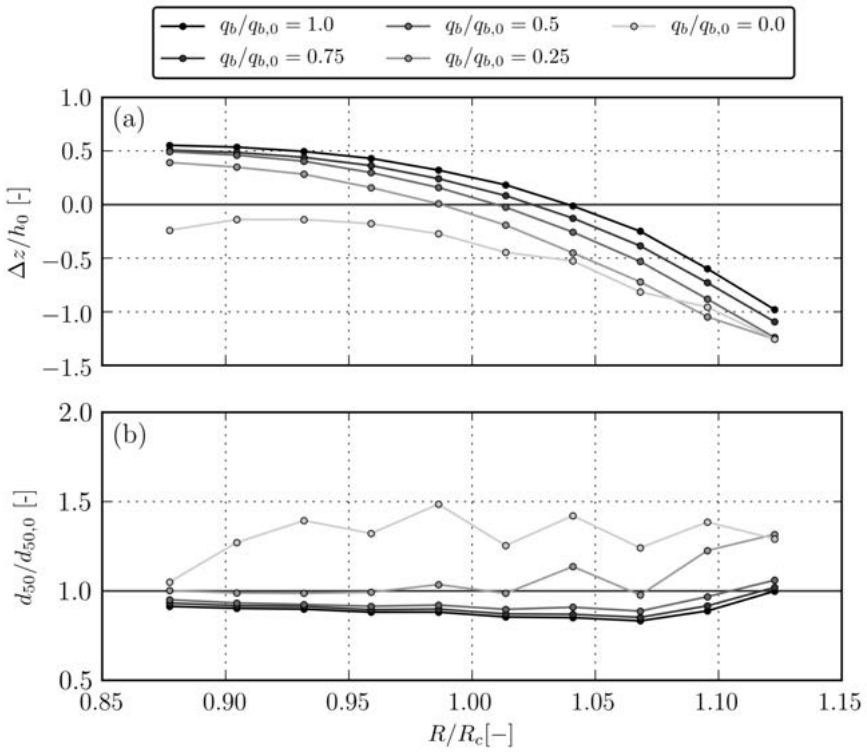

Fig. 8.11.: (a) Bed elevation change Δz_b and (b) grain sorting effect $d_{50}/d_{50,0}$ due to sediment supply reduction at CS 90°: non-uniform sediment, $Q = 500\,\mathrm{m}^3/\mathrm{s}$, $N_* = f(C)$ (setup 6)

at the inner side of the entrance of the bend compared to the outer side of the bend. Further details can be found in section 5.2, where the numerical model is validated based on the laboratory experiments of Yen & Lee (1995).

Hafner (2008) proposed a morpho-dynamic 2-D model using uniform sediment. Furthermore, he performed laboratory experiments on the self-dynamic development of two consecutive river bends with angles of 30° and 75° with erodible embankments to validate the numerical model. The most significant improvements were obtained using an equilibrium approach to account for the spiral flow motion effect on the bed load direction, similar to the approach presented here. Only minor improvements were obtained by further taking into account the development length of the curvature effect on the bed load transport direction (non-equilibrium approach) and the dispersion terms to correct the depth-averaged flow velocities due to spiral flow motion (Hafner, 2008).

In the present numerical study, grain sorting effects in the active layer developed under equilibrium bed load transport capacity. Additionally, simulations were

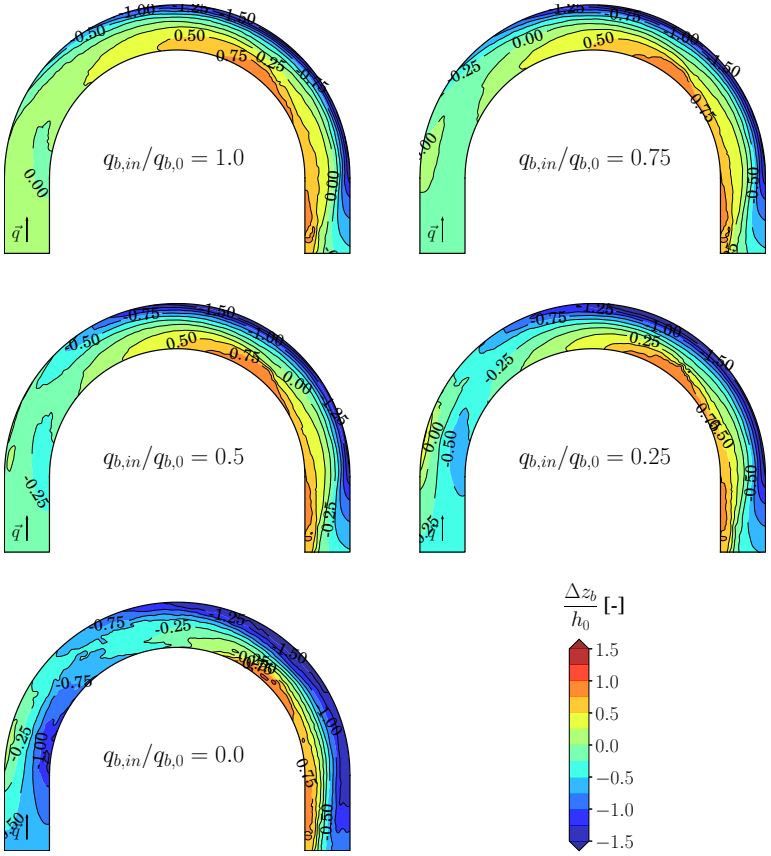

Fig. 8.12.: Bed elevation change Δz_b due to sediment supply reduction: non-uniform sediment, $Q = 500\,\mathrm{m}^3/\mathrm{s}$, $N_* = f(C)$ (setup 6)

performed with a coarser active layer, e.g. static armor, and a finer sublayer as initial condition. In this case, a significantly coarser active layer degrades into a finer substrate for reduced sediment supply. However, the simulation results for $q_{b,in}/q_{b,0} = 0.25$ showed two longitudinal streaks with higher bed elevation and a finer grain size distribution in the active layer. They started to grow from the upstream boundary and seemed to be influenced by the upper boundary condition. This behavior may indicate a potential case of ellipticity, which would require boundary conditions that depend on a future state (Stecca *et al.*, 2014). However, hyperbolic models are essential to solve the temporal evolution of state variables using initial and boundary conditions. This behavior was not further investigated

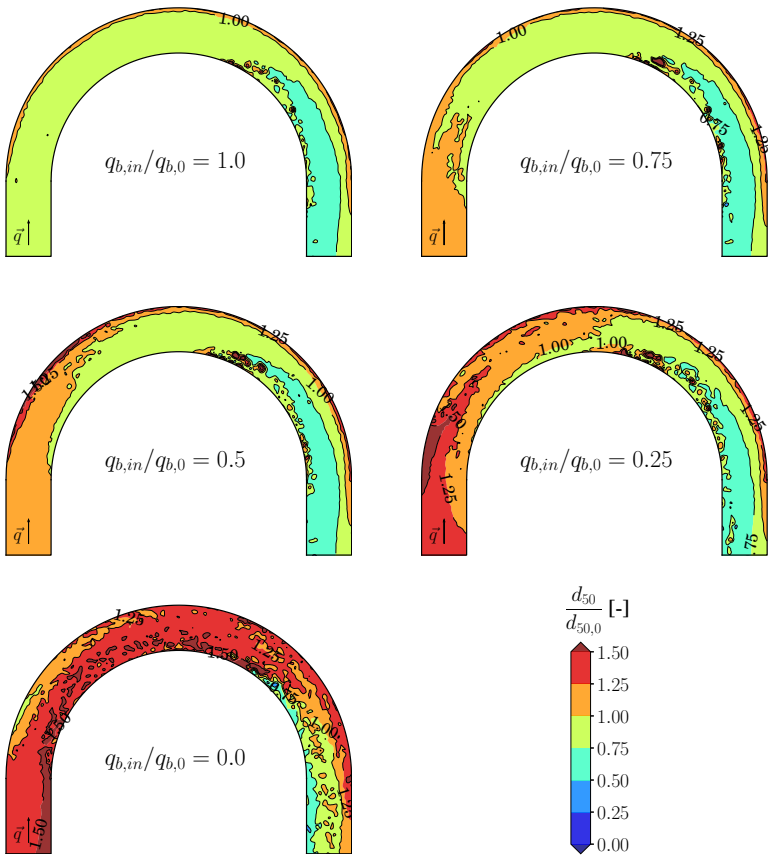

Fig. 8.13.: Grain sorting effect $d_{50}/d_{50,0}$ due to sediment supply reduction: non-uniform sediment, $Q = 500\,\mathrm{m}^3/\mathrm{s}$, $N_* = f(C)$ (setup 6)

and it should rather rise attention on this issue when using the Hirano-Exner model for such cases.

Eaton & Church (2009) performed laboratory experiments using a meandering, sinusoidal channel with non-erodible banks. Primarily, the response to sediment supply reduction was a coarsening of the bed surface texture. The bed slope was only significantly reduced beyond certain grain sorting effects. Several laboratory experiments were reported in literature investigating on the effect of sediment supply on forced steady bars in straight flumes (e.g. Venditti *et al.*, 2012; Podolak & Wilcock, 2013). In this case, however, sediment supply reduction affected both bed slope and grain sorting, e.g. coarsening of the bed surface texture. This is in

good agreement with the presented findings.

8.2.4. Summary

In a first step, the numerical model was validated based on the laboratory experiments of Yen & Lee (1995) with a 180° bend (see section 5.2). The numerical model was able to reproduce both the morphology and grain sorting effects in the flume bend with good agreement. The second step includes the investigation of the effect of sediment supply reduction on point bar morphology and grain sorting in 180° river bend described in this chapter. Thereby, the main characteristics of the Reuss River below the ROR-HPP Bremgarten-Zufikon in Switzerland were taken into account, such as bed slope, river width, grain size distribution, and bed forming discharges.

Sediment supply was reduced by applying different fractions of initial equilibrium bed load transport capacity. Bed load transport was modeled using both uniform and non-uniform sediments. In the latter case, the erosion was somewhat damped due to a coarsening of the active layer. The curvature factor, which controls the effect of spiral flow on the bed load transport direction, had a significant effect on the point bar topography. The over-deepening at the beginning of the bend was stronger for smaller discharges and reduced sediment supply.

The results suggest that sediment supply reduction affects both bed slope and grain sorting in the river bend. Bed degradation leads to a more pronounced point bar topography, especially in the lower part of the bend. The river bed surface texture coarsens due to sediment supply reduction starting from the upstream boundary. Further coarsening occurs along the outer side of the river bend and finally along the thalweg in case of complete sediment supply termination. Simulations with a dynamic curvature factor suggest that grain sorting in the upper part of the point bar, although in a small area, is already affected for minor sediment supply reduction, e.g. $q_{b,in}/q_{b,0} = 0.75$. However, further laboratory experiments are needed to better understand grain sorting effects in river bends under varying sediment supply. This would also provide valuable data for the validation of numerical models.

Even though the governing processes seemed to be reproduced fairly well by the present numerical model, it is worth to further investigate model improvements.

Clearly, the inclusion of dispersion terms would correct and improve the depth-averaged flow velocities, especially during the initial phase of the simulation with flat bed and in the second half of the 180° bend. However, it is not quite clear whether this would significantly improve the model in the case of a well developed river bend morphology. Another possible model improvement is related to the fact that the spiral flow motion in river bends generally builds up and decays over a certain distance. Such a spatial lag is taken into account with a non-equilibrium approach that includes a transport equation for the intensity of the curvature effect on the bed load transport direction (e.g. De Vriend, 1977; Struiksma *et al.*, 1985; Hafner, 2008).

River bed degradation can cause problems for infrastructure along the river, such as bridges or dykes. Degradation of bed surface texture, however, is particularly relevant for aquatic ecology, e.g. spawning ground for fish. Hence, sediment supply is of vital interest to restore gravel-bed rivers in terms of flood safety and aquatic habitat.

9. Conclusions

9.1. Effects of Sediment Supply

9.1.1. Erosion of Artificial Gravel Deposits

Sediment replenishment by artificial gravel deposits has been applied worldwide as a measure to reestablish the sediment continuum, for instance at ROR-HPPs. A composite modeling approach, combining both laboratory experiments and numerical modeling, was performed at VAW in the scope of two parallel PhD projects. Thereby, Friedl (2017) performed the laboratory experiments to gain further insights into the erosion processes of artificial gravel deposits consisting of non-uniform sediment. In the present thesis, the results of these experiments served as a basis for a detailed validation of the presented numerical model. Lateral fluvial erosion is the governing process for the degradation of artificial gravel deposits. With the numerical model the relevant approaches to successfully reproduce the involved processes were identified: (i) the gravitational bank collapse, (ii) the correction of the bed load transport direction due to lateral bed slope, and (iii) the reduction of the critical Shields stress due to local bed slope. The dynamics of the erosion process and the resulting supply rates to the downstream reach were well reproduced by the numerical model using non-uniform bed load transport. Hence, the validated model is a valuable tool for practical river engineering applications of sediment replenishment by artificial gravel deposits in gravel-bed rivers. The downstream spreading of the gravel will take place in a combination of translation and dispersion, but in most cases mainly as dispersion. The dominant mechanism and the sediment supply rate to the downstream river reach depends on the discharge (shear stress) and the volume and grain size distribution of the gravel deposit.

A large number of reported experiences and recommendations on sediment replenishment can be found in literature (see Chap. 2.1). The planning phase of sediment replenishment should ideally be based on a sediment budget estimation for the river reach of interest. Thereby, the bed load supply and the bed load transport capacity is estimated for a given hydrology. The hydrology can be based, for instance, on a typical annual duration curve and duration curves for distinctively wet and dry years. Finally, this may result in the assessment of a bed load deficit. On this basis, it will be possible to define scenarios for sediment replenishment.

From an ecological point of view, an important issue is to minimize the supply of fine sediment into the river during the placement of gravel deposits. Deposition of fines is potentially hazardous to fish egg development and may cause clogging of the river bed. For instance, fish eggs react sensitive to reduced oxygen supply. Therefore, both gravel extraction and replenishment should be performed during low flow periods without directly affecting the wetted area of the river and should consider spawning periods of the relevant fish species. The excavator should, whenever possible, not stand and operate in the river. Small dams of gravel can help to temporally disconnect side areas of the channel in order to minimize the feeding of fines into the river.

9.1.2. Response of River Morphology to Sediment Supply Reduction

In general, sediment supply has an effect on both bed slope and bed surface texture. In the case of sediment supply increase (decrease), the bed slope increases (decreases) and the bed surface will become finer (coarser) (Parker, 1990). It is not entirely clear, however, how sediment supply affects river morphology, such as alternate bars. For instance, Venditti *et al.* (2012) observed in laboratory experiments that free non-migrating bars started to migrate out of the flume after sediment supply termination. On the other hand, Lisle *et al.* (1993) observed that the top of free non-migrating bars started to emerge from the water surface after decreasing sediment supply. The study of sediment supply reduction, as opposed to sediment supply increase, is usually much more straightforward to implement for both numerical and experimental modeling. In the case of sediment supply

increase to an equilibrium bed slope, a sediment wedge with locally increased bed slope translates or disperses (or a combination of both) downstream until the bed slope in the flume adapts to the increased sediment supply. Obviously, the process of sediment supply decrease is not exactly the reversal process of sediment supply increase. Nevertheless, the governing processes of these two approaches are not completely different, such as the effect of sediment supply on the equilibrium bed slope (morphological 1-D effect). In the present thesis, the case of sediment supply reduction was studied by means of numerical simulations using constant discharge. Thereby, the focus was on migrating free bars, steady forced bars, and a point bar in a river bend. These morphological patterns can be frequently found in many confined gravel-bed rivers.

Free Migrating Bars

The linear stability theory for free bars (Colombini *et al.*, 1987; Adami *et al.*, 2016b) served as a valuable tool to plan the numerical model setup and predict the influence of free bar instability for reduced equilibrium bed slope. The starting point for the numerical experiments was a free bar morphology in a straight channel with equilibrium bed load transport capacity $q_{b,0}$. At this state, conditions were super-critical and sub-resonant ($\beta_C < \beta < \beta_R$). The sediment supply $q_{b,in}$ was then decreased using different fractions of equilibrium bed load transport capacity.

The sediment supply affects both the bed slope and the bed load transport within a river reach (morphological 1-D effect). As a consequence, the governing parameters adapt accordingly, such as the Shields stress, the relative grain roughness, and the aspect ratio. This morphological 1-D effect potentially affects free bar properties, such as bar wavelength, bar amplitude, and bar celerity (2-D effects). The results suggest that only a major morphological 1-D effect has a significant impact on 2-D effects. Indeed, a sediment supply reduction of less than fifty percent had no significant effect on relevant free bar properties, while for sediment supply of $0.125 \leq q_{b,in}/q_{b,0} \leq 0.25$ bar amplitude and wavelength slightly increased. Eventually, the top of the bars started to emerge from the water surface for very low sediment supply $q_{b,in}/q_{b,0} \leq 0.0625$. As a result, the bar wavenumber decreased to values typically found for forced steady bars ($\lambda \approx 0.15$). Furthermore, the bar amplitude increased and the bar celerity vanished, resulting

in a non-migrating free bar pattern. The morphological 1-D effect caused the relative distance to the critical aspect ratio $(\beta - \beta_C)/\beta_C$ to increase suggesting an increase of the bar amplitude. The transition from sub-resonant to super-resonant conditions indicates increasing bar wavelength, decreasing bar celerity, and upstream influence of two-dimensional bed perturbations.

Forced Steady Bars

The numerical study on the effect of sediment supply on steady forced bars was performed using a similar setup as in the case of free bars. The only difference was that steady bars were forced due to a local obstacle. After creating an initial morphology with forced bars below the obstacle and free bars further downstream using an equilibrium bed load transport capacity $q_{b,0}$, the sediment supply $q_{b,in}$ was decreased using different fractions of $q_{b,0}$.

The results suggest that the forced steady bars increase in wavelength and amplitude for decreasing sediment supply. A non-migrating steady bar pattern in the whole channel resulted in the case of complete sediment supply termination ($q_{b,in}/q_{b,0} = 0$). Hence, forced steady bars were not eroded due to complete sediment supply termination, as opposed to the observation in the laboratory experiment of Venditti *et al.* (2012). In agreement with the latter, however, the first bar just below the obstacle emerged from the water surface. Moreover, the numerical simulations suggest that the bar wavelength becomes slightly larger. Hence, the presented findings might provide new insights into observations from laboratory experiments on forced bars response to sediment supply reduction.

Point Bar in River Bend

The effect of sediment supply reduction on a point bar in a river bend was studied using a simplified 180° bend. Thereby the focus is on morphological changes and grain sorting effects. The river bend and sediment characteristics were inspired by the River Reuss below the ROR-HPP Bremgarten-Zufikon in Switzerland. First, an initial morphology with a point bar in the bend was created using equilibrium bed load transport capacity $q_{b,0}$. Then, the sediment supply $q_{b,in}$ was decreased using different fractions of $q_{b,0}$, similar to the studies

on free and forced steady bars. The results suggest that the erosion along the thalweg and the resulting relief in the bend are getting more pronounced as sediment supply decreases, especially in the lower part of the bend. In the case of complete sediment supply termination, there is a certain shift of the point bar in downstream direction and more pronounced over-deepening at the beginning of the bend. This results in a path of the thalweg as typically found for bends of meandering rivers. In return, grain sorting effects start to coarsen the active layer, first in the upper straight channel and finally also at the outer side of the river bend, especially for $q_{b,in}/q_{b,0} \leq 0.5$. In the case of complete sediment supply termination, however, the effect of grain sorting was most pronounced along the thalweg. Moreover, major parts of the river bend were significantly coarser ($1.0 \leq d_{50}/d_{50,0} \leq 1.75$) compared to the initial state at equilibrium sediment supply ($0.75 \leq d_{50}/d_{50,0} \leq 1.25$). Grain sorting in the upper part of the point bar seems to be affected already for minor sediment supply reduction, as opposed to the lower part of the point bar, which is most significantly affected due to complete sediment supply reduction.

9.2. Sediment Replenishment in the Context of River Restoration

Over the last centuries, river training works laterally restricted many gravel-bed rivers by non-erodible embankments. In such cases, sediment replenishment can be expected to mainly affect bed slope and bed surface texture through grain sorting effects. However, sediment replenishment as a single measure is unlikely to trigger morphological changes, such as turning a flat river bed morphology ($\beta < \beta_C$) into a free migrating bar pattern ($\beta > \beta_C$). However, the effect of sediment supply increase on free bars ($\beta > \beta_C$) remains an open research topic.

In general, sediment replenishment primarily leads to deposition along the thalweg (morphological 1-D effect). Furthermore, sediment replenishment affects bed surface texture especially in the case of forced bars, such as point bars in river bends. However, no significant morphological changes can be expected, as the point bar is forced by the river bend. If only sediment supply is increased, it might be that this sediment is transported through a river channel with high bed load transport capacity without any significant morphological impact. However,

sediment replenishment is still a viable measure to locally improve aquatic habitat, especially in the case of interrupted sediment continuity, such as below ROR-HPPs. In summary therefore, in most cases, river morphology would rather improve by increasing the aspect ratio, and hence the river width, for which significant bed load transport can be expected over a wide range of discharge ($\beta > \beta_C$ for $\theta >> \theta_C$). In most cases, even a small increase of the river width could lead to morphological structures, such as free bars ($m = 1$). A rough estimate on the current state and the potential for the development of free bars for selected Swiss gravel-bed rivers is given in Appendix A.5.

The reestablishment of the sediment continuum is an integral part within the context of river restoration. An objective-based strategy for river restoration, as opposed to a reference-based strategy, places the focus onto a clearly defined and achievable goal (Dufour & Piégay, 2009). Very often, it is not possible to define a clear reference state of a river due to very limited data and manifold external influences, such as river training measures of the past, land use changes, and climatic changes. Within an objective-oriented strategy, however, the reestablishment of the sediment continuum is an important objective along with, for instance, the increase of the river width, habitat variability, flood protection, and use of riverine resources (e.g. energy production). The objectives should be well defined in order to plan and to perform a meaningful and continuous monitoring. This ensures the tracking of the trajectory towards an improved state and the intervention in time if necessary. The optimization of all objectives must include all stakeholders in order to gain wide-spread acceptance.

9.3. Outlook

With regard to the future development of the numerical 2-D model of BASEMENT two particular features would help to improve morphodynamic simulations of rivers with bends and meanders. First, additional dispersion terms in the momentum equations would improve the lateral distribution of the depth-averaged flow velocity in the river bend, especially in the case of a flat bed. However, it must be ensured not to over-estimate this effect in case of well developed river bend morphology (Blanckaert, 2005). The second feature is related to the effect of spiral flow motion on the bed load transport direction. The presented equilibrium

approach can be extended to a non-equilibrium approach to account for the development and the decay of the spiral flow intensity over a certain distance (spatial lag).

Concerning the effect of sediment supply on river morphology, there is still substantial research potential. Continuing research using a composite model approach combining linear stability theory, numerical modeling, and laboratory experiments would allow to gain further insights to river morphological response to sediment supply reduction. Ideally, linear stability theory is used to plan the model setup and to predict numerical and experimental results. Then, the next step consists in the analysis of non-linear effects using numerical simulations, for instance, to study the competition of morphological 1-D and 2-D effects and additionally the effect of non-uniform sediments. Finally, selected aspects can be studied by means of laboratory experiments. This would allow to investigate, for instance, the transformation process into non-migrating steady bar pattern, the emergence of bars, and the influence of grain sorting effects in more detail. Further emphasis should be placed on the effect of sediment supply increase on free non-migrating bar pattern. This would allow to study, for instance, the re-transformation (reversal process) of the free non-migrating bar pattern, obtained in the numerical free bar simulation for complete sediment supply termination, to a migrating free bar pattern.

In the context of sediment replenishment for a specific river, further focus should be placed on the effect of the hydrology and its implications on the sediment replenishment, on the temporal time scales, and on the amount of sediments required to reach predefined objectives. The development of a coherent concept for sediment supply considering all riverine aspects is necessary to ensure ecological improvement and acceptance by all stakeholders.

Bibliography

Abderrezzak, K. E. K., Moran, A. D., Tassi, P., Ata, R. & Hervouet, J.-M. (2016). Modelling river bank erosion using a 2d depth-averaged numerical model of flow and non-cohesive, non-uniform sediment transport. *Advances in Water Resources*, 93, Part A: 75–88.

Ackers, P. & White, W. R. (1973). Sediment transport: New approach and analysis. *Journal of the Hydraulics Division*, 99(HY11): 2041–2060.

Adami, L. (2016). *Long term morphodynamics of alternate bars in straightened rivers: a multiple perspective*. PhD thesis, University of Trento, Department of Civil, Environmental and Mechanical Engineering.

Adami, L., Bertoldi, W. & Zolezzi, G. (2016a). Multidecadal dynamics of alternate bars in the alpine rhine river. *Water Resources Research*, 52(11): 8938–8955.

Adami, L., Redolfi, M., Zolezzi, G. & Tubino, M. (2016b). TREMTO: Theoretical RivEr Morphodynamic TOol.

Albertson, L. K., Cardinale, B. J., Zeug, S. C., Harrison, L. R., Lenihan, H. S. & Wydzga, M. A. (2011). Impacts of channel reconstruction on invertebrate assemblages in a restored river. *Restoration Ecology*, 19(5): 627–638.

Andrews, E. (1983). Entrainment of gravel from naturally sorted riverbed material. *Geological Society of America Bulletin*, 94(10): 1225–1231.

Asahi, K., Shimizu, Y., Nelson, J. & Parker, G. (2013). Numerical simulation of river meandering with self-evolving banks. *Journal of Geophysical Research - Earth Surface*, 118(4): 2208–2229.

Ashida, K. & Michiue, M. (1972). Study on hydraulic resistance and bedload transport rate in alluvial streams (in Japanese). *Transcript of JSCE (Japan Society of Civil Engineering)*, 206: 59–69.

Baar, A. W., de Smit, J., Uijttewaal, W. S. J. & Kleinhans, M. G. (2018). Sediment transport of fine sand to fine gravel on transverse bed slopes in rotating annular flume experiments. *Water Resources Research*.

Bagnold, R. (1966). An approach to the sediment transport problem. *General Physics Geological Survey, Prof. paper*.

Bathurst, J., Thorne, C. & Hey, R. (1977). Direct measurements of secondary currents in river bends. *Nature*, 269: 504–506.

Begnudelli, L., Valiani, A. & Sanders, B. F. (2010). A balanced treatment of secondary currents, turbulence and dispersion in a depth-integrated hydrodynamic and bed deformation model for channel bends. *Advances in Water Resources*, 33(1): 17 – 33.

Bernini, A., Caleffi, V. & Valiani, A. (2009). 7. In G. H. S. Smith, J. L. Best, C. S. Bristow, & G. E. Petts (Eds.), *Numerical Modelling of Alternate Bars in Shallow Channels*, 153–175. Blackwell Publishing Ltd.

Blanckaert, K. (2005). Discussion of investigation on the stability of two-dimensional depth-averaged models for bend-flow simulation by t. y. hsieh and j. c. yang. *Journal of Hydraulic Engineering*, 131(7): 625–628.

Blanckaert, K. (2011). Hydrodynamic processes in sharp meander bends and their morphological implications. *Journal of Geophysical Research: Earth Surface*, 116(F1). F01003.

Blondeaux, P. & Seminara, G. (1985). A unified bar-bend theory of river meanders. *Journal of Fluid Mechanics*, 157: 449–470.

Buffington, J., Jordan, C., Merigliano, M., Peterson, J. & Stalnaker, C. (2014). Review of the Trinity River Restoration Program following phase 1, with emphasis on the program′s channel rehabilitation strategy. Trinity River Restoration Program.

Buffington, J. M. & Montgomery, D. R. (1997). A systematic analysis of eight decades of incipient motion studies, with special reference to gravel-bedded rivers. *Water Resources Research*, 33(8): 1993–2029.

Buffington, J. M. & Montgomery, D. R. (1998). Correction to "a systematic

analysis of eight decades of incipient motion studies, with special reference to gravel-bedded rivers". *Water Resources Research*, 34(1): 157.

Bui, M. D. & Rutschmann, P. (2010). Numerical modelling of non-equilibrium graded sediment transport in a curved open channel . *Computers & Geosciences*, 36(6): 792–800.

Bunte, K. (2004). State of the science review gravel mitigation and augmentation below hydroelectric dams: A geomorphological perspective. prepared for stream systems technology center. Engineering Research Center, Colorado State University, Fort Collins, Colorado.

Callander, R. A. (1969). Instability and river channels. *Journal of Fluid Mechanics*, 36(3): 465–480.

Cancienne, R. M., Fox, G. A. & Simon, A. (2008). Influence of seepage undercutting on the stability of root-reinforced streambanks. *Earth Surface Processes and Landforms*, 33(11): 1769–1786.

Chen, X., Ma, J. & Dey, S. (2010). Sediment transport on arbitrary slopes: simplified model. *Journal of Hydraulic Engineering-ASCE*, 136(5): 311–317.

Cheng, N.-S. (2016). Representative grain size and equivalent roughness height of a sediment bed. *Journal of Hydraulic Engineering*, 142(1): 06015016.

Chiew, Y. M. & Parker, G. (1994). Incipient sediment motion on non-horizontal slopes. *Journal of Hydraulic Research*, 32(5): 649–660.

Choi, S.-U. & Joung, Y. (2012). Numerical prediction of morphological change of straight trapezoidal open-channel. *Journal of Hydro-environment Research*, 6(2): 111–118. Special Issue on Ecohydraulics: Recent Research and Applications.

Colombini, M., Seminara, G. & Tubino, M. (1987). Finite-amplitude alternate bars. *Journal of Fluid Mechanics*, 181: 213–232.

Crosato, A. & Mosselman, E. (2009). Simple physics-based predictor for the number of river bars and the transition between meandering and braiding. *Water Resources Research*, 45(3): W03424.

Crosato, A., Mosselman, E., Beidmariam Desta, F. & Uijttewaal, W. S. J. (2011).

Experimental and numerical evidence for intrinsic nonmigrating bars in alluvial channels. *Water Resources Research*, 47(3): W03511.

Cui, Y., Parker, G., Lisle, T. E., Gott, J., Hansler-Ball, M. E., Pizzuto, J. E., Allmendinger, N. E. & Reed, J. M. (2003a). Sediment pulses in mountain rivers: 1. Experiments. *Water Resources Research*, 39(9): 1239.

Cui, Y., Parker, G., Pizzuto, J. E. & Lisle, T. E. (2003b). Sediment pulses in mountain rivers: 2. Comparison between experiments and numerical predictions. *Water Resources Research*, 39(9): 1240.

D., V., L., A., A., S., G., Z. & D.F., V. (2017). The role of numerical diffusion in river alternate bar simulations. Proc. *RCEM 2017, 10th Symposium on River, Coastal and Estuarine Morphodynamics, Trento-Padova, 15-22 September, Book of Abstracts*, L. S., R. M., & Z. G. (Eds.), number ISBN: 978-88-8443-752-5 : 253.

Darby, S. E., Alabyan, A. M. & Van de Wiel, M. J. (2002). Numerical simulation of bank erosion and channel migration in meandering rivers. *Water Resources Research*, 38(9): 1163.

Darby, S. E., Gessler, D. & Thorne, C. R. (2000). Computer program for stability analysis of steep, cohesive riverbanks. *Earth Surface Processes and Landforms*, 25(2): 175–190.

Darby, S. E. & Thorne, C. R. (1996). Development and testing of riverbank-stability analysis. *Journal of Hydraulic Engineering-ASCE*, 122(8): 443–454.

De Vriend, H. J. (1977). A mathematical model of steady flow in curved shallow channels. *Journal of Hydraulic Research*, 15(1): 37–54.

Defina, A. (2003). Numerical experiments on bar growth. *Water Resources Research*, 39(4): 1092.

Dey, S. (2001). Experimental studies on incipient motion of sediment particles on generalized sloping fluvial beds. *Journal of Sediment Research*, 16(3): 391–398.

Dey, S. (2003). Threshold of sediment motion on combined transverse and longitudinal sloping beds. *Journal of Hydraulic Research*, 41(4): 405–415.

Dietrich, W. E. & Smith, J. D. (1983). Influence of the point bar on flow through curved channels. *Water Resources Research*, 19(5): 1173–1192.

Diplas, P. (1990). Characteristics of self-formed straight channels. *Journal of Hydraulic Engineering*, 116(5): 707–728.

Downs, P. W., Singer, M. S., Orr, B. K., Diggory, Z. E. & Church, T. C. (2011). Restoring ecological integrity in highly regulated rivers: The role of baseline data and analytical references. *Environmental Management*, 48(4): 847–864.

Duan, J. G. & Julien, P. Y. (2010). Numerical simulation of meandering evolution. *Journal of Hydrology*, 391: 34–46.

DuBoys, M. (1879). Etudes du regime et l'action exercée par les eaux sur un lit a fond de graviers indefinement affouilable. *Annals des Ponts et Chaussées*, 5: 141–195.

Dufour, S. & Piégay, H. (2009). From the myth of a lost paradise to targeted river restoration: forget natural references and focus on human benefits. *River Research and Applications*, 25(5): 568–581.

East, A. E., Pess, G. R., Bountry, J. A., Magirl, C. S., Ritchie, A. C., Logan, J. B., Randle, T. J., Mastin, M. C., Minear, J. T., Duda, J. J., Liermann, M. C., McHenry, M. L., Beechie, T. J. & Shafroth, P. B. (2015). Large-scale dam removal on the Elwha River, Washington, USA: River channel and floodplain geomorphic change. *Geomorphology*, 228: 765 – 786.

Eaton, B. C. & Church, M. (2009). Channel stability in bed load-dominated streams with nonerodible banks: Inferences from experiments in a sinuous flume. *Journal of Geophysical Research: Earth Surface*, 114(F1): F01024.

Eekhout, J. P. C., Hoitink, A. J. F. & Mosselman, E. (2013). Field experiment on alternate bar development in a straight sand-bed stream. *Water Resources Research*, 49(12): 8357–8369.

Egiazaroff, I. (1965). Calculation of nonuniform sediment concentrations. *Journal of Hydraulic Division ASCE*, 91(4): 225–247.

Einstein, H. A. (1936). *Der Geschiebetrieb als Wahrscheinlichkeitsproblem*. PhD thesis, ETH Zurich.

Einstein, H. A. (1950). The Bed-Load Function for Sediment Transportation in Open Channel Flows. technical bulletin no. 1026 United States Departement of Agriculture, Washington, D.C.

Elgueta-Astaburuaga, M. A. & Hassan, M. A. (2017). Experiment on temporal variation of bed load transport in response to changes in sediment supply in streams. *Water Resources Research*, 53(1): 763–778.

Elkins, E. M., Pasternack, G. B. & Merz, J. E. (2007). Use of slope creation for rehabilitating incised, regulated, gravel bed rivers. *Water Resources Research*, 43(5).

Engelund, F. (1974). Flow and bed topography in channel bends. *Journal of the Hydraulics Division ASCE*, 100(11): 1631–1648.

Engelund, F. & Hansen, E. (1972). A Monograph on Sediment Transport in Alluvial Streams. *Teknisk Forlag, Copenhagen.*

Faeh, R. (1997). *Numerische Simulation der Strömung in offenen Gerinnen mit beweglicher Sohle ('Numerical simulation of open channel flow with mobile bed').* PhD thesis, VAW Mitteilungen 153 (D. Vischer, ed.), ETH Zurich (in German).

Fischer-Antze, T., Ruether, N., Olsen, N. R. & Gutknecht, D. (2009). Three-dimensional (3d) modeling of non-uniform sediment transport in a channel bend with unsteady flow. *Journal of Hydraulic Research*, 47(5): 670–675.

Friedl, F. (2017). Laboratory Experiments on Sediment Replenishment in Gravel-Bed Rivers. VAW Mitteilungen 245 (R. M. Boes, Ed.) Laboratory of Hydraulics, Hydrology and Glaciology (VAW), ETH Zurich.

Friedl, F., Weitbrecht, V. & Boes, R. (2016). Physical experiments on gravel deposit erosion. Proc. *Proc. of 13th International Symposium on River Sedimentation (ISRS 2016), September 19 - 22, Stuttgart, Germany.*

Friedl, F., Weitbrecht, V. & Boes, R. M. (2018). Erosion pattern of artificial gravel deposits. *International Journal of Sediment Research*, 33(1): 57–67.

Gaeuman, D. (2014). High-flow gravel injection for constructing designed in-channel features. *River Research and Applications*, 30(6): 685–706.

Ghobadian, R. & Mohammadi, K. (2011). Simulation of subcritical flow pattern

in 180 degree uniform and convergent open-channel bends using ssiim 3-d model. *Water Science and Engineering*, 4(3): 270–283.

Graf, H. W. (1971). Hydraulics of Sediment Transport. *McGraw-Hill*.

Guan, M., Wright, N. G., Sleigh, P. A., Ahilan, S. & Lamb, R. (2016). Physical complexity to model morphological changes at a natural channel bend. *Water Resources Research*, 52(8): 6348–6364.

Habersack, H. & Doppler, C. (2011). Sediment management along rivers in Austria. Proc. *Presentation at International Workshop on Sediment Transport, Platform Water Management in the Alps of the Alpine Conference, 2011, December 16th, Vienna*.

Hafner, T. (2008). *Uferrückbau und eigendynamische Gewässerentwicklung - Aspekte der Modellierung und Abschätzungsmöglichkeiten in der Praxis ('River embankment restoration and self-dynamic river widening')*. PhD thesis, TU München, Germany (in German).

Hasegawa, K. (1981). Bank erosion discharge based on a non-equilibrium theory. *Transactions of JSCE*, 316: 37–50.

Hirano, M. (1971). River bed degradation with armouring. *Proceedings of Jpn. Soc. Civ. Eng (JSCE)*, 195(11): 55–65.

Humphries, R., Venditti, J. G., Sklar, L. S. & Wooster, J. K. (2012). Experimental evidence for the effect of hydrographs on sediment pulse dynamics in gravel-bedded rivers. *Water Resources Research*, 48: W01533.

Hunziker, R. (1995). Fraktionsweiser Geschiebetransport. VAW Mitteilungen 138 (D. Vischer, ed.) Laboratory of Hydraulics, Hydrology and Glaciology (VAW), ETH Zurich.

Ikeda, S. (1981). Self-formed straight channels in sandy beds. *Journal of the Hydraulics Division-ASCE*, 107(4): 389–406.

Ikeda, S. (1982a). Incipient motion of sand particles on side slopes. *Journal of the Hydraulics Division-ASCE*, 108(1): 95–114.

Ikeda, S. (1982b). Lateral bed-load transport on side slopes. *Journal of the Hydraulics Division-ASCE*, 108(11): 1369–1373.

Ikeda, S. (1982c). Prediction of alternate bar wavelength and height. *Journal of Hydraulic Engineering*, 110(4): 371–386.

Ikeda, S. (1984). Lateral bed-load transport on side slopes - Closure. *Journal of Hydraulic Engineering-ASCE*, 110(2): 200–202.

Ikeda, S. (1988). 13, lateral bed load transport on side slopes. In N. Cheremisinoff, Paul, P. Cheremisinoff, Nicholas, & L. Cheng, Su (Eds.), *Civil Engineering Practice 2 - Hydraulics/Mechanics*, 299–307. Technomic Publishing Company, Inc.

Ikeda, S., Parker, G. & Kimura, Y. (1988). Stable width and depth of straight gravel rivers with heterogeneous bed materials. *Water Resources Research*, 24(5): 713–722.

Iwasaki, T., Shimizu, Y. & Kimura, I. (2016). Sensitivity of free bar morphology in rivers to secondary flow modeling: Linear stability analysis and numerical simulation. *Advances in Water Resources*, 92: 57–72.

Izumi, N., Kovacs, A., Parker, G. & P., L. D. (1991). Experimental and theoretical studies of bank erosion in rivers and its prevention by low-cost means. University of Minnesota, St. Anthony Falls Hydraulic Laboratory.

Jäggi, M. (1983). Alternierende Kiesbänke. VAW Mitteilungen 62 (D. Vischer, ed.) Laboratory of Hydraulics, Hydrology and Glaciology (VAW), ETH Zurich.

Jäggi, M. (1984). Formation and effects of alternate bars. *Journal of Hydraulic Engineering*, 110(2): 142–156.

Jang, C. & Shimizu, Y. (2005). Numerical simulations of the behavior of alternate bars with different bank strengths. *Journal of Hydraulic Research*, 43(6): 596–612.

Johannesson, H. & Parker, G. (1989). Linear theory of river meanders. *River Meandering, Water Resources Monograph, American Geophysical Union*, 12: 181–214.

Kikkawa, H., Kitagawa, A. & Ikeda, S. (1976). Flow and bed topography in curved open channels. *Journal of the Hydraulics Division*, 102(9): 1327–1342.

Koch, F. & Flokstra, C. (1981). Bed level computations for curved alluvial channels. Proc. *Proceedings XIX IAHR congress, New Delhi, India*.

Kondolf, G. M., Angermeier, P. L., Cummins, K., Dunne, T., Healey, M., Kimmerer, W., Moyle, P. B., Murphy, D., Patten, D., Railsback, S., Reed, D. J., Spies, R. & Twiss, R. (2008). Projecting cumulative benefits of multiple river restoration projects: An example from the Sacramento-San Joaquin river system in California. *Environmental Management*, 42(6): 933–945.

Kondolf, M. G. (1997). Hungry water: Effects of dams and gravel mining on river channels. *Environmental Management*, 21(4): 533–551.

Kondolf, M. G. & Minear, T. J. (2004). Coarse sediment augmentation on the Trinity River below Lewiston Dam: Geomorphic perspectives and review of past projects. prepared for trinity river restoration program. College of Environmental Design, University of California, Berkeley.

Kovacs, A. & Parker, G. (1994). A new vectorial bedload formulation and its application to the time evolution of straight river channels. *Journal of Fluid Mechanics*, 267: 153–183.

Krause, A. F. (2012). History of mechanical sediment augmentation and extraction on the trinity river, california, 1912-2011. *Technical Report* tr-trrp-2012-2 (revised), Bureau of Reclamation, Trinity River Restoration Program, Weaverville, California.

Lamb, M. P., Dietrich, W. E. & Venditti, J. G. (2008). Is the critical Shields stress for incipient sediment motion dependent on channel-bed slope? *Journal of Geophysical Research - Earth Surface*, 113(F2).

Langendoen, E. J. & Alonso, C. V. (2008). Modeling the evolution of incised streams: I. Model formulation and validation of flow and streambed evolution components. *Journal of Hydraulic Engineering-ASCE*, 134(6): 749–762.

Lanzoni, S. (2000a). Experiments on bar formation in a straight flume: 1. uniform sediment. *Water Resources Research*, 36(11): 3337–3349.

Lanzoni, S. (2000b). Experiments on bar formation in a straight flume: 2. graded sediment. *Water Resources Research*, 36(11): 3351–3363.

Lanzoni, S. & Tubino, M. (1999). Grain sorting and bar instability. *Journal of Fluid Mechanics*, 393: 149–174.

Lisle, T. E. (1989). Sediment transport and resulting deposition in spawning gravels, north coastal california. *Water Resources Research*, 25(6): 1303–1319.

Lisle, T. E., Cui, Y., Parker, G., Pizzuto, J. E. & Dodd, A. M. (2001). The dominance of dispersion in the evolution of bed material waves in gravel-bed rivers. *Earth Surface Processes and Landforms*, 26(13): 1409–1420.

Lisle, T. E., Iseya, F. & Ikeda, H. (1993). Response of a channel with alternate bars to a decrease in supply of mixed-size bed-load - A flume experiment. *Water Resources Research*, 29(11): 3623–3629.

Lisle, T. E. & Lewis, J. (1992). Effects of sediment transport on survival of salmonid embryos in a natural stream - A simulation approach. *Canadian Journal of Fisheries and Aquatic Sciences*, 49(11): 2337–2344.

Lisle, T. E., Pizzuto, J. E., Ikeda, H., Iseya, F. & Kodama, Y. (1997). Evolution of a sediment wave in an experimental channel. *Water Resources Research*, 33(8): 1971–1981.

Luque, R. F. & Van Beek, R. (1976). Erosion and transport of bed-load sediment. *Journal of Hydraulic Research*, 14(2): 127–144.

Madej, M. A., Sutherland, D. G., Lisle, T. E. & Pryor, B. (2009). Channel responses to varying sediment input: A flume experiment modeled after redwood creek, california. *Geomorphology*, 103(4): 507–519.

Major, J., O'Connor, J., Podolak, C., Keith, M., Grant, G., Spicer, K., Pittman, S., Bragg, H., Wallick, J., Tanner, D., Rhode, A. & Wilcock, P. (2012). Geomorphic response of the sandy river, oregon, to removal of marmot dam. *U.S. Geological Survey Professional Paper*, 1792: 64.

Marti, C. (2006). Morphologie von verzweigten Gerinnen–Ansätze zur Abfluss-, Geschiebetransport- und Kolktiefenberechnung ('Morphology of braided rivers–approaches to estimate discharge, bed load, and scour depth'). VAW Mitteilungen 199 (H.-E. Minor, ed.) Laboratory of Hydraulics, Hydrology and Glaciology (VAW), ETH Zurich (in German).

McBain and Trush (2004). Coarse sediment management plan for the lower

tuolumne river. prepared for the tuolumne river technical advisory committee, turlock and modesto irrigation districts, usfws anadromous fish restoration program and california bay-delta authority. McBain and Trush, Inc., Arcata, California.

Merz, J. E. & Chan, L. O. K. (2005). Effects of gravel augmentation on macroinvertebrate assemblages in a regulated california river. *River Research and Applications*, 21: 61–74.

Meyer-Peter, E. & Müller, R. (1948). Formulas for bed-load transport. Proc. *Proceedings of the 2nd Meeting of the International Association of Hydraulic Structures Research (IAHSR), Appendix 2, Sweden, Stockholm* : 39–64.

Midgley, T. L., Fox, G. A. & Heeren, D. M. (2012). Evaluation of the bank stability and toe erosion model (bstem) for predicting lateral retreat on composite streambanks. *Geomorphology*, 145-146: 107–114.

Mosselman, E. (1998). Morphological modelling of rivers with erodible banks. *Hydrological Processes*, 12(8): 1357–1370.

Mosselman, E. & Le, T. B. (2016). Five common mistakes in fluvial morphodynamic modeling. *Advances in Water Resources*, 93, Part A: 15–20. Numerical modelling of river morphodynamics.

Nagata, N., Hosoda, T. & Muramoto, Y. (2000). Numerical analysis of river channel processes with bank erosion. *Journal of Hydraulic Engineering-ASCE*, 126(4): 243–252.

Nardi, L., Rinaldi, M. & Solari, L. (2012). An experimental investigation on mass failures occurring in a riverbank composed of sandy gravel. *Geomorphology*, 163-164(0): 56–69. Meandering Channels.

Nelson, P. A., Brew, A. K. & Morgan, J. A. (2015). Morphodynamic response of a variable-width channel to changes in sediment supply. *Water Resources Research*, 51(7): 5717–5734.

Nicholas, A. P., Ashworth, P. J., Smith, G. H. S. & Sandbach, S. D. (2013). Numerical simulation of bar and island morphodynamics in anabranching megarivers. *Journal of Geophysical Research-Earth Surface*, 118(4): 2019–2044.

Nino, Y. & Garcia, M. H. (1992). Sediment bars in straight and meandering

channels: Experimental study on the resonance phenomenon (hes 42). *Civil Engineering Studies, Hydraulic Engineering Series no. 42*, Department of Civil Engineering, University of Illinois, Urbana, Illinois.

Ock, G., Sumi, T. & Takemon, Y. (2013). Sediment replenishment to downstream reaches below dams: implementation perspectives. *Hydrological Research Letters*, 7(3): 54–59.

Odgaard, A. J. & Bergs, M. A. (1988). Flow processes in a curved alluvial channel. *Water Resources Research*, 24(1): 45–56.

Osman, A. M. & Thorne, C. R. (1988). Riverbank stability analysis. 1. Theory. *Journal of Hydraulic Engineering-ASCE*, 114(2): 134–150.

Paintal, A. S. (1971). Concept of critical shear stress in loose boundary open channels. *Journal of Hydraulic Research*, 9(1): 91–113.

Parker, G. (1976). On the cause and characteristic scales of meandering and braiding in rivers. *Journal of Fluid Mechanics*, 76(3): 457–480.

Parker, G. (1978). Self-formed straight rivers with equilibrium banks and mobile bed. part 2. the gravel river. *Journal of Fluid Mechanics*, 89(1): 127–146.

Parker, G. (1984). Disscusion of 'Lateral bed-load transport on side slopes' from Ikeda (1982). *Journal of Hydraulic Engineering-ASCE*, 110(2): 197–199.

Parker, G. (1990). Surface-based bedload transport relation for gravel rivers. *Journal of Hydraulic Research*, 28(4): 417–436.

Parker, G. (2004). 1d sediment transport morphodynamics with applications to rivers and turbidity currents (electronic). online: http://hydrolab.illinois.edu/people/parkerg/morphodynamics_e-book.htm [01/16/2018].

Parker, G. (2008). Chap. 3: Transport of gravel and sediment mixtures. In M. Garcia (Ed.), *Sedimentation engineering: Processes, Measurements, Modeling, and Practice, Manuals and Reports on Engineering Practice No. 110*, 165–252. ASCE.

Parker, G. & Andrews, E. D. (1985). Sorting of bed load sediment by flow in meander bends. *Water Resources Research*, 21(9): 1361–1373.

Parker, G., Klingeman, P. C. & McLean, D. G. (1982). Bedload and size distribution in paved gravel-bed streams. *Journal of the Hydraulics Division*, 108(4): 544–571.

Pasternack, G. B., Wang, C. L. & Merz, J. E. (2004). Application of a 2D hydrodynamic model to design of reach-scale spawning gravel replenishment on the Mokelumne River, California. *River Research and Applications*, 20(2): 205–225.

Pizzuto, J. E. (1990). Numerical simulation of gravel river widening. *Water Resources Research*, 26(9): 1971–1980.

Pizzuto, J. E. (2008). Streambank erosion and river width adjustment. In M. Garcia (Ed.), *Sedimentation Engineering*, 387–438. American Society of Civil Engineers (ASCE), Reston, Virginia.

Podolak, C. J. P. & Wilcock, P. R. (2013). Experimental study of the response of a gravel streambed to increased sediment supply. *Earth Surface Processes and Landforms*, 38(14): 1748–1764.

Pryor, B. S., Lisle, T., Montoya, D. S. & Hilton, S. (2011). Transport and storage of bed material in a gravel-bed channel during episodes of aggradation and degradation: a field and flume study. *Earth Surface Processes and Landforms*, 36(15): 2028–2041.

Pulg, U. (2007). Die Restaurierung von Kiesleichplätzen. Landesfischereiverband Bayern e.V., München.

Qian, H., Cao, Z., Liu, H. & Pender, G. (2017). Numerical modelling of alternate bar formation, development and sediment sorting in straight channels. *Earth Surface Processes and Landforms*, 42(4): 555–574. ESP-15-0409.R2.

Requena, P. (2008). Seitenerosion in kiesführenden Flüssen - Prozessverständnis und quantitative Beschreibung ('Lateral erosion in gravel-bed rivers–Process understanding and quantitative description'). VAW Mitteilungen 210 (H.-E. Minor, ed.) Laboratory of Hydraulics, Hydrology and Glaciology (VAW), ETH Zurich (in German).

Ribberink, J. (1987). *Mathematical modelling of one-dimensional morphological*

changes in rivers with non-uniform sediment. PhD thesis, Delft University of Technology.

Rinaldi, M. & Darby, S. E. (2008). 9. modelling river-bank-erosion processes and mass failure mechanisms: progress towards fully coupled simulations. In H. Habersack, H. Piegay, & M. Rinaldi (Eds.), *Gravel Bed Rivers 6: From Process Understanding to River Restoration*, 213–239. Elsevier, Netherlands.

Rinaldi, M., Mengoni, B., Luppi, L., Darby, S. E. & Mosselman, E. (2008). Numerical simulation of hydrodynamics and bank erosion in a river bend. *Water Resources Research*, 44(9): W09428.

Rinaldi, M. & Nardi, L. (2013). Modeling interactions between riverbank hydrology and mass failures. *Journal of Hydrologic Engineering*, 18(10): 1231–1240.

Romanov, A. M., Hardy, J., Zeug, S. C. & Cardinale, B. J. (2012). Abundance, size structure, and growth rates of Sacramento pikeminnow (Ptychocheilus grandis) following a large-scale stream channel restoration in California. *Journal of Freshwater Ecology*, 27(4): 495–505.

Roni, P., Hanson, K. & Beechie, T. (2008). Global review of the physical and biological effectiveness of stream habitat rehabilitation techniques. *North American Journal of Fisheries Management*, 28: 856–890.

Rozovskii, I. (1961). Flow of Water in Bends of Open Channels. *Academy of Science of the Ukrainian SSR*.

Samadi, A., Amiri-Tokaldany, E. & Darby, S. E. (2009). Identifying the effects of parameter uncertainty on the reliability of riverbank stability modelling. *Geomorphology*, 106(3-4): 219–230.

Schaelchli, U., Breitenstein, M. & Kirchhofer, A. (2010). Kiesschüttungen zur Reaktivierung des Geschiebehaushalts der Aare - die kieslaichenden Fische freut's ('Gravel deposits to reactivate bed load transport at the Aare River–The fish are happy'). *Wasser Energie Luft*, 102(3): 209–213 (in German).

Schielen, R., Doelman, A. & de Swart, H. E. (1993). On the nonlinear dynamics of free bars in straight channels. *Journal of Fluid Mechanics*, 252: 325–356.

Schmautz, M. (2003). *Eigendynamische Aufweitung in einer geraden Gewässerstrecke–Entwicklung und Untersuchungen an einem numerischen Mod-*

ell ('Self-dynamic river widening in a straight channel–numerical model development and investigation'). PhD thesis, TU München, Germany (in German).

Schoklitsch, A. (1930). Der Wasserbau ein Handbuch für Studium und Praxis. *Schoklitsch, Armin.*

Schuurman, F., Shimizu, Y., Iwasaki, T. & Kleinhans, M. (2016). Dynamic meandering in response to upstream perturbations and floodplain formation. *Geomorphology*, 253: 94–109.

Sekine, M. & Kikkawa, H. (1992). Mechanics of saltating grains. *Journal of Hydraulic Engineering-ASCE*, 118(4): 536–558.

Sekine, M. & Parker, G. (1992). Bed-load transport on transverse slope. *Journal of Hydraulic Engineering-ASCE*, 118(4): 513–535.

Seminara, G. (1998). Stability and morphodynamics. *Meccanica*, 33(1): 59–99.

Shen, H. W. (1971). River Mechanics, Volume 1. *Shen, Hsieh Wen.*

Shields, A. (1936). *Anwendung der Ähnlichkeitsmechanik und der Turbulenzforschung auf die Geschiebebewegung ('Application of similarity mechanics and turbulence research to bed load entrainment').* PhD thesis, Preussische Versuchsanstalt für Wasserbau und Schiffbau, Berlin (in German).

Shvidchenko, A. B., Pender, G. & Hoey, T. B. (2001). Critical shear stress for incipient motion of sand/gravel streambeds. *Water Resources Research*, 37(8): 2273–2283.

Simon, A., Curini, A., Darby, S. E. & Langendoen, E. J. (2000). Bank and near-bank processes in an incised channel. *Geomorphology*, 35(3-4): 193–217.

Siviglia, A., Stecca, G., Vanzo, D., Zolezzi, G., Toro, E. F. & Tubino, M. (2013). Numerical modelling of two-dimensional morphodynamics with applications to river bars and bifurcations. *Advances in Water Resources*, 52: 243–260.

Sklar, L. S., Fadde, J., Venditti, J. G., Nelson, P., Wydzga, M. A., Cui, Y. & Dietrich, W. E. (2009). Translation and dispersion of sediment pulses in flume experiments simulating gravel augmentation below dams. *Water Resources Research*, 45: W08439.

Springer, F., Ullrich, C. & Hagerty, D. (1985). Streambank stability. *Journal of Geotechnical Engineering*, 111(5): 624–640.

Stecca, G., Siviglia, A. & Blom, A. (2014). Mathematical analysis of the Saint-Venant-Hirano model for mixed-sediment morphodynamics. *Water Resources Research*, 50(10): 7563–7589.

Stillwater Sciences (2001). Merced river restoration baseline studies volume ii: Geomorphic and riparian vegetation investigations report. Stillwater Sciences, Berkley, California.

Stillwater Sciences (2002). Merced river corridor restoration plan. Stillwater Sciences, Berkley, California.

Struiksma, N., Olesen, K. W., Flokstra, C. & De Vriend, H. J. (1985). Bed deformation in curved alluvial channels. *Journal of Hydraulic Research*, 23(1): 57–79.

Sutarto, T., Papanicolaou, A., Wilson, C. & Langendoen, E. (2014). Stability analysis of semicohesive streambanks with concepts: Coupling field and laboratory investigations to quantify the onset of fluvial erosion and mass failure. *Journal of Hydraulic Engineering-ASCE*, 140(9): 04014041.

Sutherland, A. J. (1992). Hiding function to predict self armouring. Proc. *Grain Sorting Seminar, Laboratory of Hydraulics, Hydrology and Glaciology (VAW), ETH Zurich, Mitteilungen No. 117*, D. Vischer (Ed.) : 273–298.

Sutherland, J., Peet, A. & Soulsby, R. (2004). Evaluating the performance of morphological models. *Coastal Engineering*, 51(8-9): 917–939. Coastal Morphodynamic Modeling.

Takebayashi, H., Egashira, S. & Jin, H. (1999). Numerical simulation of alternate bar formation. Proc. *River Sedimentation, Theory and Applications, Proceeding of the seventh international symposium on river sedimentation, Hong Kong, China, 1999*, Jayawardena, Lee, & Wang (Eds.) : 733–738.

Talmon, A., Struiksma, N. & Van Mierlo, M. (1995). Laboratory measurements of the direction of sediment transport on transverse alluvial-bed slopes. *Journal of Hydraulic Research*, 33(4): 495–517.

Thorne, C., Alonso, C., Bettess, R., Borah, D., Darby, S., Diplas, P., Julien,

P., Knight, D., Li, L., Pizzuto, J., Quick, M., Simon, A., Stevens, M., Wang, S., Watson, C. & ASCE Task Comm Hydraulics, Bank Mech, M. (1998). River width adjustment. I: Processes and mechanisms. *Journal of Hydraulic Engineering-ASCE*, 124(9): 881–902.

Thorne, C. R. (1982). Chap. 9, processes and mechanisms of river bank erosion. In R. D. Hey, J. C. Bathurst, & C. R. Thorne (Eds.), *Gravel-bed Rivers - Fluvial Processes, Engineering, and Management*, 227–271. Wiley, Chichester.

Thorne, C. R. & Abt, S. R. (1993). Analysis of riverbank instability due to toe scour and lateral erosion. *Earth Surface Processes and Landforms*, 18(9): 835–843.

Thorne, C. R. & Osman, A. M. (1988). Riverbank stability analysis. 2. Applications. *Journal of Hydraulic Engineering-ASCE*, 114(2): 151–172.

Thorne, C. R. & Tovey, N. K. (1981). Stability of composite river banks. *Earth Surface Processes and Landforms*, 6(5): 469–484.

Thorne, C. R., Zevenbergen, L. W., Pitlick, J. C., Rais, S., Bradley, J. B. & Julien, P. Y. (1985). Direct measurements of secondary currents in a meandering sand-bed river. *Nature*, 315: 746–747.

Toro, E. F. (2009). Riemann Solvers and Numerical Methods for Fluid Dynamics - A Practical Introduction. *Springer Berlin Heidelberg*.

Toro, E. F., Spruce, M. & Speares, W. (1994). Restoration of the contact surface in the hll-riemann solver. *Shock Waves*, 4(1): 25–34.

Tubino, M. (1991). Growth of alternate bars in unsteady flow. *Water Resources Research*, 27(1): 37–52.

Tubino, M., Repetto, R. & Zolezzi, G. (1999). Free bars in rivers. *Journal of Hydraulic Research*, 37(6): 759–775.

Tubino, M. & Seminara, G. (1990). Free-forced interactions in developing meanders and suppression of free bars. *Journal of Fluid Mechanics*, 214: 131–159.

Utz, R. M., Mesick, C. F., Cardinale, B. J. & Dunne, T. (2013). How does coarse gravel augmentation affect early-stage Chinook salmon Oncorhynchus

tshawytscha embryonic survivorship? *Journal of Fish Biology*, 82(5): 1484–1496.

van Rijn, L. C. (1984). Sediment transport, Part I: Bed load transport. *Journal of Hydraulic Engineering-ASCE*, 110(10): 1431–1456.

van Rijn, L. C. (1989). Handbook. Proc. *Sediment transport by currents and waves*, number Report H 461 in Delft Hydraulics. Delft Hydraulics.

Vanzo, D., Siviglia, A., Zolezzi, G., Stecca, M. & Tubino, M. (2001). Interaction between steady and migrating bars in straight channels. Proc. *River, Coastal and Estuarine Morphodynamics: RCEM 2011*: Tsinghua University Press, Beijing.

Venditti, J. G., Dietrich, W. E., Nelson, P. A., Wydzga, M. A., Fadde, J. & Sklar, L. (2010). Effect of sediment pulse grain size on sediment transport rates and bed mobility in gravel bed rivers. *Journal of Geophysical Research - Earth Surface*, 115.

Venditti, J. G., Nelson, P. A., Minear, J. T., Wooster, J. & Dietrich, W. E. (2012). Alternate bar response to sediment supply termination. *Journal of Geophysical Research: Earth Surface*, 117(F2): F02039.

Vetsch, D., Siviglia, A., Kammerer, S., Koch, A., Vanzo, D., Vonwiller, L., Gerber, M., Volz, C., Farshi, D., Mueller, R., Rousselot, P., Veprek, R. & Faeh, R. (2017a). *BASEMENT Basic Simulation Environment for Computation of Environmental Flow and Natural Hazard Simulation (2017). Version 2.7, ETH Zurich, VAW, 2006-2017.* VAW, ETH Zurich.

Vetsch, D. F., Siviglia, A. & D., V. (2017b). River Morphodynamic Modelling, Lecture Notes ETH Zurich, Spring semester.

Vigilar, G. & Diplas, P. (1997). Stable channels with mobile bed: Formulation and numerical solution. *Journal of Hydraulic Engineering-ASCE*, 123(3): 189–199.

Vigilar, G. & Diplas, P. (1998). Stable channels with mobile bed: Model verification and graphical solution. *Journal of Hydraulic Engineering-ASCE*, 124(11): 1097–1108.

Viparelli, E., Gaeuman, D., Wilcock, P. & Parker, G. (2011). A model to predict

the evolution of a gravel bed river under an imposed cyclic hydrograph and its application to the Trinity River. *Water Resources Research*, 47: W02533.

Vollmer, S. & Kleinhans, M. G. (2007). Predicting incipient motion, including the effect of turbulent pressure fluctuations in the bed. *Water Resources Research*, 43(5).

Volz, C. (2013). Numerical simulation of embankment breaching due to overtopping. VAW Mitteilungen 222 (R. M. Boes, ed.) Laboratory of Hydraulics, Hydrology and Glaciology (VAW).

Volz, C., Rousselot, P., Vetsch, D. & Faeh, R. (2012). Numerical modelling of non-cohesive embankment breach with the dual-mesh approach. *Journal of Hydraulic Research*, 50(6): 587–598.

Vonwiller, L., Vetsch, D. & Boes, R. (2015). On the role of modelling approach for simulation of bank erosion in straight, trapezoidal channel. Proc. *E-proceedings of the 36th IAHR World Congress, The Hague, The Netherlands* : 1485–1492.

Wilcock, P. R. & Crowe, J. C. (2003). Surface-based transport model for mixed-size sediment. *Journal of Hydraulic Engineering*, 129(2): 120–128.

Wong, M. & Parker, G. (2006). Reanalysis and correction of bed-load relation of meyer-peter and mueller using their own database. *Journal of Hydraulic Engineering*, 132(11): 1159–1168.

WSA (2006). Tracerversuch Iffezheim ('Tracer test at Iffezheim'). Wasser- und Schifffahrtsamt Freiburg (WSA), Bundesamt für Gewässerkunde (BFG) (in German).

WSV (2008). Sohlstabilisierungskonzept für die Elbe–von der Mündung bis zur Saalemündung ('River bed stabilization at the Elbe River–from the mouth to the confluence of the Saale River'). Wasser- und Schifffahrtsverwaltung des Bundes (WSV), Bundesanstalt für Gewässerkunde (BFG), Bundesanstalt für Wasserbau (BAW) (in German).

Wu, W. (2008). Computational River Dynamics. *Taylor & Francis, London.*

Wu, W., Wang, S. S. & Jia, Y. (2000). Nonuniform sediment transport in alluvial rivers. *Journal of Hydraulic Research*, 38(6): 427–434.

Yalin, M. & da Silva, A. (2001). Fluvial Processes. *International Association of Hydraulic Engineering and Research (IAHR), Delft, The Netherlands*.

Yang, C. T. (2006). Erosion and Sedimentation Manual. *U.S. Departement of the Interior, Bureau of Reclamation*.

Yen, C. & Lee, K. T. (1995). Bed topography and sediment sorting in channel bend with unsteady flow. *Journal of Hydraulic Engineering*, 121(8): 591–599.

Zanke, U., Roland, A., Saenger, N., Wiesemann, J. & Dahlem, G., Eds. (2008). *On the gravitational effects induced by transverse sloping beds*. Chinese-German Joint Symposium on Hydraulic and Ocean Engineering, Techn. Univ. Darmstadt, Darmstadt, Germany, Aug 24-30, 2008.

Zarn, B. (1992). Lokale Gerinneaufweitung–eine Massnahme zur Sohlenstabilisierung der Emme bei Utzenstorf ('Local river widening–an approach to prevent bed degradation of the Emme River at Utzenstorf). VAW Mitteilungen 118 (D. Vischer, ed.) Laboratory of Hydraulics, Hydrology and Glaciology (VAW), ETH Zurich (in German).

Zeug, S. C., Sellheim, K., Watry, C., Rook, B., Hannon, J., Zimmerman, J., Cox, D. & Merz, J. (2014). Gravel augmentation increases spawning utilization by anadromous salmonids: A case study from California, USA. *River Research and Applications*, 30(6): 707–718.

Zolezzi, G., Guala, M., Termini, D. & Seminara, G. (2005). Experimental observations of upstream overdeepening. *Journal of Fluid Mechanics*, 531: 191–219.

Zolezzi, G. & Seminara, G. (2001). Downstream and upstream influence in river meandering, part 1: General theory and application to overdeepening. *Journal of Fluid Mechanics*, 438: 183–211.

Nomenclature

List of Symbols

Greek symbols

α	[-]	Bed load pre-factor (MPM bed load formula)
β	[-]	Aspect ratio, half width to depth ratio, $\beta = W/(2h_0)$
β_C	[-]	Critical aspect ratio for free bar instability
β_R	[-]	Resonant aspect ratio: critical aspect ratio for free bar upstream migration
Δ	[-]	Relative sediment density under water, $\Delta = s - 1$
δ_f	[-]	Bed slope in flow direction
δ_l	[-]	Bed slope lateral to flow direction
φ_b	[rad]	Bed load transport direction with respect to main flow direction
φ_q	[rad]	main flow direction
γ	[°]	Angle of repose
λ	[-]	dimensionless wavenumber of alternate bars, $\lambda = \pi W/L$
ν	[m^2/s]	kinematic viscosity, $\nu = 10^{-6}\,m^2/s$ at temperature T=20 °C
ω	[rad/s]	Angular frequency of free bar migration (downstream, upstream)
Ω	[s^{-1}]	Growth rate of free bar instability
ρ	[kg/m^3]	Density of water, $\rho \approx 1000$ kg/m^3
ρ_b	[kg/m^3]	Bulk density of sediment, $\rho_b = (1-p)\rho_s$
ρ_s	[kg/m^3]	Density of sediment, $\rho_s \approx 2650$ kg/m^3

θ	[-]	Shields stress, dimensionless bed shear stress, $\theta = \|\vec{\mathbf{u}}\|^2/(c_f^2 g(s-1)d_m)$
θ_i	[-]	Shields stress, dimensionless bed shear stress, $\theta_i = \|\vec{\mathbf{u}}\|^2/(c_f^2 g(s-1)d_i)$
θ_c	[-]	Critical Shields stress for incipient motion
$\theta_{c,\delta}$	[-]	Critical Shields stress for incipient motion on arbitrary bed slope
θ_{cm}	[-]	Critical Shields stress for incipient motion of mean grain size diameter d_m of the mixture
σ	[mm]	Standard deviation of GSD
σ_ψ	[-]	Standard deviation of GSD on ψ-scale, $\sigma_\psi^2 = \int \left(\psi - \psi_m\right)^2 p(\psi) d\psi$
σ_g	[-]	Geometric standard deviation of GSD, $\sigma_g = 2^{\sigma_\psi}$ for log-normal GSD: $\sigma_g = \sqrt{d_{84}/d_{16}}$
τ_b	[N/m^2]	Bed shear stress, $\tau_b = u_0^2 \rho / c_f^2$ or $\tau_b = \|\vec{\mathbf{u}}\|^2 \rho / c_f^2$
τ_c	[N/m^2]	Critical bed shear stress for incipient motion
ψ	[-]	ψ-scale of grain size diameter d, $\psi = \log_2(d) = \ln(d)/\ln(2)$
ψ_m	[-]	Arithmetic mean of GSD on ψ-scale, $\psi_m = \int \psi p(\psi) d\psi$

Latin symbols

A	[m]	Amplitude of alternate bars, $A = z_{b,left} - z_{b,right}$
A_w	[m^2]	Area of water flow in cross section
c'	[kPa=kN/m^2]	soil cohesion
C	[m$^{1/2}$/s]	Chézy friction coefficient
c_f	[-]	Dimensionless Chézy friction coefficient, $c_f = C/\sqrt{g}$
c_L	[-]	Ratio of lift coefficient to drag coefficient
d	[mm]	Grain size diameter of sediment particle
d_{50}	[mm]	Grain size diameter of sediment mixture where 50 percent is finer
$d_{50,0}$	[mm]	Initial grain size diameter of sediment mixture where 50 percent is finer

d_{xx}	[mm]	Grain size diameter of sediment mixture where xx percent is finer, e.g. $xx = 16, 50, 84, 90$
d_g	[mm]	Geometric mean grain size diameter of GSD, $d_g = 2^{\psi_m}$, for log-normal GSD: $d_g = \sqrt{d_{84} d_{16}}$
d_i	[mm]	Grain size diameter of grain class i
d_m	[mm]	Mean grain size diameter of sediment mixture
d_s	[-]	Relative grain roughness, $d_s = d_{50}/h_0$
e	[-]	Bed load exponent (MPM bed load formula)
g	[m^2/s]	Gravitational acceleration, $g \approx 9.81$
$\vec{g}$	[m^2/s]	Gravitational acceleration vector
g_s	[kg^2/s]	Specific weight bed load transport rate
$g_{s,sub}$	[kg^2/s]	Specific bed load rate of the submerged weight
h_0	[m]	Reference uniform approach flow depth
f_s	[-]	Grain shape factor, $1 \leq f_s \leq 2$
F_{hc}	[m]	Hiding function applied on critical Shields stress
F_{ht}	[m]	Hiding function applied on Shields stress
H_{BM}	[m]	Bar height of free bars at equilibrium
H_d	[m]	Gravel deposit height
L	[m]	Wavelength of alternate bars
L_a	[m]	Thickness of active layer or mixing layer
L_c	[m]	Channel length
L_d	[m]	Gravel deposit length
L_g	[m]	Obstacle length
m	[-]	Lateral bar mode
M_l	[-]	Exponent for lateral bed slope effect
N_l	[-]	Factor for lateral bed slope effect (Ikeda parameter)
N_*	[-]	Curvature factor
p	[-]	Porosity of sediment mixture
$p(\psi)$	[-]	Probability density of GSD associated with size ψ
P_w	[m]	Wetted perimeter in cross section
Q	[m^3/s]	Water discharge
Q'	[m^3/s]	Reduced water discharge due to sidewall roughness
Q_b	[m^3/s]	Volumetric bed load transport rate (compact volume, no porosity)

$Q_{b,in}$	[m^3/s]	Volumetric bed load input at upper boundary (compact volume, no porosity)
q	[m^2/s]	Specific water discharge
q_b	[m^2/s]	Specific volumetric bed load transport rate (compact volume, no porosity)
$q_{b,in}$	[m^2/s]	Specific volumetric bed load input at upper boundary
$q_{b,0}$	[m^2/s]	Initial specific volumetric equilibrium bed load transport rate
R	[m]	Radius of river bend
R_c	[m]	Radius to center line of river bend
R_h	[m]	Hydraulic radius $R_h = A_w/P_w$
Re^*	[-]	Particle Reynolds number $Re^* = u_* d/\nu$
Re_c^*	[-]	Critical particle Reynolds number $Re_c^* = u_{*c} d/\nu$
S	[-]	Bed slope (meter elevation per meter length)
S_0	[-]	Initial bed slope at equilibrium bed load transport
s	[-]	Specific density, $s = \rho_s/\rho \approx 2.65$
$\vec{\mathbf{u}}$	[m/s]	Depth-averaged flow velocity vector, $\vec{\mathbf{u}} = (u, v)^T$
u	[m/s]	Depth-averaged flow velocity in x-direction
u_0	[m/s]	Average approach flow velocity
u_*	[m/s]	Shear velocity $u_* = \sqrt{\tau_b/\rho}$
u_{*c}	[m/s]	Critical shear velocity $u_{*c} = \sqrt{\tau_c/\rho}$
v	[m/s]	Depth-averaged flow velocity in y-direction
W	[m]	River channel width
W_d	[m]	Gravel deposit width
W_g	[m]	Obstacle width
x	[m]	Horizontal x-coordinate
y	[m]	Horizontal y-coordinate
z	[m, m a.s.l.]	Vertical z-coordinate, elevation
z_b	[m, m a.s.l.]	Elevation of river bed topography
$z_{b,left}$	[m, m a.s.l.]	Elevation of river bed topography on the orographic left side of the channel
$z_{b,right}$	[m, m a.s.l.]	Elevation of river bed topography on the orographic right side of the channel

List of Acronyms

BSS	Brier Skill Score
FFT	Fast Fourier Transform
FOEN	Federal Office for the Environment of Switzerland
GSD	grain size distribution
HPP	hydropower plant
MAE	mean absolute error
MPM	Meyer-Peter & Müller (1948) (bed load formula)
MSE	mean square error
RMSE	root mean square error
ROR	run-of-river
SWE	shallow-water equations

A. Appendix

A.1. Sensitivity Analysis of Model Parameters for Ikeda's Experiment at Cross Section CS9

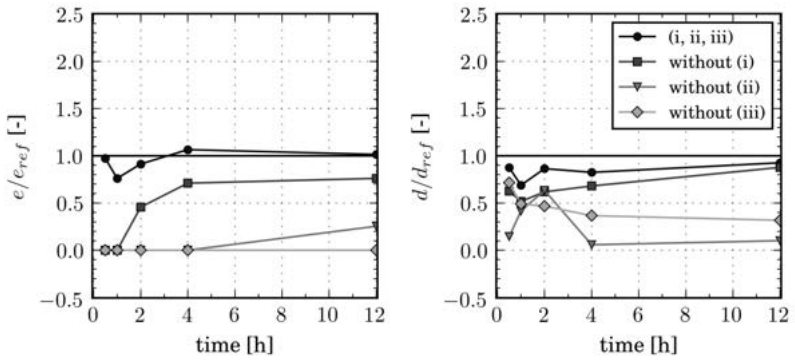

Fig. A.1.: Sensitivity of (i) Shields correction due to local bed slope, (ii) lateral transport approach, and (iii) gravitational transport approach with regard to bank erosion e (left) and deposition d (right) at CS9

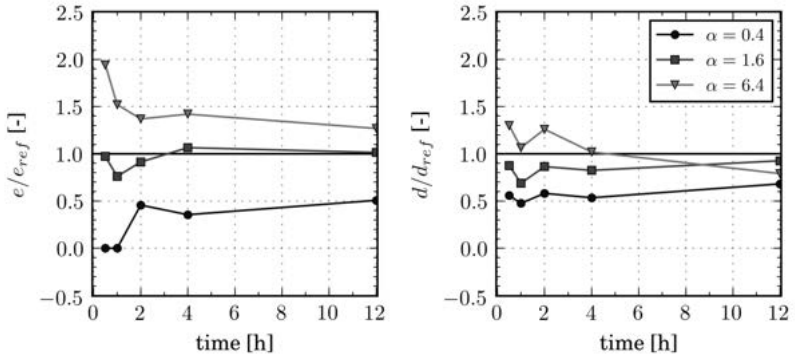

Fig. A.2.: Sensitivity of bed load calibration factor α with regard to lateral erosion e (left) and deposition d (right) at CS9

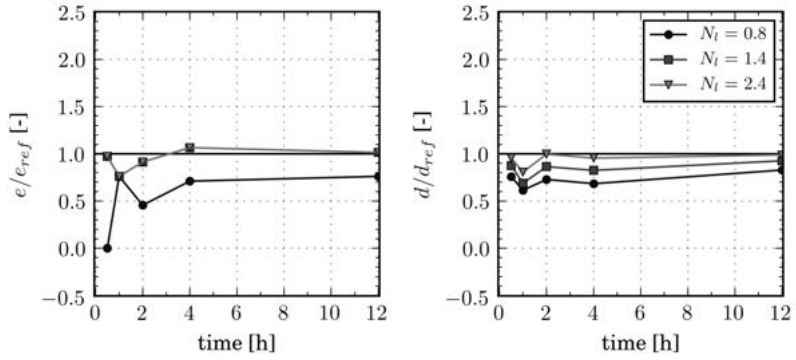

Fig. A.3.: Sensitivity of lateral bed slope factor N_l with regard to lateral erosion e (left) and deposition d (right) at CS9

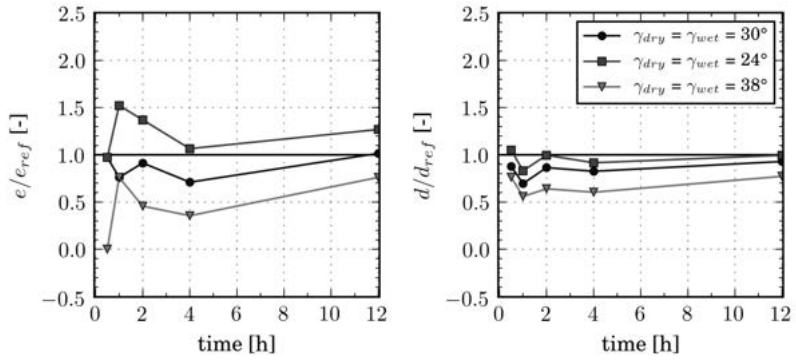

Fig. A.4.: Sensitivity of angle of repose for dry and wet material (γ_{dry} and γ_{wet}) with regard to lateral erosion e (left) and deposition d (right) at CS9

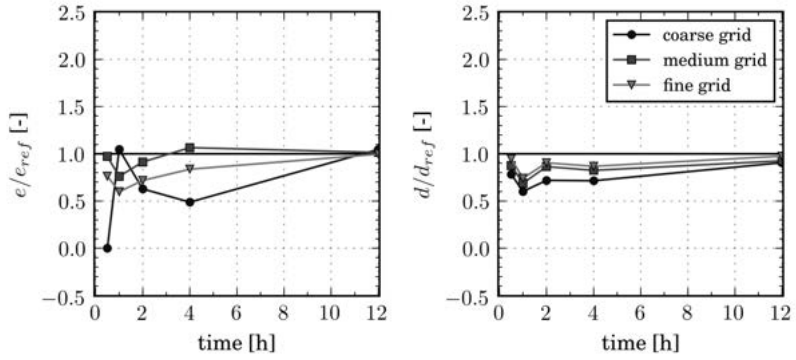

Fig. A.5.: Sensitivity of grid resolution with regard to lateral erosion e (left) and deposition d (right) at CS9

A.2. Free Bars Response to Sediment Supply Reduction

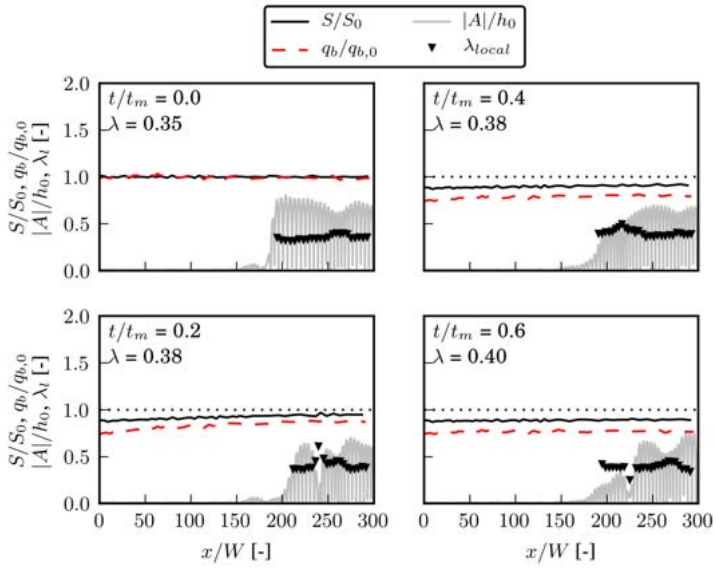

Fig. A.6.: Response of free bar morphology to sediment supply reduction and morphological 1-D effect for $q_{b,in}/q_{b,0} = 0.75$

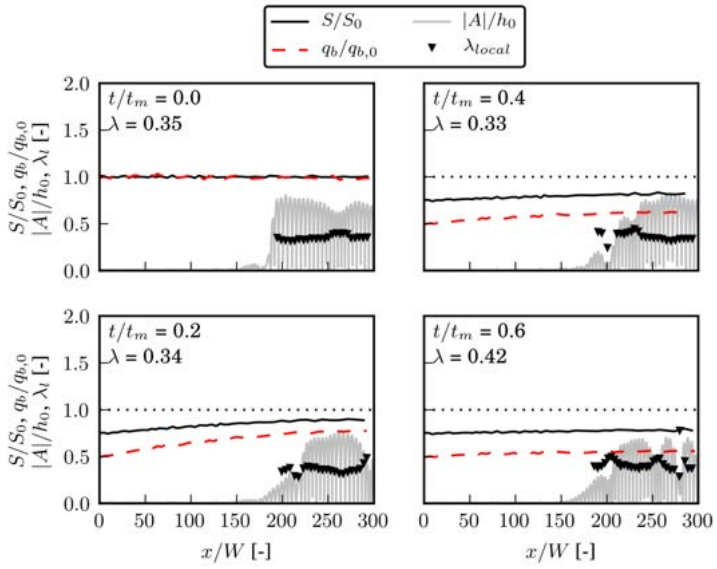

Fig. A.7.: Response of free bar morphology to sediment supply reduction and morphological 1-D effect for $q_{b,in}/q_{b,0} = 0.5$

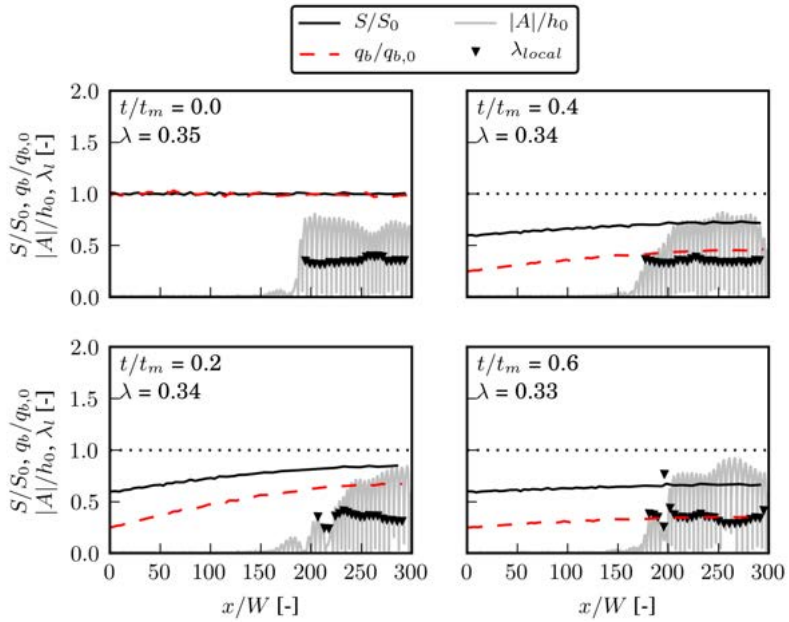

Fig. A.8.: Response of free bar morphology to sediment supply reduction and morphological 1-D effect for $q_{b,in}/q_{b,0} = 0.25$

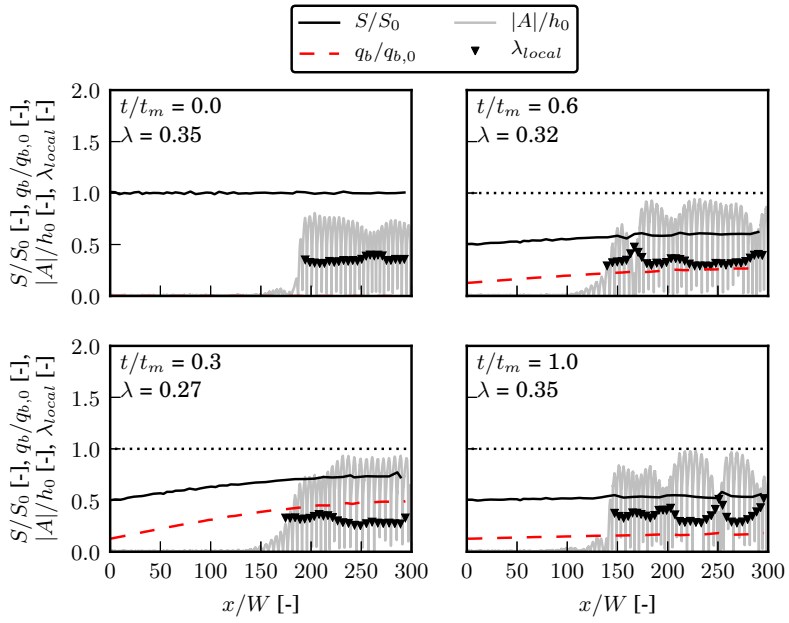

Fig. A.9.: Response of free bar morphology to sediment supply reduction and morphological 1-D effect for $q_{b,in}/q_{b,0} = 0.125$

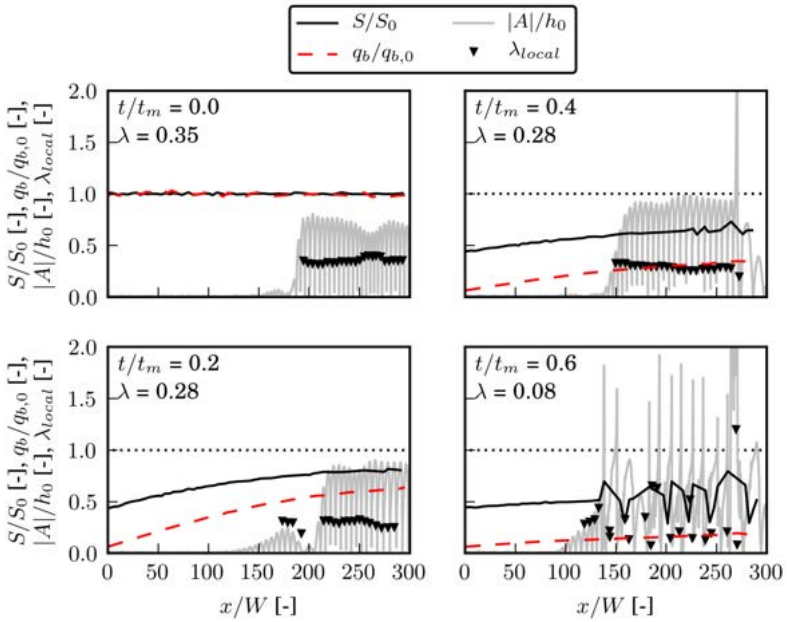

Fig. A.10.: Response of free bar morphology to sediment supply reduction and morphological 1-D effect for $q_{b,in}/q_{b,0} = 0.0625$

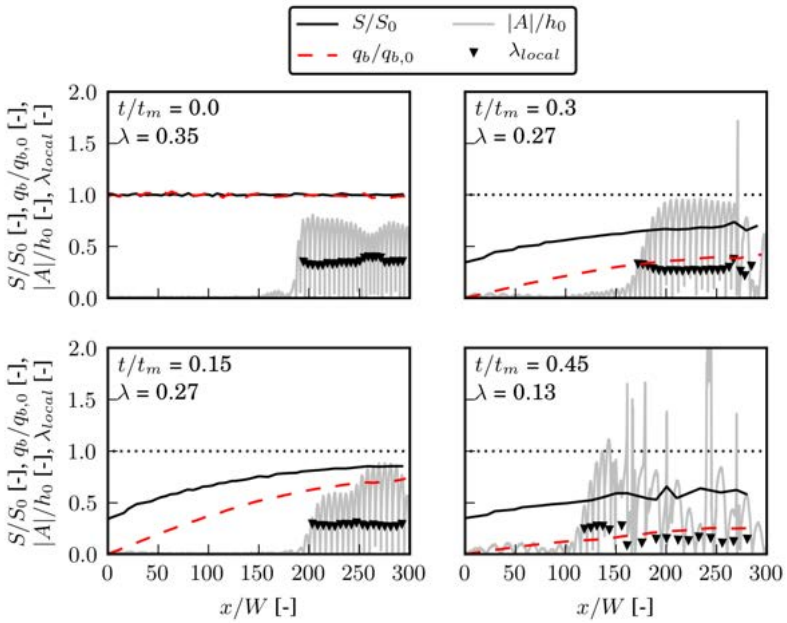

Fig. A.11.: Response of free bar morphology to sediment supply reduction and morphological 1-D effect for $q_{b,in}/q_{b,0} = 0.0$

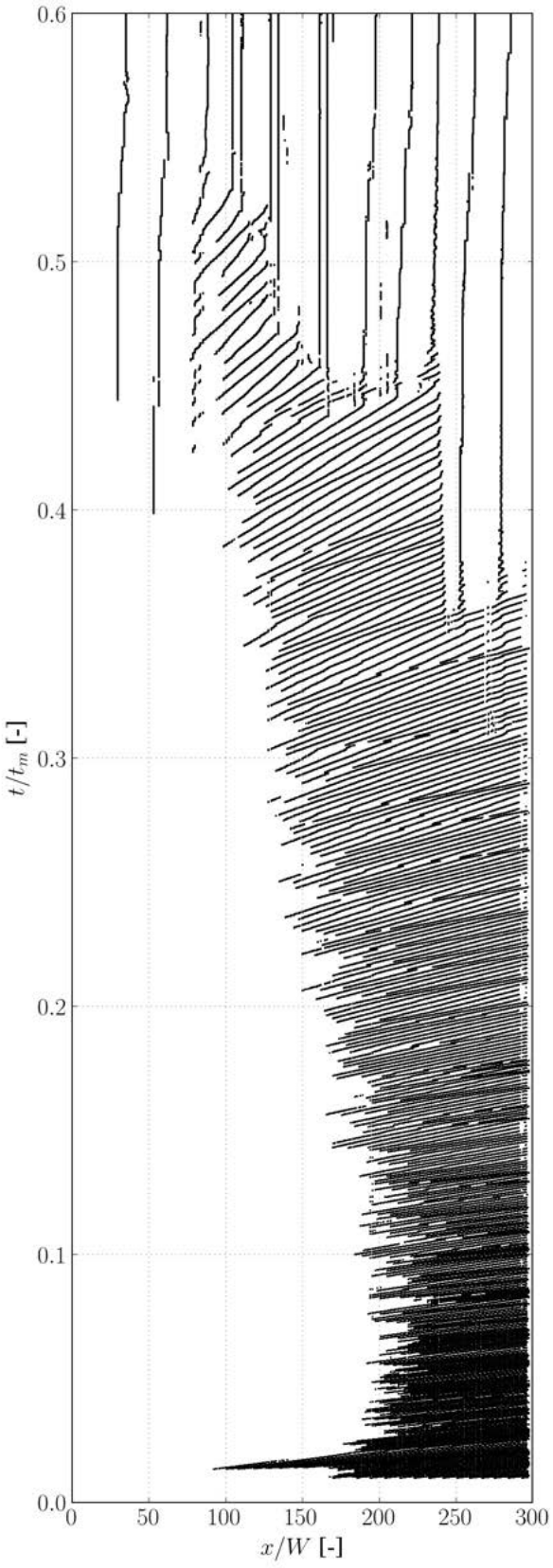

Fig. A.12.: Bar head tracking over time, free bars response to sediment supply termination $q_{b,in}/q_{b,0} = 0.0$

A.3. Steady Bars Response to Sediment Supply Reduction

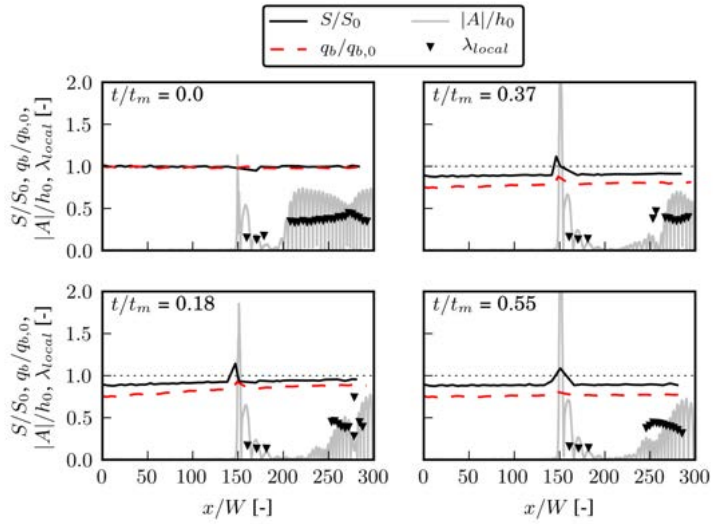

Fig. A.13.: Response of steady bar morphology to sediment supply reduction and morphological 1-D effect for $q_{b,in}/q_{b,0} = 0.75$

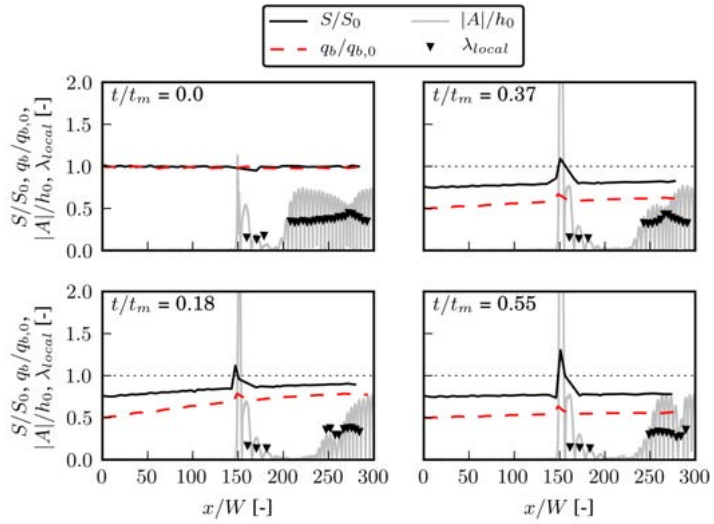

Fig. A.14.: Response of steady bar morphology to sediment supply reduction and morphological 1-D effect for $q_{b,in}/q_{b,0} = 0.5$

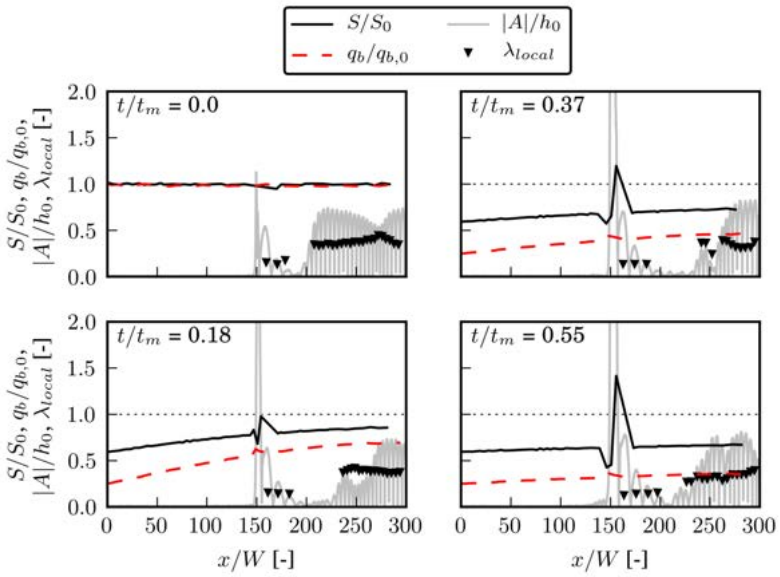

Fig. A.15.: Response of steady bar morphology to sediment supply reduction and morphological 1-D effect for $q_{b,in}/q_{b,0} = 0.25$

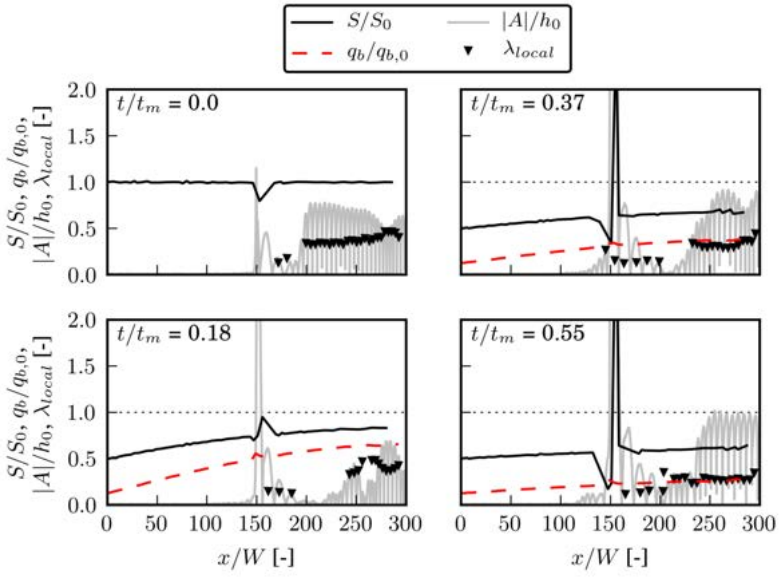

Fig. A.16.: Response of steady bar morphology to sediment supply reduction and morphological 1-D effect for $q_{b,in}/q_{b,0} = 0.125$

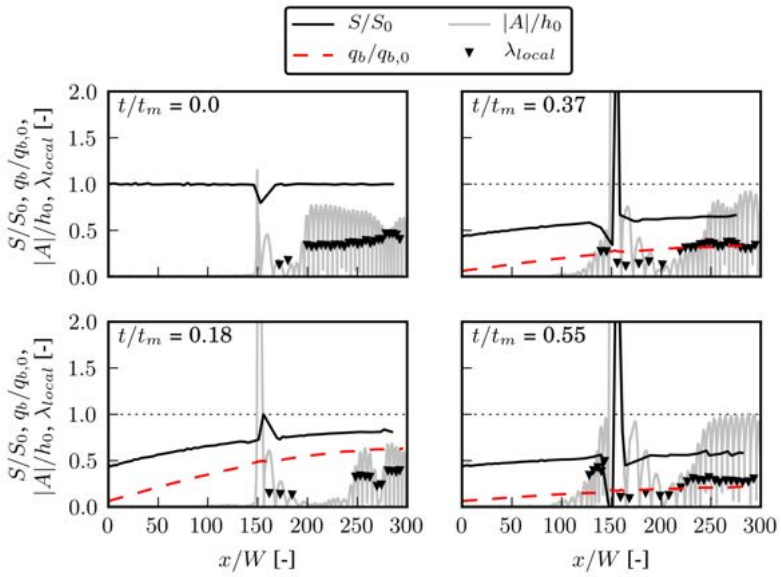

Fig. A.17.: Response of steady bar morphology to sediment supply reduction and morphological 1-D effect for $q_{b,in}/q_{b,0} = 0.0625$

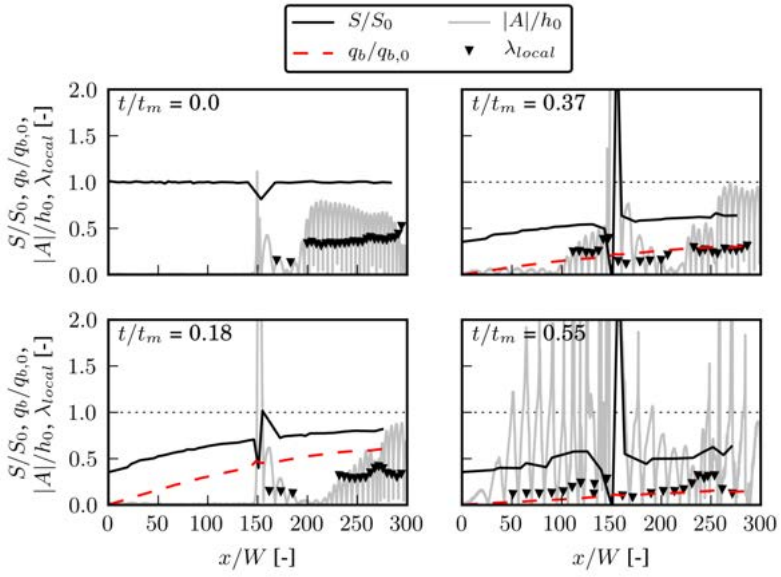

Fig. A.18.: Response of steady bar morphology to sediment supply reduction and morphological 1-D effect for $q_{b,in}/q_{b,0} = 0.0$

A.4. Point Bar in 180° River Bend: Response to Sediment Supply Reduction

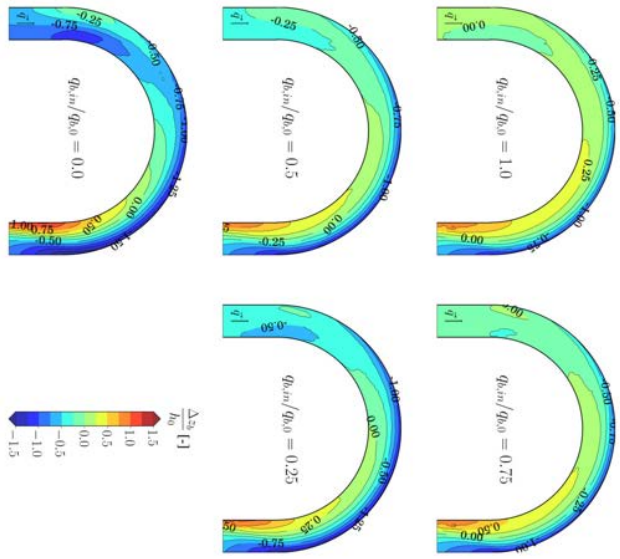

Fig. A.19.: Bed elevation change Δz_b due to sediment supply reduction: uniform sediment, $Q = 500\,\mathrm{m}^3/\mathrm{s}$, $N_* = 7$ (setup 1)

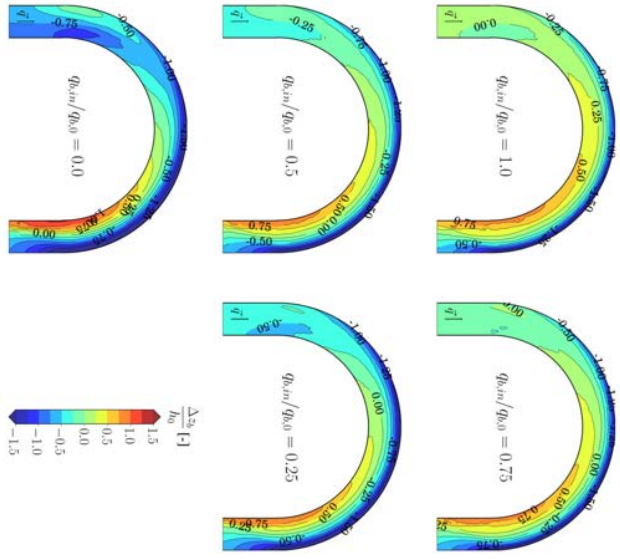

Fig. A.20.: Bed elevation change Δz_b due to sediment supply reduction: uniform sediment, $Q = 500\,\mathrm{m}^3/\mathrm{s}$, $N_* = f(C)$ (setup 2)

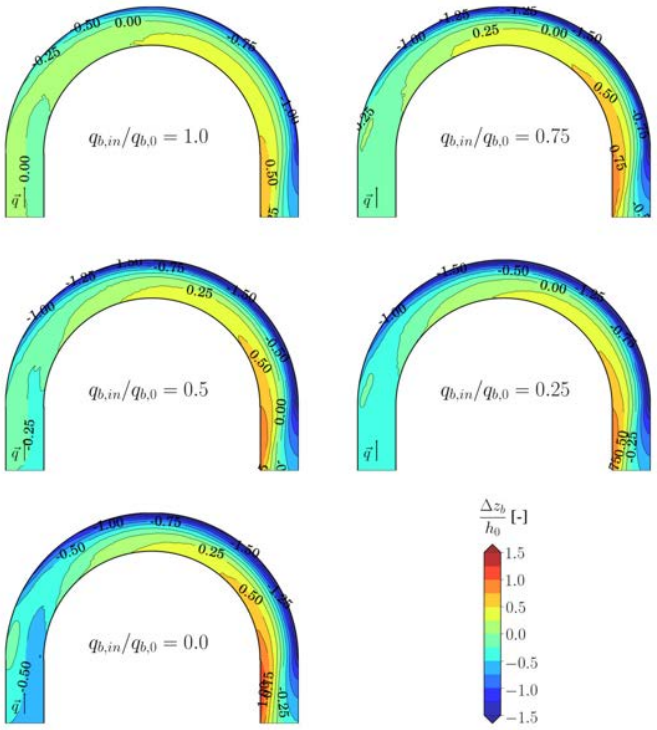

Fig. A.21.: Bed elevation change Δz_b due to sediment supply reduction: uniform sediment, $Q = 800\,\mathrm{m}^3/\mathrm{s}$, $N_* = 7$ (setup 3)

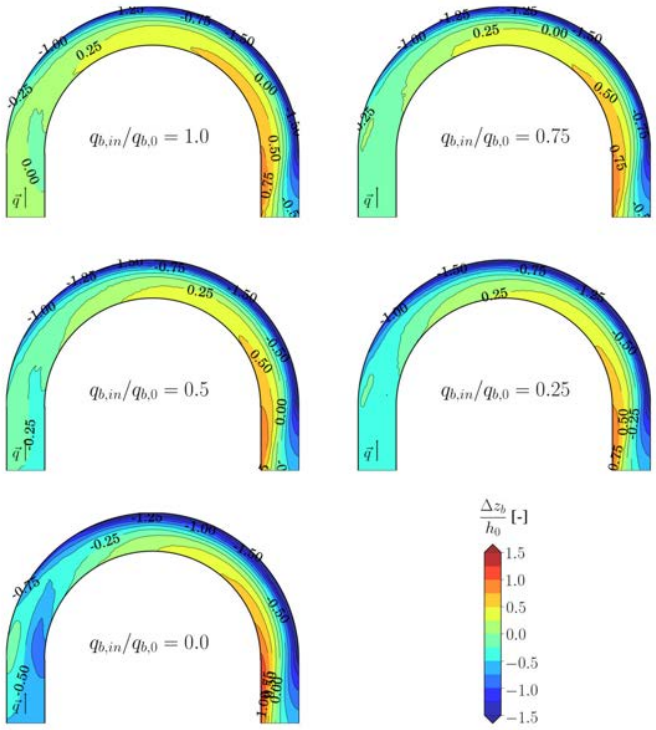

Fig. A.22.: Bed elevation change Δz_b due to sediment supply reduction: uniform sediment, $Q = 800\,\mathrm{m}^3/\mathrm{s}$, $N_* = f(C)$ (setup 4)

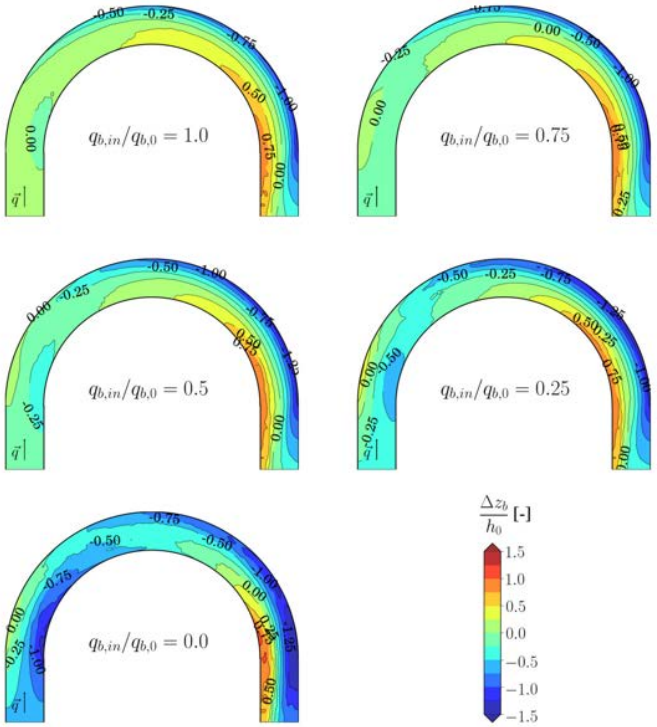

Fig. A.23.: Bed elevation change Δz_b due to sediment supply reduction: non-uniform sediment, $Q = 500\,\mathrm{m}^3/\mathrm{s}$, $N_* = 7$ (setup 5)

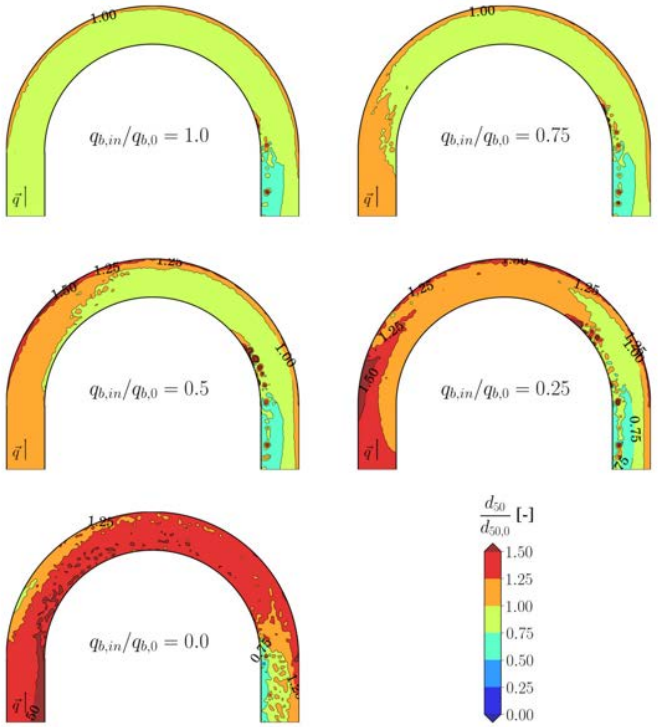

Fig. A.24.: Grain sorting effect $d_{50}/d_{50,0}$ due to sediment supply reduction: non-uniform sediment, $Q = 500\,\mathrm{m}^3/\mathrm{s}$, $N_* = 7$ (setup 5)

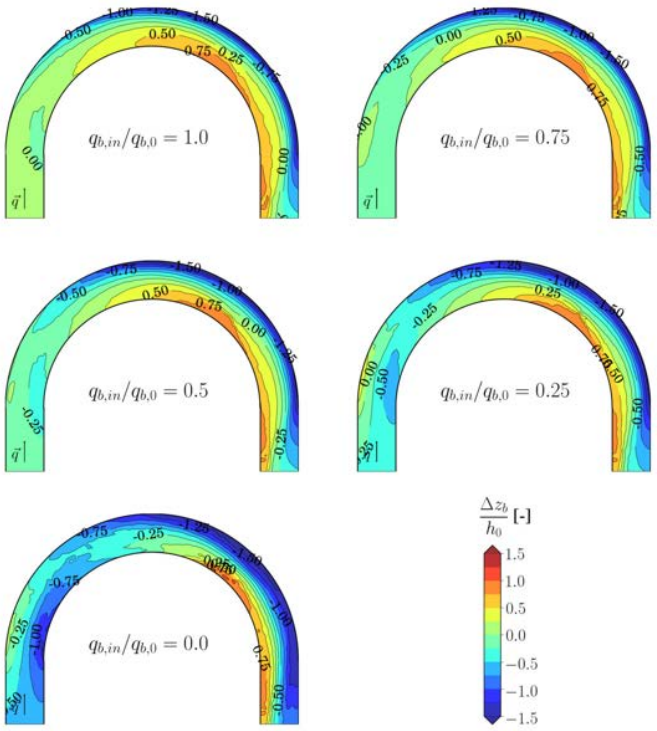

Fig. A.25.: Bed elevation change Δz_b due to sediment supply reduction: non-uniform sediment, $Q = 500\,\mathrm{m}^3/\mathrm{s}$, $N_* = f(C)$ (setup 6)

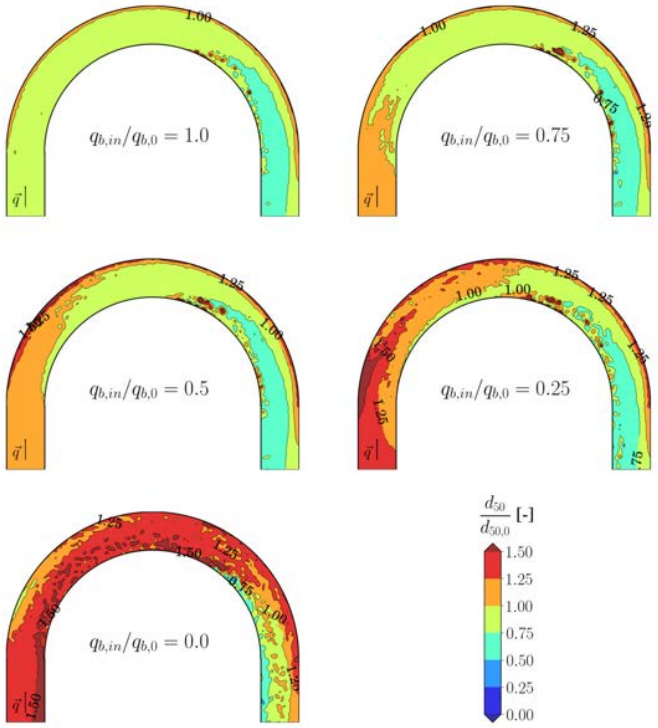

Fig. A.26.: Grain sorting effect $d_{50}/d_{50,0}$ due to sediment supply reduction: non-uniform sediment, $Q = 500\,\mathrm{m}^3/\mathrm{s}$, $N_* = f(C)$ (setup 6)

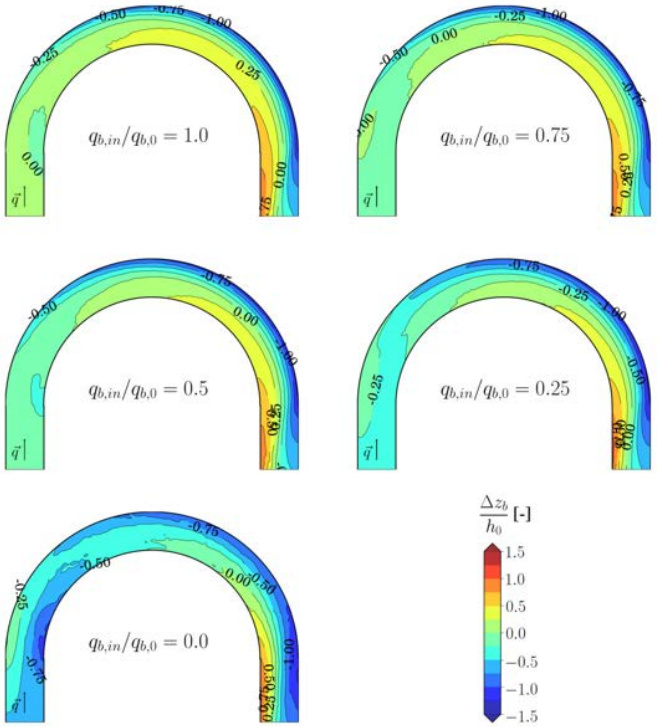

Fig. A.27.: Bed elevation change Δz_b due to sediment supply reduction: non-uniform sediment, $Q = 800\,\mathrm{m}^3/\mathrm{s}$, $N_* = 7$ (setup 7)

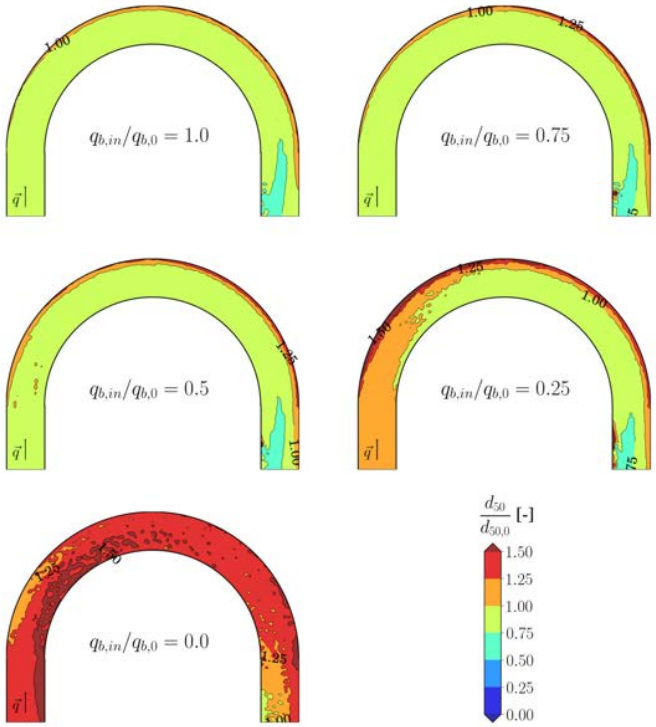

Fig. A.28.: Grain sorting effect $d_{50}/d_{50,0}$ due to sediment supply reduction: non-uniform sediment, $Q = 800\,\mathrm{m}^3/\mathrm{s}$, $N_* = 7$ (setup 7)

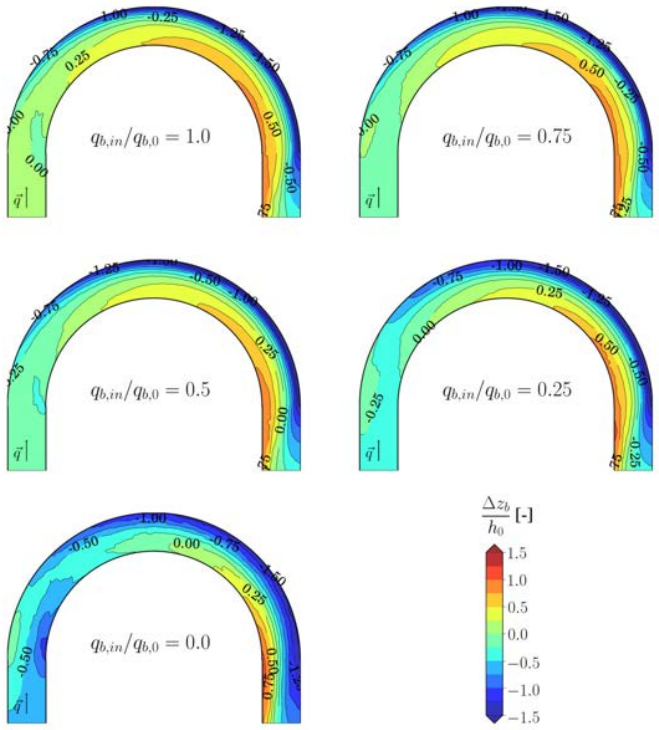

Fig. A.29.: Bed elevation change Δz_b due to sediment supply reduction: non-uniform sediment, $Q = 800\,\mathrm{m}^3/\mathrm{s}$, $N_* = f(C)$ (setup 8)

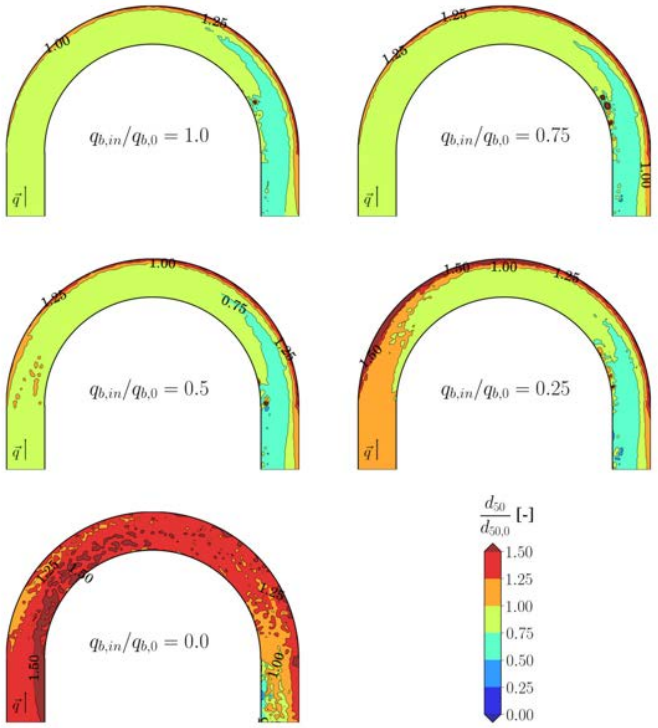

Fig. A.30.: Grain sorting effect $d_{50}/d_{50,0}$ due to sediment supply reduction: non-uniform sediment, $Q = 800\,\mathrm{m}^3/\mathrm{s}$, $N_* = f(C)$ (setup 8)

A.5. Free Bars Potential of Swiss Gravel-Bed Rivers

Alternate free bars are a morphological pattern of first lateral mode ($m = 1$) that occur as an intrinsic instability of water flow and non-cohesive sediment transport in nearly straight river reaches (Colombini *et al.*, 1987). Higher mode bars, such as central bars ($m = 2$) or braided rivers ($m \geq 3$, see Fig. 3.13) require an even larger aspect ratio β during stages of significant bed load transport. However, very often β is too small during significant bed load transport and hence alternate free bars are suppressed resulting in a flat river bed.

Table A.1 shows a rough estimate of the bar mode m according to the physically based predictor of Crosato & Mosselman (2009) (Eq. 3.48) for selected Swiss gravel-bed rivers. Thereby, the discharge corresponded to a flood with a return period of five years (HQ_5). Note that the values for the median grain size diameter d_{50}, bed slope S, river width W, and Chézy friction coefficient C are partly rough assumptions and partly originate from various VAW-reports (e.g. Zarn, 1992; Marti, 2006; Requena, 2008). This analysis provides a rough overview on the potential of alternate free bars in Swiss gravel-bed rivers. A good example for free bars is the Alpine Rhine River between the Landquart River tributary upstream and the Ill River tributary downstream. For this river section, the predictor of Crosato & Mosselman (2009) suggests a bar mode of $m \approx 0.94$ giving a reasonable indication of alternate free bars. Many trained and straightened gravel-bed rivers in Switzerland have the potential to form alternate free bars. For certain rivers, a minor increase of the aspect ratio and hence of the river width would favor the formation of alternate free bars. In some cases, there are indications of alternate bars, such as in the Emme River near Utzensdorf. However, it seems that free bars are additionally suppressed by vertical bed sills and ramps.

In a next step, the analysis on free bar formation would include the evaluation of the relative distance to the critical aspect ratio for varying discharge ($(\beta - \beta_C)/\beta_C = f(Q)$), such as shown in Fig. A.31 for the case of the Alpine Rhine River. The range for free bar formation is delimited on one side by the discharge below incipient motion (no bed load transport) and on the other side by the discharge above which free bar formation is suppressed (sub-critical conditions). Finally, the influence of flood hydrographs on free bar instability can be evaluated using the analytical non-linear theory of Tubino (1991) or non-linear numerical simulations.

Table A.1.: Estimation of free bar mode m of selected gravel-bed rivers in Switzerland according to the predictor of Crosato & Mosselman (2009) for a flood with a return period of five years (HQ_5)

River	Location	d_{50} [m]	S [-]	W [m]	C [$m^{1/2}/s$]	HQ_5 [m^3/s]	m [-]
Aare	Wynau	0.05	0.001	80	49	860	0.71
Alpine Rhine	Buchs	0.042	0.0018	90	51	1300	0.94
Emme	Utzensdorf	0.043	0.0042	30	43	200	0.75
Kleine Emme	Malters-Emmen	0.10	0.005	40	39	400	0.77
Limmat	Dietikon	0.054	0.0015	50	46	400	0.63
Reuss	Perlen-Gisikon	0.05	0.002	60	46	560	0.81
Sihl	Adliswil	0.08	0.0038	35	37	165	0.92
Toess	Daettlikon	0.04	0.0033	20	41	48	0.78

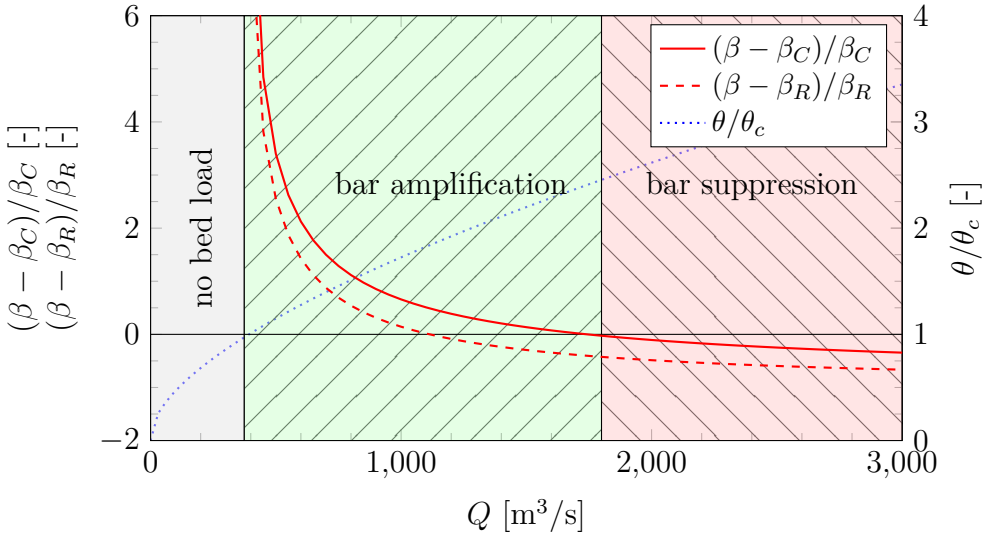

Fig. A.31.: Relative distance to the critical aspect ratio ($(\beta - \beta_C)/\beta_C$) and relative distance to the resonant aspect ratio ($(\beta - \beta_R)/\beta_R$) for varying discharge Q of the Alpine Rhine River using Chézy's friction law, bed load formula of Wong & Parker (2006), $N_l = 1.38$ ($r = N_l\sqrt{\theta_c} = 0.3$), $d_{50} = 0.042\,\mathrm{m}$, $S = 0.0018$, and $W = 90\,\mathrm{m}$ (Adami *et al.*, 2016b)